Winter 12-16-2022

Implementation and Testing of Surface Acoustic Wave Strain Sensors for Harsh Environment Applications

David W. Leff
University of Maine, david.leff@maine.edu

IMPLEMENTATION AND TESTING OF SURFACE ACOUSTIC WAVE STRAIN SENSORS FOR HARSH ENVIRONMENT APPLICATIONS

By

David Winston Leff

B.S. SUNY Polytechnic Institute, 2019

A THESIS

Submitted in Partial Fulfillment of the

Requirements for the Degree of

Master of Science

(in Electrical Engineering)

The Graduate School

The University of Maine

December 2022

Advisory Committee:

Mauricio Pereira da Cunha, Professor of Electrical and Computer Engineering, Advisor

Donald Hummels, Professor of Electrical and Computer Engineering

Robert Lad, Professor of Physics

Senthil Vel, Professor of Mechanical Engineering

IMPLEMENTATION AND TESTING OF SURFACE ACOUSTIC WAVE STRAIN SENSORS FOR HARSH ENVIRONMENT APPLICATIONS

By David W. Leff
Thesis Advisor: Dr. Mauricio Pereira da Cunha

An Abstract of the Thesis Presented
In Partial Fulfillment of the Requirements for the
Degree of Master of Science
(in Electrical Engineering)
December 2022

Static and dynamic strain sensing is needed in high-temperature, harsh environment applications for structural health monitoring, condition-based maintenance, process efficiency monitoring, and operator safety in power plants, oil wells, metallurgy, aerospace, and automotive industries. Some challenges for sensors in these environments include device integrity, stability, mounting, packaging, and data acquisition techniques. In addition, it is desirable for sensors in high-temperature harsh-environments to be compact, operate without a battery, and have wireless interrogation capabilities so that they can be installed in small, hard-to-reach locations that otherwise could not be monitored.

Surface acoustic wave resonator (SAWR) sensors can respond to the demands of high-temperature, harsh-environment applications due to: (i) the existence of piezoelectric substrates and thin film electrode technology capable of operating at high temperatures (above 1000°C); (ii) sensor response to static and dynamic strain components; (iii) small sensor size; (iv) wireless interrogation capability; (v) and battery-free operation. SAWR strain sensing for harsh-

environment applications needs to address some of the issues inherent to these environments, such as: (i) sensor mounting techniques to metal parts, (ii) stability of the sensor and sensor mounting technique, (iii) packaging of the sensor, and (iv) cross-sensitivity between strain and temperature.

In this work, langasite (LGS) SAWR sensors were used, due to the proven performance of these devices at high temperature at UMaine, for static and dynamic strain measurements. Simulation of the strain due to thermal expansion and mechanical loads was performed to determine where there were concentrations of high strain at the adhesive/LGS and adhesive/metal interfaces as well as adhesive shaping designs aimed at minimizing this strain. Wireless interrogation of SAWR static and dynamic strain sensors using inductive coupling techniques was achieved up to 400°C. After temperature cycling, it was determined that cracking was taking place within the ceramic adhesive layer and along the borders of the SAWR sensor chip that causes degradation and inconsistency in the SAWR strain response. Based on these results, further investigation of static and dynamic strain sensors using alternative adhesives was done limited to 200°C. Two polymer epoxy adhesives showed stability after temperature cycling between 50°C and 250°C. Using the polymer epoxy that showed greater stability for the static strain, dynamic strain was measured. The test setup implementation was investigated towards improving the stability of dynamic strain sensor measurements after temperature cycling. Finally, a method for extracting temperature and the dynamic strain magnitude and spectral components was devised and implemented using a single SAWR sensor.

DEDICATION

This thesis is dedicated in memory of my grandmother, Esther Leff.

ACKNOWLEDGEMENTS

Firstly, I want to thank my advisor, Prof. Mauricio Pereira da Cunha, for his help, support, and guidance throughout my graduate education. His advice, knowledge, and readiness to help was invaluable in my research and coursework.

I want to acknowledge Prof. Robert Lad for weekly input on my research work over the course of my degree as a co-principal investigator on the project I was on and for being on my advisory committee and Prof. Donald Hummels and Prof. Senthil Vel, for their time and help in my research as part of my advisory committee.

I want to thank Dr. Syeda Fizzah Jilani, Dr. Anin Maskay, and Shane Winters for their collaboration in this work; Armando Ayes for teaching me important laboratory skills; Dr. George Bernhardt and Michael Call for device fabrications and general assistance; Nicholas Aiken for antenna design and fabrication; Luke Doucette, Dr. Morton Greenslit, and Sri Lekha Srimat Kilambi for their willingness to help in periodic, research-related tasks; Environetix Technologies Corporation for lending test beams, the EVHT-300 system, and sensor antennas used in this work; and John Belding and the AMC staff for fabrication of a static strain beam and beam mount.

I also want to thank the Department of Energy (Grant # DE-FE0031550) for funding my work and the ECE department and FIRST for allowing me to conduct research at their facilities.

Finally, I want to thank God for the grace, knowledge, and perseverance during my time at the University of Maine. I want to thank my parents, Mark and Karen Leff, and brother, Dan Leff, for their love and support throughout my life, my friends, the Newman Center community, FOCUS missionaries, Parish of the Resurrection of the Lord, my spiritual director Fr. Kyle Doustou, and Wayne Melanson for their support and encouragement during my time at the University of Maine.

TABLE OF CONTENTS

LIST OF TABLES

LIST OF FIGURES

CHAPTER 1
INTRODUCTION

Sensors for high-temperature (HT), harsh-environment (HE) applications, including power plants, oil wells, metallurgy, aerospace, and automotive, are needed for structural health monitoring (SHM), condition-based maintenance (CBM), process efficiency monitoring, and worker safety [1]-[9]. These environments can reach temperatures from 100°C to over 1000°C and typically have particles in the air that can compromise sensors and interrogation equipment if they are not properly protected from the environment [10]. Because of this, high-temperature harsh environments pose challenges for sensor system implementation including sensor integrity and stability, mounting, packaging, and data acquisition.

Surface acoustic wave (SAW) sensor technology can address the difficulties for high-temperature harsh-environment sensor operation while providing a stable sensor response over a long period of time [10], [11]. SAW sensors can be used for a multitude of sensing applications, including temperature [12], static and dynamic strain [13], [14], torque [15], pressure [16], and gas [17], and can be utilized in high-temperature environments depending on the piezoelectric substrate/thin film and electrode material used [10]. In addition to operation at high-temperature, SAW sensors have additional features, including the ability to be interrogated wirelessly, battery-free operation, and small size that make them attractive for use in high-temperature harsh environments. Wireless operation is especially important because it allows sensors to be placed in: (i) moving and rotating parts; and (ii) hard-to-reach locations and eliminates the need for fragile bond wires that can easily break, in particular in the presence of dynamic strain or vibration [10].

In this thesis, SAW resonator (SAWR) sensors are explored as static and dynamic strain sensors in high-temperature environments. When using SAWR sensors for high-temperature static

and dynamic strain sensing, challenges that arise include: (i) long-term attachment of the sensor to metal parts for strain transfer between the part and sensor and stable under temperature cycling to allow sensor calibration; (ii) cross-sensitivity between static strain, dynamic strain, temperature, and other measurands; (iii) packaging and sensor protection; and (iv) data collection methods. The contributions of this thesis are: (i) development of a model in COMSOL Multiphysics to simulate and separate the thermal from the load related strain; (ii) implementation of wireless sensor platforms for static and dynamic strain sensing up to 400°C; (iii) analysis of adhesive layer deterioration under temperature cycling for the SAWR dynamic strain sensor; and (iv) creating and implementing a procedure to measure temperature, dynamic strain magnitude, and dynamic strain spectral components using a single SAWR sensor.

1.1 Motivation

According to the U.S. Energy Information Administration, world energy consumption from 2020 to 2050 is expected to increase by almost 50%, as shown in Figure 1.1a [18]. With an increasing demand for energy and a changing environment of energy production sources (Figure 1.1b) [18], there is an increased need for sensor systems that can measure static and dynamic strain in powerplant and other energy related harsh environments to ensure the proper operation and structural integrity of these structures and equipment as well as in other industrial equipment and processes which operate under similar conditions. In powerplant environments, sensing is required on many structures, including boiler tubes, combustion chambers, turbines, and exhaust ducts to ensure proper operation of equipment to increase efficiency, reduce operation and repair costs, and ensure worker safety [1]-[4], [6].

Sensors for metal fabrication are also needed to increase process efficiency, implement process automation, ensure structural integrity, and ensure stability in operations [9], [19]. In ladle

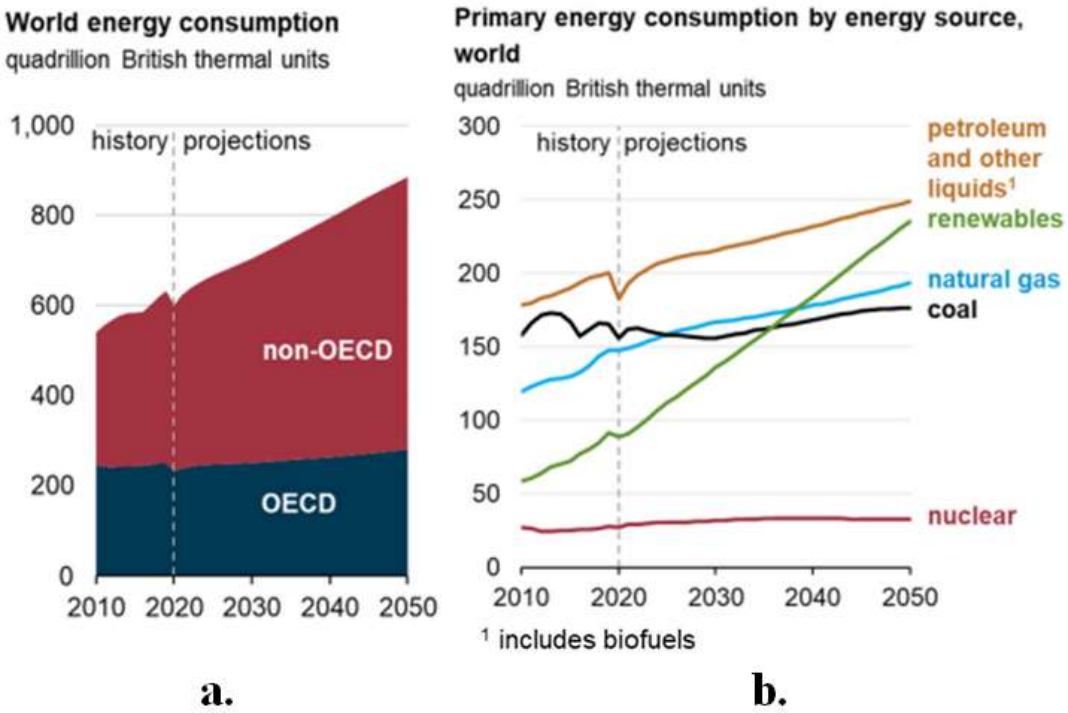

Figure 1.1 (a) The world energy consumption history and predictions from 2010-2050. The energy consumption is separated by the countries that are members of the Organisation for Economic Co-operation and Development (OECD, blue) and countries that are not members of the OECD (non-OECD, red). (b) The primary energy consumption by energy source history and predictions from 2010-2050. Data and predictions were from the U.S. Energy Information Administration [18].

metallurgical processes, the metal temperature, molten metal composition, and other system aspects are often manually measured or observed [20], [21], which leads to inefficiency and/or lack of consistency in the processes. In addition, strain and vibration sensors for SHM and CBM are needed to ensure the integrity, for planned maintenance, and for safe operation of structures and equipment, especially those that are subjected to high temperatures.

Harsh environment sensors are needed in aerospace applications for system monitoring, ensuring structural integrity, navigation, anticipation of structural failure, and system control [7], [11], [22]. For these applications, sensors are needed to measure gas, pressure, vibration, static and dynamic strain, and temperature. This requires sensors to be placed in various high-temperature locations, including engines and turbines [11], [22], [23]. There is also a need for wireless sensing

for aerospace applications, especially for sensing on moving parts [22], [23]. There is also a need for gas, strain, pressure, position, and torque sensors for automotive applications [5], [22], [24]. These sensors are used for a multitude of applications to ensure proper operation of the automobile, including fuel efficiency monitoring, measurement of structural integrity of moving parts of the vehicle, and fluid level monitoring.

1.2 SAW Sensor Technology

Surface acoustic wave (SAW) technology utilizes piezoelectricity to implement frequency control filters, signal processing devices, and sensors. When an alternating voltage is applied to the devices, an alternating stress field is induced by electromechanical coupling, which generates a SAW guided at the surface of the piezoelectric substrate.

SAW devices are used in a wide range of applications including radio frequency (RF) communications, filters, signal processing, and sensing applications [11], [25], [26]. Applications for SAW sensors include temperature [12], static and dynamic strain [13], [14], torque [15], pressure [16], and gas [17]. SAW technology is attractive for sensing applications because SAW sensors can have the following features: small size; ability to operate in high-temperature environments; capability of battery-free operation; and wireless operation [10], [27]; which allow these sensors to be installed in small, hard-to-reach places and moving parts that normally cannot be easily implemented by other technologies.

1.2.1 SAW Device Configurations

There are three configurations of SAW devices that are most frequently used for sensing purposes: SAW delay line configurations, two-port SAWR, and a one-port SAWR [25], [27], [28]. To generate a SAW, a RF signal is applied to interdigitated transducer electrodes (IDTs) fabricated on a piezoelectric substrate or thin film. Delay lines consist of two sets of IDTs that are positioned

apart (Figure 1.2a, [29]). The phase delay is measured by the phase of the output signal with respect to the input signal. For sensing applications, the change in phase through the device is affected by a measurand, as exposure to the particular measurand can change dimensions and/or the acoustic wave properties of the piezoelectric material where the SAW propagates and, therefore the phase velocity. For one and two-port SAWRs (Figure 1.2 b and c), the IDTs are placed between sets of open-circuited or short-circuited reflector gratings that reflect the SAW generated back to the

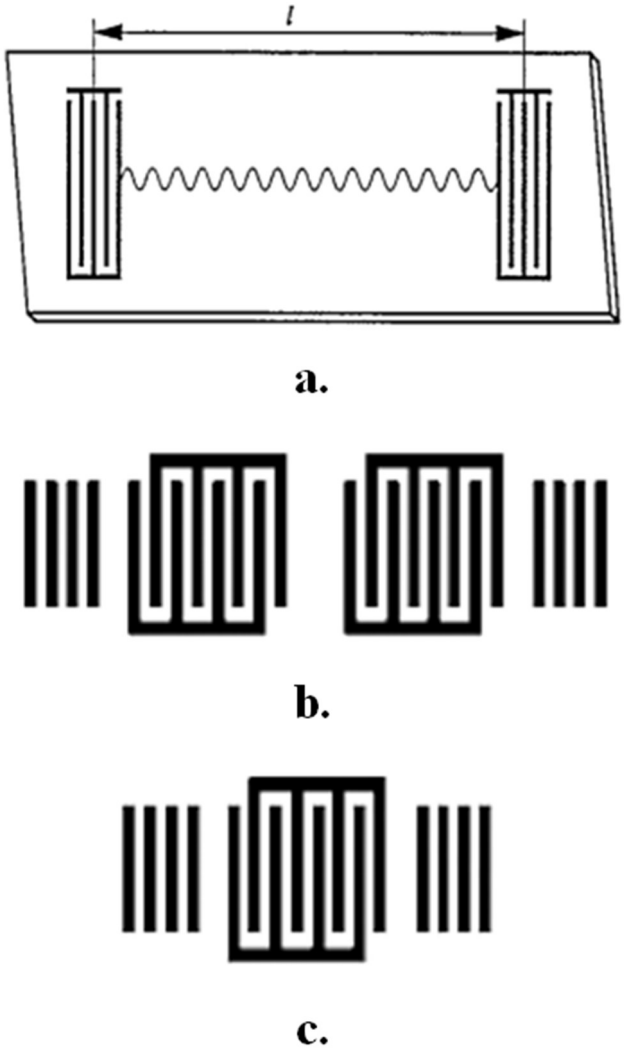

Figure 1.2 (a) SAW delay line configuration [29], (b) SAW two-port resonator [26], and (c) SAW one port resonator [26].

IDTs. For two-port SAWRs (Figure 1.2b), there are two sets of IDTs: one to generate the SAW and one detects the SAW. For one-port SAWRs (Figure 1.2c), a single set of IDTs is used to generate the SAW and receives the standing wave. The IDTs are designed so that they constructively interfere with each other to generate a SAW at a certain resonant frequency, f_0. This frequency is determined by the periodicity, p, of the IDTs and reflector gratings, which is equal to one half wavelength, and the SAW velocity for the crystal orientation being used, v_{SAW}, as shown in Equation 1.1:

$$f_0 = \frac{v_{SAW}}{2p} \tag{1.1}$$

For a SAWR with an applied electrical signal at or near f_0, the SAW is generated in both directions on either side of the IDT and reflected back by the reflector gratings. This generates a standing wave within the IDT structure that can be detected by the IDTs for both one and two-port resonators.

The equivalent circuit of a SAWR is shown in Figure 1.3 [30]. The equivalent circuit has a static capacitance, C_0, which is due to the capacitance from the IDTs, in parallel with the motional inductance, L_1, modal capacitance, C_1, and modal resistance, R_1.

1.2.2 SAW Sensing Principles

As discussed in Section 1.2.1, SAW sensing typically utilizes the phase change for delay line configurations or resonant frequency change for resonator configuration as the sensing parameter for a particular measurand. In this thesis, the targeted SAW measurands are temperature, static strain, and dynamic strain, discussed in the following sections.

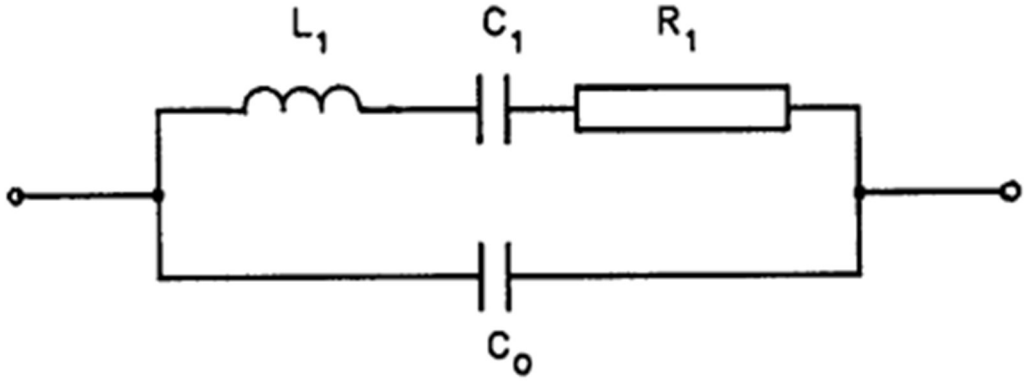

Figure 1.3 SAWR equivalent circuit [30].

1.2.2.1 SAWR Temperature Sensing

The temperature dependence of a SAWR device can be determined using the temperature coefficient of frequency (TCF) and the device operational frequency (f) or the temperature coefficient of delay (TCD) and the device time delay (τ). TCF relates the change in SAW operational frequency to change in temperature, given by [28]:

$$TCF = \frac{1}{f}\frac{df}{dT} \tag{1.2}$$

TCD relates the change in response delay to change in temperature, represented by [28]:

$$TCD = \frac{1}{\tau}\frac{d\tau}{dT} \tag{1.3}$$

TCD and TCF are related by [28]:

$$TCF = -TCD \tag{1.4}$$

For the one-port SAWRs used in this thesis, the resonant frequency is used to track the operational temperature, which can be modeled by a second order polynomial fit [13]. SAW temperature sensor mounting and implementation requires close contact to the structure or part being measured but does not require rigid attachment to the surface like a strain sensor does.

1.2.2.2 SAWR Static Strain Sensing

Applying static deformation to a SAWR substrate will alter the piezoelectric, dielectric, and elastic properties of the piezoelectric crystal or thin film and change the spacing of the IDTs and reflectors which cause a shift in the resonant frequency of the device [13]. This phenomenon is the basis for SAWR sensor operation in applications including torque, pressure, and static strain [13], [15], [16]. The measurement of static strain on mechanical parts [13], [31], requires that the SAWR sensor is rigidly attached to the part so that the static strain on the part can be transferred to the sensor [13], [32]. The attachment of the SAWR is a critical step for static strain sensing and can be a limiting factor for high temperature measurements because of the differences in coefficient of thermal expansion (CTE) between the piezoelectric substrate, adhesive, and part the SAWR is being attached to [13], [32], which can cause cracking in the sensor and adhesion layer, lack of stability, and failure of the sensor.

1.2.2.3 SAWR Dynamic Strain Sensing

A dynamic deformation or vibration of a SAWR causes a periodic change in the IDT pitch and stiffness coefficients of the piezoelectric substrate [33], [34]. The change in resonant frequency that is observed for static strain varies cyclically under a dynamic load. Because of this, signal demodulation is performed to measure the dynamic strain magnitude and spectral components [33]. The technique to extract dynamic strain from these measurements will be discussed in Chapter 3. To measure the dynamic strain on a metallic part, the SAWR sensor must be rigidly attached to the part like for static strain sensing. The dynamic load and temperature cycling need to be considered in addition to temperature when evaluating the stability of an adhesive layer for dynamic strain sensing on metallic parts.

1.3 SAWR Sensors for High-Temperature Harsh-Environments

Implementation of SAWR sensor technology in high-temperature harsh environments introduces challenges that are not observed at temperatures below 100°C. The three major challenges in the SAWR sensor system design at high temperature that need to be considered are: (i) piezoelectric substrate or thin film used, (ii) electrode material, and (iii) sensor attachment method [10], [13], [32].

1.3.1 SAWR Piezoelectric Substrates and Thin Films for High-Temperature Sensing

Use of a stable substrate is necessary for SAWR sensing. Common piezoelectric substrates that are used for SAWR devices, including quartz (QTZ, SiO_2), lithium niobate (LNO, $LiNbO_3$), and lithium tantalate (LTO, $LiTaO_3$), are often used for low temperature purposes, but are not suitable for high-temperature operation up to 1000°C [10], [11]. Quartz undergoes a α to β phase transition at 573°C after which it loses its piezoelectric properties [10], [11], [35], which limits quartz around or above that temperature. LNO and LTO experience crystal decomposition starting at 300°C, which limits use and compromises the integrity, stability, and thus the longevity of the substrates above 300°C [10], [11], [36].

For SAWR sensing above 600°C, other substrates are typically used [10], [11], [36], [37], including gallium orthophosphate (GPO, $GaPO_4$), aluminum nitride/scandium aluminum nitride (AlN/ScAlN) and gallium nitride (GaN), and the langasite family of piezoelectric crystals (LGX), which includes langasite (LGS, $La_3Ga_5SiO_{14}$), langanite (LGN, $La_3Ga_{5.5}Nb_{0.5}O_{14}$), and langatate (LGT, $La_3Ga_{5.5}Ta_{0.5}O_{14}$). GPO provides stability up to 970°C, which makes it a potential candidate for harsh environment sensing [38]. However, GPO is hard to grow and is typically produced in small wafers, which currently poses issues for commercial use [39]. AlN, ScAlN, and GaN are promising for harsh environment sensing as they can retain piezoelectricity up to 1150°C [10],

[11], [37], [40], but are limited to 700°C in environments where film oxidation can occur. Protective films will be required with these materials to reduce film oxidation for temperatures above 700°C [39]-[41]. Langasite does not undergo any phase transitions up to its melting point around 1470°C [36] and has been shown to operate above 1000°C in oxidizing environments [42], [12]. In this thesis, LGS is used as the piezoelectric substrate for high-temperature strain sensing.

1.3.2 SAWR Electrode Materials for High Temperature

In addition to the use of a piezoelectric substrate that is suitable for high-temperature environments, it is also necessary to consider the stability and temperature limits of the IDT and reflector electrode materials. If the electrode film is not stable, it can cause drift in the SAWR sensor response, meaning the resultant measured strain and temperature, etc. measurement would be inaccurate.

When choosing an electrode film for high-temperature operation, some of the main considerations relating to film stability are electrode oxidation, agglomeration, delamination, and hillock formation [10], [39], [43]. Metal films, such as iridium (Ir), palladium (Pd), platinum (Pt), and rhodium (Rh) are often used for thin film electrodes at high temperature due to their high melting point and reduced oxidation. Iridium, palladium, and rhodium show oxidation at temperatures above 700°C [10], [44], [45]. Although platinum does no oxidize at temperatures up to 1000°C [45], it experiences agglomeration around and above 650°C [10], [46], as shown in Figure 1.4a. Pt-alloy films, including Pt-Al, Pt-Al_2O_3, Pt-Co, Pt-Cr, Pt-Ni, Pt-Ni/Pt-Zr, Pt-Rh, Pt-Rh/HfO_2, and Pt-Rh/ZrO_2, have been shown to operate beyond 700°C [10], [12], [43], [47]-[49]. Use of an insulating interfacial layer or capping layer can further mitigate agglomeration of films. The appearance of stress-induced hillocks (Figure 1.4b [50]) is also observed in Pt/Al_2O_3 films [43], which increases SAWR diffraction and scattering, which can lead to inconsistency and drift

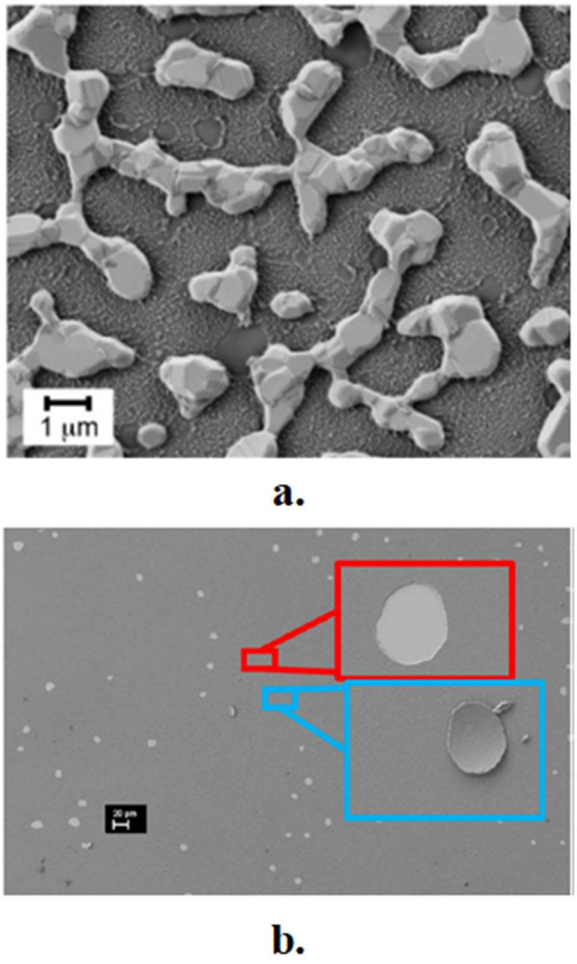

Figure 1.4 (a) Image of agglomeration of a Pt-Rh film heated to 1000°C for 4 hours [48] and (b) image of stress hillock formation in a Pt/Al_2O_3 film [50].

in the sensor response. Graded electrode films that gradually introduced the alloy to platinum have been implemented to reduce the stress on the film to mitigate the issue of stress hillocks [43].

1.3.3 SAWR Strain Sensor Attachment

Attachment of the SAWR sensor to mechanical parts is critical for strain sensor purposes and is currently a major limitation in high temperature SAWR strain sensor technology [32], [51]. In order for the SAWR sensor to measure static or dynamic strain on a metal part, it needs to be rigidly attached by an adhesion layer so that strain can be transferred from the part to the sensor.

However, because the difference in CTE of LGS (~5 ppm/°C) and metal parts (13-17 ppm/°C) is large, it is difficult to find an adhesion layer that is capable of absorbing stress induced by thermal expansion mismatch up to 1000°C, in particular after temperature cycling up and down to those temperature levels. Current reported work [13], [31], [52] use commercially available high-temperature adhesives, but none are capable of adhering the SAW to a metal part at 1000°C while still transferring static and dynamic strain from the part to the sensor. The thickness of the adhesion layer is an important consideration for SAWR strain sensor technology [53]. Adhesive layers that are too thin will not sustain sensor attachment at high temperature due to thermal expansion. However, if the adhesive layer is too thick (above 0.5mm), then mechanical strain won't be transferred to the SAWR sensor [32]. In addition, SAWR attachment for dynamic strain is more difficult than attachment for static strain because it is more demanding of the frequency component of the applied load.

1.4 Current Harsh Environment Strain Sensor Technology

Current technologies for high-temperature static and dynamic strain sensors consist of three types of sensors: wired strain gauges, fiber optic sensors, and SAW sensors. Wired strain gauges and fiber optic strain sensors will be discussed in this section and SAW strain sensors will be further detailed in Section 1.4.1.

Wired strain gauges are typically resistive sensors that correlate change in resistance to static or dynamic strain. Resistive strain gauges are commercially available and are shown to operate up to 1150°C [54]-[57]. These sensors are attached to mechanical parts either by spot welding or bonding using a high-temperature adhesive. These sensors, however, have characteristics that limit their use in high-temperature, harsh environments. One limitation is that these wired sensors do not allow for small implementation of wireless sensor units. This means

that these sensors have limited or no use in monitoring parts that are moving or rotating. Another limitation is that resistive strain gauges are bulky and require a large surface area once packaging is implemented. This means that these sensors cannot accurately monitor small areas and cannot be installed in small, hard-to-reach places, such as superheater tubes [58], [59], that can cause costly shutdowns of the boiler.

Optical strain sensing is another technology that is utilized for high temperature harsh-environment static and dynamic strain sensing [7], [60]-[63]. One of the most common types of high-temperature optical strain sensors is fiber Bragg grating (FBG) strain sensors [60], [61]. FBG strain sensors have been reported up to 1700°C [64] and have high sensitivity. However, these sensors are difficult to install, can require special packaging, and require complex, high-cost instrumentation, which is not desirable in harsh environments.

1.4.1 Current State of SAW Static and Dynamic Strain Sensor Technology

At the University of Maine, high-temperature static strain measurements for LGS SAWR sensors have been reported up to 400°C [13]. Temperature correction of the SAWR static strain sensor response was also implemented by subtracting the response of a SAWR temperature sensor sliding on the surface of the beam used for calibration. All measurements were taken in a box furnace for high temperature testing. Recent work by Yan *et al.* reports SAWR wired static strain sensing up to 700°C [52]. Wireless SAWR static strain sensing, reported in this work, has been performed up to 250°C in a box furnace environment [53]. The effects of adhesive thickness on the SAWR static strain sensitivity and maximum operational temperature are analyzed. Other work by Shu *et al.* reports wireless static strain sensing up to 500°C [31]. The SAWR resonant frequency was calibrated to strain by measuring the beam deflection and correlating beam deflection to strain.

Work on SAW dynamic strain sensors is limited. Wired dynamic strain sensing has been performed up to 500°C at the University of Maine using LGS SAWR sensors [32], [65]. The SAWR response was calibrated to dynamic strain using a resistive dynamic strain gauge. The signal processing of the SAWR dynamic strain response will be explained in greater detail in Section 3.5.2. Wireless SAW dynamic strain sensing has not yet been reported in high-temperature harsh-environments above 100°C. However, SAW dynamic strain sensing was reported for cutting tools at room temperature by Stoney *et al.* [66]. This work reports wireless SAWR dynamic strain sensing up to 400°C [14].

1.5 Objectives of this Thesis

As discussed in Section 1.1, static and dynamic strain sensing in high-temperature harsh-environments is necessary for ensuring worker safety and lowering repair and maintenance cost of structures.

The major objectives for the work presented in this thesis are as follows:

1. Model the stress and strain at the metal/adhesive/SAWR interface at high temperature and under a static strain bias to determine where attachment failure is most likely to occur.
2. Determine alternate methods of mounting the SAWR strain sensor to reduce the maximum strain at the metal/adhesive/SAWR interface at high temperature.
3. Implement a platform for wireless SAWR static and dynamic strain measurements at high temperature and perform wireless static and dynamic strain measurements at high temperature.
4. Evaluate the stability of the adhesive used for the SAWR strain sensor by subjecting it to temperature cycling using different high temperature adhesives.

5. Determine a method for temperature correction for high temperature SAWR dynamic strain sensing in a powerplant environment.

To address these topics and report the findings in this thesis, the chapters will be organized in the following manner:

- **Chapter 2** presents the strain modeling done to determine the stress in strain present when the SAWR sensor mounted on the strain is heated to 400°C under a static strain bias. Also, alternative mounting methods utilizing a lower coverage of the bottom interface of the LGS will be discussed to reduce the stress at the metal/adhesive/SAWR interface at high temperature.
- **Chapter 3** introduces a platform for wireless interrogation of SAWR static and dynamic strain sensors up to 400°C while attaining a strong signal that provides the necessary resolution to measure static and dynamic strain.
- **Chapter 4** discusses the effects of temperature cycling on the SAWR sensor adhesive that was used to perform the wireless strain testing in Chapter 3. It also analyzes adhesives for use in static and dynamic strain testing up to 200°C.
- **Chapter 5** presents a method to experimentally measure temperature and dynamic strain (magnitude and spectral components) in a variable temperature environment using a single SAWR sensor.
- **Chapter 6** concludes the work done in this thesis and suggests future work.

CHAPTER 2
SIMULATION OF THERMAL AND MECHANICAL STATIC STRAIN IN THE MOUNTED SAWR STRAIN SENSOR

This chapter discusses simulation on the effect of thermal strain due to heating the SAWR strain sensor and the strain due to an applied static load to the SAWR strain sensor using COMSOL Multiphysics (COMSOL, Inc, Burlington, MA). COMSOL is a finite element method (FEM) multiphysics software that is appropriate for simulations of the mounted SAWR sensor (LGS, propagation direction Euler angles {0°, 138.5°, 32.9°}) under mechanical and thermal strain. Because there is a mismatch in CTE between the metal part that is being measured, the adhesive used to attach the SAWR to the metal part, such as Aremco 668 [67], and the SAWR sensor, there is high strain at high temperature due to thermal expansion mismatch. Failure to attach LGS to Inconel at 800°C using commercial high-temperature ceramic adhesives has also been shown in [32]. However, the magnitude of the thermal strain needs to be quantified and compared to strain that is caused by static and dynamic deformation of a metal part. It is also important to observe the strain magnitude at the metal/adhesive and LGS/adhesive interfaces to locate regions of high strain concentration which can cause attachment failure. Alternate methods of SAWR mounting were also simulated that utilize adhesive shaping to reduce the strain magnitude at the adhesive/metal and adhesive/LGS interfaces. This information is critical to investigate alternative adhesion methods to provide stable SAWR strain sensor response at temperatures above 500°C.

2.1 Comparison of COMSOL Multiphysics with Abaqus FEM Software

In previous work at the University of Maine, Abaqus software (Dassault Systems, Waltham, MA), which employs FEM techniques, was used to predict the strain on the strain beam used for static strain testing [13]. In that paper, the Abaqus model accuracy was confirmed

experimentally at room temperature using a room temperature strain gauge up to approximately 200με [13]. High temperature strain values were obtained by manually changing the Inconel 625 material constants in the program. These simulations showed a slight increase in the slope of the strain magnitude vs. beam load plot obtained from the simulation. In this work, a COMSOL model was created to simulate the static strain on the test beam and the simulation results are compared to the results obtained using Abaqus to confirm the accuracy of the COMSOL model. That comparison served to increase the confidence of the COMSOL model and simulations in predicting the temperature effects of the SAWR mounted on a metallic beam.

2.1.1 Static and Dynamic Strain Test Beams

Use of test beams with a constant stress region is beneficial for sensor calibration and comparison/correlation of multiple strain sensors because it reduces uncertainty that may arise with strain variation due to sensor location on the beam. To make a beam with a region of constant stress, either the width, *b*, or thickness, *t*, of the beam can be varied according to [68]:

$$\sigma = \frac{12Px}{E \cdot b \cdot t^2} \tag{2.1}$$

where *P* is the force applied at the free end of the beam, *x* is the distance from the loaded end of the beam, and *E* is the modulus of elasticity. In the case where the width, *b*, is varied such that $b = b(x)$ (Figure 2.1), a beam with a region of constant stress can be fabricated when:

$$b(x) = \frac{b_{max} \cdot x}{l} \tag{2.2}$$

where *l* is the length of the beam. Substituting $b(x)$ into Equation 2.1, the stress on the beam will be given as [68]:

$$\sigma = \frac{12 \cdot P \cdot x}{E \cdot b(x) \cdot t^2} = \frac{12 \cdot P \cdot l \cdot x}{E \cdot b_{max} \cdot x \cdot t^2} = \frac{12 \cdot P \cdot l}{E \cdot b_{max} \cdot t^2} = constant \tag{2.3}$$

In the case where the thickness, *t*, is varied such that $t = t(x)$ (Figure 2.2), a beam with a region of constant stress can be fabricated when:

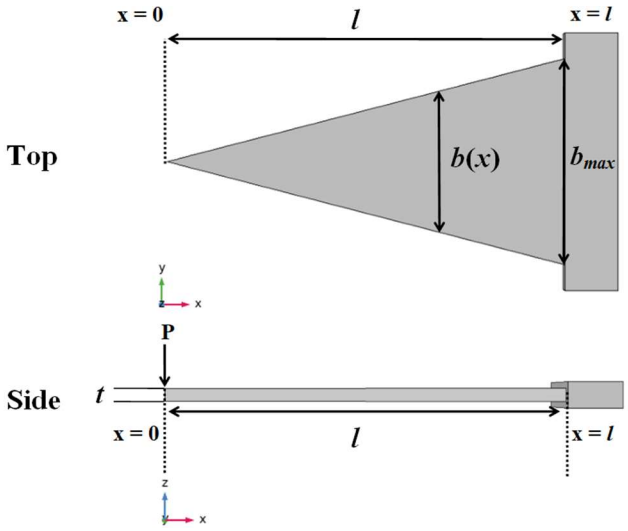

Figure 2.1 A variable width beam designed such that it has a region of constant stress when a load is applied at the end of the beam.

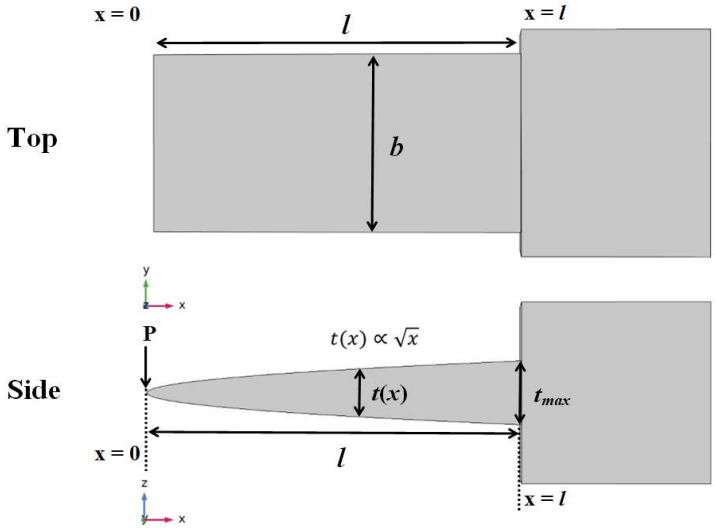

Figure 2.2 A variable thickness beam designed such that it has a region of constant stress when a load is applied at the end of the beam.

$$t(x) = \frac{t_{max}\sqrt{x}}{\sqrt{l}} \tag{2.4}$$

Substituting $t(x)$ into Equation 2.1, the stress on the beam will be given as [68]:

$$\sigma = \frac{12 \cdot P \cdot x}{E \cdot b \cdot t(x)^2} = \frac{12 \cdot P \cdot l \cdot x}{E \cdot b \cdot t_{max}^2 \cdot x} = \frac{12 \cdot P \cdot l}{E \cdot b \cdot t_{max}^2} = constant \tag{2.5}$$

For static strain sensing, a beam with a variable width constant stress region was used (Figure 2.3a) [13], [53]. Design and fabrication of this beam was done by Environetix

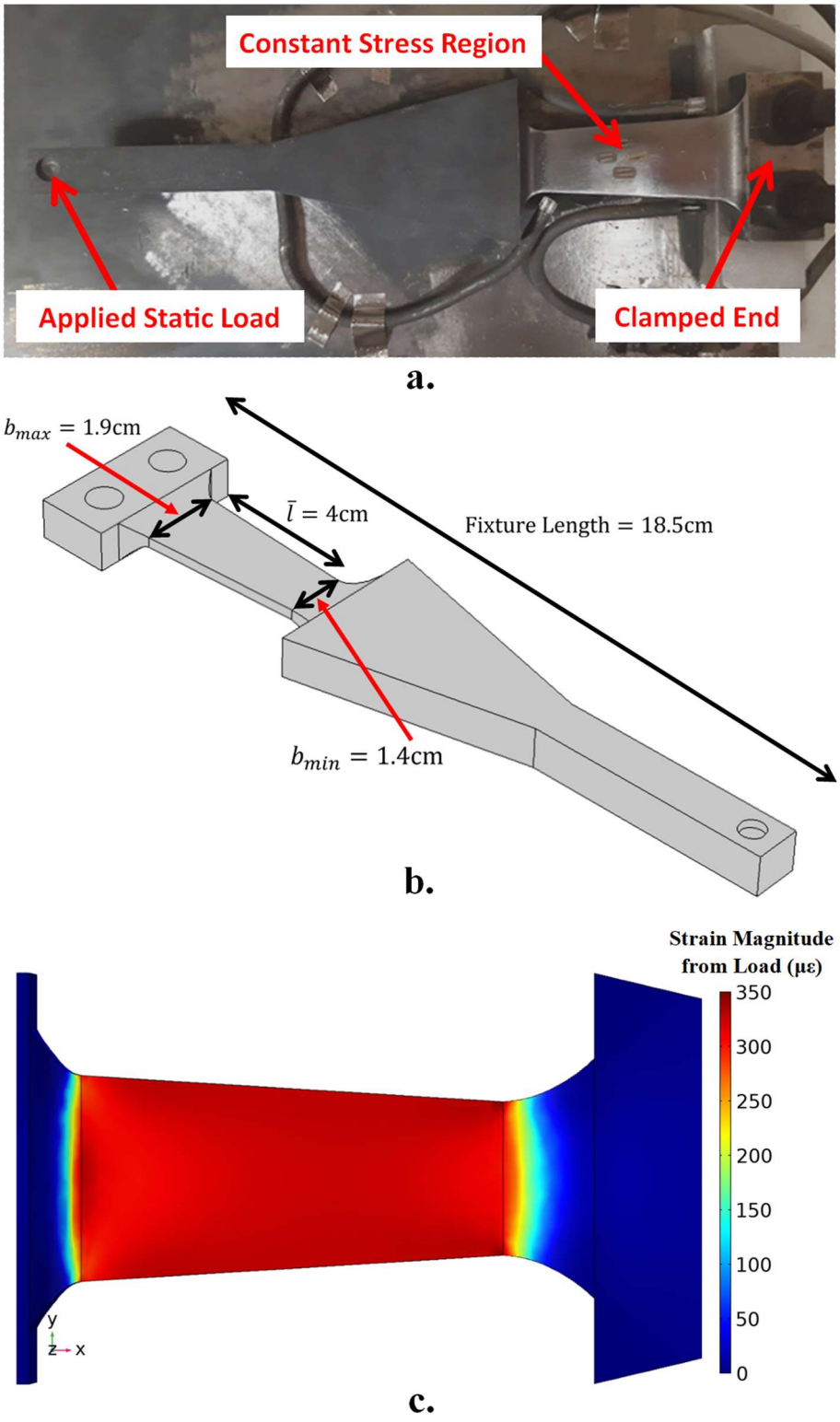

Figure 2.3 (a) The beam with a variable width constant stress region used for static strain tests. (b) A schematic of the static strain beam used. (c) A simulation showing the strain on the constant stress region of the beam due to an applied load of 800g.

Technologies Corporation and the UMaine Advanced Manufacturing Center (AMC). Figure 2.3b shows a schematic of the static strain beam. The length of the constant stress region, $\bar{l}$, is 4cm and the thickness, *t*, of the constant stress region is 2.5mm. The length of the constant stress region is not equal to *l* because the beam was not fabricated such that the edges converge to a single point at $x = 0$ like in Figure 2.1. However, simulation in COMSOL Multiphysics shows (Figure 2.3c) that this principle can still be applied with this beam. The length of the entire static strain fixture is 18.5cm. The beam was fabricated with Inconel 625 alloy for strain testing above 800°C [69].

For dynamic strain sensing, a separate beam with a variable thickness was used [32], as shown in Figure 2.4a. A different beam was used for dynamic strain measurements because the

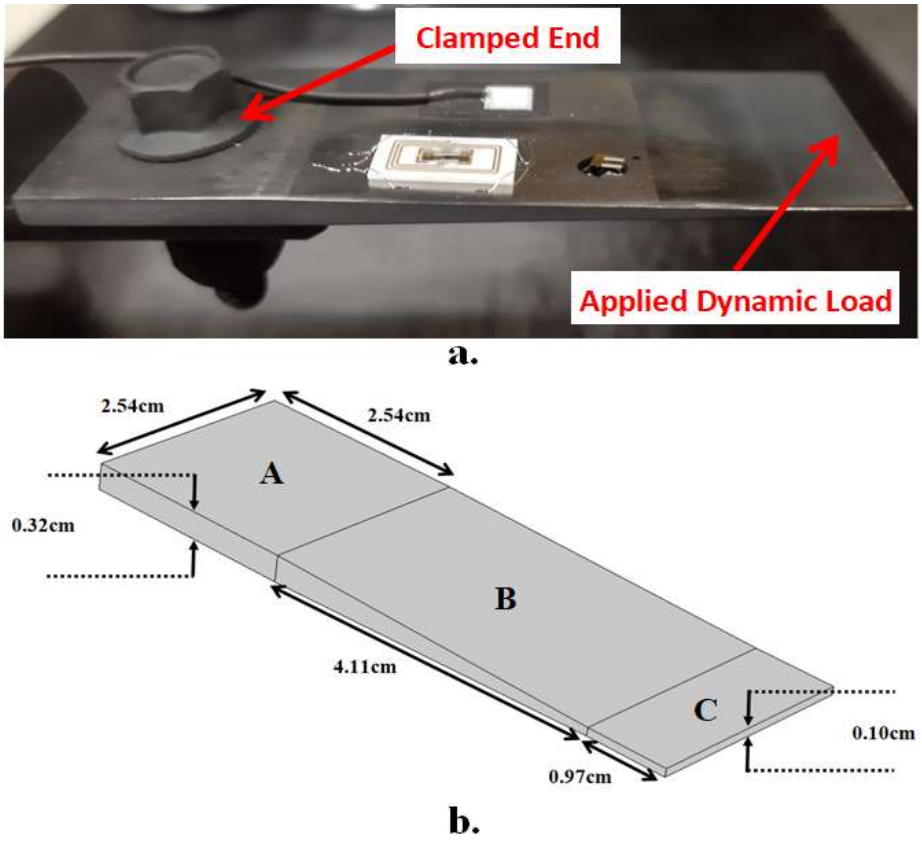

Figure 2.4 (a) The beam with a variable thickness used for dynamic strain tests. (b) A schematic of the dynamic strain beam with measurements as described in [32]. Section A has a constant thickness and is used to mount the beam (described in the next chapter), Section B has a varying thickness and is the location where sensors are mounted, and Section C has a constant thickness and is used as the location to apply the dynamic load.

natural frequency of the beam used for static strain sensing was close to the target dynamic strain frequency range (300Hz – 1000Hz) and could not be used for dynamic strain tests. Like for the static strain beam, this beam was fabricated with Inconel 625 [69]. Design of the beam was done in [32] and fabrication of the beam was done by AMC. A schematic of the beam with dimensions is shown in Figure 2.4b which is based on the schematic described in Figure 5.1 from [32]. From Figure 5.1 from [32], it is unclear whether the region of variable thickness varies with x according to Equation 2.5 or if it varies linearly with x. To determine this, the beam thickness was measured as a function of x starting at the loaded end of the beam. The measured thickness values are shown in Figure 2.5. The region of variable thickness in Figure 2.5 is located between 1cm and 5cm from the loaded end of the beam. The correlation coefficient (R^2) of the linear fit of the variable thickness region was found to be 0.995. Because of this, it can be concluded that the thickness of

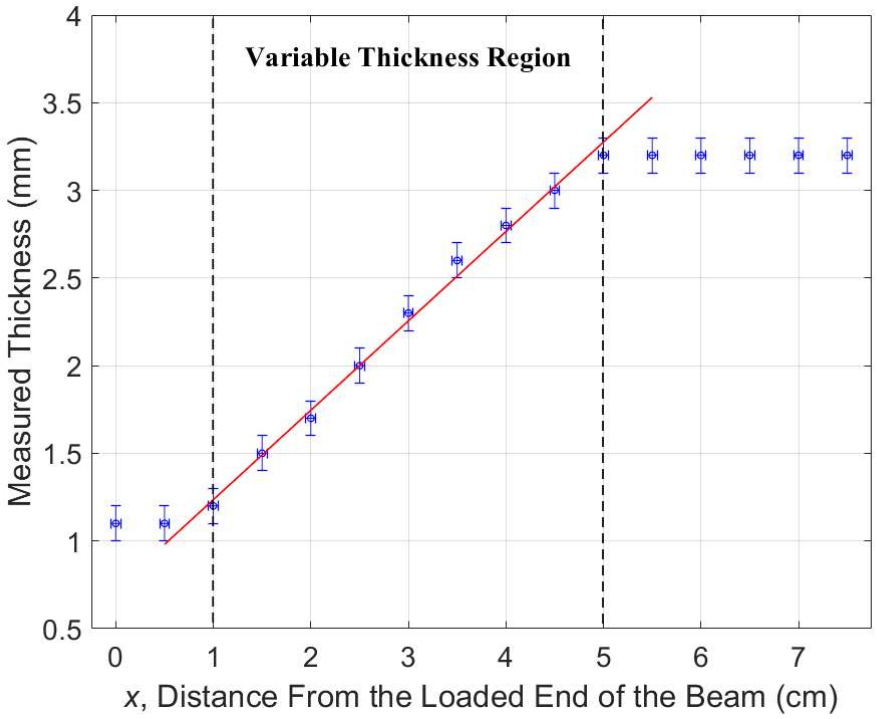

Figure 2.5 Thickness measurements of the dynamic strain beam and the linear fit of the measurements in the variable thickness region between x = 1cm and x = 5cm.

the beam varies linearly with distance from the end of the beam and, therefore, does not satisfy the condition for a constant stress region based on the calculations in Equation 2.5.

Since it cannot be assumed that the dynamic strain beam has a region of constant stress, simulation in COMSOL was done to determine the strain distribution on the beam. This simulation is shown in Figure 2.6a. For these simulations, the beam was assumed to be fixed in place by the five faces exposed in Section A of the beam shown in Figure 2.4b. The remainder of the beam was suspended freely and was subject to deformation due to the applied load. The simulation shows

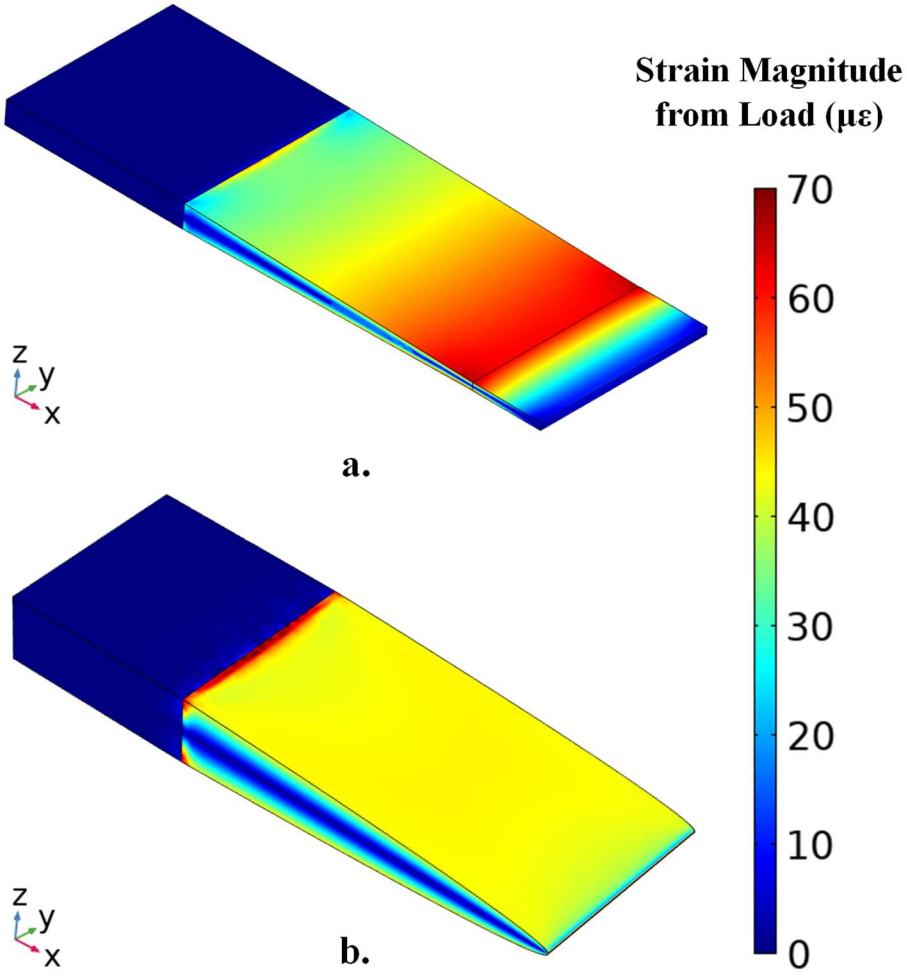

Figure 2.6 A COMSOL simulation of (a) the dynamic strain beam described in Figure 2.4b and (b) a beam with a thickness that had a square root dependence on *x* with an applied load at the end of the beam

that the beam, which was fabricated with a linear thickness variation profile with *x*, does not have a region of constant stress (about 36% variation), as would be the case if it has a square root dependency on x shown in Equation 2.5 and Figure 2.6b (strain variation of about 1.3%). This strain variation along the beam for the fabricated structure (Figure 2.4) contrasts with the simulation results plotted in Figure 5.2 from [32], which does not have the dynamic strain color scale and suggests that a significant constant stress region exists for the beam. Although the fabricated beam does not have a region of constant stress, Figure 2.6a shows that there is no significant strain variation along the *y* direction. Therefore, if two sensors of comparable dimensions are mounted at a particular *x*-position, they will measure the same strain magnitude.

2.1.2 Comparison of COMSOL to Abaqus Results

Models of the static strain beam were made in COMSOL and Abaqus to simulate the strain on the beam to determine if the results from the COMSOL model are consistent with Abaqus simulations that were done previously at the University of Maine [13]. An AutoCAD drawing of the static strain beam, shown in Figure 2.3a, was imported into COMSOL and Abaqus and the material properties for Inconel 625 [69] were entered into both programs.

To compare the simulation results of COMSOL and Abaqus simulations, masses from 100g to 800g in increments of 100g were applied to the static strain beam at 25°C, 300°C, and 400°C. The magnitude of the static strain was plotted on the top surface of the constant stress region of the static strain beam and the strain magnitude average over the constant stress region surface was taken at each mass simulated. The strain magnitude, |ε|, was calculated from simulation using:

$$|\varepsilon| = \sqrt{|\varepsilon_x|^2 + |\varepsilon_y|^2 + |\varepsilon_z|^2} \tag{2.6}$$

The results from these simulations are shown in Figure 2.7. The strain magnitude vs. beam load slopes and percent differences between the COMSOL and Abaqus simulations are shown in Table

2.1. The slope of the strain magnitude vs. beam load increases due to change in the Young's modulus of the Inconel 625 with temperature. The simulations show that there was less than a 5% discrepancy in the strain magnitude of the constant stress region when comparing the results from the COMSOL simulation to the results from the Abaqus simulation. The simulations show that the COMSOL model is consistent with the Abaqus model in calculating the strain magnitude on the

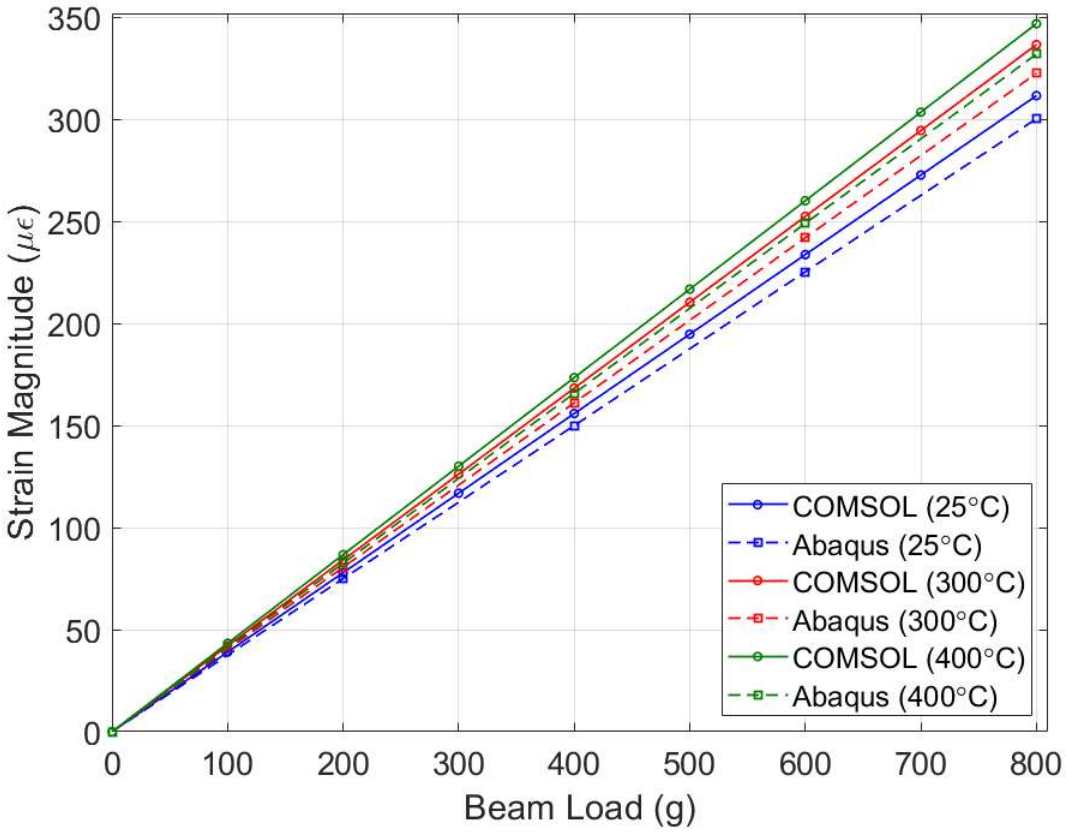

Figure 2.7 The strain magnitude vs. beam load data obtained from the COMSOL (solid, circles) and Abaqus (dashed, squares) simulations and the linear fits at 25°C (blue), 300°C (red), and 400°C (green).

Table 2.1 The strain magnitude vs. beam load slopes for the COMSOL and Abaqus simulations at 25°C, 300°C, and 400°C and the percent difference between the slopes obtained by COMSOL and Abaqus.

	25°C	300°C	400°C
COMSOL	0.390 με/g	0.421 με/g	0.434 με/g
ABAQUS	0.375 με/g	0.403 με/g	0.415 με/g
% Difference	3.8%	4.3%	4.4%

static strain beam and, therefore, can be used to simulate the thermal and mechanical strain for the mounted SAWR at elevated temperatures.

2.2 Modeling the Strain for LGS Attachment

After the verification of the COMSOL model for the static strain beam, a new model was made that incorporated the SAWR and the adhesive layer so that the mechanical and thermal strain in the whole system could be simulated at varying temperatures and applied loads. The COMSOL geometry of the SAWR mounted on the beam is shown in Figure 2.8 with the coordinate system displayed in the bottom left corner of the figure. Similar to the models in Section 2.1, the material used for the static strain beam was Inconel 625 (CTE = 13.7ppm/°C at 427°C, [69]). The adhesive used for all simulations was Aremco 668 (CTE = 7.2ppm/°C, [67]), which was the adhesive used to mount SAWR sensors for static and dynamic strain testing [32]. The CTE of the LGS orientation {0°, 138.5°, 32.9°}, which is the orientation of the SAWR sensor used in this work, is 4.9 ppm/°C along the direction of propagation and 4.6 ppm/°C perpendicular to the direction of propagation. These values and the rotated elastic constants for the LGS orientation were calculated using

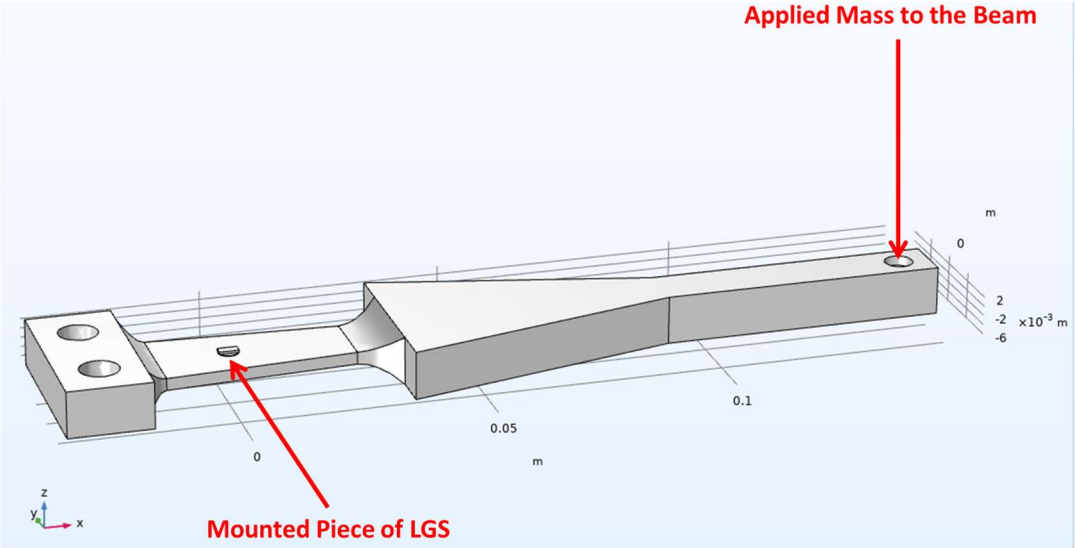

Figure 2.8 The geometry of the COMSOL thermal expansion and applied load simulations. Shown is the static strain beam with a sample of LGS mounted on the constant stress region of the beam. The LGS sample and point of applied force are indicated in the figure.

MATLAB scripts written by Professor Mauricio Pereira da Cunha and the LGS elastic constants reported in Malocha *et al.* [70]. The LGS dimensions were those of the SAWR sensor chip: 4mm length, 2mm width, and 0.5mm height. The adhesive/Inconel and the adhesive/LGS interfaces are assumed to have perfect adhesion to each other in this model.

2.2.1 Simulation of the Full Interface Adhesive Mounting Scheme

The first COMSOL model made aimed at to simulate the thermal and mechanical strain of the Inconel/adhesive/LGS interface where the adhesive is covering the full bottom interface (FI) of the LGS chip (FI mounting scheme) shown in Figure 2.9. This is the mounting scheme that was being used for mounting SAWR sensors. The adhesive was modeled as having a circular shape with a diameter of 4.2mm and a thickness of 0.15mm, which are typical dimensions of the Aremco 668 adhesive layer used for current SAWR static and dynamic strain measurements. Simulation of the FI mounting scheme targeted the identification of potentially highly concentrated strain when the beam is heated to 400°C and when a mechanical load is applied to the beam. In the simulations, the initial temperature, T_0 was set to 25°C, in which case the model predicts no thermal strain is

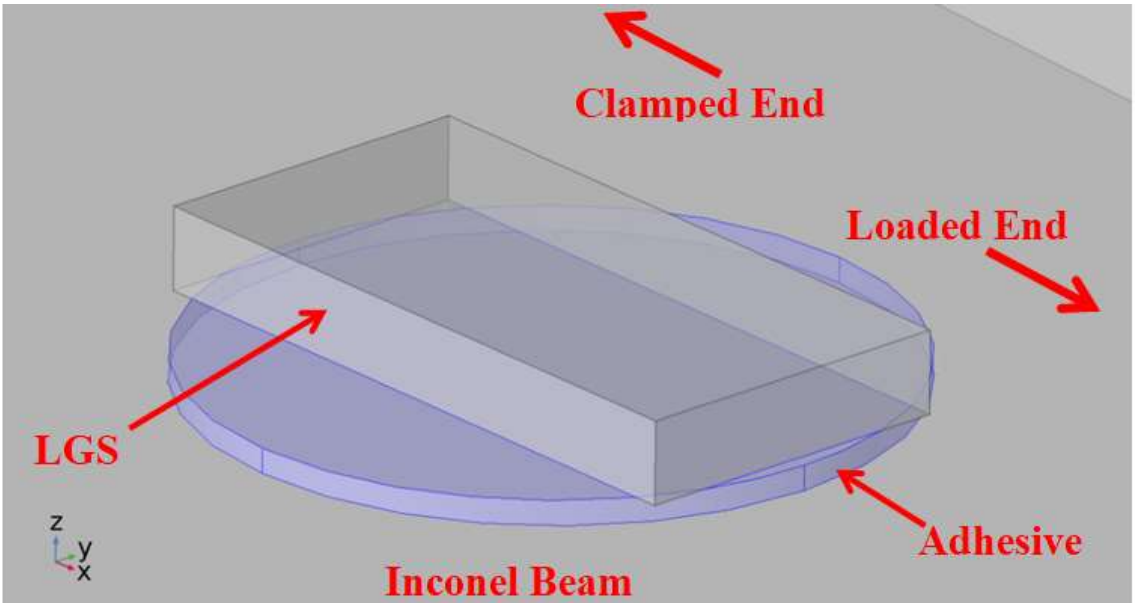

Figure 2.9 The geometry used for the FI mounting scheme simulations. The LGS, Aremco 668 adhesive layer (highlighted in blue), and the Inconel beam are labeled.

present. Simulations were performed by viewing the Inconel/adhesive/LGS interface temperature to 400°C with no mechanical load. The 400°C temperature value was chosen for simulations because it is the maximum temperature limit of the Aremco 668 adhesive for LGS attachment to Inconel 625 identified in previous work for strain applications [13], [14]. Further simulations were done viewing the Inconel/adhesive/LGS interface with an 800g mechanical load (347με from the simulations in Figure 2.7 and Table 2.1). The 800g mass was chosen as the static load on the beam because it is the maximum mass used for the static strain testing performed. By observing the thermally induced strain at 400°C, one can identify locations of high strain concentration, and from there perform investigation on ways to reduce the thermal strain in those locations. Furthermore, simulating the strain at the Inconel/adhesive/LGS interface subjected to an 800g load allows the analysis of mechanical strain transfer from the part to the LGS crystal, and the establishment of a baseline to compare against that of other adhesive designs for thermal strain reduction.

For each simulation, the strain on four 2-D plane cuts was analyzed as shown in Figure 2.10: (i) an X-Z plane cross-section in the center of the LGS showing the strain throughout the entire Inconel/adhesive/LGS stack, (ii) an X-Y plane cross-section on the top surface of the LGS (where the SAW propagates), (iii) an X-Y plane cross-section at the LGS/adhesive interface 5nm into the LGS, and (iv) an X-Y plane cross-section at the Inconel/adhesive interface 5nm into the adhesive. Observing these regions will give information on how strain is transferred from the metallic part to the LGS crystal and will give insight on where there is a high strain concentration at the LGS/adhesive and Inconel/adhesive interfaces. For each slice, the magnitude, X-component, Y-component, and Z-component of the strain vector was calculated and plotted.

The first simulations that were done were to model the thermal expansion of the Inconel/adhesive/LGS interface at 400°C with no mechanical load. Figure 2.11 shows an X-Z

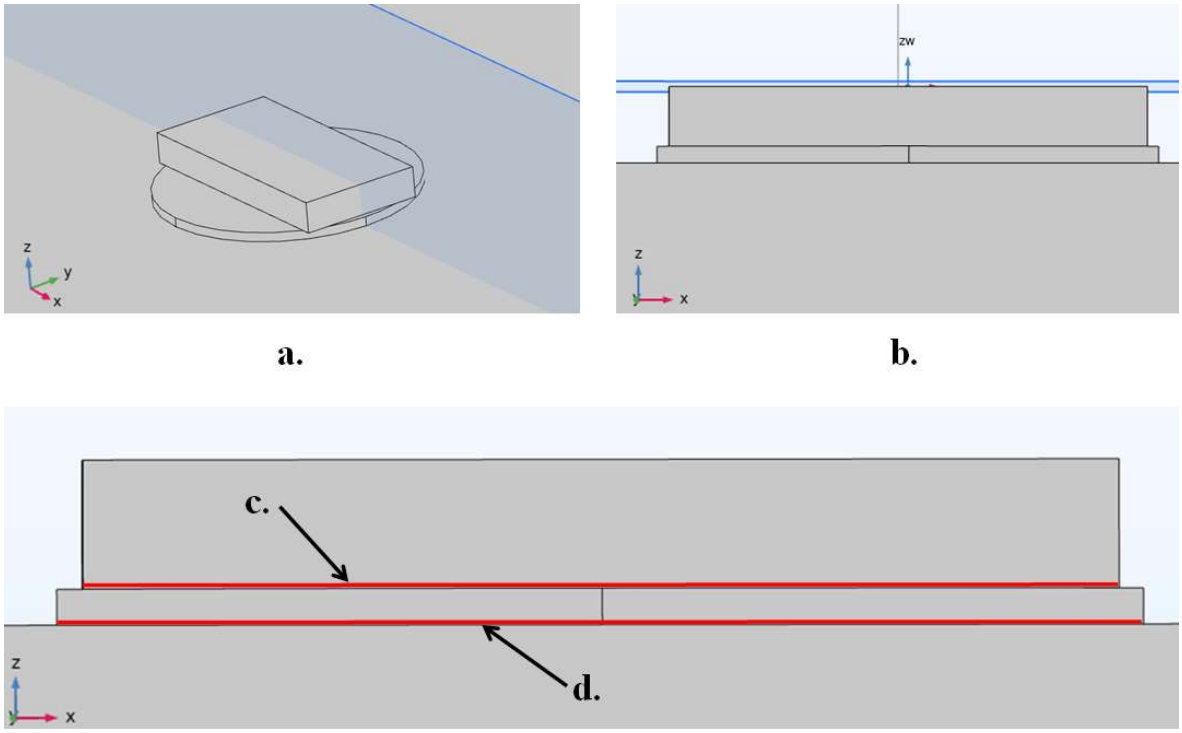

Figure 2.10 The locations of the (a) X-Z plane cross-section, (b) X-Y plane cross-section of the top surface of the LGS, (c) X-Y plane cross-section of the LGS/adhesive interface 5 nm into the LGS, and (iv) X-Y plane cross-section of the Inconel/adhesive interface 5 nm into the adhesive.

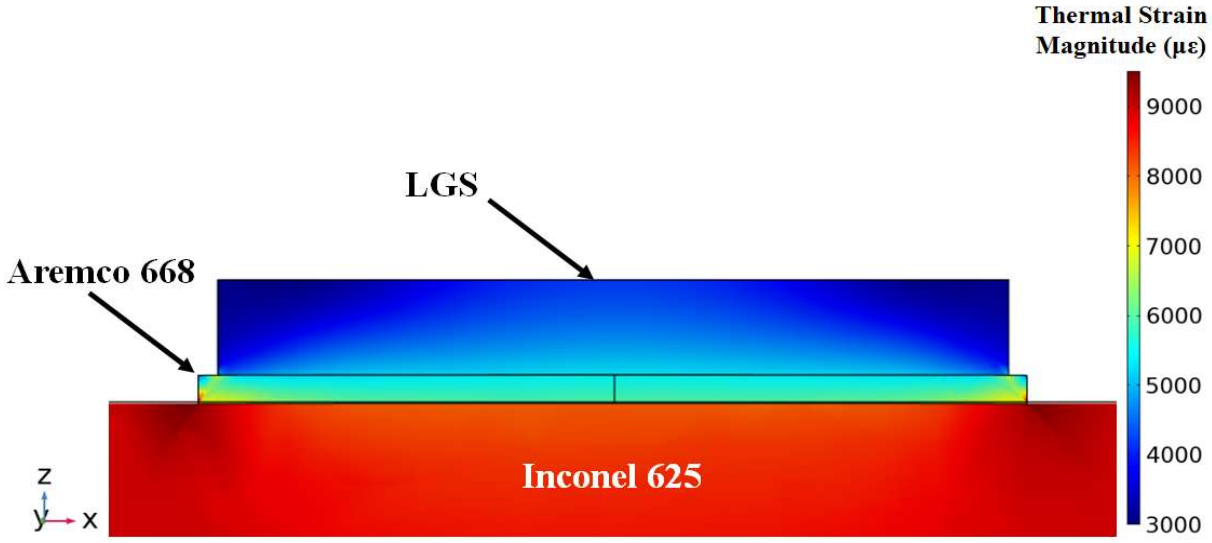

Figure 2.11 An X-Z plane cross-section through the LGS, adhesive layer, and Inconel 625 displaying the magnitude of thermally induced strain at 400°C under no mechanical load.

plane cross-section through the center of the Inconel/adhesive/LGS stack displaying the magnitude of thermally induced strain at 400°C. The figure shows how the strain is distributed throughout the stack. To gain more information on the strain distribution at each interface, the strain on the X-Y cross-sections taken at the LGS/adhesive and Inconel/adhesive interfaces need to be analyzed. The separate X, Y, and Z-component plots for this cross-section can be found in Appendix A.

Figure 2.12 shows the thermally induced strain magnitude on an X-Y plane cross-section at the LGS/adhesive interface 5nm into the LGS. The reason the cross-section was placed 5nm into the LGS is to avoid boundary condition fluctuations from the COMSOL FEM simulation. The maximum strain at this interface was found to be 7840με and was located on the borders of the LGS chip. The cross-section shows that there is a high concentration of strain at the borders of the LGS crystal when heated to 400°C. The X, Y, and Z-component plots (figures shown in Appendix A) show that the X and Y strain components contribute the most to the high strain concentration

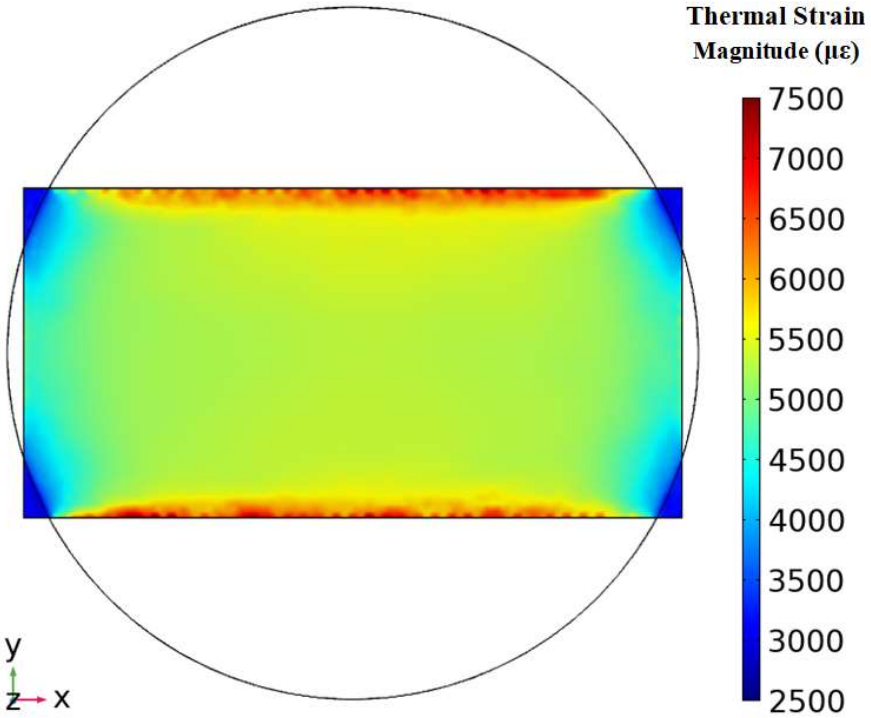

Figure 2.12 An X-Y plane cross-section at the LGS/adhesive interface 5nm into the LGS displaying the magnitude of thermally induced strain at 400°C under no mechanical load.

at the LGS borders. This could limit the temperature range of the sensor because the LGS borders are likely the weakest point of the sensor chip due to the dicing of the wafer. Dicing of the LGS wafer leaves minor faults on the borders of the LGS chip, which are the most likely places for cracking of the LGS crystal to initiate. Figure 2.13 shows the thermally induced strain magnitude on an X-Y plane cross-section at the Inconel/adhesive interface 5nm into the adhesive. The maximum strain observed at the Inconel/adhesive interface was found to be 9770με, which is observed in the high strain concentration regions on the edges of the adhesive. The patterns near the top and bottom edges of the adhesive are likely a result of the mesh and would not be observed experimentally.

The second simulations performed were to model the strain in the Inconel/adhesive/LGS stack due to applying a static mechanical load of 800g (347με) applied to the beam at 25°C. Figure 2.14 shows an X-Z plane cross-section through the center of the Inconel/adhesive/LGS stack

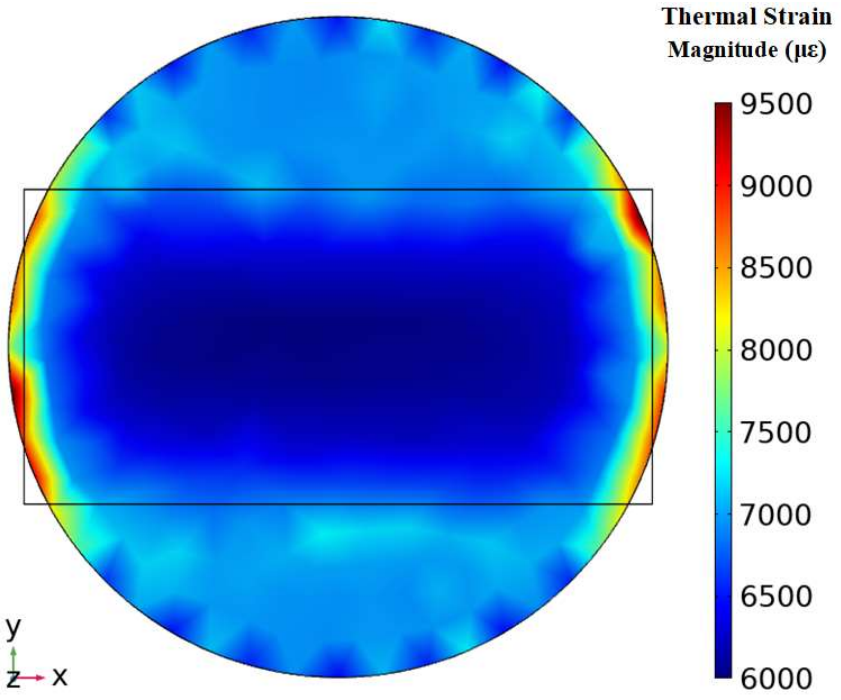

Figure 2.13 An X-Y plane cross-section at the Inconel/adhesive interface 5nm into the adhesive displaying the magnitude of thermally induced strain at 400°C under no mechanical load.

displaying the magnitude of the mechanical strain. By comparing the mechanical load of 347με and the thermal strain at 400°C (Figure 2.11), one can see that the strain caused by heating the sample from 25°C to 400°C is on the order of 10 times larger than the strain resulting from applying the 800g or 347με load to the beam. Therefore, it can be concluded that thermal strain is the primary cause of sensor attachment failure for high temperature static strain testing where temperature variations are around several hundred °C with respect to room temperature, as analyzed here. For dynamic strain sensing, the presence of a dynamic load is expected to affect attachment more than that of a static load of the same magnitude due to the cycling nature of the dynamic strain. More work needs to be done in this area to determine the effect of a dynamic load on sensor attachment compared to a static load.

In addition to observing the strain at the LGS/adhesive and Inconel/adhesive interfaces, it is important to monitor the strain on the top surface of the LGS because that is where the SAW is propagating and thus affecting the sensor sensitivity. These calculations will be used as a baseline in the comparison of the SAWR response to strain of the FI adhesive mounting scheme and new adhesive geometries that will be discussed in the next section. Figure 2.15 shows the mechanical

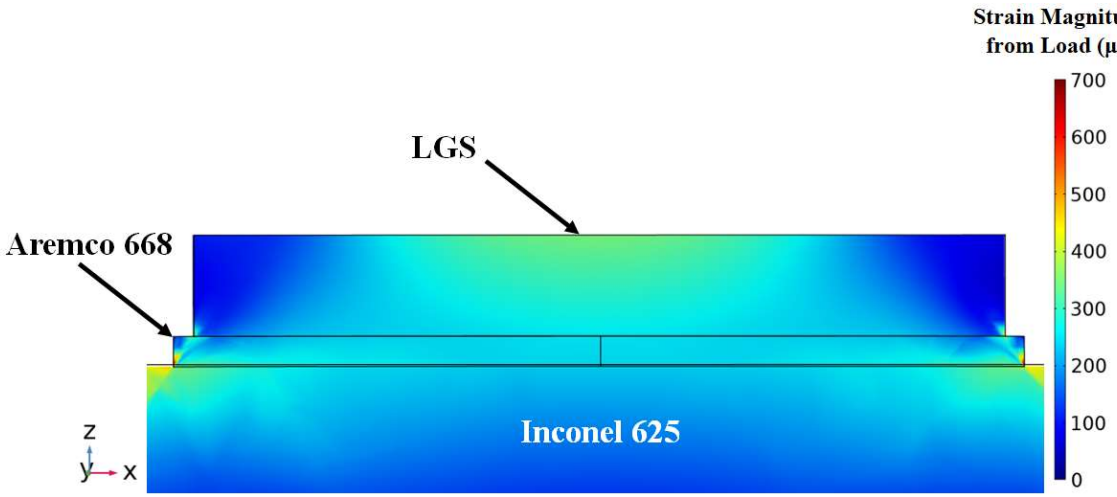

Figure 2.14 An X-Z plane cross-section through the LGS, adhesive layer, and Inconel 625 displaying the magnitude of mechanical strain under a load of 800g at 25°C.

strain magnitude on the top surface of the LGS where the SAW propagates. The IDT and reflectors respective area and position are labeled in the figure for reference. For this device fabricated with heavy Pt/Al_2O_3 electrodes, some of the reflection starts taking place within the IDTs, and it is expected that most of the energy in the resonator is contained in the resonator within 160 wavelengths from each side of the IDTs. At the point where the IDTs are located, the mechanical strain was found to be 348με. This simulation result shows that a 0.15mm Aremco 668 adhesive layer allows the transfer of mechanical strain from the beam to the sensor at comparable magnitudes between the beam and top surface of the LGS. However, imperfect adhesion of the adhesive to the beam and the SAWR will reduce the actual strain transferred from the beam to the top surface of the LGS. The X-component of the strain dominates over the X, Y, and Z-components of the mechanical strain at the LGS top surface. This is expected because the constant

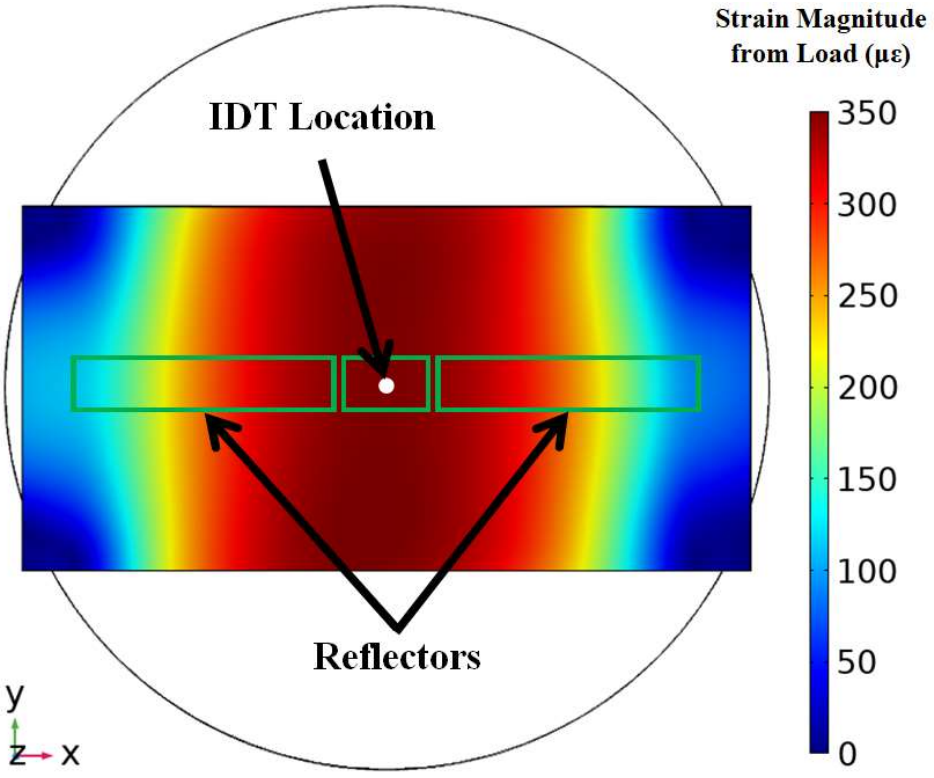

Figure 2.15 An X-Y plane cross-section at the LGS top surface displaying the magnitude of mechanical strain under a load of 800g at 25°C.

stress region on the static strain beam was designed to be strongly predominant along the X-direction. The plots for the X, Y, and Z-components of mechanical strain for the LGS top surface are shown in Appendix A.

Figure 2.16 shows the mechanical strain magnitude with a load of 800g on an X-Y plane cross-section at the LGS/adhesive interface 5nm into the LGS. The maximum strain at this interface was found to be 340με and was located on the borders of the LGS. The individual X, Y, and Z-component plots (Appendix A) show that the high strain concentration on the borders is dominated by the X and Z-components of strain. However, this magnitude of mechanical strain is not expected that this is the primary cause of adhesive or crystal failure at high temperature due to the 23 times larger thermal strain values observed when heating to 400°C, as discussed earlier in this section. Figure 2.17 shows the mechanical strain magnitude with a load of 800g on an X-Y

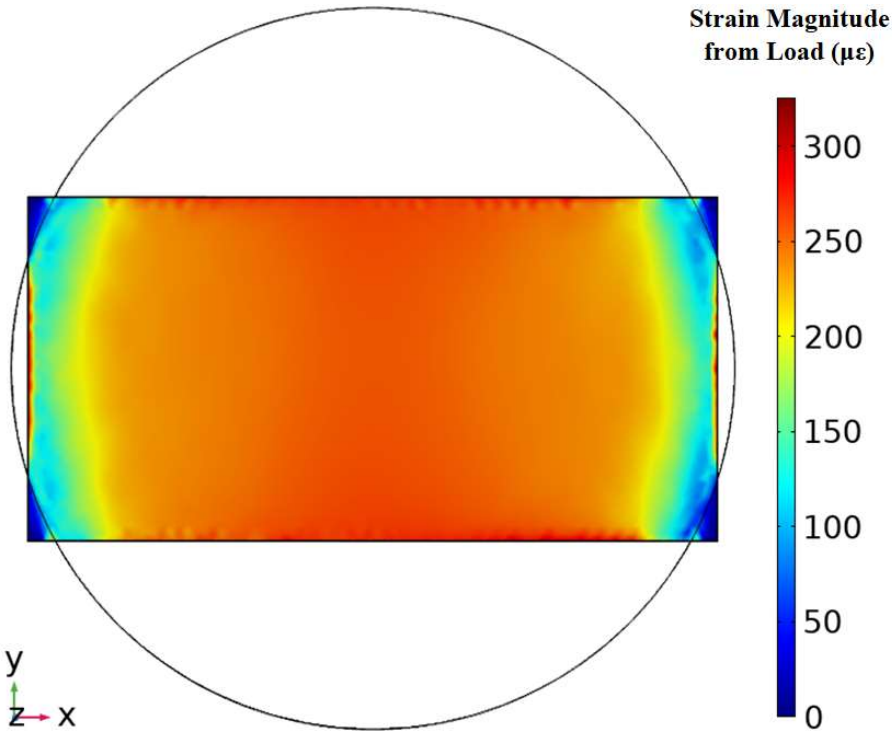

Figure 2.16 An X-Y plane cross-section at the LGS/adhesive interface 5nm into the LGS displaying the magnitude of mechanical strain under a load of 800g at 25°C.

plane cross-section at the Inconel/adhesive interface 5nm into the adhesive. The maximum mechanical strain magnitude found at this interface was found to be 644με and the regions of high maximum strain are found on the edges of the adhesive layer. The highest strain on the edges of the adhesive due to thermal variation between 25°C and 400°C was 15 times larger than the strain caused by the 800g applied load.

Table 2.2 summarizes the results discussed in this section. The results for modeling the LGS attached to Inconel 625 using a 0.15mm thick Aremco 668 adhesive covering the entire bottom interface show that thermal strain up to 400°C is significantly (over 10 times at the interfaces analyzed) higher than the strain caused by a static mechanical load of 800g applied to the beam. Therefore, thermally induced strain should be considered as the most likely cause of adhesive of crystal failure at high temperatures. When observing the thermal strain plots at the

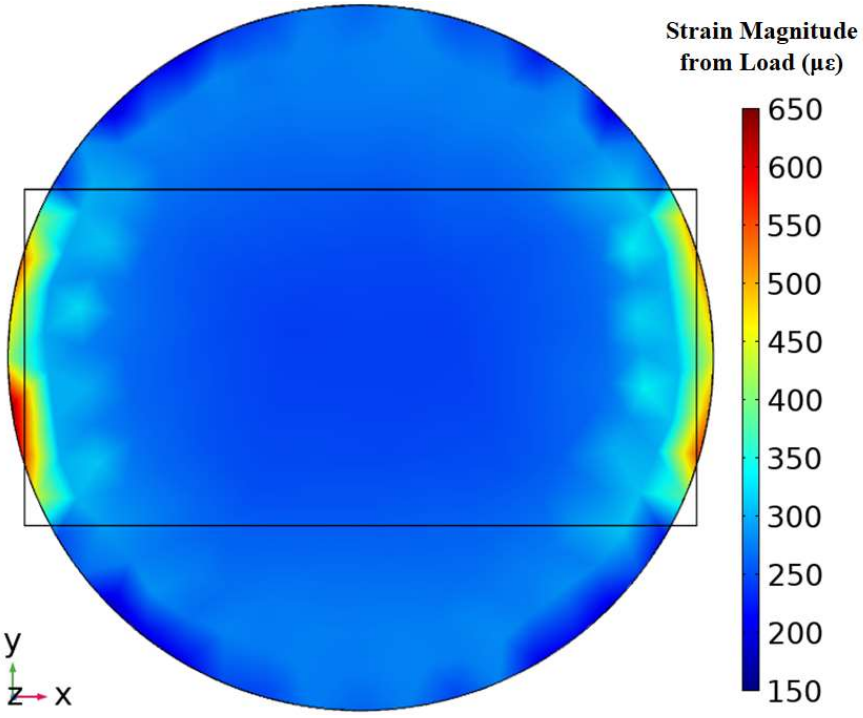

Figure 2.17 An X-Y plane cross-section at the Inconel/adhesive interface displaying the magnitude of mechanical strain under a load of 800g at 25°C.

Table 2.2 The strain magnitude data on the LGS Top Surface at the IDT location and the maximum strain magnitude at the LGS/adhesive and Inconel/adhesive interfaces for simulations of the thermal strain at 400°C and the mechanical strain from an 800g mechanical load.

Simulation Description	LGS Top Surface Strain Magnitude at IDT Location (με)	LGS/Adhesive Interface Maximum Strain Magnitude (με)	Inconel/Adhesive Interface Maximum Strain Magnitude (με)
Thermal Strain at 400°C	N/A	7840	9770
Mechanical Strain from an 800g Load	348	340	644

LGS/adhesive and Inconel/adhesive interfaces at 400°C, the maximum strain is found along the borders of the LGS chip and on the edges of the adhesive layer. This is problematic since the LGS chip borders are the weakest parts of the sensor chip due to the LGS wafer dicing, which causes chipping on the borders, and thus becomes the location where cracking initiates. The next section will investigate the thermal and mechanical strain for alternate adhesive geometries in an attempt to reduce the strain at the LGS borders and increase the strain transfer and thus the sensor sensitivity.

2.2.2 Simulation of Mounting Schemes Targeting Adhesion on Reduced Areas

One possible way to increase the temperature range of the SAWR strain sensor is to adjust the adhesive layer mounting scheme by using smaller adhesive shapes (adhesive shaping) to reduce the adhesion area on the LGS and distribute the thermal strain more efficiently, which could reduce the thermal strain magnitude and relocate the high strain regions away from the LGS borders. In this work, mounting schemes implementing two adhesive dots and two adhesive triangles were implemented to reduce the thermal strain at the LGS/adhesive interface. The implementation of the of the dot and triangle mounting schemes in COMSOL are shown in Figure 2.18.

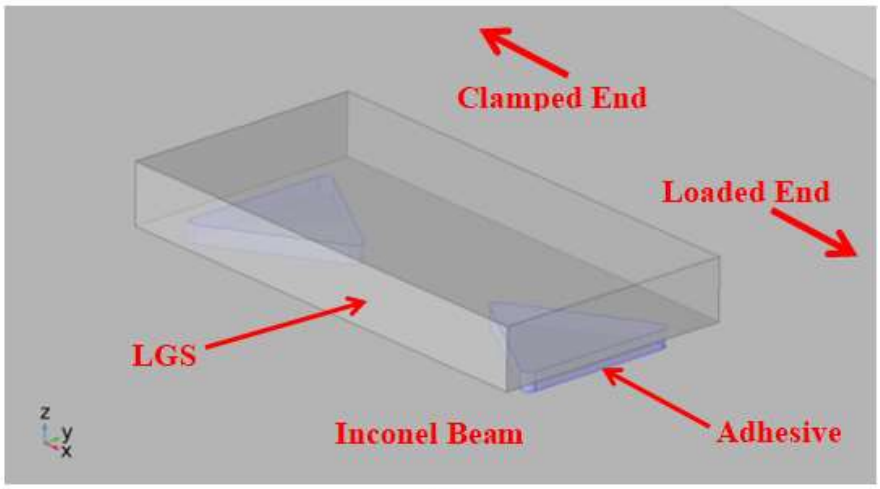

a.

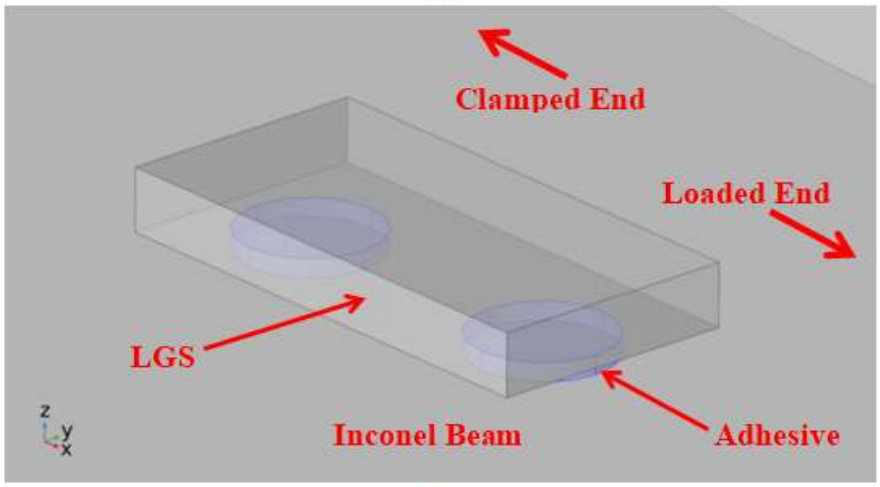

b.

Figure 2.18 The (a) triangle adhesive mounting scheme and (b) dot adhesive mounting scheme for high temperature and mechanical strain simulations. The LGS, Aremco 668 adhesive layer (highlighted in blue), and the Inconel beam are labeled.

The triangles have a height of 1.14mm and a thickness of 0.15mm, as measured in COMSOL. The tips of the triangles were pointed inwards for these simulations, as shown in Figure 2.18a. The separation between the two triangles is 1.4mm tip to tip. The dots (Figure 2.18b) have a circular shape with a diameter of 1.14mm and a thickness of 0.15mm, as measured in COMSOL. The diameter was set to 1.14mm so the dot diameter was the same as the height of the triangle mounting scheme. The separation of the two adhesive dots is 1.4mm edge to edge. The corners of the triangles were rounded to more closely mimic what would be observed experimentally if a

mask was used to apply the adhesive layer. Similar to the FI mounting scheme, two separate types of simulations were performed: in one, the beam was heated to 400°C with no mechanical load and in the other, an 800g (347με) load was applied to the beam at 25°C. These two tests were performed with the dot and triangle geometries.

Figure 2.19 shows an X-Z plane cross-section through the center of the Inconel/adhesive/LGS stack for the FI, dot, and triangle geometries displaying the magnitude of thermally induced strain magnitude at 400°C. The FI cross-section results shown are from the same simulation shown in Figure 2.11, but with the color legend adjusted to the single color legend in Figure 2.19 for all geometries. Figure 2.19 results reveal that the use of adhesive shaping does affect how strain is transferred throughout the stack when heated to 400°C. There is a lower strain magnitude at the LGS/adhesive interface when using adhesive shaping, but a higher strain magnitude at the Inconel/adhesive interface near the edges of the adhesive. Further analysis of the

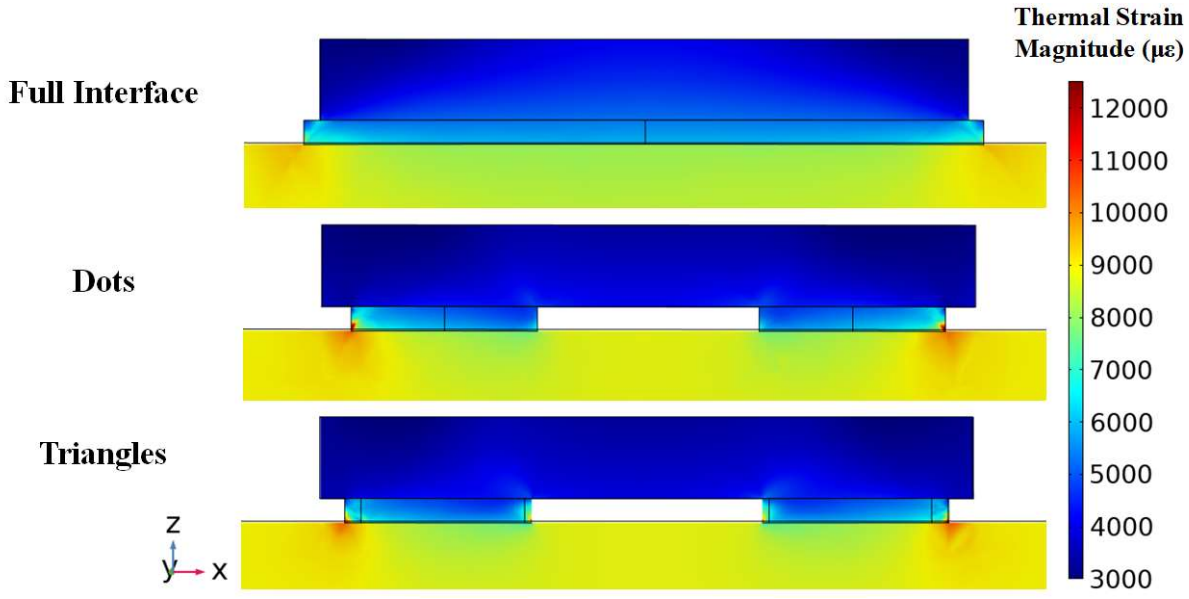

Figure 2.19 An X-Z plane cross-section through the LGS, adhesive layer, and Inconel 625 for the FI, dot, and triangle geometries displaying the magnitude of thermally induced strain at 400°C under no mechanical load.

X-Y plane cross-sections studied in Section 2.2.1 will need to be done to draw a conclusion on the effectiveness of adhesive shaping on LGS attachment to Inconel at high temperature.

Figure 2.20 shows the thermally induced strain magnitude at 400°C on an X-Y plane cross-section at the LGS/adhesive interface 5nm into the LGS for the FI, dot, and triangle geometries. The maximum strain magnitude measured for the dot and triangle geometries at this interface was 5440με and 5780με, respectively. The ratio of the maximum strain for the dot compared to the FI mounting scheme is 0.69 and the ratio of the maximum strain for the triangles compared to the FI mounting scheme is 0.74. Both geometries show a decrease in the maximum strain at the

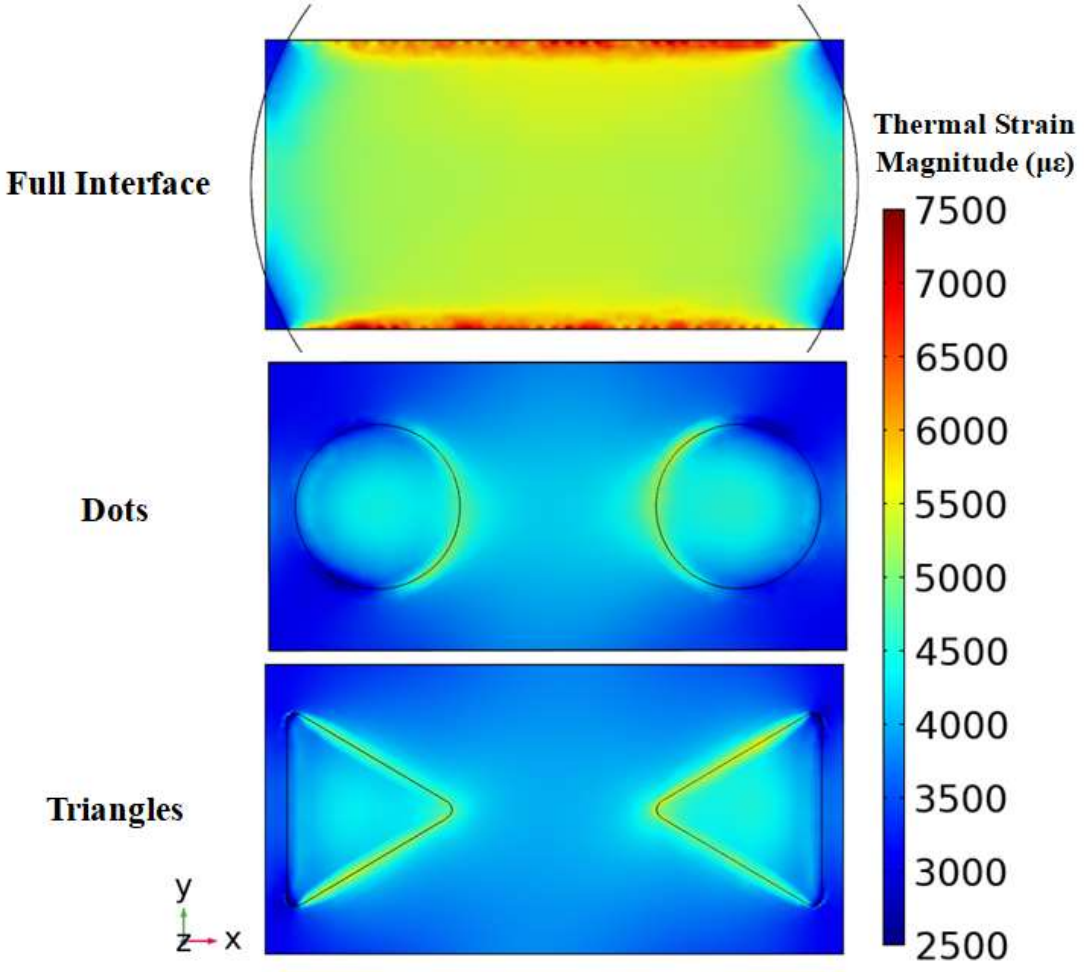

Figure 2.20 An X-Y plane cross-section at the LGS/adhesive interface 5nm into the LGS for the FI, dot, and triangle geometries displaying the magnitude of thermally induced strain at 400°C under no mechanical load.

LGS/adhesive interface when compared to the FI mounting scheme. In addition, the maximum strain is also removed from the borders of the LGS crystal. The ratio of the maximum strain at the LGS borders for the dots and triangles compared to the FI mounting scheme is 0.49. The results from the simulations for the maximum strain and maximum strain at the LGS borders for the FI, dot, and triangle simulations is summarized in Table 2.3. Both the dots and triangles decrease the strain at the LGS borders by over 50%, greatly reducing the strain at the most vulnerable part of the LGS chip. For both the dots and triangles, the primary component of strain is along the X-direction, evident from the plots shown in Appendix A.

Table 2.3 The maximum thermal strain magnitude (unloaded beam heated to 400°C) for the FI, dot, and triangle geometries over the entire LGS/adhesive interface and at the LGS borders. The ratio of the maximum strain for the adhesive shape mounting schemes and over the full interface is also included.

Mounting Scheme	LGS/Adhesive Interface Maximum Strain Magnitude (με)	LGS/Adhesive Interface Maximum Strain Ratio	LGS/Adhesive Interface Maximum Strain Magnitude at LGS Borders (με)	LGS/Adhesive Interface Maximum Strain Ratio at LGS Borders
FI	7840	-	7840	-
Dot	5440	0.69	3860	0.49
Triangle	5780	0.74	3840	0.49

Figure 2.21 shows the thermally induced strain magnitude at 400°C on an X-Y plane cross-section at the Inconel/adhesive interface 5nm into the adhesive layer for the FI, dot, and triangle mounting schemes. The maximum strain magnitude measured for the dot and triangle geometries at this interface was 13100με and 27400με, respectively. The color legend in Figure 2.21 has a maximum of 22000με (5400με lower than the maximum strain observed for the triangle adhesive mounting scheme) so that the strain distribution in the FI and dot geometries would be easier to analyze. Unlike the LGS/adhesive interface, the use of adhesive shaping increases the strain magnitude at the interface. The ratio of the maximum strain for the dots compared to the FI mounting scheme is 1.34 and the ratio of the maximum strain for the triangles compared to the FI

mounting scheme is 2.80. The simulation data for the maximum strain and maximum strain at the LGS borders for the FI, dot, and triangle simulations is summarized in Table 2.4. This increase in strain at the Inconel/adhesive interface could lead to adhesion issues at high temperature, especially for the triangle adhesive shaping, which shows the highest strain of the three mounting schemes. Although the simulations show that strain at the LGS borders is reduced when using adhesive shaping, the maximum strain at the Inconel/adhesive interface was found to increase

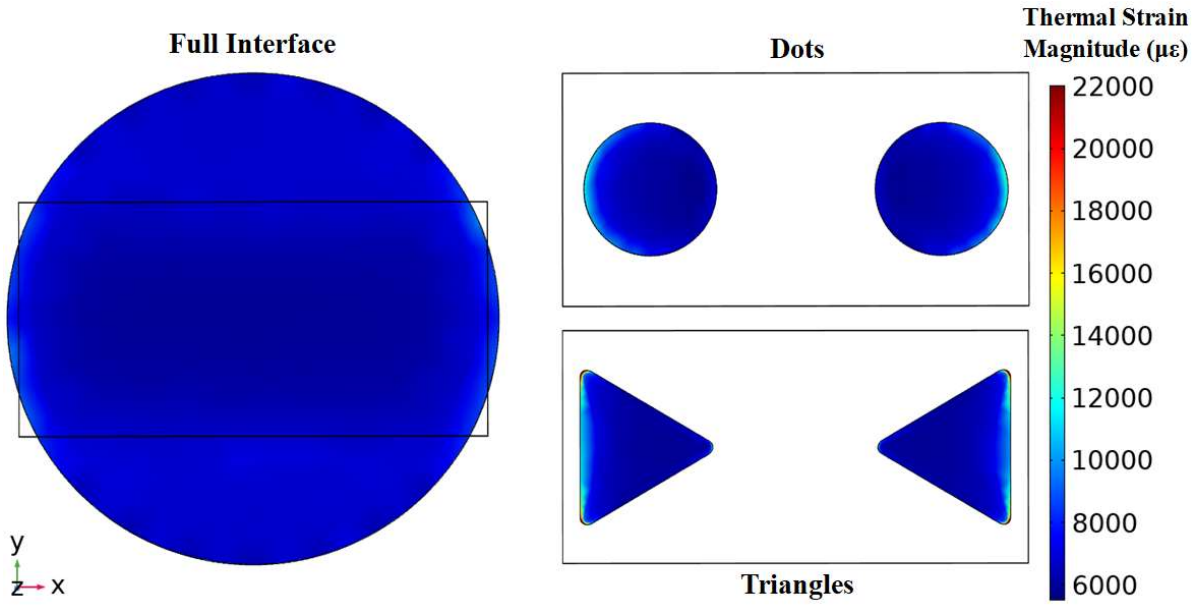

Figure 2.21 An X-Y plane cross-section at the Inconel/adhesive interface 5nm into the adhesive for the FI, dot, and triangle geometries displaying the magnitude of thermally induced strain at 400°C under no mechanical load.

Table 2.4 The maximum thermal strain magnitude (unloaded beam heated to 400°C) for the FI, dot, and triangle geometries over the entire Inconel/adhesive interface. The ratio of the maximum strain for the adhesive shape mounting schemes and over the entire interface is also included.

Mounting Scheme	LGS/Adhesive Interface Maximum Strain Magnitude (με)	LGS/Adhesive Interface Maximum Strain Ratio
FI	9770	-
Dot	13100	1.34
Triangle	27400	2.80

when adhesive shaping is implemented, which increases the likelihood of adhesion failure at that interface.

The next simulations performed on the dot and triangle adhesive shaping mounting schemes was loading the beam with an 800g mechanical load. Figure 2.22 shows an X-Z plane cross-section through the center of the Inconel/adhesive/LGS stack for the FI, dot, and triangle geometries displaying the magnitude of the mechanical strain due to an 800g load on the beam. The plots reveal that the dot and triangle geometries show more than 1.75 times greater strain at the edges of the adhesive later than for the FI mounting scheme. It is also difficult to tell from these graphs how much strain is transferred from the beam to the top surface of the LGS where the SAW is propagating. Analysis of the X-Y cross-sections analyzed in Section 2.1 was done to further analyze the strain throughout the Inconel/adhesive/LGS stack.

Figure 2.23 shows the mechanical strain due to an 800g load on the beam at 25°C for an X-Y plane cross-section on the top surface of the LGS for the FI, dot, and triangle geometries. The

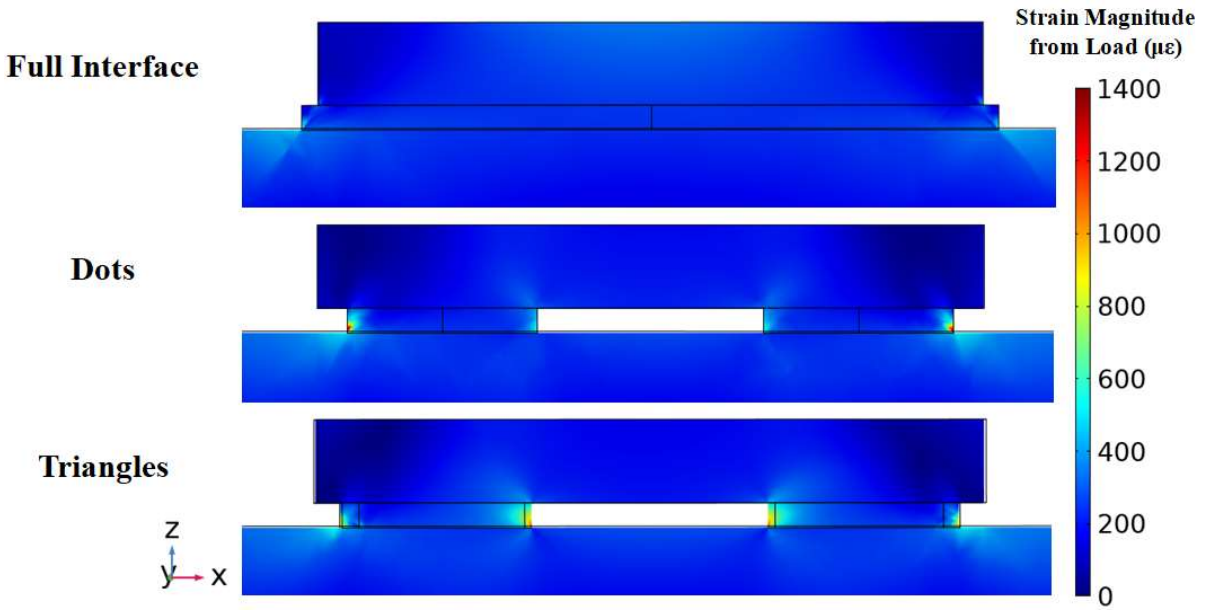

Figure 2.22 An X-Z plane cross-section through the LGS, adhesive layer, and Inconel 625 for the FI, dot, and triangle geometries displaying the magnitude of mechanical strain under a load of 800g at 25°C.

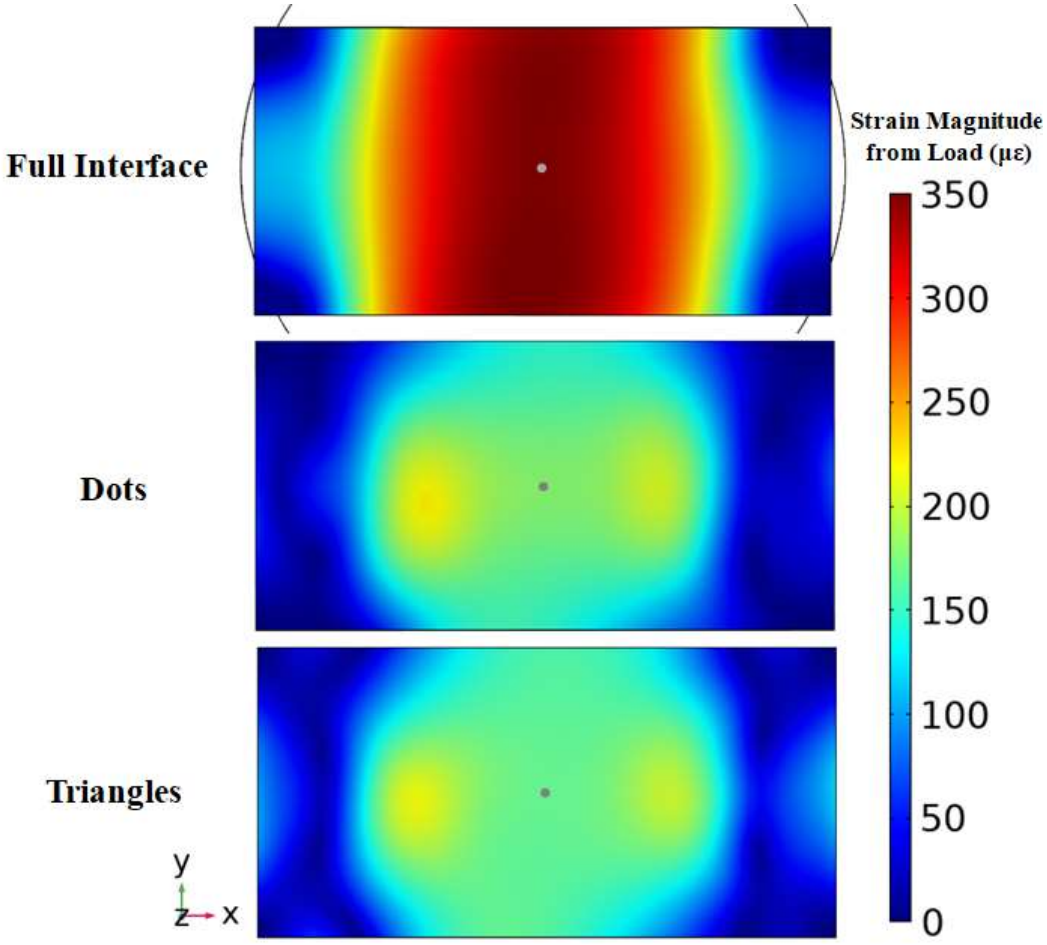

Figure 2.23 An X-Y plane cross-section at the LGS/adhesive interface 5nm into the LGS for the FI, dot, and triangle geometries displaying the magnitude of mechanical strain under a load of 800g at 25°C. The grey dots on the figures indicate the location where the IDTs are located on the LGS surface.

strain magnitude measured at the center of the IDTs on the top surface of the LGS (as indicated by the grey dots in Figure 2.23) for the dot and triangle configurations is 179με and 168με, respectively. Table 2.5 summarizes the strain magnitude measured at the IDT location on the top surface of the LGS for the FI, dot, and triangle adhesive geometries. The simulations show that adhesive dots show a slightly higher (6.5% higher) amount of strain is transferred to the top of the LGS than the triangles. However, neither are close to the strain magnitude observed for the FI mounting scheme. The simulations show that the dot and triangle adhesive shapes show approximately a 50% decrease in the amount of strain transferred from the beam to the top surface

Table 2.5 The maximum mechanical strain magnitude (beam loaded with 800g at 25°C) for the FI, dot, and triangle geometries over the entire LGS top surface. The ratio of the maximum strain for the adhesive shape mounting schemes and over the entire interface is also included.

Mounting Scheme	LGS/Adhesive Interface Maximum Strain Magnitude (με)	LGS/Adhesive Interface Maximum Strain Ratio
FI	348	-
Dot	179	0.51
Triangle	168	0.48

of the LGS when compared to the FI adhesive mounting scheme. This means that the SAWR sensitivity to strain using the dot or triangle configurations would most likely be about half of what it would be if the FI adhesive mounting scheme was used. Depending on the noise level resulting from the environment SAWR interrogation method, this lower sensitivity could be acceptable if the use of adhesive shaping can increase the maximum operational temperature of the SAWR.

Figure 2.24 shows the mechanical strain due to an 800g load on the beam at 25°C on an X-Y plane cross-section at the LGS/adhesive interface 5nm into the LGS for the FI, dot, and triangle geometries. The maximum strain magnitude measured for the dot and triangle geometries at this interface was 393με and 512με, respectively. The ratio of the maximum strain for the dots compared to the FI mounting scheme is 1.16 and the ratio of the maximum strain for the triangles compared to the FI mounting scheme is 1.51. Use of the dots shows a slight increase in strain at the LGS/adhesive interface and use of triangles shows more than a 50% increase in strain at the LGS/adhesive interface. This should not be the primary factor contributing to adhesion failure at this interface considering the comparative magnitude of the thermally induced strain, but it could become relevant if a dynamic load is applied. Figure 2.25 shows the mechanical strain due to an 800g load on the beam at 25°C on an X-Y plane cross-section at the Inconel/adhesive interface 5nm into the LGS for the FI, dot, and triangle geometries. The maximum strain magnitude measured for the dot and triangle geometries at this interface was 1210με and 2040με, respectively.

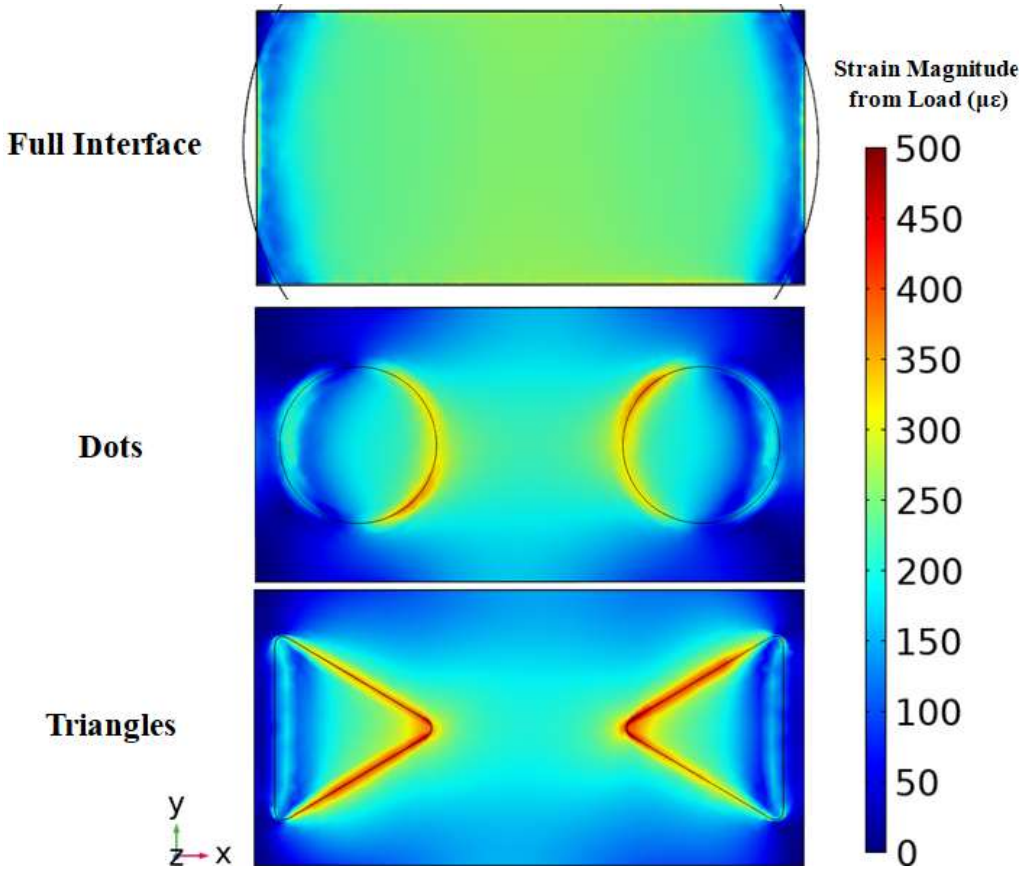

Figure 2.24 An X-Y plane cross-section at the LGS/adhesive interface 5nm into the LGS for the FI, dot, and triangle geometries displaying the magnitude of mechanical strain under a load of 800g at 25°C.

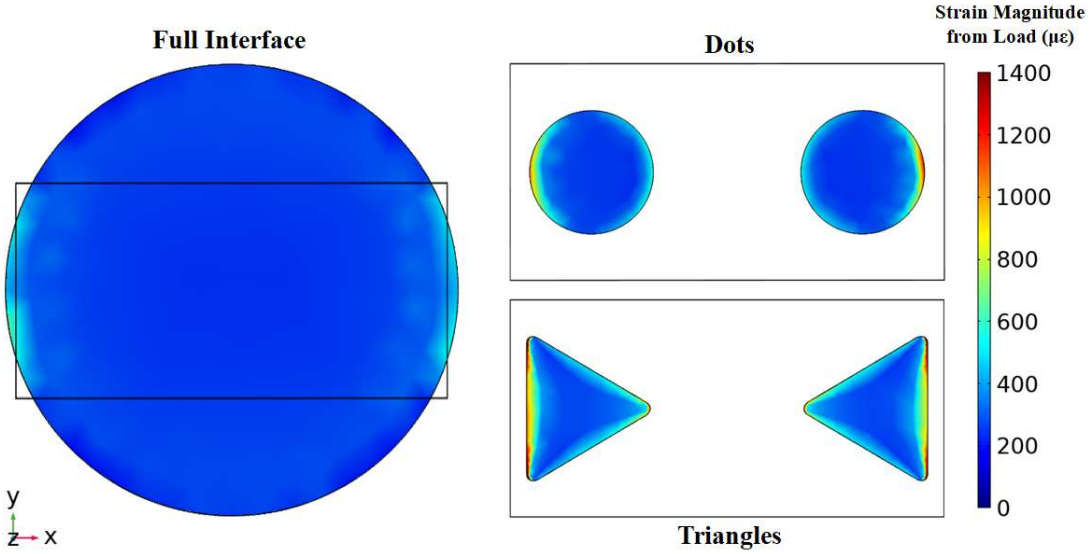

Figure 2.25 An X-Y plane cross-section at the Inconel/adhesive interface 5nm into the adhesive for the FI, dot, and triangle geometries displaying the magnitude of mechanical strain under a load of 800g at 25°C.

The ratio of the maximum strain for the dots compared to the FI mounting scheme is 1.89 and the ratio of the maximum strain for the triangles compared to the FI mounting scheme is 3.17. Use of adhesive shaping increases the maximum mechanical strain at the Inconel/adhesive interface compared to the FI adhesive mounting scheme, but comparatively, it is much lower than the magnitude of thermal strain observed at this interface, so it would not be the primary cause of adhesion failure at this interface. Table 2.6 summarizes the simulation results at the LGS/adhesive and Inconel/adhesive interfaces.

Table 2.6 The maximum strain magnitude (beam loaded with 800g at 25°C) for the FI, dot, and triangle geometries over the entire LGS/adhesive interface and at the Inconel/adhesive interface. The ratio of the maximum strain is also included.

Mounting Scheme	LGS/Adhesive Interface Maximum Strain Magnitude (με)	LGS/Adhesive Interface Maximum Strain Ratio	Inconel/Adhesive Interface Maximum Strain Magnitude (με)	Inconel/Adhesive Interface Maximum Strain Ratio
FI	340	-	644	-
Dot	393	1.16	1210	1.89
Triangle	512	1.51	2040	3.17

2.3 Conclusions

This chapter analyzes the strain experienced by the mounted SAWR sensor at 400°C and under a mechanical load of 800g using COMSOL Multiphysics. In addition, new proposed mounting techniques that make use of adhesive dots and triangles with a lower area of adhesion to the LGS and beam to reduce the strain at those interfaces. At 400°C, the simulations show that the strain magnitude at the LGS/adhesive interface is reduced when using adhesive shaping when compared to the FI configuration. However, at the Inconel/adhesive interface, the maximum strain magnitude increased when using the adhesive dots and triangles. Also, when comparing the dot and triangle configurations, the dots showed a lower strain magnitude at the LGS/adhesive and Inconel/adhesive interfaces. When applying an 800g load to the beam, it was found that the overall

mechanical strain at the LGS/adhesive and Inconel/adhesive interfaces for all three adhesive configurations was significantly lower than the thermal strain when heating to 400°C. Therefore, under static conditions, the thermal strain due to thermal expansion at high temperature would be the primary cause of adhesion failure. However, it has not yet been determined how a dynamic load affects adhesion. The top surface of the LGS was also measured when applying an 800g load to the beam. This surface is important because it is where the SAW propagates and thus related to the sensor sensitivity. The simulations show that the FI configuration transfers about twice as much mechanical strain from the beam to the top surface of the LGS as the dot and triangle configurations do, thus reducing the SAWR strain sensitivity by about half. Depending on the noise floor and resolution of the equipment being used, this may or may not be acceptable for strain sensing.

Overall, the ideal adhesive mounting configuration depends on where adhesion failure occurs above 400°C. If the failure is at the LGS/adhesive interface, use of adhesive dots or triangles would help to reduce the strain at that interface. If the adhesion failure is at the Inconel/adhesive interface, then the dot and triangle configurations provide no advantage over the FI configuration. Furthermore, when comparing the dot and triangle configurations, the dots should be favored over the triangles. In simulations, the triangles showed a higher maximum thermal strain at 400°C at the LGS/adhesive and Inconel/adhesive while providing no advantage in mechanical strain transfer from the beam to the top surface of the LGS when compared to the dots. Also, application of adhesive in the shape of a triangle is more difficult to implement based on the small dimensions of the features. In this thesis, it was decided that use of the FI configuration was the best way to mount the SAWR sensors because it provides a higher SAWR sensitivity to strain and has been used previously for wired static and dynamic strain sensing in previous work [13], [32].

CHAPTER 3
WIRELESS STATIC AND DYNAMIC STRAIN MEASUREMENTS AT HIGH TEMPERATURE

This chapter discusses the implementation of wireless interrogation of SAWR static and dynamic strain sensors. At the University of Maine, wired static and dynamic strain sensing has been implemented up to 400°C [13], [32], [65]. As discussed in Chapter 1, wireless interrogation of SAWR static and dynamic strain sensors is desirable to allow interrogation on moving and vibrating parts and to avoid fragile connections between the SAWR and a high temperature cable and so that the sensor can be installed in small, hard-to-reach places. However, close proximity to metal and rapid field decay of field coupling antennas can make it difficult to extract the SAWR response. This chapter discusses details on attachment of the SAWR sensor to metal parts and the implementation of wireless sensing. Static and dynamic strain test setups are described and the results for the wireless strain measurements are presented.

3.1 SAWR Sensor Fabrication

The SAWR sensors used in this work were one-port resonators fabricated on LGS along Euler angles {0°, 138.5°, 32.9°}. The SAWR devices were fabricated with six different wavelengths between 8.00μm and 9.60μm in 0.32μm increments. The devices have room temperature resonant frequencies varying from approximately 280MHz and 330MHz in approximately 10MHz increments. This was done so that once heating one of the SAWR devices up to around 800°C, its resonant frequency would not reach the value of the lower frequency resonator. This is important for implementation of multi-sensor systems which, in some cases, are measuring different temperatures at different locations [13]. The SAWR electrodes consisted of 80 finger-pair IDTs and two 800 open-circuited reflector gratings, one on each side of the IDT, with a mark-to-space ratio of 1:1.

The IDT and reflector electrodes were fabricated using Pt/Al_2O_3 co-deposited films. A 10nm zirconium adhesion layer was first deposited on the LGS through e-beam evaporation. Then a graded co-deposited Pt/Al_2O_3 layer was deposited, as reported in [43]. This technique uses a transition layer that transitions the film from pure Pt to Pt/Al_2O_3 by slowly introducing Al in an oxygen rich environment. After the Zr layer was deposited, a 10nm Pt layer was deposited followed by a 10nm Pt/Al_2O_3 transition layer. After the transition layer, 100nm of Pt/Al_2O_3 was deposited. The total electrode thickness for the SAWR sensors was 130nm. A 50nm alumina capping layer was deposited on the electrodes to protect them from the environment and to mitigate electrode de-wetting if the device is exposed to temperatures around and above 900°C. Platinum paste was deposited over the bond pads, utilizing capacitive coupling of the IDTs [71], so the SAWR could be bonded to the sensor antenna with 1 mil platinum wires.

3.2 High Temperature Adhesives for Static and Dynamic Strain Sensing

To measure static or dynamic strain on a metal part, the SAWR sensor must be rigidly mounted to the part so that the strain can be transferred from the part to the sensor. Current work in high temperature strain sensing uses commercially available high temperature adhesives to adhere the SAWR to the metallic part [13], [31], [52]. The adhesive is critical because it needs to be able to absorb the stress due to thermal expansion at high temperature while transferring mechanical strain from the metallic part to the SAWR sensor. Also, the CTE of LGS (~5 ppm/°C) is much smaller than the typical CTE of the metal parts used in high temperature environments (13-17 ppm/°C), which makes it more difficult to find an adhesive for high temperature sensor operation.

At the University of Maine, Aremco 668, which is an alumina and silica-based adhesive, has been used to mount SAWR static and dynamic strain sensors for operation between room

temperature and 400°C [13], [14], [53], [67]. An example of a mounted SAWR sensor using this adhesive is shown in Figure 3.1. The process for mounting a SAWR sensor using Aremco 668 is described in Appendix B. As mentioned in Section 2.2, Aremco 668 has a CTE of 7.2ppm/°C, which allows for sensor operation up to about 500°C [13], [65].

3.3 Implementation of Wireless Interrogation of SAWR Strain Sensors

3.3.1 Inductive Field Coupling Antennas for SAWR Strain Sensing

The SAWR sensors used for static and dynamic strain sensing were wirelessly interrogated through inductive coupling techniques [72]. Both the interrogating and the sensor antennas consist of coils coupled through a magnetic field in a two-way signal flow: interrogating the sensor and receiving back the sensor response. Figure 3.2 shows the (a) sensor antenna, (b) sensor antenna and SAWR sensor, and (c) the interrogating antenna. The sensor and interrogating antennas were fabricated with gold paste on ceramic substrates using screen printing technique. Design and fabrication of these antennas were based on the work of Nicholas Aiken [72] and Environetix Technologies Corporation. The sensor antennas have dimensions of 12mm x 7mm x 0.5mm and the interrogating antennas used have dimensions of 21mm x 16mm x 1mm. A hole the size of the SAWR sensor was cut in the center of the sensor antenna substrate (Figure 3.2a) so that the sensor

Figure 3.1 A SAWR strain sensor mounted on metal using the Aremco 668 high temperature adhesive.

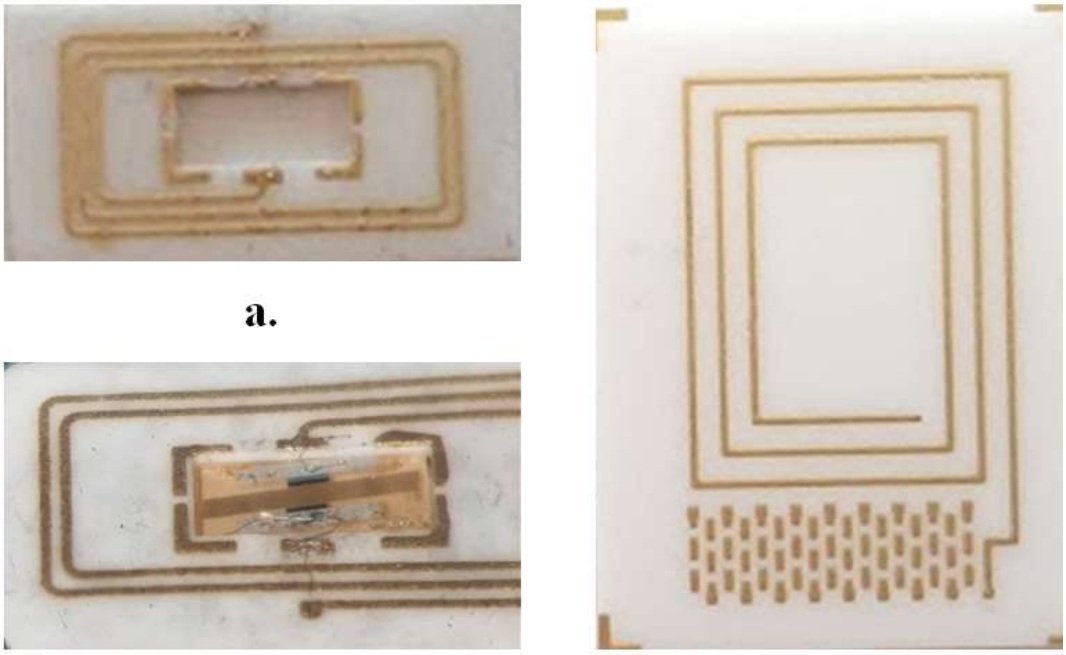

Figure 3.2 (a) The sensor antenna used to interrogate the SAWR static and dynamic strain sensors, designed and fabricated by Environetix Techngies Corp., (b) the sensor antenna placed around the LGS substrate and electrically connected to the SAWR sensor, and (c) the interrogating antenna [72].

antenna could be placed around the SAWR to facilitate packaging and minimize the length and fragility of the connection between the SAWR and sensor antenna. The SAWR sensor was electrically connected to the sensor antenna using 1-mil platinum wires (Figure 3.2b). The interrogating antenna (Figure 3.2c) was assembled in an Inconel antenna mount and secured by spot welding shim stock around the corners of the antenna chip. Aremco 668 adhesive was applied to the corners to further guarantee that there was a stable mounting of the interrogating antenna chip. The antenna was electrically connected to a high-temperature Inconel coaxial cable fed through the mount using 1-mil platinum wires so that it could be used in high temperature environments. The interrogating antenna was also fabricated with a tuning structure so that the operational frequency of the antenna could be adjusted to the resonant frequency of the SAWR sensors, by impedance matching, so the strongest possible signal could be attained. A simple setup for interrogating a

SAWR sensor using this wireless interrogation technique is shown in Figure 3.3. The test setups for the static and dynamic strain tests will be described later in this chapter.

When measuring the SAWR using wireless interrogation, it is necessary to implement time-gating to the interrogating antenna response to extract the SAWR response. For wired sensing, the SAWR resonant frequency could be directly measured from a vector network analyzer (VNA), but for wireless sensing, there is interference from reflections from the environment that affect the interrogating antenna response measured by the VNA. Therefore, the received signal must be signal processed by converting it to the time domain using an inverse fast Fourier transform (IFFT). Because the SAW travels slower than electromagnetic interference, the noise being picked up by the interrogating antenna decays within the first 500ns whereas the SAWR response will be observed between 1μs and 6μs. When an FFT is taken on the window of 0.5μs and 6μs, the result will show the SAWR response without electromagnetic interference.

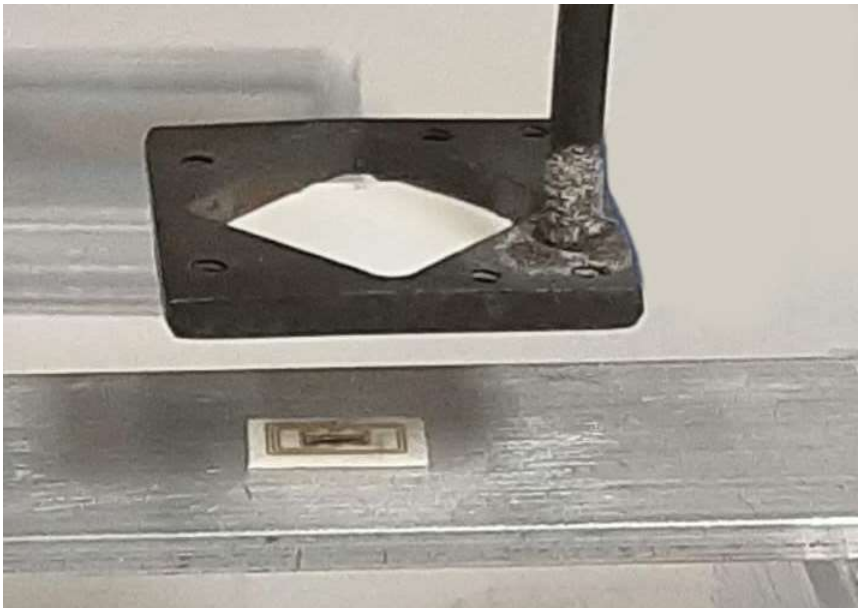

Figure 3.3 The interrogating antenna and sensor antenna used to interrogate the SAWR static and dynamic strain sensors [14].

3.3.2 SAWR Strain Sensor Packaging

Packaging of the SAWR static and dynamic strain sensors after mounting to the metallic part to be measured is crucial for sensor stability because if particles from the environment are deposited on the SAWR surface, they would load the device surface and change the SAWR frequency response [73]. The wireless sensing platform described in Section 3.3.1 was developed by Environetix Technology Corporation and used in this work. The assembling allows for simplicity in SAWR packaging when compared to wired strain sensing interrogation procedures. The SAWR strain sensor packaging is composed of three different alumina layers bonded together and sealed with Cotronics 940HT alumina-based adhesive [74]. The three separate layers for the SAWR packaging are shown in Figure 3.4a. The first layer is the sensor antenna that is placed around the SAWR strain sensor as described in Section 3.3.1. The second layer is an alumina spacer that has a hole cut into it to protect the bond wires from the SAWR to the sensor antenna. The hole in the middle is specifically designed so that as much of the SAWR sensor is covered while avoiding disturbances at the bond locations on the sensor antenna. The third layer is an alumina cover that prevents particles from falling on the SAWR sensor. This layer does not have any holes in it. All three layers have the same length and width as the sensor antenna, which are 12mm and 7mm, respectively. The spacer and cover layers have a thickness of 0.25mm, which is

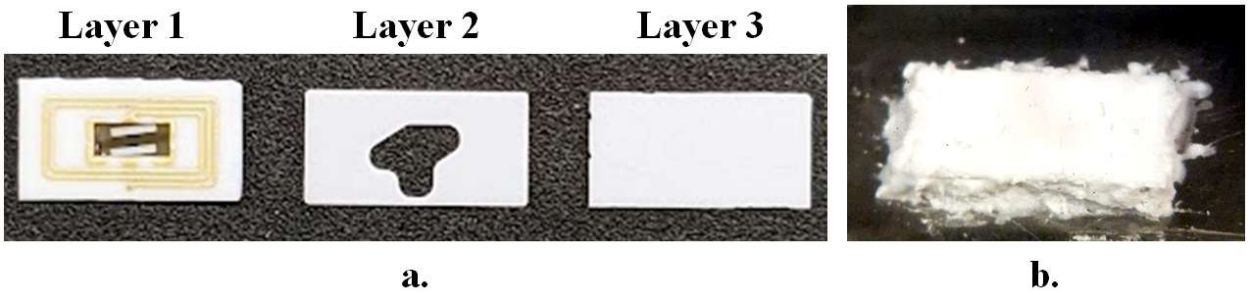

Figure 3.4 (a) The three layers of the SAWR package before the construction of the package and (b) the fully packaged SAWR strain sensor.

thinner than that of the sensor antenna. The alumina adhesive was applied on the outer edges of each layer to bond the layers together and along the sides to seal the remaining openings. The final packaged sensor sealed with the Cotronics 940HT adhesive is shown in Figure 3.4b.

3.4 Static and Dynamic Strain Test Measurement Systems

3.4.1 Static Strain Test Measurement System

The SAWR static strain measurement setup in this chapter was done in collaboration with Dr. Syeda Fizzah Jilani [53] and was built based on the previous static strain setup described in [32]. Figure 3.5 shows an image (a) and block diagram (b) of the wireless SAWR static strain sensing setup. The static strain beam fixture is composed of three components: the beam, the base, and the stand. All three parts were fabricated using Inconel 625. The static strain beam used was the same one that was used in the simulations in Chapter 2. The base is a piece of Inconel 625 that is used to stabilize the beam during testing and the stand was placed between the beam and the base so the beam was suspended above the base. The three parts were fixed together using stainless steel screws. The SAWR sensor was mounted to the static strain beam using the Aremco 668 ceramic adhesive. The adhesive thickness was 135µm. The results for this sensor will be compared

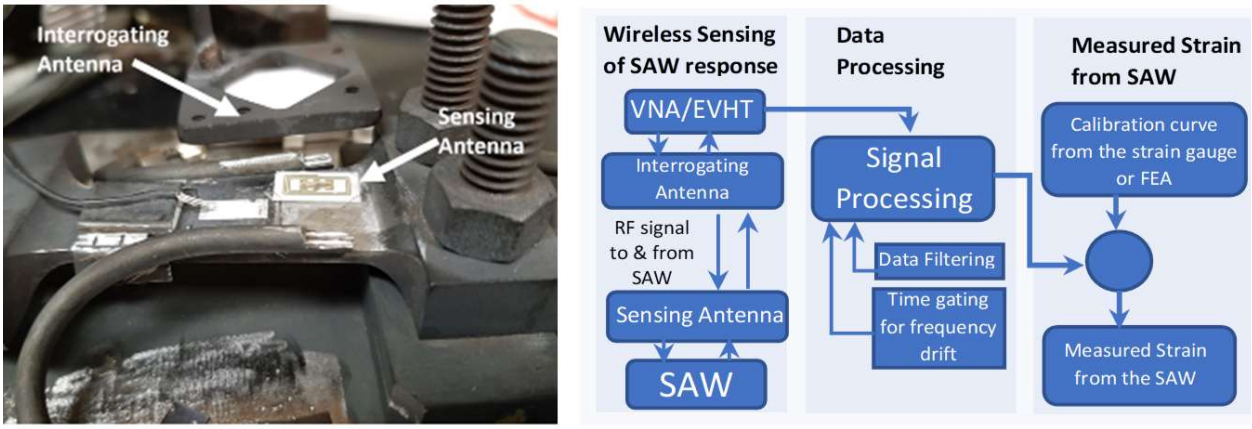

a. **b.**

Figure 3.5 (a) The wireless SAWR static strain sensing setup and (b) the block diagram of the wireless data acquisition of the sensor [53].

in Section 3.5.1 to the results of a wired sensor with an adhesive thickness of 150μm to determine the impact of adhesive thickness on the SAWR strain sensitivity [53]. The wireless SAWR data acquisition was done by the EVHT 300 monitoring system (Environetix Technologies Corporation, Orono, ME). The system performs post processing and time-gating of the SAWR signal and allows for real-time device monitoring and multiple sensor data logging capabilities.

High temperature static strain sensing was performed by placing the static strain beam in a Thermolyne Model 48000 box furnace (Thermo Fisher Scientific, Inc., Waltham, MA), as shown in Figure 3.6. The interrogating antenna was fed through a hole in the back of the furnace and clamped outside the furnace so it could be suspended approximately 5mm above the SAWR and sensor antenna. A static load was applied to the beam by adding weights to an alumina rod placed at the end of the beam. The rod was fed through the top of the furnace so that weights could be

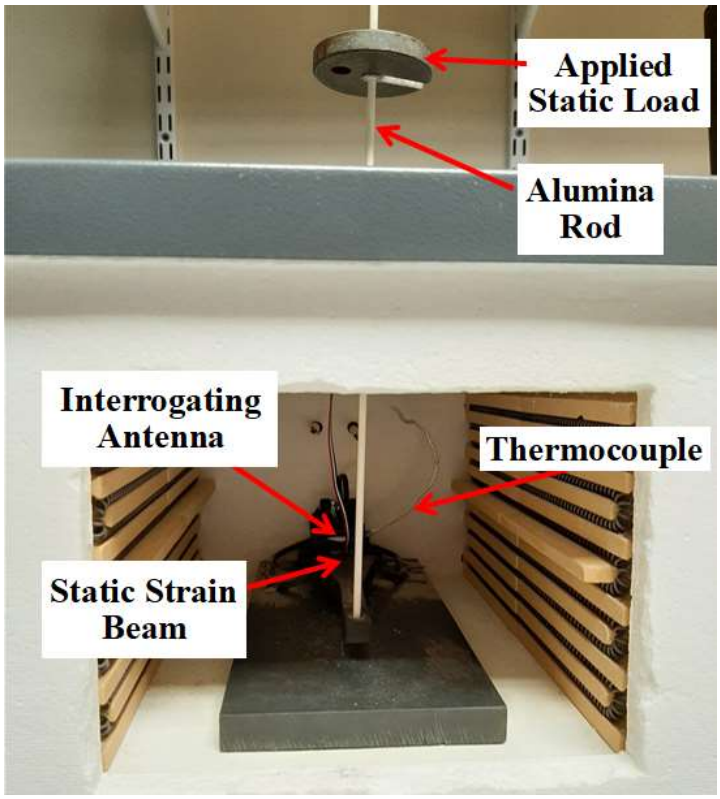

Figure 3.6 The static strain beam setup inside the box furnace for high temperature testing.

added and removed outside of the furnace. The SAWR sensor was calibrated to static strain using a commercially available static strain gauge (HBWAH-12-125-X-8MG-HB, HITEC Products Inc., HPI, Pepperell, MA) and the FEM simulations done in [53].

3.4.2 Dynamic Strain Test Measurement System

As mentioned in Chapter 2, a different beam was used for dynamic strain testing because targeted components of the applied load. Figure 3.7 shows the dynamic strain test fixture used for high temperature testing [32], [75]. The SAWR dynamic strain sensor was mounted in the same way that the SAWR static strain sensor was mounted using Aremco 668. A small piece of LGS substrate from the same SAWR wafer fabrication was mounted on the beam similarly to the SAWR sensor and in close proximity to it. A thermocouple was positioned on its surface in order to monitor temperature variations of the SAWR. The SAWR sensor was calibrated to dynamic strain using a high-temperature weldable strain gauge with an Inconel shielded cable (HBWANV-12-063-X-8MG, HITEC Products Inc., HPI, Pepperell, MA). The dynamic strain beam was mounted

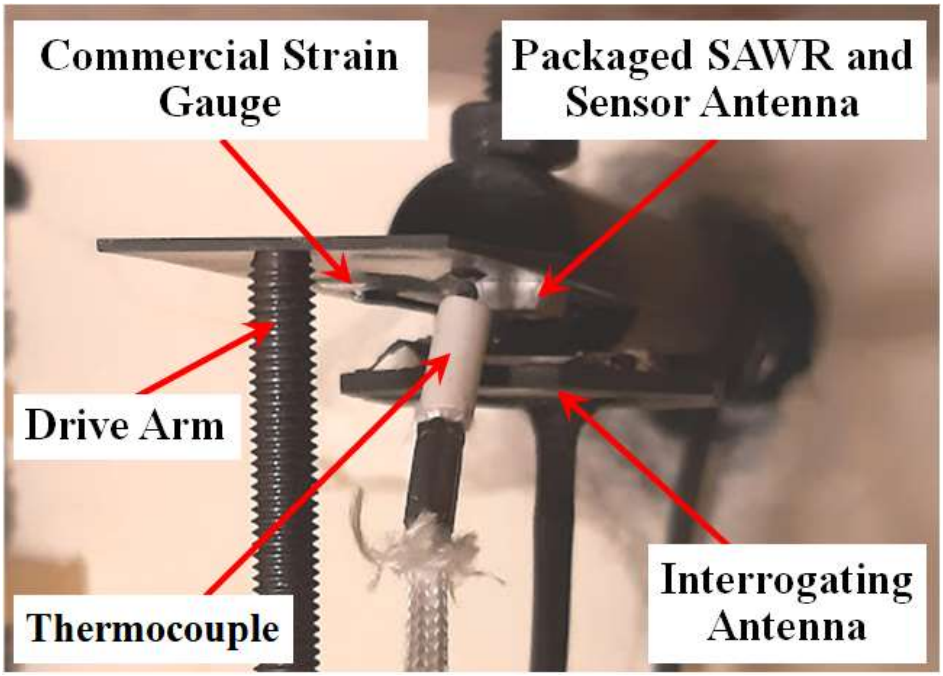

Figure 3.7 The dynamic strain fixture with the SAWR sensor and commercial strain gauge mounted in a box furnace. The thermocouple placement is also indicated in the figure [75].

to a stainless-steel support rod so that it could be fed through the back of a Thermolyne 48000 (Thermo Fischer Scientific, Waltham, MA) box furnace. The beam was clamped outside the furnace, so it is freely suspended inside the furnace. The interrogating antenna structure was secured to the stainless-steel support rod by spot welding shim stock around the high-temperature coaxial cable connected to the structure. The interrogating antenna was suspended approximately 5mm above the SAWR and sensor antenna. The beam receives the dynamic strain signal through a drive arm connected to an LDS V203 vibration generator (Bruel & Kjaer, Naerum, Denmark). The drive arm is a threaded rod that is screwed into a threaded hole in the vibration generator. The drive arm was screwed towards the beam, thus applying a static strain on the beam at all times during dynamic strain testing. This static strain is small, but enough so that the drive arm would not bang against the beam by being in contact with the surface of the beam during the entire vibration cycle.

Figure 3.8a shows the block diagram and Figure 3.8b the respective photo of the experimental setup with the appropriate equipment labeling for the SAWR dynamic strain testing. This setup was initially constructed by Dr. Anin Maskay, reported in [32]. In this work, two modifications were made to the setup: (i) the SAWR dynamic strain sensor was wirelessly interrogated rather than being measured by wired connections and (ii) a different commercial strain gauge was used for these experiments. The remaining components of the setup are the same as in [32]. The SAWR sensor measurement consisted of a 2μs excitation cycle followed by a 4μs listen cycle controlled by a ZYSWA-2-50DR RF switch (Mini-Circuits, Brooklyn, NY) [14], [34]. The SAWR was excited by an Agilent N9310 RF synthesizer (Keysight Technologies, Santa Rosa, CA), which provided the 2μs excitation at the unstrained SAWR resonant frequency (f_0). Since the SAWR resonant frequency varies with temperature, an Agilent 4396B VNA was used to measure

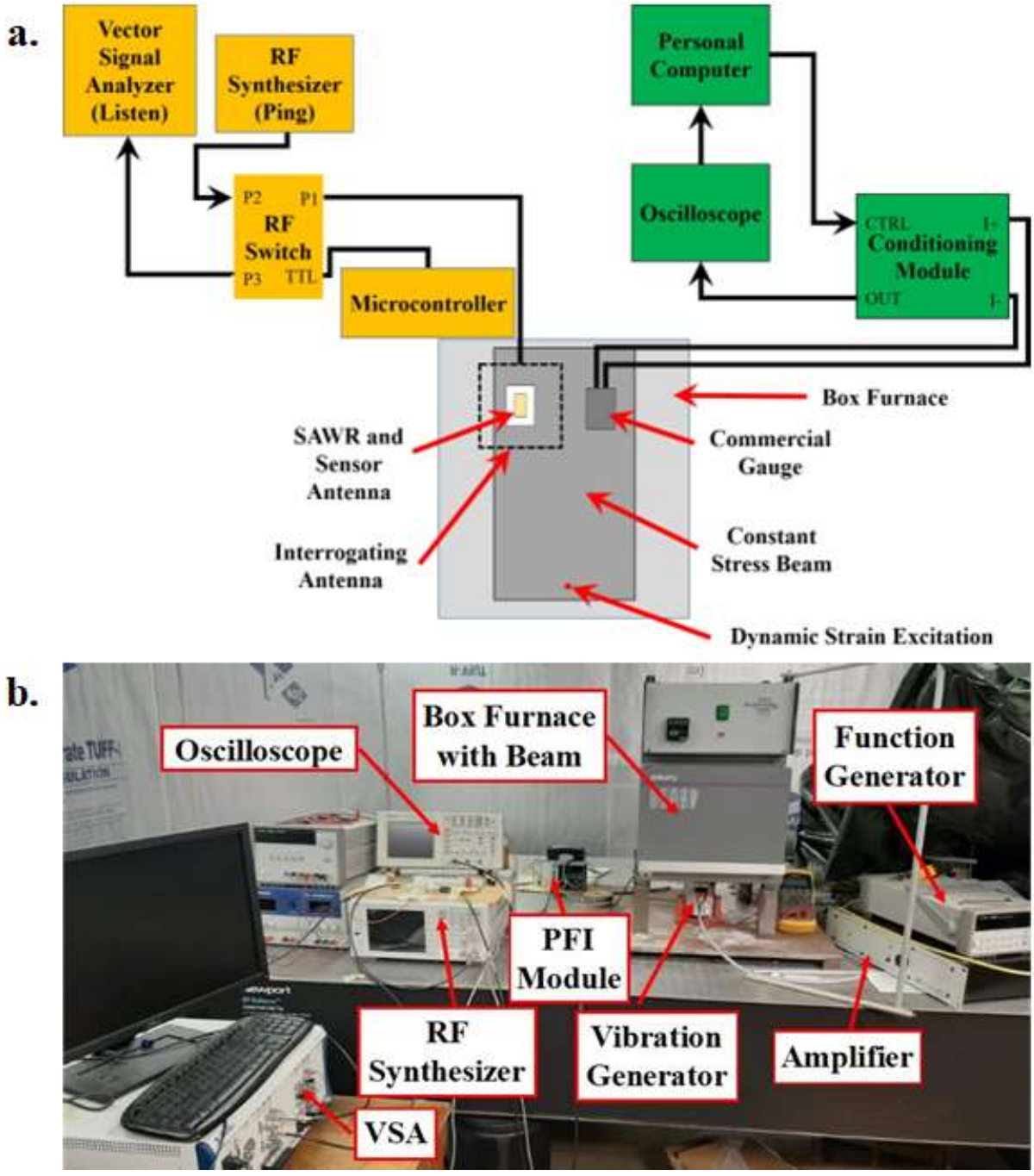

Figure 3.8 (a) The block diagram of the high-temperature test setup used in the wireless interrogaton of the SAWR dynamic strain sensor. (b) Respective photo of the experimental setup including equipment labeling [14], [32].

the resonant frequency after stabilization of the furnace temperature and before the dynamic strain data was acquired. A NI-PXIe-5663 vector signal analyzer (VSA) (National Instruments, Austin, TX) measured the echo response of the SAWR sensor during the listen cycle to obtain the power spectrum of the SAWR. The HPI strain gauge was excited using a PFI-9452 dynamic strain conditioning module (Precision Filters, Inc., Ithica, NY) to provide a constant current to the strain gauge and to amplify the sensor output. The output signal was measured using a Tektronix TDS2024 oscilloscope (Tektronix, Beaverton, OR).

3.5 Wireless Static and Dynamic Strain Measurements

3.5.1 Wireless Static Strain Measurements

The wireless SAWR static strain measurements reported in this section were done in collaboration with Dr. Syeda Fizzah Jilani [53]. For the tests performed with the wirelessly connected SAWR, the load applied to the static strain beam was varied in an ascending then descending order from 0 to 600g, in 200g increments. The EVHT-300 system was used for the real-time SAWR resonant frequency peak data acquisition. Each plot in Figure 3.9 depicts the wirelessly measured SAWR frequency peak values on the left vertical axis and the corresponding strain values (FEM model, [53]) on the right vertical axis, as a function of time, at room temperature (24°C) and from 50°C to 250°C, in steps of 50°C. The maximum temperature was set to 250°C because the adhesive thicknesses used for these tests were too thin (135μm and 150μm) to survive at 400°C [53]. A thicker adhesive layer (300μm) has the capability of operation at 400°C with a lower static strain sensitivity [53]. As can be noted from the plots in Figure 3.9, in several instances there are differences in the measured SAWR frequencies while increasing and decreasing the strain loads as a function of time. The LGS orientation of the fabricated SAWRs is not temperature compensated, and thus the observed variations in frequency are credited to the ±1°C

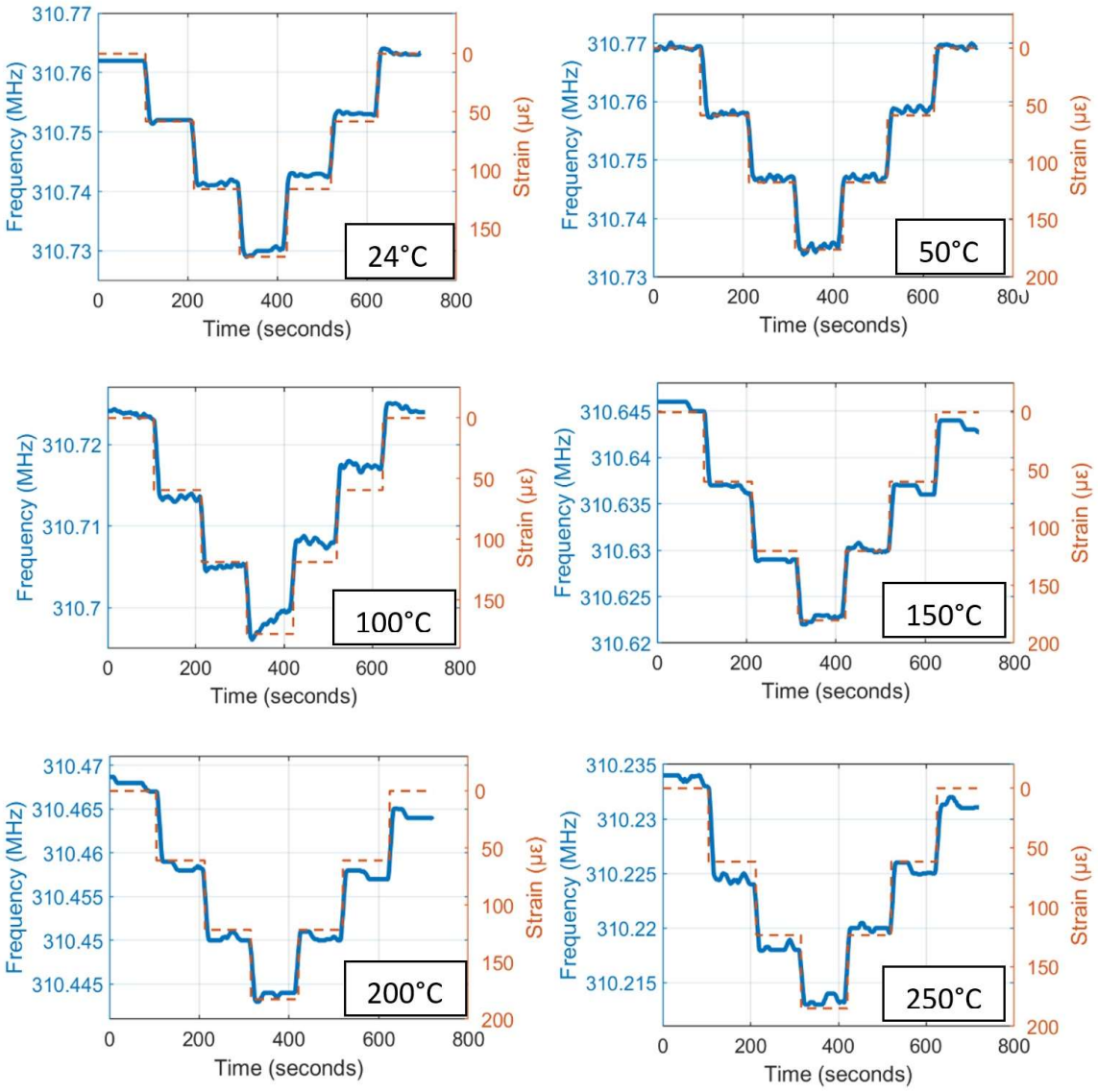

Figure 3.9 Wireless interrogation of SAWR strain sensor depicting the resonant frequency shift with respect to the respective strain [53].

fluctuation in the furnace temperature, which confirms the need to know temperature in a temperature-varying environment.

The strain sensitivities of the wireless SAWR at 24°C, 100°C, and 200°C with respective FEA are -182 Hz/με, -146 Hz/με, and -133 Hz/με, respectively. Table 3.1 lists these values with the respective correlation coefficients (R^2) for a linear regression analysis in the third and fifth columns. As can be noted from Table 3.1, the increase in strain sensitivity in the wireless SAWR

Table 3.1 Sensitivity for the SAWR Static Strain device for attachment with 150μm and 135 μm thick adhesive layer [53].

Temp. (°C)	SAWR Strain Sensor Sensitivity			
	150 μm thick adhesive		*135 μm thick adhesive*	
	Sensitivity (Hz/με)	R^2	***Sensitivity*** (Hz/με)	R^2
24	-131	0.9998	-182	0.9994
100	-104	0.9998	-146	0.9953
200	-86	0.9990	-133	0.9996

interrogation (fourth column) with respect to the wired SAWR interrogation (second column) is due to the reduction in adhesive thickness to 135 μm from 150 μm. Comparing the wired and wireless SAWR sensitivity values at 24°C, one can calculate from Table 3.1 that for a 10% decrease in thickness, the sensitivity increased by 39% [53].

3.5.2 Wireless Dynamic Strain Measurements

Wireless dynamic strain SAWR sensor measurements were obtained from 25°C to 400°C using the experimental setup described in Section 3.4.2. Figure 3.10 shows the SAWR power spectra relative to the center peak power taken at 400°C under unstrained conditions (blue) and dynamic strain excitations of 9.9με (red), 22.1με (green), and 32.6με (purple) at a frequency of 500Hz, as measured by the commercial strain gauge. The frequency on the x-axis was shifted to the baseband frequency by subtracting the SAWR resonant frequency at 400°C (f_0 = 286.98MHz). The sidelobes in the power spectra shown in Figure 3.10 are due to modulation of the SAWR response when the dynamic strain excitation is applied. The sidelobe frequency relative to the center peak frequency is the frequency of the dynamic strain applied. As shown in Figure 3.10, the sidelobe peaks increase with increasing dynamic strain magnitude. Under dynamic strain of 9.9με, 22.1με, and 32.6με their relative magnitudes with respect to the main peak are -46.1dBr, -40.8dBr, and

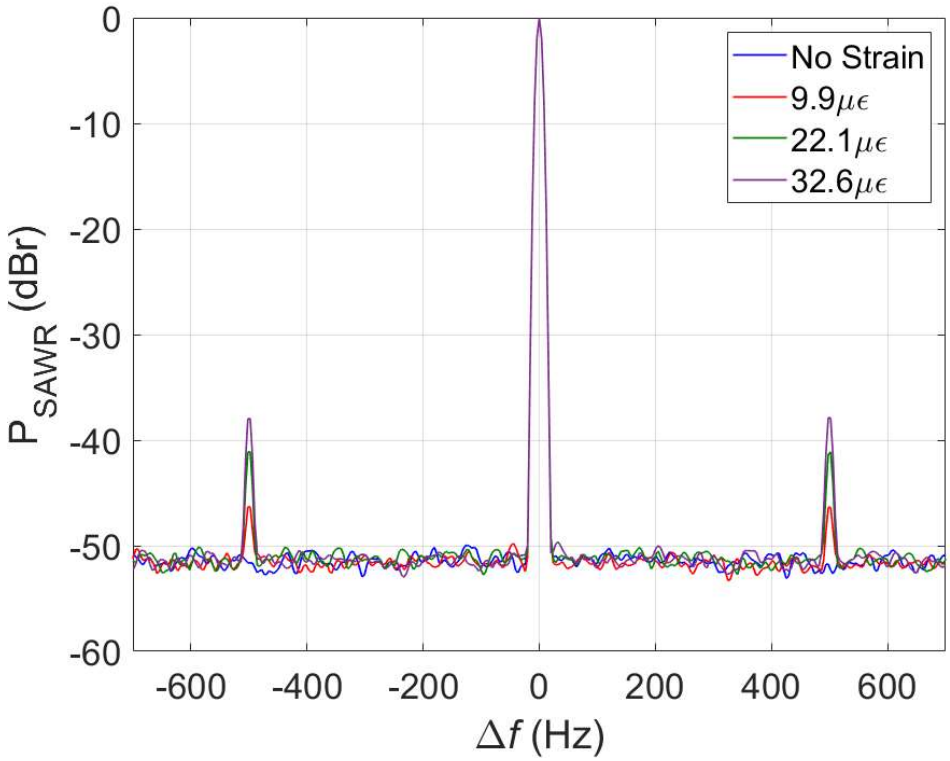

Figure 3.10 Wirelessly interrogated SAWR dynamic strain sensor: power spectra measured at 400°C relative to the excitation peak power under no dynamic strain excitation (blue) and under dynamic strain excitations of 9.9με (red), 22.1με (green), and 32.6με (purple); the horizontal axis plots the dynamic strain excitation frequency, 500Hz in this test (frequency shifted to the baseband frequency by subtracting the SAWR resonant frequency at 400°C, f_0 = 286.98MHz) [14].

-37.5dBr, respectively. The dynamic strain magnitude applied to the dynamic strain beam in this work did not exceed 40με because there is uncertainty in the quality of the SAWR attachment at high temperature under a dynamic load beyond 60-70με [32]. An equivalent sidelobe voltage, V_{SAWR}, can be calculated from the measured dynamic strain sidelobe amplitude relative to the SAWR resonant peak shown in Figure 3.10 by [14], [32]:

$$V_{SAWR} = \sqrt{R \cdot P_0 \cdot 10^{\frac{\Delta P_{SAWR}}{10}}} \tag{3.1}$$

where ΔP_{SAWR} is the sidelobe power relative to the excitation peak in dBr, R is 50Ω, and P_0 is an arbitrary selected reference power in watts. For these measurements, P_0 was chosen as 2.512nW or -56 dBm, which is a value close to the SAWR center peak power at room temperature, which

is different from the P_0 = 1mW used in previous work [32]. Although changing the value of P_0 does not affect the result, it was changed to more accurately reflect the actual SAWR voltage.

Figure 3.11 plots the extracted V_{SAWR} using Equation 3.1, from the measured ΔP_{SAWR} at 25°C (red), 100°C (blue), and 400°C (green) versus different dynamic strain values set by the vibration generator according to the calibration established by the HT strain gauge. Linear regression analysis was used as indicated by the straight lines in Figure 3.11 to determine the SAWR sensitivity to dynamic strain at each temperature tested. The resulting SAWR sensitivity to dynamic strain at 25°C, 100°C, and 400°C was 0.44μV/με, 0.36μV/με, and 0.14μV/με, respectively, as summarized in Table 3.2, which also includes the corresponding correlation coefficients (R^2) to each of the linear regressions. These curves show that the SAWR voltage has a linear relationship with dynamic strain for the range of dynamic strain magnitude tested. One should also observe that the SAWR sensitivity to dynamic strain decreased with increasing

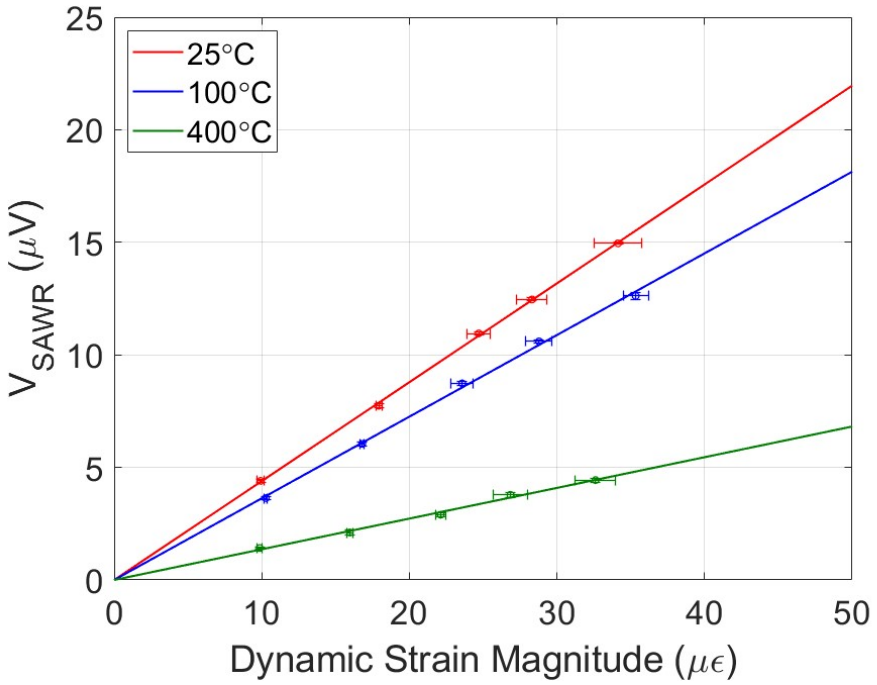

Figure 3.11 Plot of the extracted V_{SAWR} from the measured SAWR ΔP_{SAWR} at 25°C (red), 100°C (blue), and 400°C (green) and the respective linear regression curves. The dynamic strain frequency for all tests was kept at 500Hz [14].

Table 3.2 SAWR resonant frequency, dynamic strain sensitivities, and correlation coefficients at 25°C, 100°C, and 400°C [14].

Temperature (°C)	Resonant Frequency, f_0, (MHz)	SAWR Sensitivity (μV/με)	R^2
25	288.81	0.44	0.9995
100	288.76	0.36	0.9979
400	286.98	0.14	0.9935

temperature. As the temperature was increased from 25°C to 100°C, the SAWR sensitivity to dynamic strain decreased by 17%. From 25°C to 400°C, the decrease in SAWR sensitivity was 69%. The decrease in sensitivity is most likely related to an increase in the adhesive compliance and/or adhesive deterioration at higher temperatures, which causes less strain to be transferred from the dynamic strain beam to the SAWR sensor.

3.6 Conclusions

This chapter presents the results for the wireless SAWR static and dynamic strain tests performed. For both static and dynamic strain measurements, wireless interrogation was successfully implemented using field coupling antennas in close proximity to metal parts which lowers the signal. Utilizing the EVHT-300 system gives real-time data acquisition and signal processing the is desirable for SAWR static strain measurements. The static strain sensitivities for sensors mounted with two different adhesive layer thicknesses were also compared. It was found that at room temperature, a 10% decrease in adhesive thickness corresponds to a 69% increase in SAWR static strain sensitivity. However, reduction of adhesive thickness also lowers the maximum SAWR operational temperature. Wireless SAWR dynamic strain measurements up to 32.6με were achieved between 25°C and 400°C. A clear signal was observed at dynamic strain magnitudes as low as 10με (approximately 5dB above noise level), confirming that the inductive coupling wireless interrogation technique be used for high temperature dynamic strain sensing.

CHAPTER 4
SAWR DYNAMIC AND STATIC STRAIN SENSORS UNDER TEMPERATURE CYCLING

This chapter discusses the effects of temperature cycling on the SAWR dynamic and static strain sensors. Temperature cycling is needed to stabilize the SAWR electrode films to ensure that the SAWR response before mounting to a metal beam or part isn't changing over time [73]. After the SAWR sensor is mounted to a metal beam or part, it is likely that the adhesive will need temperature cycling to ensure that it provides a stable response to dynamic and static strain. Investigation into Aremco 668 other ceramic adhesives after thermal cycling show that commercially available ceramic adhesives cannot provide a stable SAWR attachment for strain at 400°C. Because of this, high temperature polymer epoxies were tested for potential use in achieving stable SAWR static and dynamic strain sensors after temperature cycling up to a lower maximum operational temperature of 200°C.

4.1 Considerations on Temperature Cycling for Strain Sensors

Temperature cycling is needed to stabilize the Pt/Al_2O_3 SAWR electrode films to ensure that the SAWR resonant frequency does not drift over time due to changes in the film at high temperature, as discussed in previous work at the University of Maine [73]. This is a critical step in characterizing SAWR strain sensors because if there is confidence that the SAWR film is stable, then variation in the SAWR response to static or dynamic strain can only be attributed to the stability of the adhesive used or the test setup. Because of this, the SAWR sensors used in this thesis were subjected to three rounds of temperature cycling between 300°C and 750°C, where one round is composed of four cycles between 300°C and 750°C with four hour hold times, a ten-hour soak at 750°C, and four cycles between 300°C and 750°C with four hour hold times as shown in

Figure 4.1. Between each round, the SAWRs were cooled to room temperature and measured to confirm that the resonant frequency was stable after the third round of temperature cycling. The plot of the magnitude of S_{11} of one of the SAWR sensors used in this work before cycling and after one round, two rounds, and three rounds of temperature cycling is shown in Figure 4.2, showing that there was no drift in the SAWR resonant frequency after three rounds of cycling as described in Figure 4.1.

To gain confidence in the stability of the Aremco 668 adhesive used to mount the SAWR sensor to the dynamic strain beam, temperature cycling was performed. Because the maximum target temperature was 400°C for this sensor, temperature cycling between 100°C and 425°C was performed. For cycling of the adhesive, one round of cycling consisted of three cycles between 100°C and 425°C with one hour hold times at each temperature, as described in Figure 4.3. This temperature cycling profile was applied to the SAWR sensor reported in Section 3.5.2 and the

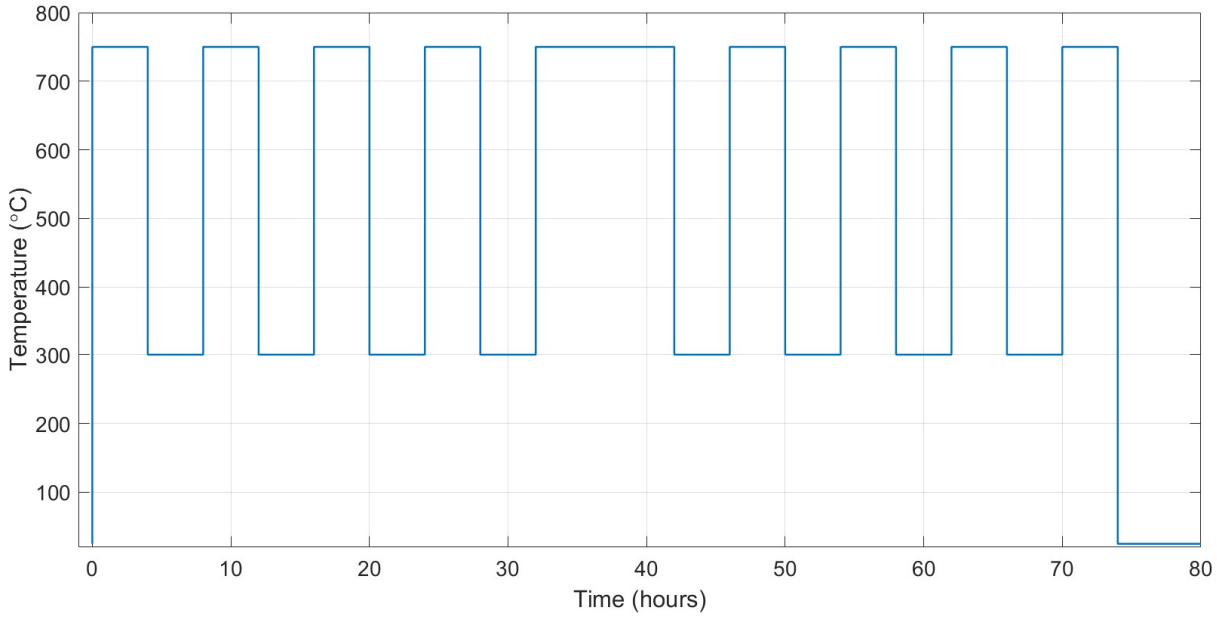

Figure 4.1 The temperature profile for one round of cycling between 300°C and 750°C for stabilization of the SAWR electrode film.

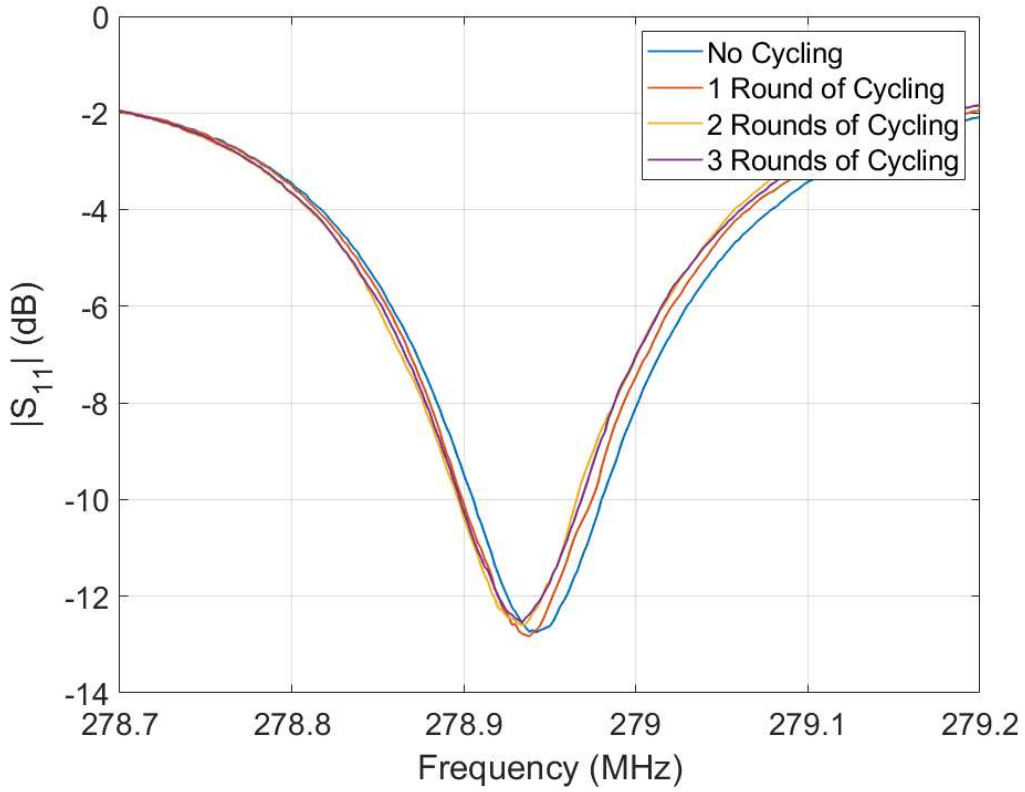

Figure 4.2 The $|S_{11}|$ of one of the SAWR sensors used in this work before temperature cycling and after one round, two rounds, and three rounds of temperature cycling between 300°C and 750°C

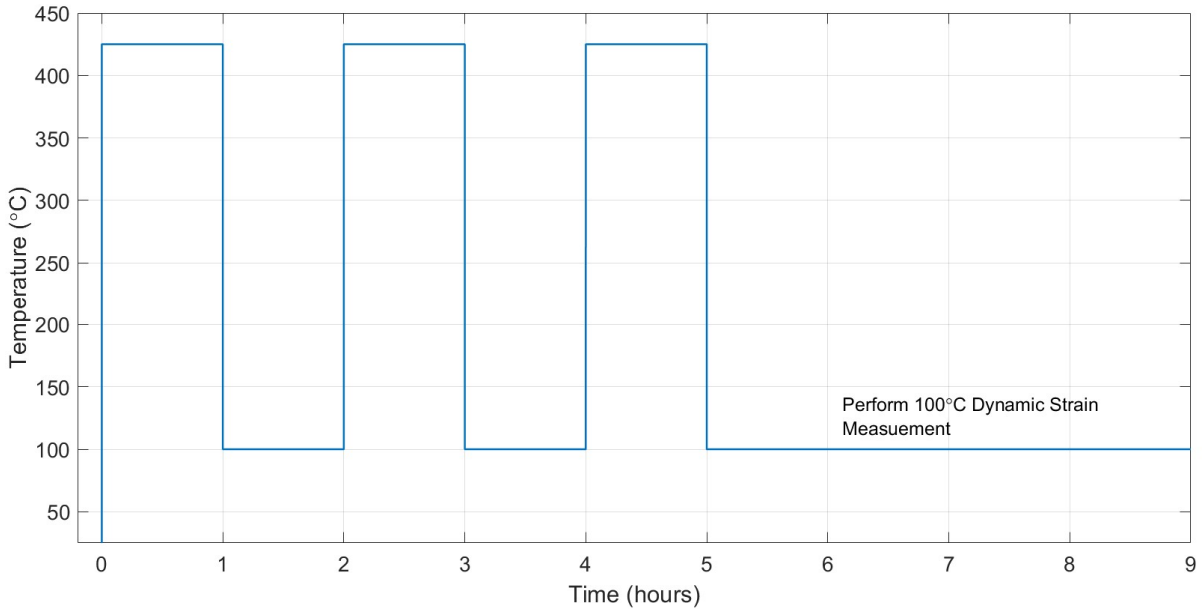

Figure 4.3 The temperature profile for one round of cycling between 100°C and 425°C to test the stability of the Aremco 668 adhesive for SAWR dynamic strain sensing.

dynamic strain response was measured at 100°C and 400°C between each round of cycling as presented in Section 4.2.1.

4.2 High Temperature Adhesives for Strain Sensing

4.2.1 SAWR Dynamic Strain Response after Temperature Cycling

Wireless dynamic strain measurements up to 400°C were performed for the SAWR dynamic strain sensor reported in Section 3.5.2. The mounted SAWR sensor was subjected to two rounds of thermal cycling between 100°C and 425°C as described in Section 4.1. For these tests, the dynamic strain frequency remained at 500Hz and with dynamic strain magnitudes between 0με and 38.1με. SAWR dynamic strain measurements were taken before each round and after the second round at 100°C and 400°C to check for the stability of the sensor response to dynamic strain.

Figure 4.4 shows the SAWR dynamic strain measurements at 400°C before and after one round of cycling. The SAWR sensitivity to dynamic strain decreased from 0.136μV/με to 0.037μV/με at 400°C, which is a 73% decrease. After two rounds of cycling, the SAWR response to dynamic strain fell below noise floor for wireless measurements and could no longer be detected at 400°C. Figure 4.5 shows the SAWR dynamic strain measurements at 100°C before one round of temperature cycling, after one round of temperature cycling, and after two round of temperature cycling. The SAWR sensitivity to dynamic strain decreased from 0.363μV/με to 0.073μV/με (80% decrease) at 100°C after one round of temperature cycling. After two rounds of temperature cycling, the SAWR sensitivity to dynamic strain decreased to 0.026μV/με, which is a 93% decrease from the initial measurement. The SAWR dynamic strain sensitivities at 100°C and 400°C are shown in Table 4.1. The results show that after mounting and temperature cycling, the SAWR dynamic strain sensitivity is not stable. Furthermore, the decrease of the SAWR dynamic strain sensitivity below noise level at 400°C after temperature cycling to 425°C suggests failure of

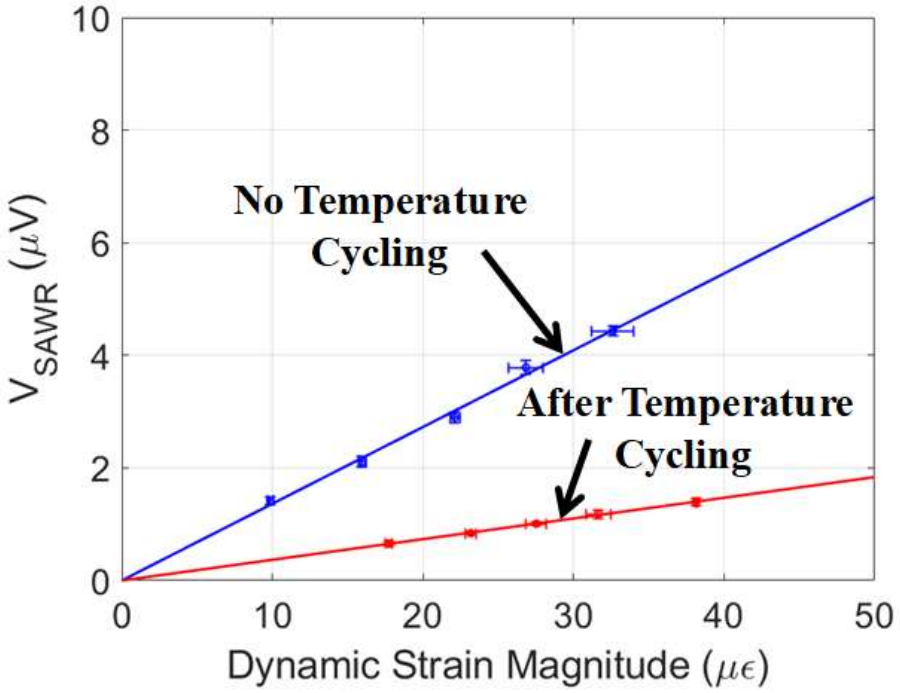

Figure 4.4 SAWR sensor response to dynamic strain at 400°C prior to temperature cycling (blue) and after one round of temperature cycling (red), as described in Section 4.1 [51].

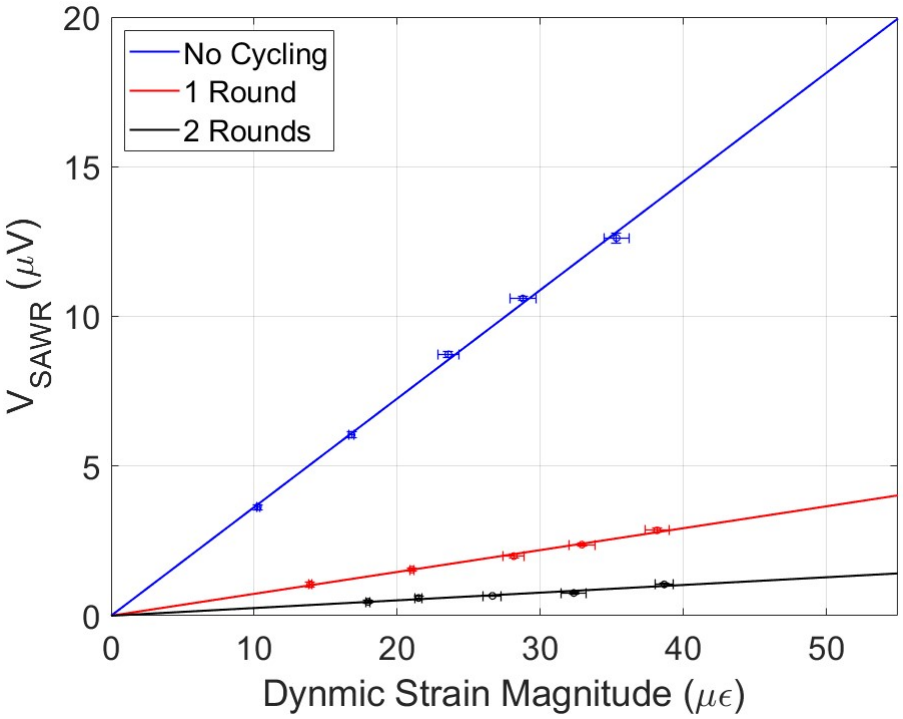

Figure 4.5 SAWR sensor response to dynamic strain at 100°C prior to temperature cycling (blue), after one round of temperature cycling (red), and after two rounds of temperature cycling (black), as described in Section 4.1.

Table 4.1 The SAWR sensitivity to dynamic strain at 100°C and 400°C before one round of temperature cycling, after one round of temperature cycling, and after two round of temperature cycling.

Thermal History	SAWR Sensitivity to Dynamic Strain at 100°C (μV/με)	R^2 (100°C)	Percent Difference from No Cycling	SAWR Sensitivity to Dynamic Strain at 400°C (μV/με)	R^2 (400°C)	Percent Difference from No Cycling
No Cycling	0.363	0.9979	-	0.136	0.9935	-
1 Round	0.073	0.9949	-80%	0.037	0.9980	-73%
2 Rounds	0.026	0.9483	-93%	-	-	-

the SAWR mounting. To identify the cause of the dramatic decrease in SAWR sensitivity to dynamic strain after thermal cycling, further SAWR crystal mounting experiments under thermal testing were performed, which are discussed in the next section.

4.2.2 Cracking of the LGS After Temperature Cycling

Additional LGS sensor chips were mounted to Inconel 625 using the Aremco 668 ceramic adhesive and submitted to one round of temperature cycling between 100°C and 425°C using the same procedure described in Section 4.1. For these experiments, in addition to studying the LGS chip mounted to Inconel 625, tests were done where the adhesive was attached only to the LGS in some samples and only to an Inconel substrate in other samples, thus allowing for the two interfaces, the adhesive/LGS interface and the adhesive/Inconel interface, to be studied independently as well as together for potential adhesive attachment issues.

Figure 4.6a shows the result after heating for one round (three temperature cycles) between 100°C and 425°C at the adhesive/LGS interface (no attachment to Inconel). As can be seen from Figure 4.6a, failure at the adhesive/LGS interface is observed, including cracking of the LGS crystal. This type of result is currently credited to the differences between the coefficient of thermal expansion (CTEs) of the adhesive (7.2 ppm/°C) and LGS (between 4.5-5 ppm/°C for this LGS crystal orientation) and the respective brittleness of the materials involved. The cracking also

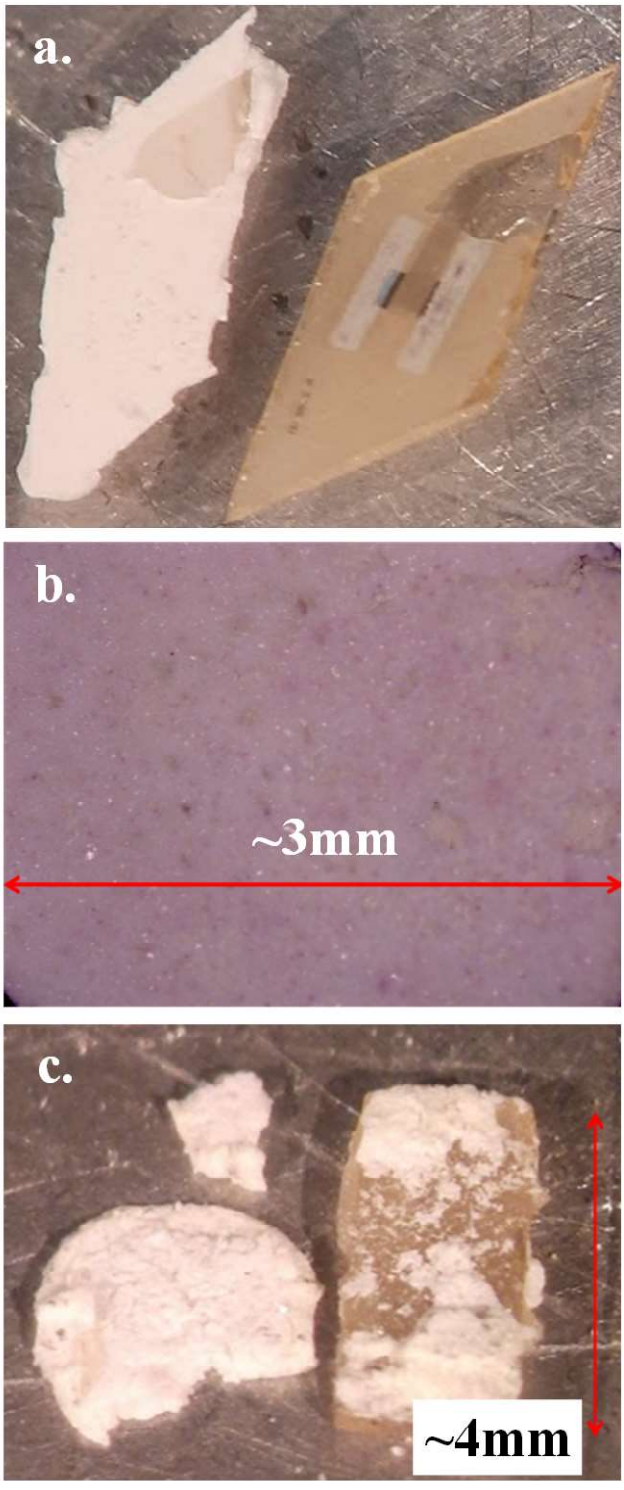

Figure 4.6 (a) Cracking of the LGS crystal at the the adhesive/LGS interface (no attachment to Inconel 625) after being subjected to one round of temperature cycling, (b) the top view of the adhesive/Inconel 625 interface after being subjected to one round of temperature cycling, and (c) adhesion failure of the LGS/adhesive/Inconel 625 sample after being subjected to one round of temperature cycling.

appears to have originated at the border of the LGS chip, which is the weakest part of the crystal and was found to have a high concentration of thermally induced strain in Chapter 2.

Figure 4.6b shows the top of the adhesive layer after heating for one round of temperature cycling between 100°C and 425°C at the adhesive/Inconel interface with no attachment to LGS. There is no indication of cracking at the adhesive/Inconel interface and the Aremco 668 adhesive layer could not be removed from the Inconel by applying a significant shear force with the tweezers. Since the difference in CTE of the adhesive (7.2ppm/°C) and the Inconel (13.7ppm/°C), is larger than the CTE difference between the adhesive and LGS, it is interesting that the adhesive did not fail dramatically in this instance. However, it could not be confirmed whether there is microcracking at the adhesive/Inconel interface or within the adhesive.

Figure 4.6c shows the results from the Inconel/adhesive/LGS stack after heating for one round of temperature cycling between 100°C and 425°C. Failure at the adhesive/LGS interface and within the adhesive itself are observed after temperature cycling. There is also some failure at the adhesive/Inconel interface that was not observed when there was no LGS attached. This shows that there is consistent failure at the adhesive/LGS interface after thermal cycling and that adhesion between the adhesive and the Inconel is inconsistent when connected to LGS.

Lack of stability and/or failure at the adhesive/LGS interface and adhesive/Inconel interface due to thermal cycling is problematic for both static and dynamic strain sensors. Lack of integrity at this interface lowers the strain transfer between the part and sensor, which leads to: (i) decrease the SAWR sensitivity to dynamic strain; (ii) lack of sensor stability; (iii) inconsistency in the SAWR response to dynamic strain between similar sensors; (iv) rendering of any sensor calibration useless; and (v) ultimately sensor failure; thus, significantly compromising the sensor performance.

4.2.3 Adhesives for Static and Dynamic Strain Sensing at 200°C

Because SAWR strain sensor was not achieved at 400°C due to attachment failure observed with the Aremco 668 adhesive, new adhesives were tested. Because of prior investigation of adhesives in [32], it was determined that commercially available ceramic adhesives are not capable of providing the necessary stability for static and dynamic strain measurements at 400°C. Therefore, the target temperature was lowered to 200°C. To allow the investigation of polymer epoxies for the attachment of SAWR static and dynamic strain sensors.

Six epoxies were purchased and tested for potential use for SAWR static and dynamic strain testing at 200°C. Two epoxies from Aremco Products were tested: Aremco 805 and Aremco 526N [76]. Both of these are polymer epoxies and have maximum nominal operating temperatures of 300°C. Four epoxies from Cotronics Corporation were tested: Resbond 940HT [74], Durabond 952FS [77], Duralco 4525 [78], and Duralco 4461 [79]. Resbond 940HT is a ceramic epoxy with a maximum operating temperature of 1538°C. Although it was shown that ceramic adhesives can cause failure of SAWR attachment to metal parts at 400°C, it was hypothesized that operation at 200°C should not result in failed SAWR attachment. Therefore, Resbond 940HT was considered based on a recommendation from the company. Durabond 952FS is a nickel-based adhesive that has a maximum operational temperature of 1093°C. This adhesive was considered because the nickel base could aid in attachment to Inconel, which has a high nickel concentration (approximately 58% nickel for Inconel 625 [69]). Duralco 4525 and Duralco 4461 are polymer epoxies with maximum operating temperatures of 260°C.

4.2.3.1 Aremco Epoxies for Static and Dynamic Strain Sensing

In initial mounting tests using Aremco 805 and Aremco 526N, glass slide pieces, with similar dimensions to the SAWR sensors, were mounted to steel and Inconel. Steel was used in

addition to Inconel because structures in powerplants are typically made of steel. Glass slide pieces (CTE of approximately 0.5ppm/°C) were used before attempting with LGS so that any adhesion problems to metal could be identified before using LGS, which is more expensive and in lower supply than glass slides. It was also hypothesized that if the adhesive could adhere the glass slide piece to steel and Inconel, then it would adhere LGS as well since the CTE difference between LGS and steel/Inconel is lower than that of glass and steel/Inconel. Adhesives that could adhere glass to metal and withstand heating above 200°C were then tested with LGS.

Figure 4.7 shows the post-cure images of a glass slide sample mounted on steel using Aremco 805 before and after heating to 250°C for six hours. The curing protocol for Aremco 805 is one hour at room temperature, 24 hours at 37°C, two hours at 93°C [76]. There is no visual evidence of cracking or adhesion failure after heating to 250°C and the glass could not be removed by applying a large shear force with tweezers. The results for the glass slide on Inconel showed similar results before and after heating to 250°C and could not be removed using tweezers. Figure 4.8 shows the post-cure images of a glass slide sample mounted on Inconel using Aremco 526N before and after heating to 250°C for six hours. The curing protocol for Aremco 526N is one hour

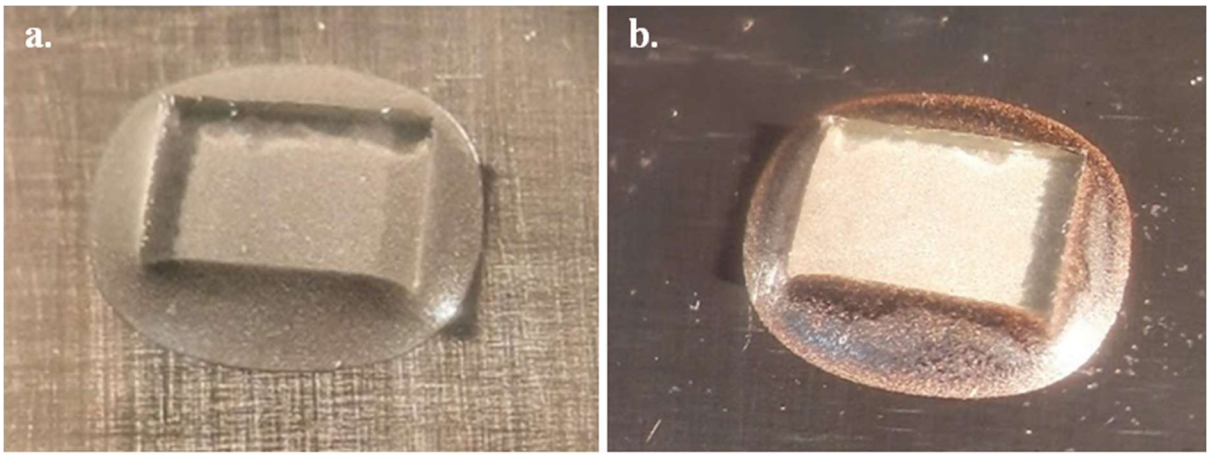

Figure 4.7 The post-cure glass slide sample mounted on steel using Aremco 805 (a) before and (b) after heating to 250°C for six hours. The samples on Inconel visually looked similar to the ones shown in this figure.

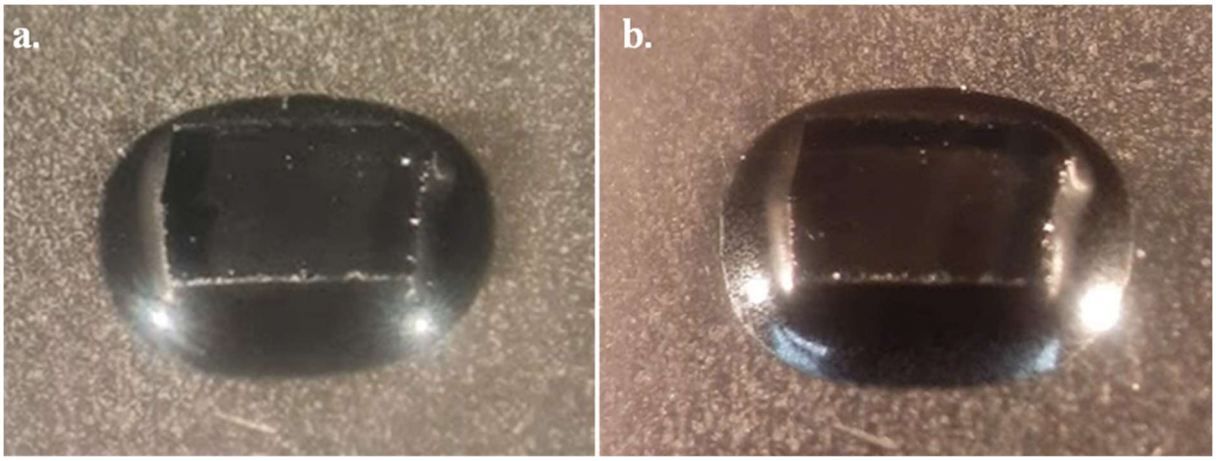

Figure 4.8 The post-cure glass slide sample mounted on Inconel using Aremco 526N (a) before and (b) after heating to 250°C for six hours. The samples on steel visually looked similar to the ones shown in this figure.

at room temperature, two hours at 93°C, two hours at 163°C [76]. There is no visual evidence of cracking or adhesion failure after heating to 250°C and the glass could not be removed by applying a significant shear force with tweezers. Similar results were observed for the glass slide samples mounted on steel. Based on these results, LGS mounting was attempted for both Aremco 805 and Aremco 526N.

The next testing done was mounting LGS pieces to steel and Inconel using Aremco 805 and Aremco 526N. The LGS pieces used were chips with damaged electrodes taken from the same wafer where the SAWR sensors were fabricated. Figure 4.9 shows LGS mounted on Inconel using (a) Aremco 805 and (b) Aremco 526N after curing and heating to 275°C for six hours. The temperature for these tests was increased from 250°C to 275°C to test to limits of attachment for these adhesives since the maximum operational temperature of the adhesives is 300°C. Both samples remained attached to the Inconel coupon after applying a large shear force using tweezers and neither showed cracking. The Aremco 805 in Figure 4.9a shows discoloration under the LGS crystal after heating. However, there is no evidence suggesting that this affects the stability of the

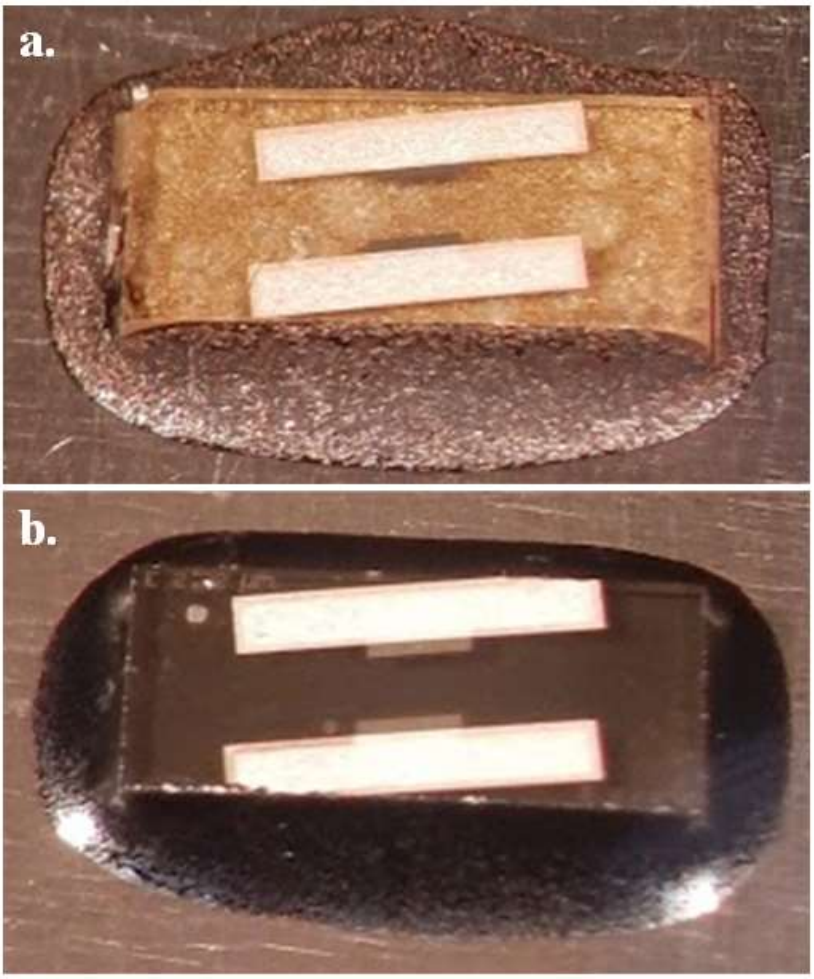

Figure 4.9 A piece of LGS mounted on Inconel using (a) Aremco 805 and (b) Aremco 526N after curing and heating to 275°C for six hours.

adhesive for strain sensing purposes. The next step taken was mounting SAWR sensors to the static strain beam for stability testing.

4.2.3.2 Cotronics Adhesives for Static and Dynamic Strain Sensing

Like for the initial adhesion tests done the Aremco epoxies, glass slide pieces were used for the first heating tests to identify any adhesion problems before using LGS. All four adhesives were used to mount glass slide pieces to Inconel. In addition, adhesive without glass slide attachment was applied to the Inconel. Only Inconel was used for these tests because the steel and Inconel samples for the Aremco epoxies in Section 4.2.3.1 showed the same quality of adhesion,

so it was expected that the same would be for the Cotronics adhesives. The recommended cure procedures for the four Cotronics adhesives are described in Table 4.2. For these tests, the Resbond 940HT and Durabond 952FS were cured on the same coupon because both have a curing step at 93°C after the room temperature cure and the Duralco 4525 and Duralco 4461 were cured on the same coupon because both have a curing step at 121°C after the room temperature cure. The curing procedure used for Resbond 940HT and Durabond 952FS was 24 hours at room temperature, two hours at 93°C, two hours at 275°C. The curing procedure for Duralco 4525 and Duralco 4461 was 24 hours at room temperature, four hours at 121°C, one hour at 177°C.

Table 4.2 The recommended curing procedures for the four Cotronics adhesives considered for SAWR static and dynamic strain attachment at 200°C. The procedure used for each is underlined if the manufacturer gave multiple curing options.

Adhesive Name	Adhesive Base	Curing Procedure
Resbond 940HT	Alumina-based	24 hours at room temperature or 5-15 min at 93°C
Durabond 952FS	Ni-based	24 hours at room temperature, 2 hours at 93°C; Post Cure: 2 hours at 204°C-315°C.
Duralco 4525	Polymer	16-24 hours at room temperature, Post Cure: one hour at 121°C, one hour at 177°C.
Duralco 4461	Polymer	16-24 hours at room temperature, Post Cure: four hours at 121°C.

After curing, the Resbond 940HT provided inconsistent attachment as shown in Figure 4.10a. Of the two samples with the glass slide and the two without the glass slide that were applied to the Inconel at the same time, one of each detached from the Inconel after applying a moderate shear force with the tweezers and one of each remained attached after applying a significant shear force using tweezers. Because of this inconsistency in attachment to Inconel, Resbond 940HT was rejected for use in SAWR static and dynamic strain sensing up to 200°C. After curing the Durabond 952FS, all samples (with and without the glass slide) remained attached to the Inconel

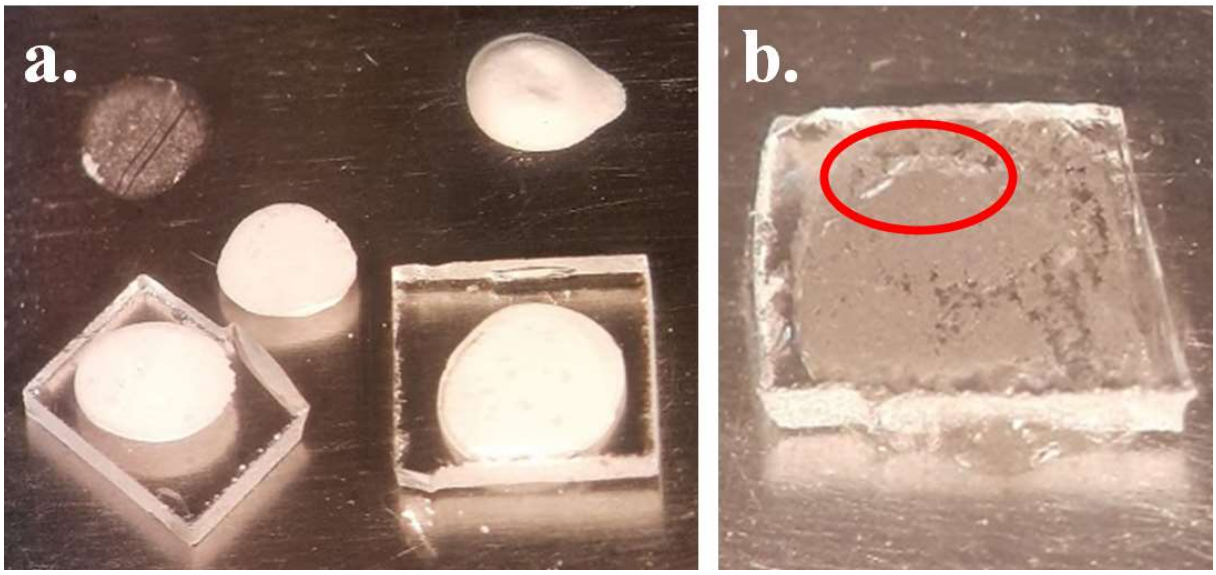

Figure 4.10 (a) The Resbond 940HT samples with and without the glass slide mounted on Inconel after curing. Detachment of the Resbond 940HT from the Inconel was observed for the samples on the left. (b) One of the Durabond 952FS glass slide samples after curing. Circled in red is a location of cracking.

after curing (Figure 4.10b). However, bubbling and cracking of the glass was observed in the glass slide samples. Although the cracking might not be observed when using LGS since the CTE difference between LGS and Inconel is less than the CTE difference between Inconel and glass, it is likely that bubbling would occur when LGS is used. Therefore, Durabond 952FS was rejected for SAWR static and dynamic strain sensor attachment up to 200°C.

The remaining two adhesives (Duralco 4525 and Duralco 4461) adhered to the Inconel after heating to 250°C for six hours Figure 4.11. There were also no signs of cracking when using these epoxy adhesives and the glass slide samples could not be removed by applying a significant shear force to the glass slide. Duralco 4525 had discoloration around the edges of the glass slide (Figure 4.11a) that looked to be inconsistency in the coverage of the epoxy on the bottom of the

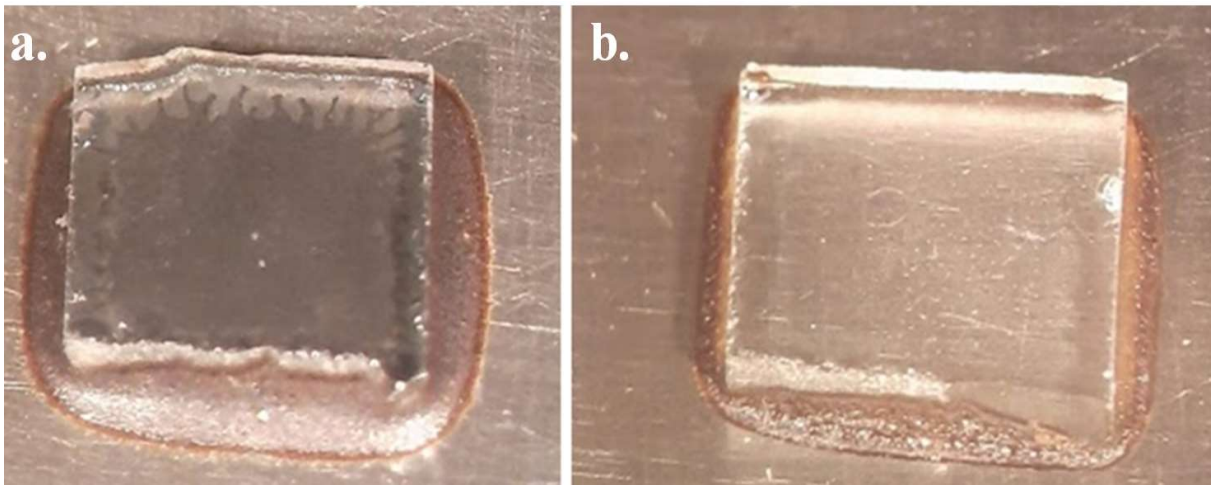

Figure 4.11 The glass slide samples mounted using (a) Duralco 4525 and (b) Duralco 4461 after curing and heating to 250°C for six hours.

glass, but because this was only observed around the edges, it was not rejected for SAWR static and dynamic strain sensor attachment up to 200°C.

After confirming that the glass slide samples mounted using Duralco 4525 and Duralco 4461 could not be removed, SAWR sensors were mounted on a static strain beam for stability testing. The intermediate step of testing the adhesion of LGS pieces with damaged electrodes after heating to 250°C was not done before SAWR sensors were mounted. This was done because when testing the Aremco epoxies in Section 4.2.3.1, the LGS samples and glass slide samples both showed good adhesion to steel and Inconel, so it was expected that if the glass slide samples showed successful adhesion to Inconel with the Cotronics epoxies, then the LGS samples would as well.

4.2.4 SAWR Static Strain Stability Testing

Following the adhesion testing of the Aremco and Cotronics adhesives to glass slide samples and LGS pieces, SAWR sensors were mounted to the static strain beam and tested for static strain stability after temperature cycling. For these tests, wired SAWR sensors were used to

improve the dynamic range by minimizing the noise inherent to wireless interrogation. Two static strain beams were used for these tests: one beam tested the stability of Aremco 526N and Aremco 805 and one tested the stability of Duralco 4525 and Duralco 4461. Images of the beams will be shown in the next sections. Each beam had four SAWR sensors mounted in the constant stress region: two sensors were mounted with one epoxy and two with the other. The measurements were taken using an Agilent E5071C VNA rather than the EVHT-300 because time-gating is not needed for wired sensing.

4.2.4.1 Room Temperature Stability of Aremco 526N and 805 After Temperature Cycling

Two sensors were mounted for Aremco 526N and Aremco 805 (Figure 4.12), but after curing, one sensor that was mounted using Aremco 526N cracked after applying a load to the beam. Therefore, there are only results from one device mounted on 526N. Figure 4.13 describes

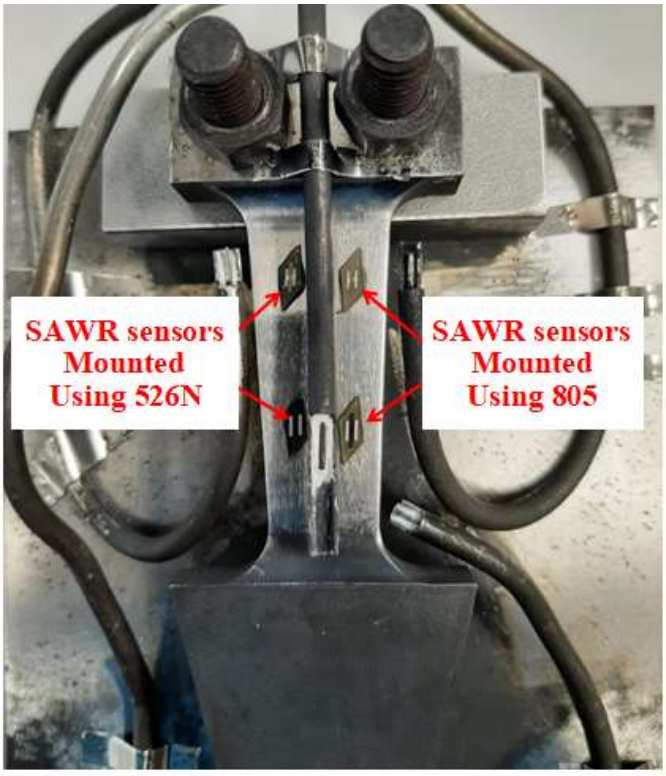

Figure 4.12 An image of the mounted SAWR sensors using Aremco 526N and Aremco 805.

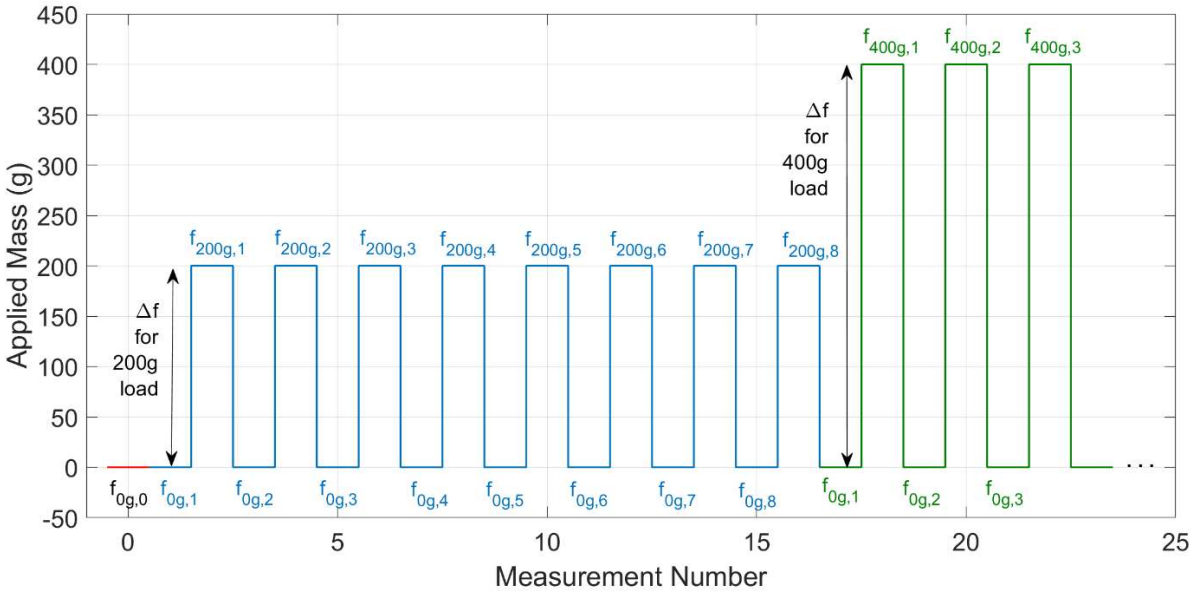

Figure 4.13 The testing procedure for static strain measurements at a fixed temperature. Measurement $f_{0g,0}$ represents the initial 0g measurement value before applying any mass to the static strain beam. The blue trace indicates testing while loading and unloading a 200g load. The green trace indicates testing while loading and unloading a 400g load. The same sequence was repeated for 600g and 800g loads.

the static strain test that was conducted before and in between temperature cycling profiles. An initial measurement (measurement #0) with a load of 0g was taken with a resonant frequency of $f_{0g,0}$. The blue trace indicates testing while loading and unloading a 200g load. The green trace indicates testing while loading and unloading a 400g load. In total, eight loaded and eight unloaded measurements were taken for each mass being measured. This same sequence was repeated for masses of 600g and 800g.

To test the stability of the SAW response to applied load, temperature cycling needs to be performed with strain testing in between cycling rounds to determine when the SAW response to strain is stable. For these tests, one round of cycling (Figure 4.14) consisted of four cycles between 250°C and 50°C (2-hour hold at 250°C, 6-minute hold at 50°C), a 10-hour soak at 250°C, and four cycles between 250°C and 50°C (2-hour hold at 250°C, 6-minute hold at 50°C). These temperature values were programed and read by a TC measuring the internal furnace temperature and not the

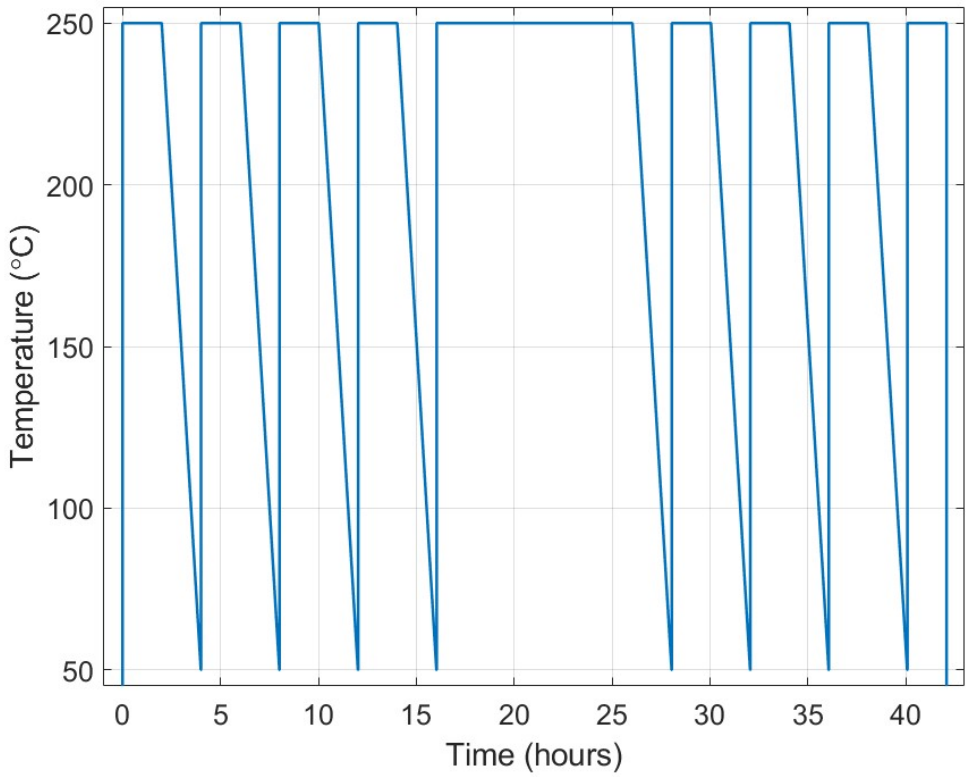

Figure 4.14 One round temperature profile used in the verification of SAWR static strain sensor stability.

sample temperature. Three rounds of temperature cycling were performed on these sensors and static strain measurements were taken before the first round, in between each round of temperature cycling, and after the last round of temperature cycling.

Figure 4.15 shows the SAWR response to applied mass to the static strain beam for one of the devices mounted using Aremco 526N before and after 1 round of cycling. Table 4.3 shows the SAWR sensitivity values to applied mass calculated from a linear fit to the measured data before and after the one round of temperature cycling presented in Figure 4.15 and the respective correlation coefficients. Table 4.3 also includes the SAWR sensitivity to applied mass that was observed when mounting with Aremco 668 prior to any temperature cycling, and thus before the sensitivity was significantly compromised due to adhesive cracking. The SAWR sensitivity to strain decreased by 82% after one round of temperature cycling when mounting the SAWR using

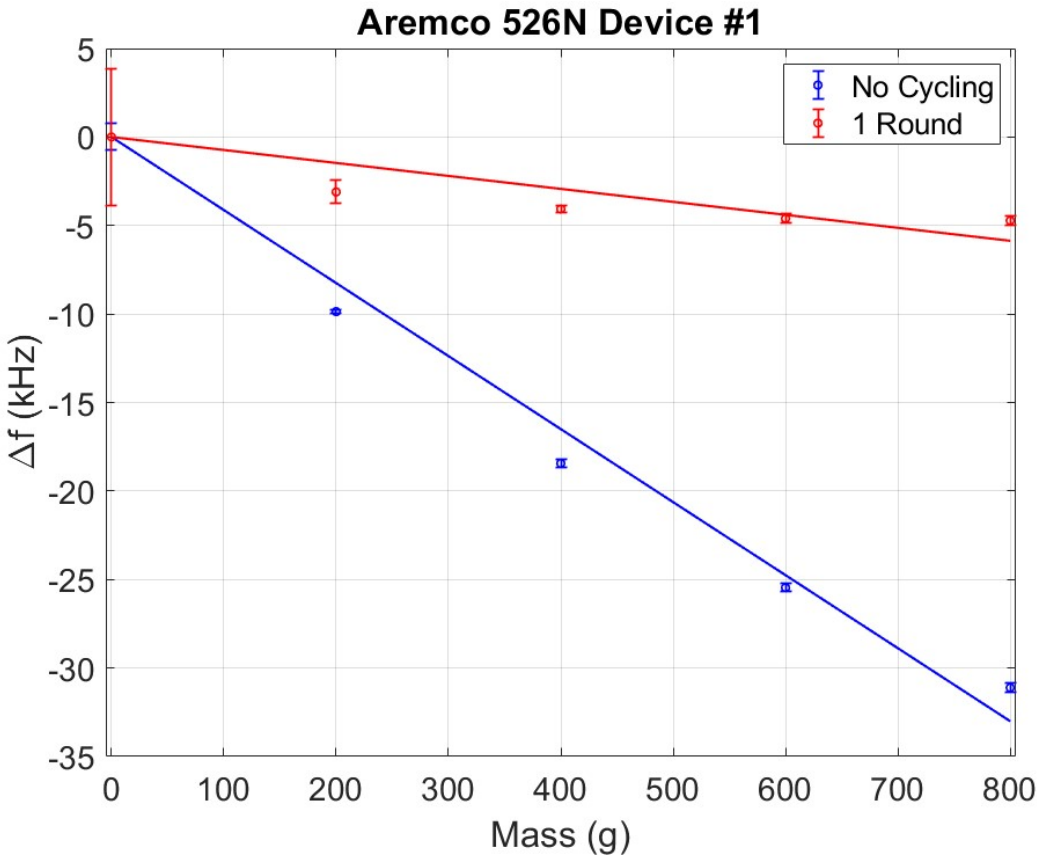

Figure 4.15 The change in SAWR resonant frequency due to applied load (i.e. $f_{loaded} - f_{0g}$) at room temperature for Device #1 mounted using Aremco 526N before and after one round of temperature cycling.

Table 4.3 The SAWR sensitivity to applied mass and correlation coefficients for the data in Figure 4.15 as well as the SAWR sensitivity when using Aremco 668.

Device and Thermal History	SAWR Sensitivity to Static Strain (Hz/g)	R^2
SAWR Device #1 on 526N; No Temperature Cycling	-41.2	0.995
SAWR Device #1 on 526N; 1 Round of Temperature Cycling	-7.3	0.924
SAWR Device on Aremco 668; No Temperature Cycling	-113	0.999

Aremco 526N. In addition, the correlation coefficient for the linear fit to static strain decreased from 0.995 to 0.924 after one round of temperature cycling. Based on this result, coupled with the fact that one of SAWR sensors cracked after applying a load to the beam, it was determined that Aremco 526N is not suitable for SAW strain sensing. Therefore, this device was not measured after the first round of temperature cycling.

In testing the Aremco 805 epoxy for stability in static strain measurements, a total of three rounds of temperature cycling (Figure 4.14) were performed with strain measurements taken before the first round of temperature cycling, between each round of temperature cycling, and after the third round of temperature cycling. Figure 4.16 shows the results from the room temperature tests for one of the devices mounted on Aremco 805. The other device showed similar results. The measured SAWR sensitivities to strain for each test is shown in Table 4.4. One static strain test,

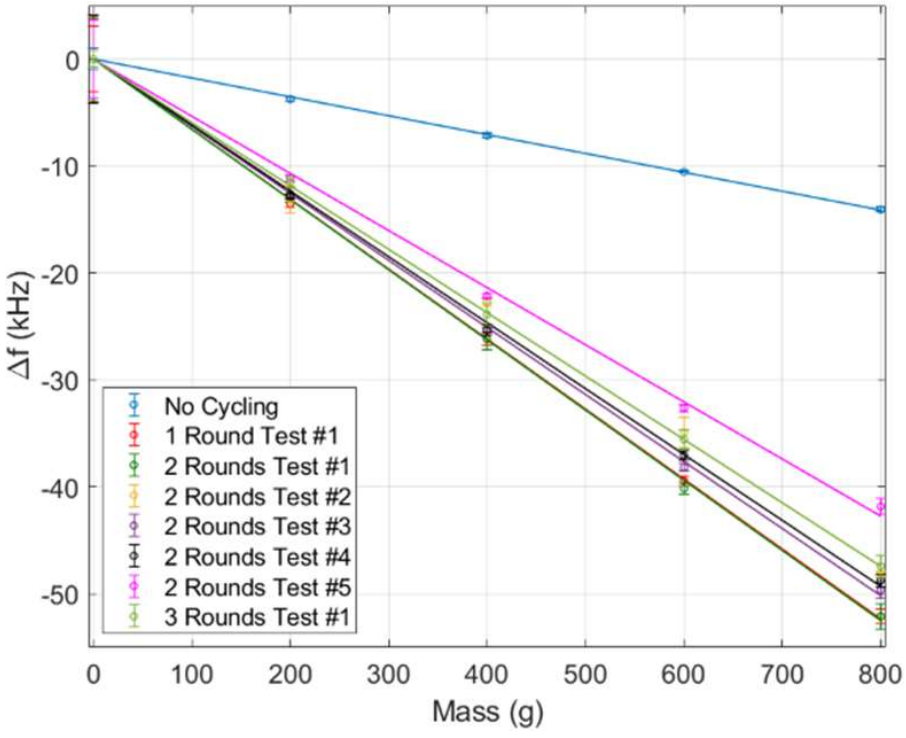

Figure 4.16 The results from the room temperature static strain tests using Aremco 805 before cycling and after one, two, and three rounds of cycling. The linear fits are also included.

Table 4.4 The SAWR sensitivity to applied mass and correlation coefficients at room temperature using Aremco 805 before cycling and after one, two, and three rounds of cycling.

Test Thermal History	SAWR Sensitivity to Strain (Hz/g)	R^2
No Cycling	-17.6	0.9999
1 Round Test #1	-65.4	0.9999
2 Rounds Test #1	-65.6	0.9998
2 Rounds Test #2	-59.3	0.9991
2 Rounds Test #3	-62.7	0.9999
2 Rounds Test #4	-61.1	0.9998
2 Rounds Test #5	-53.4	0.9994
3 Rounds Test #1	-59.3	0.9999

according to the procedure in Figure 4.13, was done before temperature cycling and after one round of temperature cycling. After one round of temperature cycling, the SAWR sensitivity to static strain increased by 272%. After two rounds of temperature cycling, five static strain tests were done to confirm that the measured sensitivity is repeatable. After three rounds, only one static strain test was done because the measured SAWR sensitivity to static strain was consistent with those measured after one and two rounds of temperature cycling. The results show consistency in the SAWR sensitivity to strain after two rounds of temperature cycling.

4.2.4.2 Room Temperature Stability of Duralco 4525 and 4461 After Temperature Cycling

SAWR devices were mounted using Duralco 4525 and Duralco 4461 in a similar manner as the devices shown in Figure 4.12. After curing, it was observed that for the SAWR sensors mounted using Duralco 4525, discolored features around three of the borders of the SAWR device were observed that appear to be failure of adhesion between the LGS and epoxy in those locations (Figure 4.17). Although neither device could be removed by applying a moderate shear force with tweezers, consistency in adhesion between the metal and the SAWR is a necessary condition for obtaining a stable response to strain, but the discolored features around the border of the SAWR devices and the glass slide piece discussed in Section 4.2.3.2 caused by lack of adhesion between

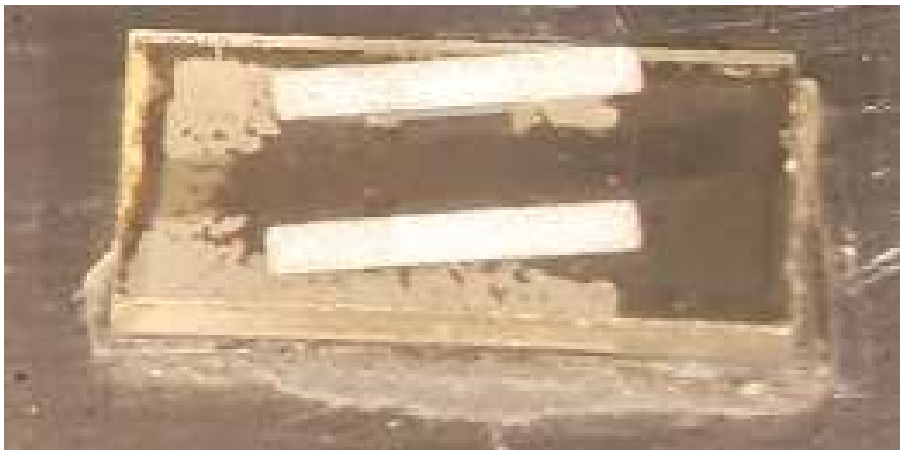

Figure 4.17 An image of one of the SAWR sensors mounted on static strain beam using Duralco 4525.

the LGS and the epoxy raise concerns about the quality of the SAWR attachment. Therefore, Duralco 4525 was rejected for SAWR attachment for static and dynamic strain testing.

The static strain response for the SAWR mounted using Duralco 4461 was tested at room temperature before and after one round of cycling. Each static strain test followed the same procedure outlined in Figure 4.13 and one round of temperature cycling followed the same procedure outlined in Figure 4.14. Only one round of cycling was done for this sensor because (i) it was determined that protection of the SAWR from particles is necessary to confirm whether the SAWR frequency response to strain is stable and (ii) for testing at high temperature, a SAWR temperature sensor is needed to accurately measure strain, neither of which were implemented in this setup. It was expected though that cycling for one round should show whether the usage of Duralco 4461 as the adhesive layer leads to consistency or degradation of the SAWR sensitivity to strain.

Figure 4.18 shows the static strain results for the room temperature tests before and after one round of cycling. The room temperature test for the Aremco 805 after three rounds of cycling is also shown on the plot for reference. Table 4.5 shows the measured SAWR sensitivities for the

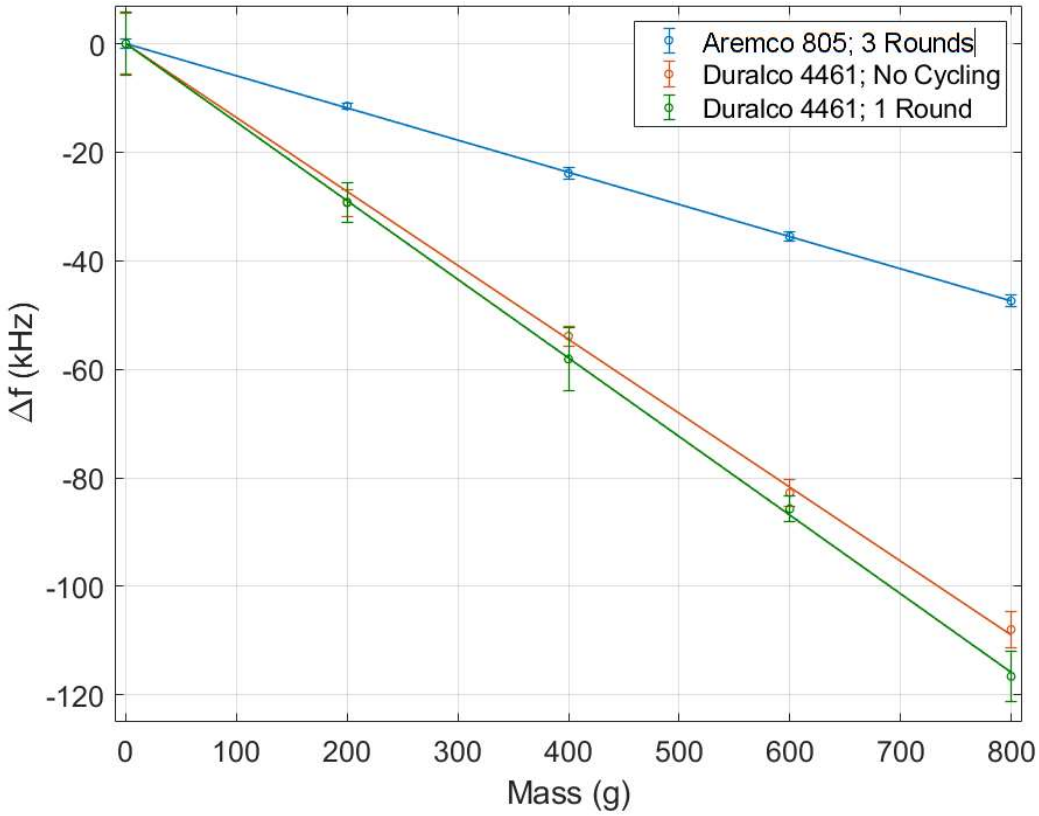

Figure 4.18 The results from the room temperature static strain tests using Duralco 4461 before and after one round of cycling. The Aremco 805 room temperature test done after three rounds is also included for reference.

Table 4.5 The SAWR sensitivity to applied mass and correlation coefficients at room temperature using Duralco 4461 before and after one round of cycling. The Aremco 805 room temperature test after three rounds of cycling is included for reference.

Test	SAWR Sensitivity to Strain (Hz/g)	Correlation Coefficient R^2
3 Rounds Aremco 805 Test #1	-59.3	0.9999
No Cycling Duralco 4461 Test #1	-136	0.9997
1 Round Duralco 4461 Test #1	-145	0.9999

data displayed in Figure 4.18. It was found that after one round of temperature cycling, the SAWR mounted using Duralco 4461 showed no degradation in the SAWR sensitivity to static strain, actually increasing slightly by 6.6% after the one round in temperature cycling. It should also be noted that the using Duralco 4461 provides a 145% increase in sensitivity when compared to the SAW mounted using Aremco 805. Based on this information and the information in this section

and Section 4.2.4.1, Aremco 805 and Duralco 4461 were both considered for the SAWR strain sensor mounting and stability tests that followed.

4.2.4.3 Modifications to the Stability Testing Setup Static Strain Measurements

In sections 4.2.4.1 and 4.2.4.2, there were two issues with the static strain setups that needed to be addressed: (i) protection of the SAWR sensors from particles in the furnace to avoid changes in the SAWR frequency response; and (ii) temperature correction to ensure that the amount of frequency variation due to temperature fluctuation can be corrected when measuring strain. To prevent particles from depositing on the surface of the SAWR sensors, packaging or covering is needed. Because wired sensors are being used in this test, full packaging of the SAWR sensors is not possible. Covering the SAWR sensors with an alumina structure is the best alternative to protect them from the deposition of eventual particles coming from the furnace walls. Figure 4.19 shows an image of this structure. A box-like structure was constructed out of alumina sheets with the front and back ends open so that the static strain beam could be easily removed

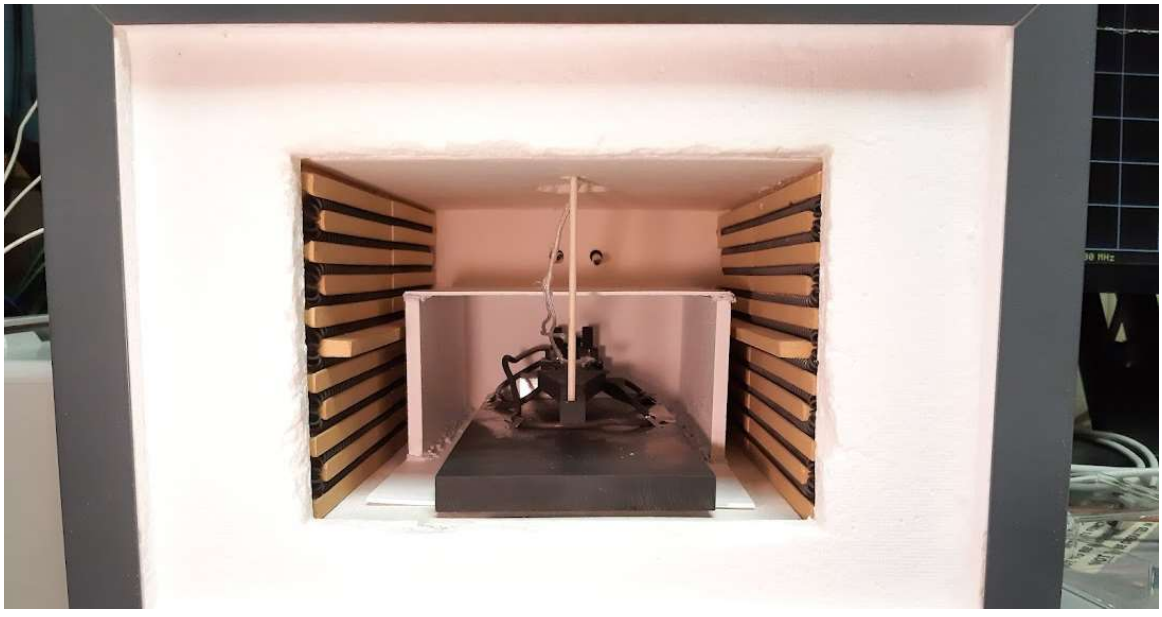

Figure 4.19 The alumina box designed to cover the SAWR sensors in the furnace. The beam for static strain testing is also shown in the figure.

from the furnace. The top of the enclosure is long enough so that the portion of the beam where the SAWRs are mounted is covered while allowing the end of the beam to remain exposed so that the load can be applied as it was previously. This should mitigate the problem of large particles from the furnace depositing on the SAWR sensors during static strain tests.

To address temperature correction that is necessary to ensure that the SAWR resonant frequency is stable, the setup shown in Figure 4.20 was implemented using a SAWR temperature sensor. In total, three SAWR sensors were mounted for these tests. Two SAWR sensors were rigidly mounted to the static strain beam to measure strain (one SAWR with Aremco 805 and one SAW with Duralco 4461). The third SAWR was used purely as a temperature sensor (indicated on Figure 4.20). The SAWR temperature sensor was mounted using 4 mil wires that secure the sensor chip to the beam without rigid mounting with an adhesive so that the device can slide along the beam surface so the SAWR would not measure strain (due to temperature variation induced stress of the beam and due to an applied load on the beam). The SAWR temperature sensor was mounted near the SAWR strain sensors and it was assumed that all the devices were at the same temperature.

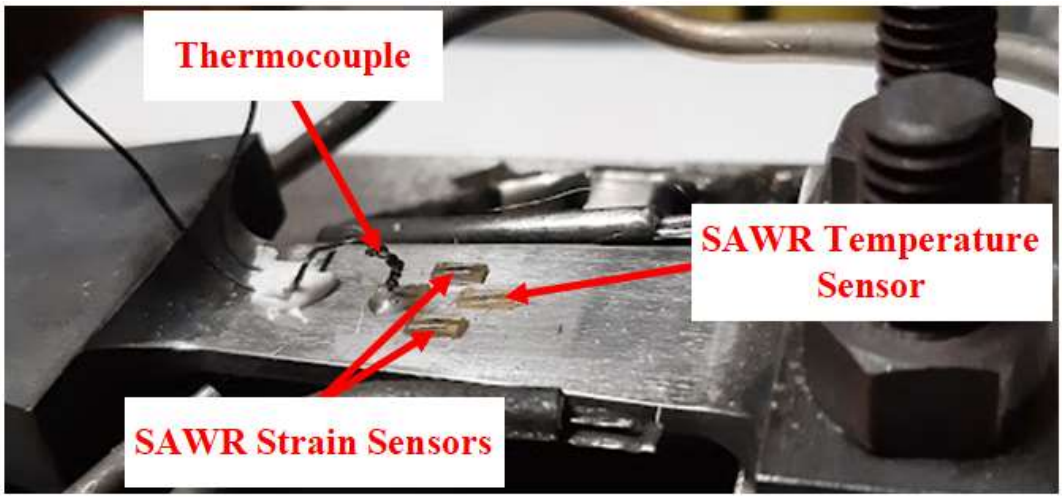

Figure 4.20 The static strain setup implementing a SAWR temperature sensor so that temperature correction can be performed.

Thus, only the frequency variation due to temperature fluctuations is measured by the SAWR temperature sensor, which can then be subtracted from the full frequency response of the SAWR strain sensors, leading to the calculation of the change in frequency due to strain only. A piece of LGS was also mounted near the three SAWR sensors and a thermocouple was placed on that piece of LGS so that the temperature could be monitored during testing. The close proximity of the thermocouple/LGS crystal with the three SAWR sensors ensured that the thermocouple temperature was very close (within 1 to 2 °C) to the temperature of the SAWR strain sensors. With the two test setup adjustments discussed in this section, the effect of SAWR frequency variations due to temperature variations and particle deposition on the surface that affect the verification of the epoxies' stability were mitigated.

4.2.4.4 High Temperature Static Strain Measurements for Adhesive Stability Tests

4.2.4.4.1 Results for Duralco 4461

To measure the two SAWR strain sensors and the SAWR temperature sensor at the same time during static strain tests, two VNAs were used. The two SAWR strain sensors were measured by an Agilent 8753D VNA using a MATLAB code with automatic data acquisition. Using the static strain procedure outlined in Figure 4.13 with hold times of approximately three minutes at each loaded and unloaded stage, about six measurements were taken at each loaded and unloaded stage. The SAWR temperature sensor was measured on a Copper Mountain Technologies R60 VNA. For these measurements, one sweep was used at each loaded and unloaded stage except for one of the tests after two rounds of temperature cycling in which three sweeps were used at each loaded and unloaded stage. That test will be presented later in this section.

Figure 4.21 shows the plots of the SAWR response to static strain with increasing load for the SAWR mounted using Duralco 4461 before temperature cycling, after one round of

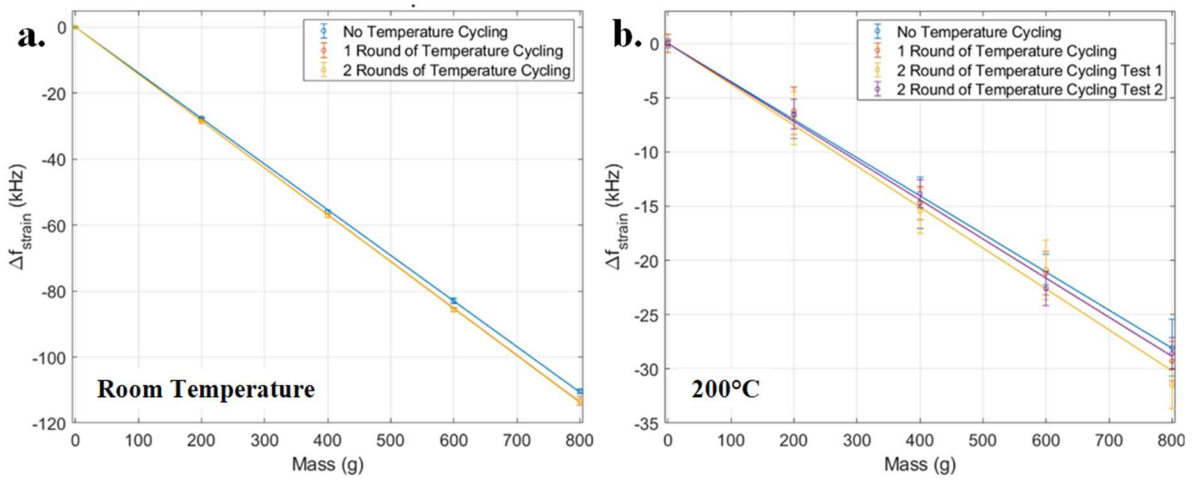

Figure 4.21 (a) The room temperature static strain curves for the SAWR mounted using Duralco 4461 taken before temperature cycling, after one round of temperature cycling, and after two rounds of temperature cycling. The red curve has a very similar slope to that of the yellow curve and, therefore, it is difficult to see in the plot. (b) The 200°C static strain curves for the SAWR mounted using Duralco 4461 taken before temperature cycling, after one round of temperature cycling, and after two rounds of temperature cycling.

temperature cycling, and after two rounds of temperature cycling. Table 4.6 shows the measured SAWR sensitivities and correlation coefficients for the results plotted in Figure 4.21. After two rounds of temperature cycling, two tests were performed at 200°C. In Test 1, each SAWR temperature sensor sample consisted of one sweep on the Copper Mountain VNA. In Test 2, each SAWR temperature sensor sample consisted of three sweeps on the Copper Mountain VNA to

Table 4.6 The SAWR sensitivity to static strain and correlation coefficients for the SAWR mounted using Duralco 4461 taken before temperature cycling, after one round of temperature cycling, and after two rounds of temperature cycling at room temperature and 200°C.

Test	Room Temp. SAWR Sensitivity to Static Strain (Hz/g)	Correlation Coefficient R^2	200°C SAWR Sensitivity to Static Strain (Hz/g)	Correlation Coefficient R^2
No Temperature Cycling	-138	0.9999	-35.1	0.9996
1 Round of Temp Cycling	-142	0.9999	-36.1	0.9991
2 Rounds of Temp. Cycling #1	-142	0.9999	-37.7	0.9969
2 Rounds of Temp. Cycling #2	N/A	N/A	-36.1	0.9988

reduce noise in the temperature corrected strain reading. From Test 1 to Test 2, the average standard deviation for the measurements at 200g, 400g, 600g, and 800g decreased from 2.35 kHz to 1.43 kHz (39% decrease) showing an improvement when more samples were taken. After two rounds of temperature cycling, the SAWR sensitivity to static strain seems stable at room temperature and 200°C. In addition, the SAWR static strain sensitivity measured at room temperature this quarter are consistent with the SAWR static strain sensitivity for the SAWRSs mounted using Duralco 4461 reported in Section 4.2.4.2 within 2.1%. Based on the data in Section 4.2.4.2 and Section 4.2.4.4.1, it is concluded that Duralco 4461 shows the necessary stability for strain sensing up to 200°C and thus should be considered for dynamic strain sensing as well.

4.2.4.4.2 Results for Aremco 805

Similar to the strain measurement results using Duralco 4461, Figure 4.22 shows the plots of the SAWR response to static strain with increasing load for the SAWR mounted using Aremco 805 before temperature cycling, after one round of temperature cycling, and after two rounds of

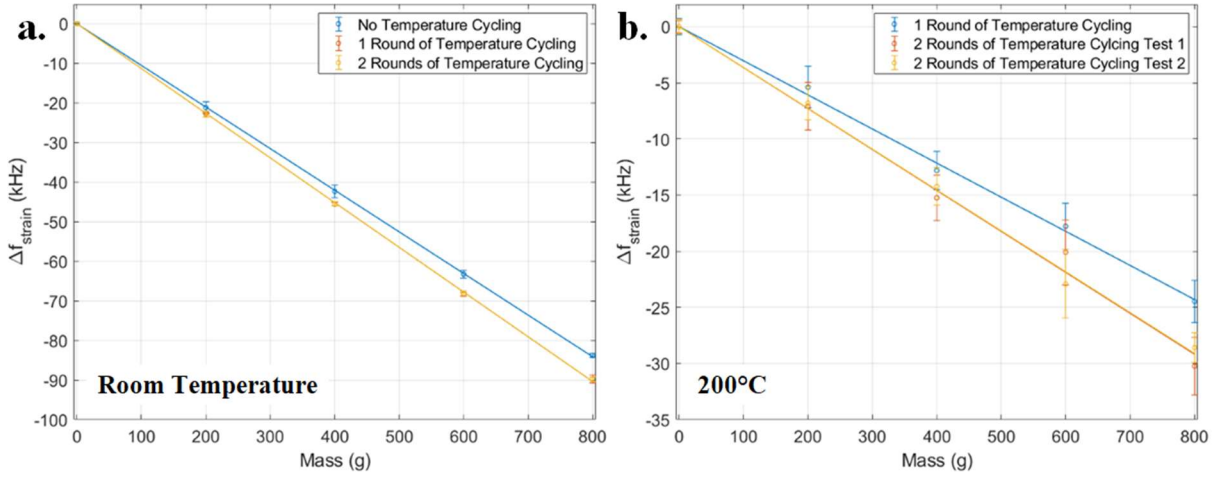

Figure 4.22 (a) The room temperature static strain curves for the SAWR mounted using Aremco 805 taken before temperature cycling, after one round of temperature cycling, and after two rounds of temperature cycling. The red curve has a very similar slope to that of the yellow curve and, therefore, it is difficult to see in the plot. (b) The 200°C static strain curves for the SAWR mounted using Aremco taken before temperature cycling, after one round of temperature cycling, and after two rounds of temperature cycling. The red curve has a very similar slope to that of the yellow curve and, therefore, it is difficult to see in the plot.

temperature cycling. Table 4.7 shows the measured SAWR sensitivities and correlation coefficients for the results plotted in Figure 4.22. Figure 4.22b and Table 4.7 do not show data for the tests done before any temperature cycling at 200°C due to an error in the measurement caused by a poor cable connection. As in the previous section for Duralco 4461, Test 1 after 2 rounds of temperature cycling indicates one sweep on the Copper Mountain VNA for each SAWR temperature sensor sample; and Test 2 indicates three sweeps on the Copper Mountain VNA for each SAWR device temperature sensor sample. From Test 1 to Test 2, the average standard deviation for the measurements at 200g, 400g, 600g, and 800g decreased from 2.41 kHz to 1.89 kHz (22% decrease). The data in Figure 4.22 and Table 4.7 for the SAWR devices mounted using Aremco 805 showed a stable response to static strain at room temperature and 200°C after two rounds of temperature cycling. When compared with SAWR devices mounted with the same Aremco 805 epoxy reported in Section 4.2.4.1, the devices reported this section had a 73% higher sensitivity to strain at room temperature and a 62% higher sensitivity to static strain at 200°C. This most likely resulted from differences in epoxy thickness when the SAWR was mounted. Taking this into account, the results shown in Section 4.2.4.1 and Section 4.2.4.4.2 indicate that Aremco

Table 4.7 The measured SAWR sensitivity to static strain and correlation coefficients for the SAWR mounted using Aremco 805 taken before temperature cycling, after one round of temperature cycling, and after two rounds of temperature cycling at room temperature and 200°C.

Test	Room Temp. SAWR Sensitivity to Static Strain (Hz/g)	Correlation Coefficient R^2	200°C SAWR Sensitivity to Static Strain (Hz/g)	Correlation Coefficient R^2
No Temperature Cycling	-105	0.9999	Error in Measurement	-
1 Round of Temp Cycling	-113	0.9999	-30.4	0.9990
2 Rounds of Temp. Cycling #1	-113	0.9999	-36.5	0.9970
2 Rounds of Temp. Cycling #2	N/A	N/A	-36.4	0.9989

805 possesses the necessary stability for strain sensing up to 200°C and thus should be considered for dynamic strain sensing.

4.2.5 SAWR Dynamic Strain Stability Testing

4.2.5.1 Choice of Adhesive for Testing of Dynamic Strain Temperature Correction Methods

After the completion of the stability tests performed in Section 4.2.4, it was concluded that both Aremco 805 and Duralco 4461 could be used for dynamic strain sensing tests based on the stability of the SAWR device response to static strain. Duralco 4461 was chosen to test temperature correction methods for dynamic strain because it provided a stable and adequate SAWR sensitivity to static strain at room temperature and 200°C and had a 24% lower standard deviation during strain measurements when compared to Aremco 805 during Test 2 after two rounds of temperature cycling. A SAWR strain sensor was mounted on the dynamic strain beam using Duralco 4461 and packaged according to the procedure outlined in Section 3.3.2.

4.2.5.2 Stability Testing of the SAWR Dynamic Strain Sensor

Dynamic strain testing was done to verify the stability of the Duralco 4461 epoxy. The same experimental setup discussed in Section 3.4.2 was used. Prior to dynamic strain testing, the packaged SAWR sensor was heated through two rounds of temperature cycling (the schedule for one round is shown in Figure 4.14) which was the amount of cycling performed before the SAWR static strain response was stable. After the required temperature cycling, dynamic strain testing was performed at room temperature, 215°C, and 200°C. The schedule for the testing is shown in Figure 4.23. As shown in Figure 4.23, this is a temperature cycling test, meaning the room temperature and high temperature tests were done in an alternating order, and thus between two room temperature tests, a high temperature test was performed. After the third room temperature test, the maximum temperature was lowered from 215°C to 200°C. The reasoning for this is

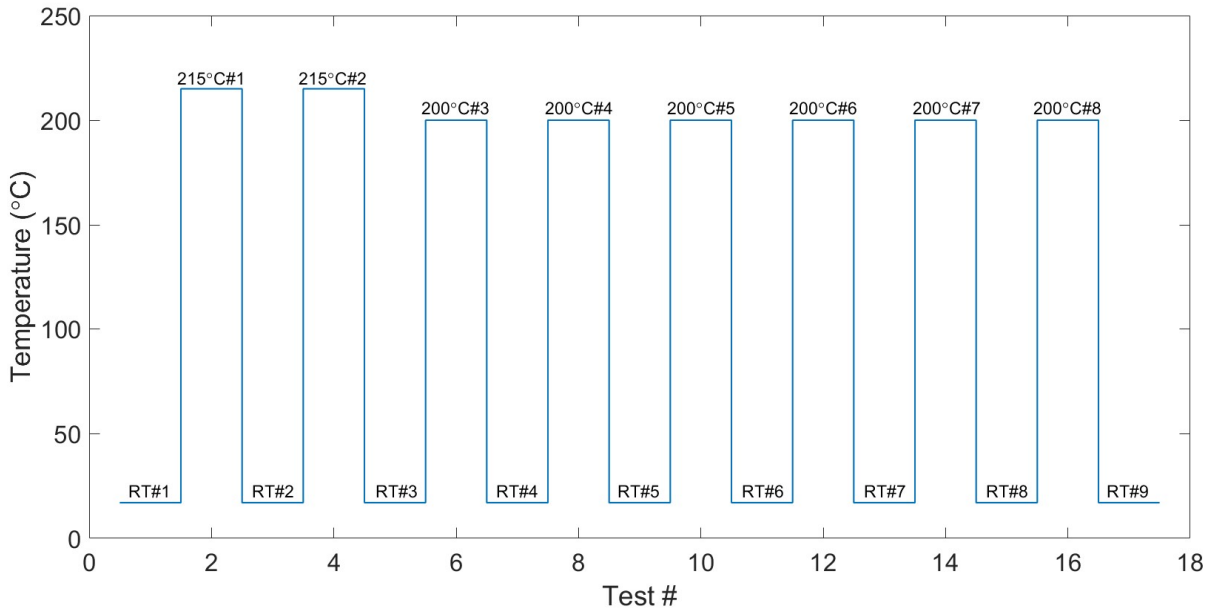

Figure 4.23 The schedule for dynamic strain testing at room temperature, 215°C, and 200°C.

discussed later in this section. For each SAWR dynamic strain test, five different dynamic loads (magnitude between 5με and 40με; frequency of 500Hz) were applied in an increasing order and eight measurements were taken and averaged at each dynamic load.

The results and linear fits for the room temperature dynamic strain tests are shown in Figure 4.24. The slope of the linear fits, correlation coefficients, and percent difference from RT#1 are shown in Table 4.8. The room temperature data shows that the sensor results are not stable since there is a significant variation in the sensor sensitivity response to dynamic strain (up to 36%). The data shows that there is a general decrease in the SAWR sensitivity to dynamic strain over time, but that there is some fluctuation in the measured sensitivity, meaning that a decrease in sensitivity is not consistently observed after each heating and cooling cycle. These results led to the questioning of the experimental setup consistency to ensure that the variation is not caused by an unpredictability in the setup.

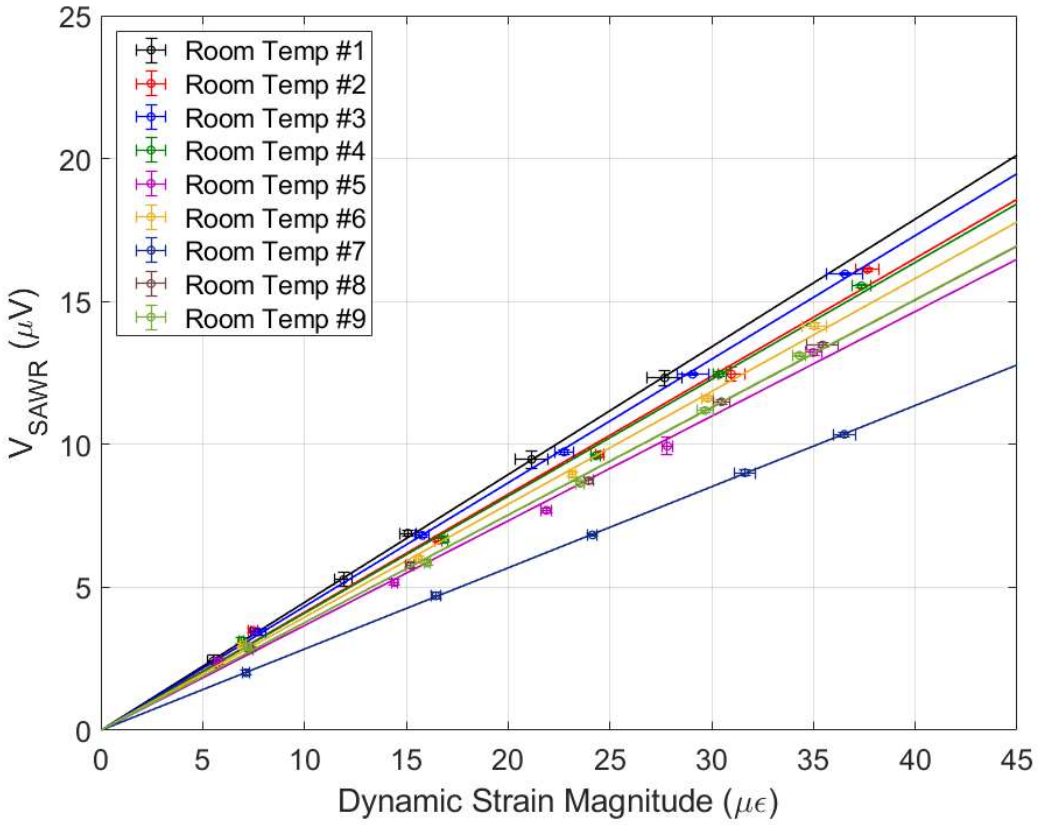

Figure 4.24 The SAWR dynamic strain measurements and linear fits for the room temperature tests using a SAWR mounted on Duralco 4461.

Table 4.8 The measured SAWR sensitivities to dynamic strain, correlation coefficients, and percent differences of the room temperature dynamic strain measurements using a SAWR mounted on Duralco 4461.

Test	SAWR Sensitivity to Dynamic Strain (μV/με)	R^2	% Difference from RT#1
RT#1	0.447	0.9995	0
RT#2	0.413	0.9911	-7.6
RT#3	0.433	0.9994	-3.1
RT#4	0.409	0.9964	-8.5
RT#5	0.366	0.9941	-18
RT#6	0.395	0.9969	-12
RT#7	0.284	0.9999	-36
RT#8	0.376	0.9985	-16
RT#9	0.377	0.9973	-16

Figure 4.25 shows the results and linear fits for the tests at 215°C and 200°C. The slope of the linear fits, correlation coefficients, and percent difference from 215°C #1 for the 215°C tests are shown in Table 4.9. After the second test at 215°C, a decrease of 37% in SAWR dynamic strain sensitivity was observed. Because of this, it was determined that the maximum temperature should be lowered to 200°C to ensure that the polymer would not degrade significantly, and thus the SAWR sensor response to dynamic strain remains above the minimum level detected by the system

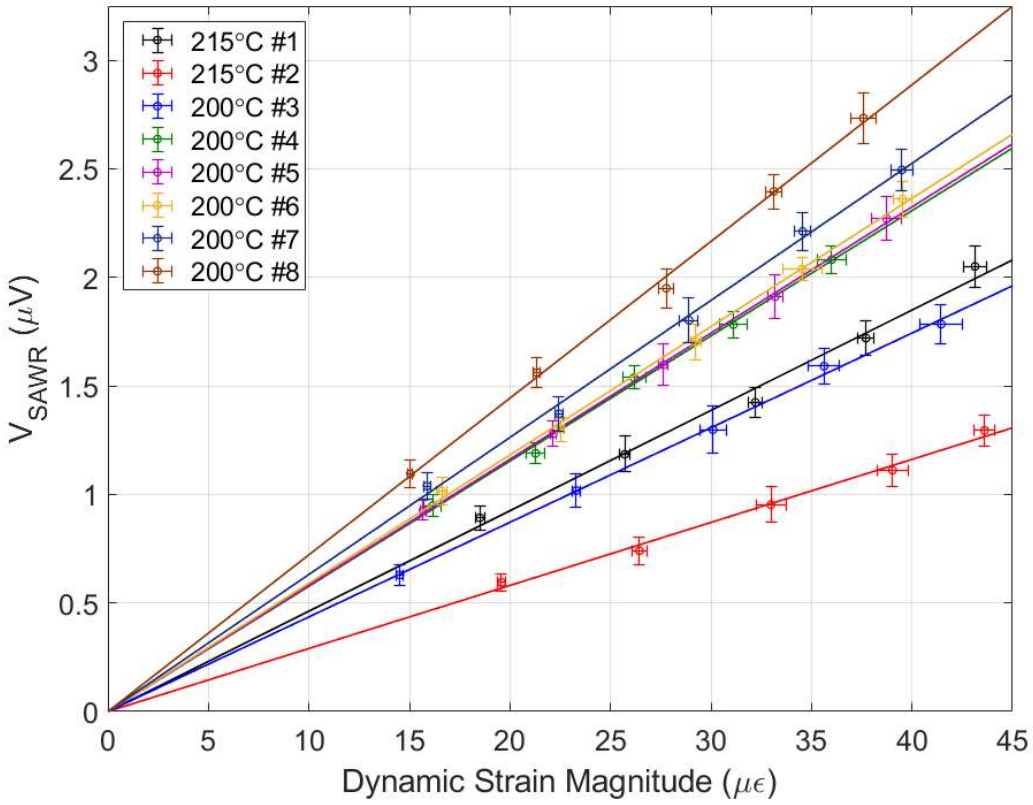

Figure 4.25 The SAWR dynamic strain measurements and linear fits for the high temperature tests using a SAWR mounted on Duralco 4461.

Table 4.9 The measured SAWR sensitivities to dynamic strain, correlation coefficients, and the percent differences from 215°C #1 of the 215°C dynamic strain measurements using a SAWR mounted on Duralco 4461.

Test	SAWR Sensitivity to Dynamic Strain (μV/με)	R^2	% Difference from 215°C #1
215°C #1	0.046	0.9886	0
215°C #2	0.029	0.9913	-37

(noise level on the dynamic strain measurement is around -108dBm). The slope of the linear fits, correlation coefficients, and percent differences with respect to 200°C #3 for the 200°C tests are shown in Table 4.10. The testing at 200°C shows that stability has not been achieved but does not show the fluctuation in the SAWR sensitivity to dynamic strain that was observed in the room temperature testing but rather a consistent increase. With the exception of 200°C #4 - 200°C #6, where the sensitivity seemed to become stable an increase in SAWR sensitivity to dynamic strain was observed.

Table 4.10 The measured SAWR sensitivities to dynamic strain, correlation coefficients, and the percent differences from 200°C #3 of the 200°C dynamic strain measurements using a SAWR mounted on Duralco 4461.

Test	SAWR Sensitivity to Dynamic Strain (μV/με)	R^2	% Difference from 200°C #3
200°C #3	0.044	0.9974	0
200°C #4	0.058	0.9967	+32
200°C #5	0.058	0.9990	+32
200°C #6	0.059	0.9971	+34
200°C #7	0.063	0.9966	+43
200°C #8	0.072	0.9976	+64

4.2.5.3 Investigation of Experimental Setup to Determine the Cause of the Inconsistencies in the SAWR Dynamic Strain Response

Because the static strain test showed that the SAWR mounted using Duralco 4461 gave a stable sensor response, the reliability of the dynamic strain setup was put into question, and it was decided that verification of the consistency of commercial strain gauge response is necessary. The first thing that was done to shed light on the cause of the inconsistency in the results was to plot the SAWR response and the commercial gauge response vs. the vibration generator voltage, V_{gen}, which is shown in Figure 4.26. V_{gen} can give insight into which sensor (if any) is causing the lack of consistency in the measured SAWR dynamic strain response.

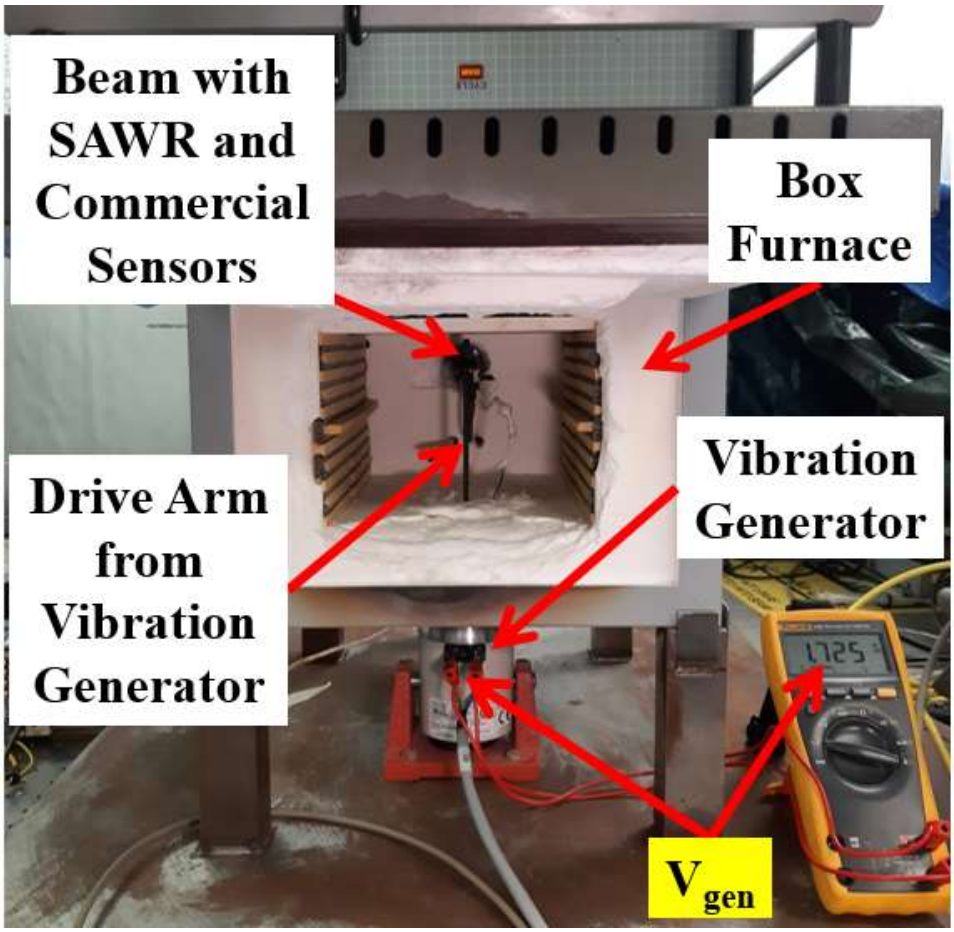

Figure 4.26 The dynamic strain setup with the V_{gen} measurement location labeled.

Figure 4.27 shows the slopes (strain sensor sensitivity) for SAWR, V_{SAWR} vs. V_{gen} curves (blue) and for the commercial gauge, με vs. V_{gen} curves (red) for the nine tests performed at room temperature. Each of the points shown on the graph represents one full dynamic strain test as described in the previous section. For example, each blue point correlates to a linear fit (R^2 of 0.988 or better) of V_{SAWR} vs. V_{gen} measured at five different dynamic strain loads. Figure 4.27 shows that both the SAWR and commercial strain gauge decrease with increasing number of heating and cooling cycles. If the SAWR response and the commercial sensor response to dynamic strain were stable, and assuming that the strain generator amplitude is stable, one would expect that the curves in Figure 4.27 to be flat (meaning all the slopes would be the same). It is also

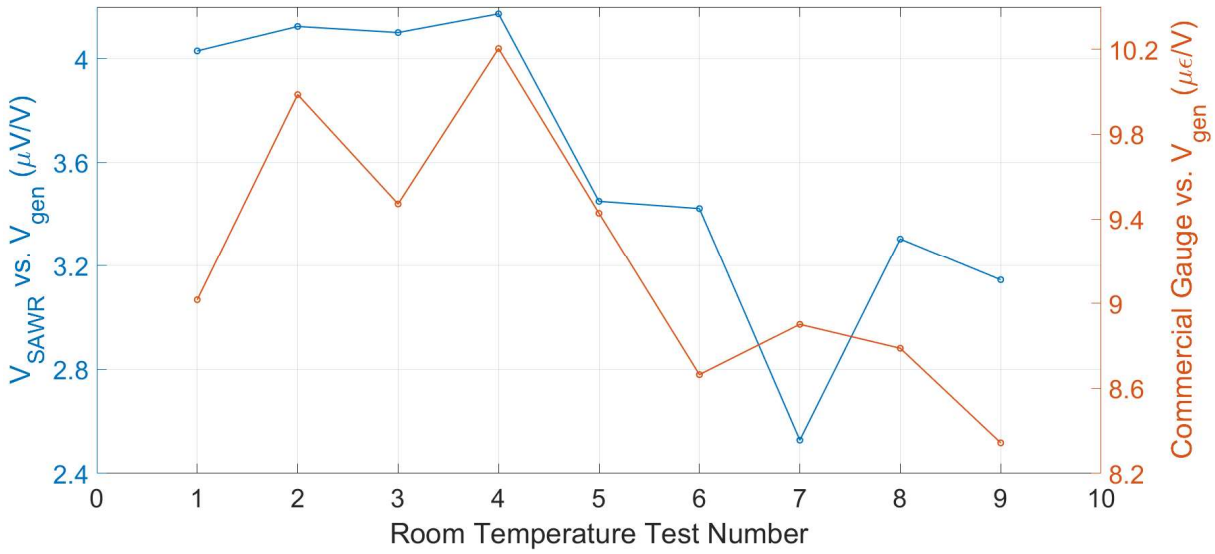

Figure 4.27 The V_{SAWR} vs. V_{gen} and commercial gauge vs. V_{gen} slopes for tests 1-9 at room temperature.

important to note that between tests 4 and 5 and tests 6 and 7, the thermocouple in the furnace had to be adjusted because it was not in firm contact with the beam. This plot suggests that the experimental setup may not be allowing a stable dynamic strain measurement, since neither SAWR nor commercial sensor is reading the same dynamic strain sensitivity once the system is submitted to strain cycling over the nine tests after temperature cycling.

Figure 4.28 shows plots similar to those in Figure 4.27 for the tests performed at 215°C and 200°C. For these tests, the adjustment of the thermocouple occurred between tests 3 and 4 and tests 6 and 7. Similarly to the room temperature plot, the results show lack of consistency, indicating that there is likely variation in the dynamic strain test setup.

After comparing V_{SAWR} and the commercial gauge response to V_{gen}, two parts of the experimental setup were identified as possible causes of the variation in the V_{SAWR} vs. V_{gen} and commercial gauge response vs. V_{gen} curves. The first possible cause is movement of the thermocouple measuring the SAWR temperature during the tests in Figure 4.24 and Figure 4.25 could have affected the sensor responses of the SAWR and commercial gauge due to a change in

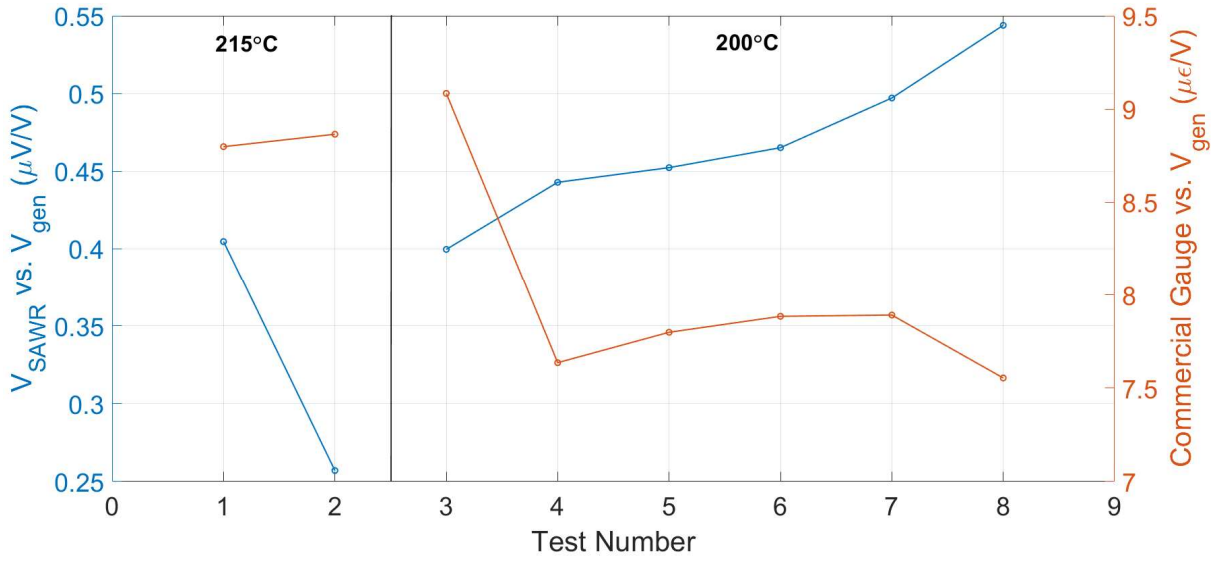

Figure 4.28 The V_{SAWR} vs. V_{gen} slopes and commercial gauge vs. V_{gen} slopes for tests at 215°C and 200°C.

the pressure the thermocouple was putting on the beam. The second potential cause for the variation in the V_{SAWR} vs. V_{gen} and commercial gauge response vs. V_{gen} curves is movement of the drive arm when the thermocouple was being adjusted. Room temperature measurements were performed to test these hypotheses.

The first test done was to determine whether the dynamic strain results changed when the thermocouple was removed from the beam. Figure 4.29 shows the experimental setup for these two tests. The left image shows the condition for the test done with the thermocouple placed on the beam and the right image shows the conditions for the test done with the thermocouple removed from the beam. For these tests, the thermocouple was removed from the beam and kept inside the furnace without touching the beam or drive arm.

Figure 4.30 shows the V_{SAWR} vs. commercial gauge response for the room temperature dynamic strain tests with and without the thermocouple placed on the beam. The slopes and correlation coefficients for the data are shown in Table 4.11. For this test, there was no heating between the two tests, so the only change in the measurement was the placement of the

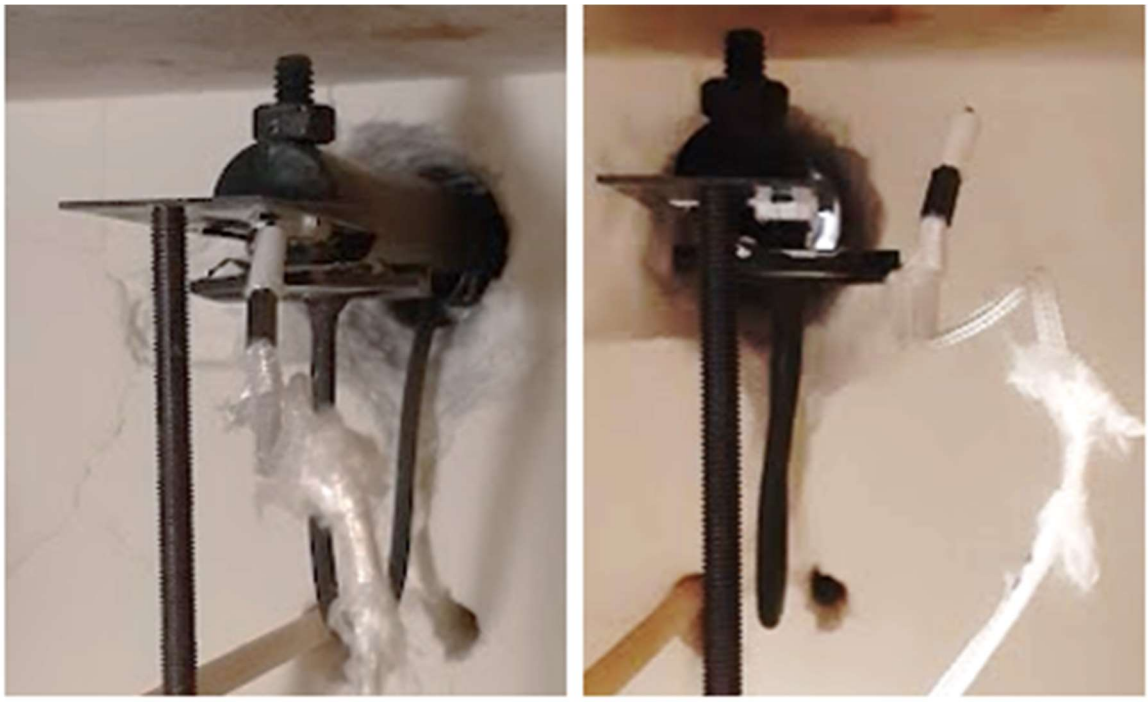

Figure 4.29 (Left) The experimental setup for the room temperature test with the thermocouple placed on the beam and (Right) the experimental setup for the room temperature test with the thermocouple removed from the beam but remaining in the furnace.

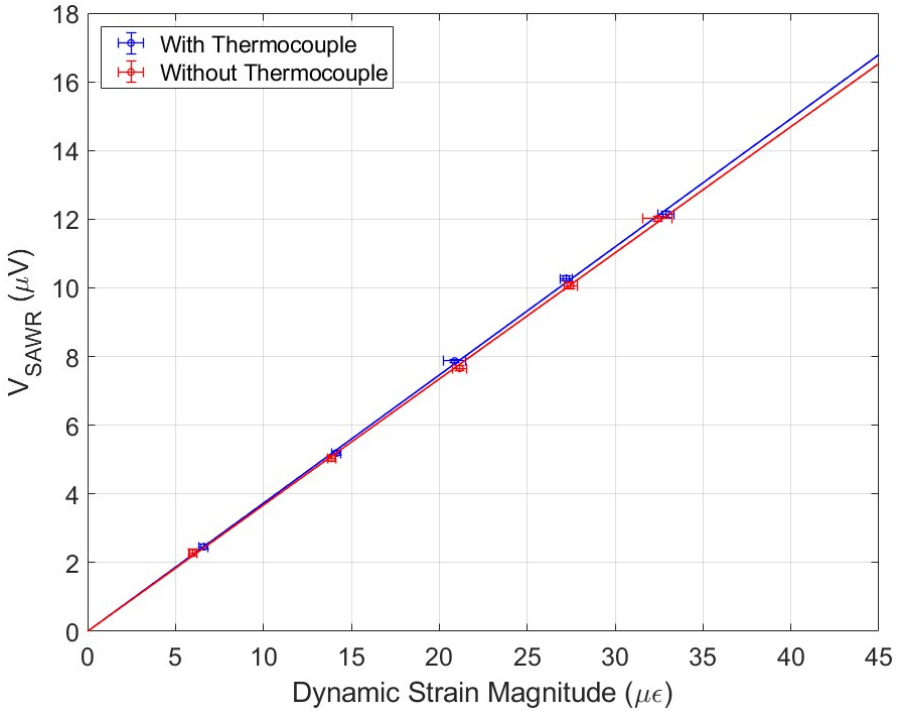

Figure 4.30 The V_{SAWR} vs. commercial gauge data and linear fits for the room temperature test with and without the thermocouple placed on the beam.

Table 4.11 The measured SAWR sensitivities to dynamic strain and correlation for the room temperature dynamic strain tests with and without the thermocouple placed on the beam during testing.

Test	SAWR Sensitivity to Dynamic Strain (μV/με)	R^2
With Thermocouple	0.373	0.9993
Without Thermocouple	0.367	0.9994

thermocouple on the beam. The results show that there is little variation (1.6%) in the responses of the SAWR sensor and the commercial strain gauge when the thermocouple is removed meaning that the loading on the beam caused by the thermocouple is negligible and likely not the cause of the variation in the dynamic strain results.

Next, a test was done where the placement of the drive arm was changed. Figure 4.31 shows a schematic of the dynamic strain test beam that indicates where the drive arm was placed for these tests. The location in blue (Edge-Center) correlates to the normal and ideal position for dynamic testing. The location in red (Back-Center) has the drive arm moved approximately 5mm away from the ideal location on the edge of the beam. The location in green (Edge-Side) had the drive arm on the edge of the beam but moved approximately 5mm towards the commercial gauge side of the beam. By design, the two 5mm movements of the drive arm represent a much larger

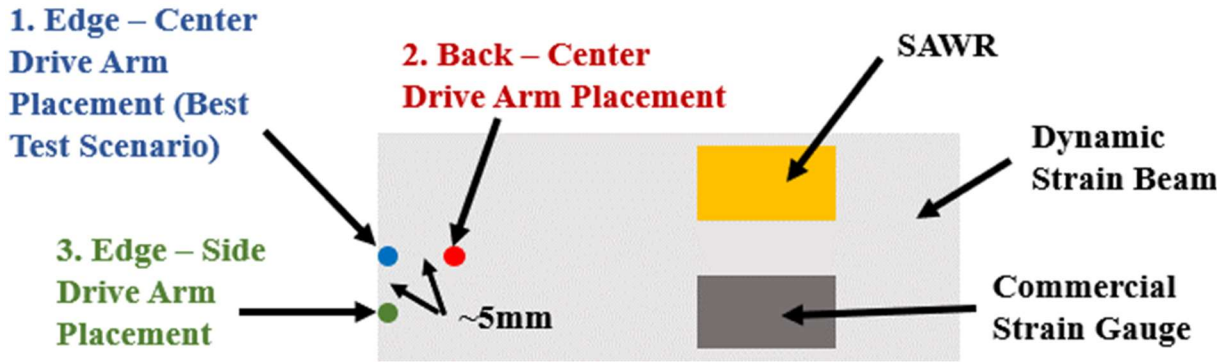

Figure 4.31 A schematic of the dynamic strain test beam showing the location of the different drive arm placements that were tested for the SAWR and commercial gauge dynamic strain response.

range of movements than would be expected for variations in the arm position that would result from e.g., thermal expansion, vibration, or other factors in the experimental setup.

Figure 4.32 shows the VSAW vs. commercial gauge response for the three drive arm positions described in Figure 4.31. The linear fits, correlation coefficients, and percent differences from the Edge-Center condition are shown in Table 4.12, which indicated that the dynamic strain responses were consistent (within 5%) despite these relatively large differences in the arm position.

The next experimental verification done at room temperature was changing the static strain on the beam due to the drive arm. This experiment targeted the verification of whether a variation in the static strain on the beam during dynamic strain tests could affect the SAWR sensitivity to

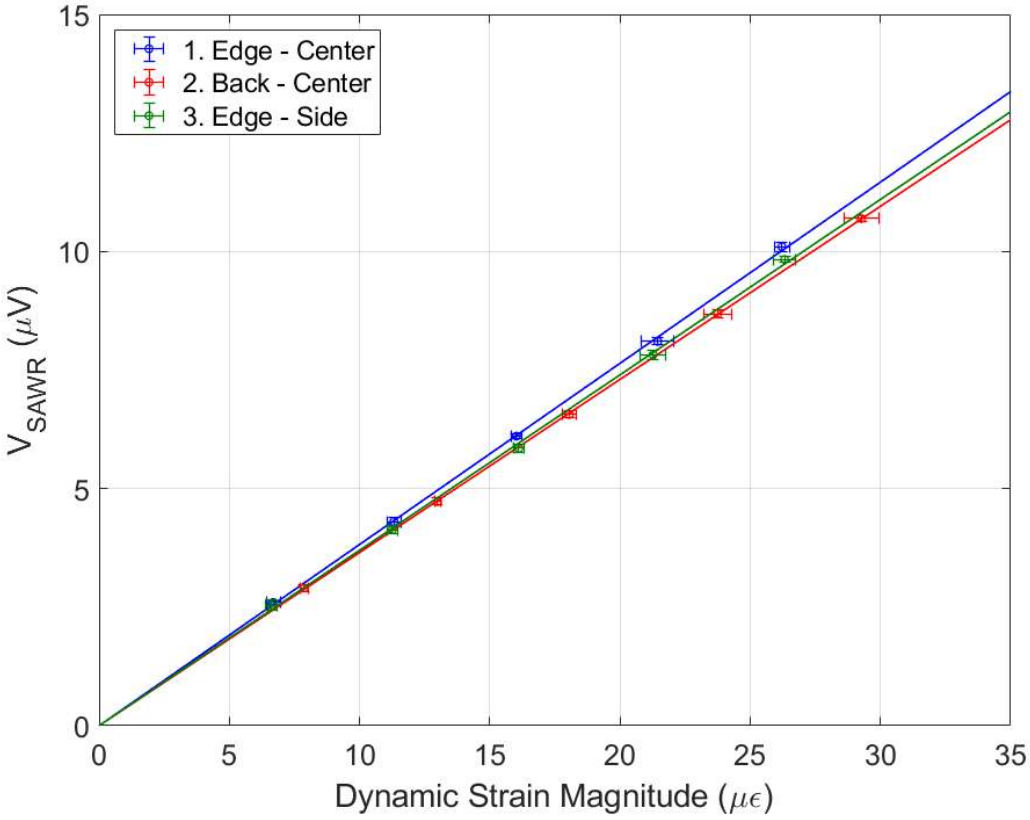

Figure 4.32 The V_{SAWR} vs. commercial gauge response for the three drive arm positions shown in Figure 4.31.

Table 4.12 The linear fits, correlation coefficients, and percent differences from the Edge-Center, Back-Center, and Edge-Side condition for the V_{SAWR} vs. commercial gauge response data.

Test	SAWR Sensitivity to Dynamic Strain (μV/με)	R^2	% Difference from Edge-Center
Edge-Center	0.382	0.9995	0
Back-Center	0.365	0.9999	-4.5
Edge-Side	0.370	0.9990	-3.1

dynamic strain. For this test dynamic strain was applied at room temperature with the drive arm height adjusted as described in Section 3.4.2 and with the drive arm height increased by one half turn. Based on the calibration curves in Figure 4.22a, it was determined that the increase in static strain was approximately 10με. The results from these tests are shown in Figure 4.33. The maximum strain variation between the two different static strain load conditions on the beam is less than 0.5% for the fitted curves. This shows that such small variations in static strain do not significantly affect the dynamic strain response of the SAWR and the commercial gauge. Based on these findings, the likely causes for the observed inconsistencies in the dynamic strain response were hypothesized to be a result of the heating and cooling of the dynamic strain measurement system setup components during these tests.

Because it was determined that thermal cycling was the most probable cause of the lack of stability in the SAWR dynamic strain measurement, the tests with the thermocouple removed from the beam needed to be repeated after heating and cooling was carried out to determine if removal of the thermocouple affects the stability of the SAWR measurement. For these tests, the thermocouple was completely removed from the furnace to ensure that the thermocouple was not interfering with the beam or the drive arm. After the thermocouple was removed, the beam was heated to 200°C and cooled to room temperature two times. From this heating and cooling profile, three room temperature tests and two 200°C tests were performed. Each dynamic strain test

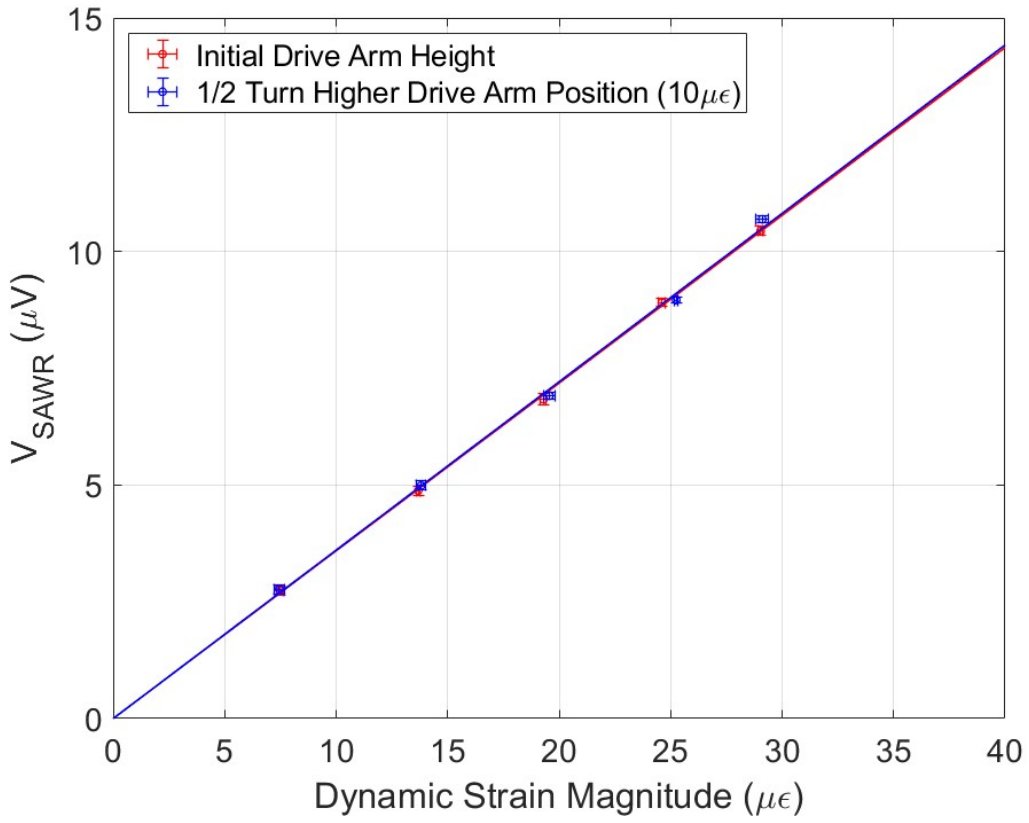

Figure 4.33 V_{SAWR} vs. commercial strain gauge response for the room temperature measurements at the typical drive arm height (red) and after increasing the drive arm height be one half turn (blue), which increases the static strain by about 10με.

consisted of six measurements at five different dynamic strain magnitudes between 5με and 40με. The 200°C tests were performed in between room temperature tests, meaning no room temperature tests were taken without heating in between.

Figure 4.34 shows V_{SAWR} vs. the commercial strain gauge response for the room temperature measurements before heating, after heating to 200°C once, and after heating to 200°C a second time. Table 4.13 shows the slopes for the room temperature dynamic strain tests shown in Figure 4.34, the correlation coefficients, and percent differences from the test before heating. After heating to 200°C once, there was little change (less than 1%) observed in the SAWR sensitivity to dynamic strain, but after heating to 200°C two times, there was a 12% decrease in SAWR sensitivity to dynamic strain at room temperature. This suggests that removing the

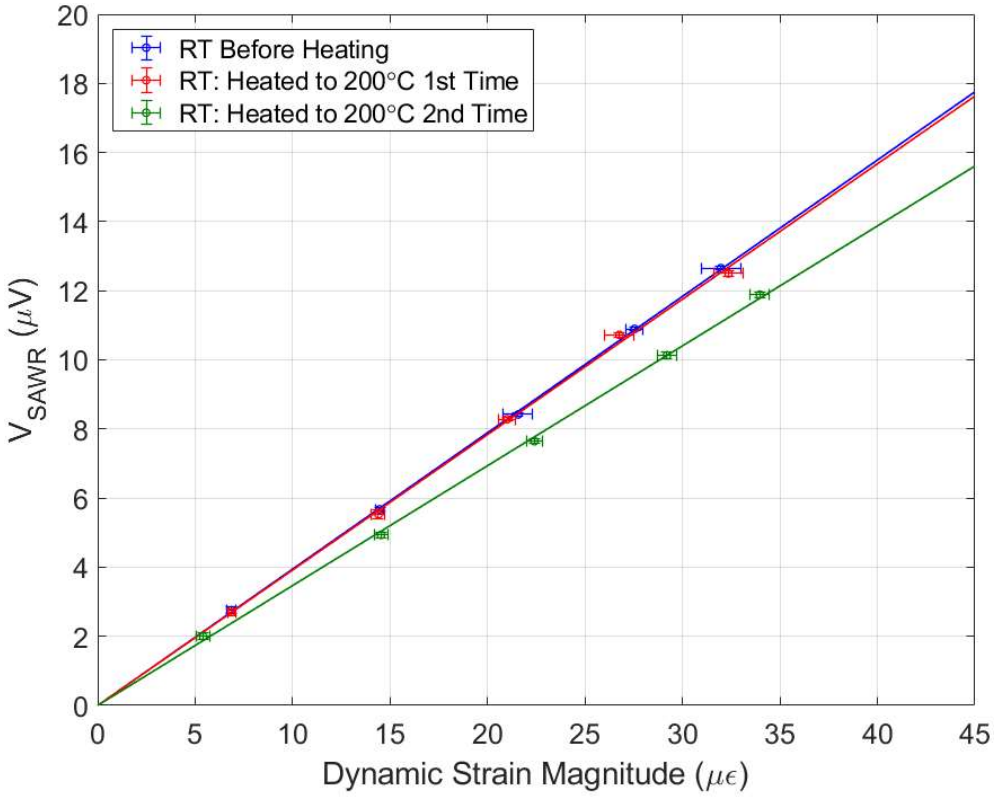

Figure 4.34 V_{SAWR} vs. commercial strain gauge response for the room temperature measurements before heating (blue), after heating to 200°C once (red), and after heating to 200°C a second time (green).

Table 4.13 The measured SAWR sensitivity to dynamic strain, correlation coefficients, and percent difference from the room temperature tests with the thermocouple removed from the dynamic strain beam.

Test	SAWR Sensitivity to Dynamic Strain (μV/με)	R^2	% Difference
No Heating	0.395	0.9998	0
Heating to 200°C Once	0.392	0.9983	-0.8
Heating to 200°C Twice	0.347	0.9991	-12

thermocouple from the dynamic strain beam may not significantly affect the stability of the SAWR sensitivity to dynamic strain at room temperature.

Figure 4.35 shows V_{SAWR} vs. the commercial strain gauge response for the 200°C dynamic strain tests. The first test was performed before cooling to room temperature and the second test was performed after cooling to room temperature and heating to 200°C again. Table 4.14 shows

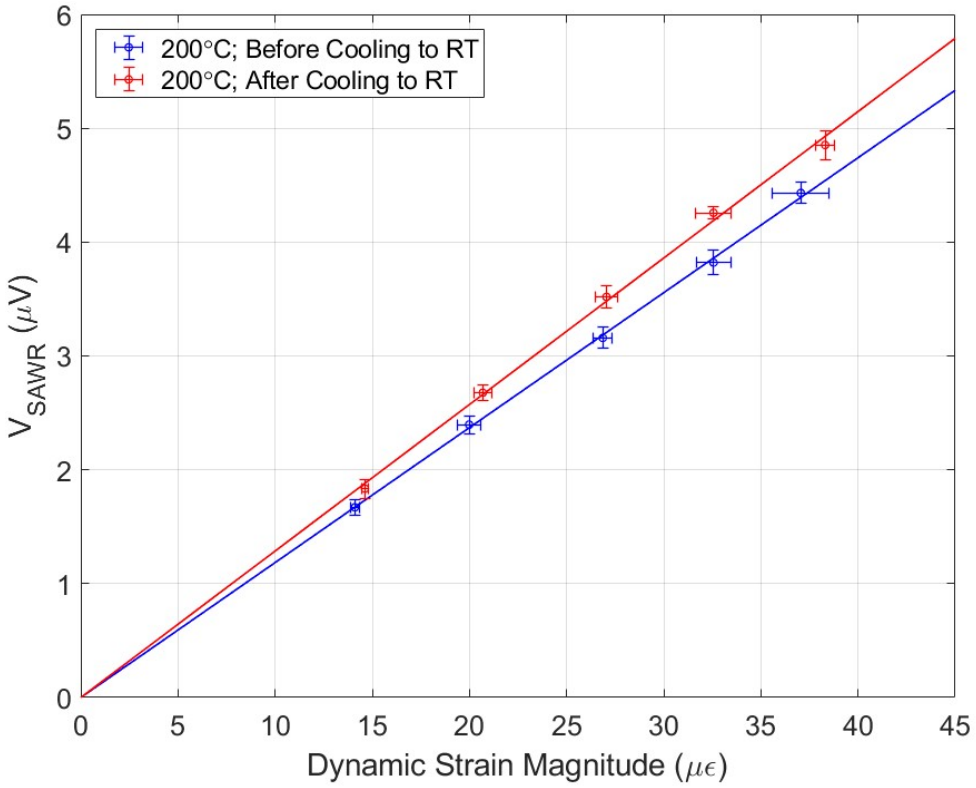

Figure 4.35 V_{SAWR} vs. commercial strain gauge response for the 200°C measurements before cooling to room temperature (blue) and after cooling to room temperature and heating to 200°C once (red).

Table 4.14 The measured SAWR sensitivity to dynamic strain, correlation coefficients, and percent difference from the 200°C tests with the thermocouple removed from the dynamic strain beam.

Test	SAWR Sensitivity to Dynamic Strain (μV/με)	R^2	% Difference
Before Cooling to Room Temp.	0.119	0.9990	0
Cooling to Room Temp. Once	0.129	0.9976	+8.4

the slopes of the linear fits for the 200°C dynamic strain tests shown in Figure 4.35. After cooling to room temperature and heating back to 200°C, there was an 8.4% increase in SAWR sensitivity to dynamic strain. Based on this result and the results from the room temperature dynamic strain tests with the thermocouple removed from the furnace, it appeared that the thermocouple loading the dynamic strain beam was not the cause for the lack of stability in the SAWR sensitivity to dynamic strain.

The next test setup modification that was made was the removal of the drive arm from the dynamic strain beam when heating and cooling. When placing the drive arm on the dynamic strain beam, it was positioned such that static strain is applied to the beam. This is done to ensure that the drive arm does not lose contact with the beam while the sinusoidal input is at a minimum. It also prevents hammering action between the drive and the beam while the vibration generator is on, which can create additional noise harmonics in the dynamic strain measurement. This static strain, however, could also introduce inconsistencies in the epoxy when it is heated and cooled and was therefore investigated as a potential source of variability in the SAWR and commercial gauge dynamic strain measurements.

Figure 4.36 shows the V_{SAW} vs. commercial strain gauge measurements for the room temperature tests removing the drive arm while heating and cooling. Similar to the thermocouple

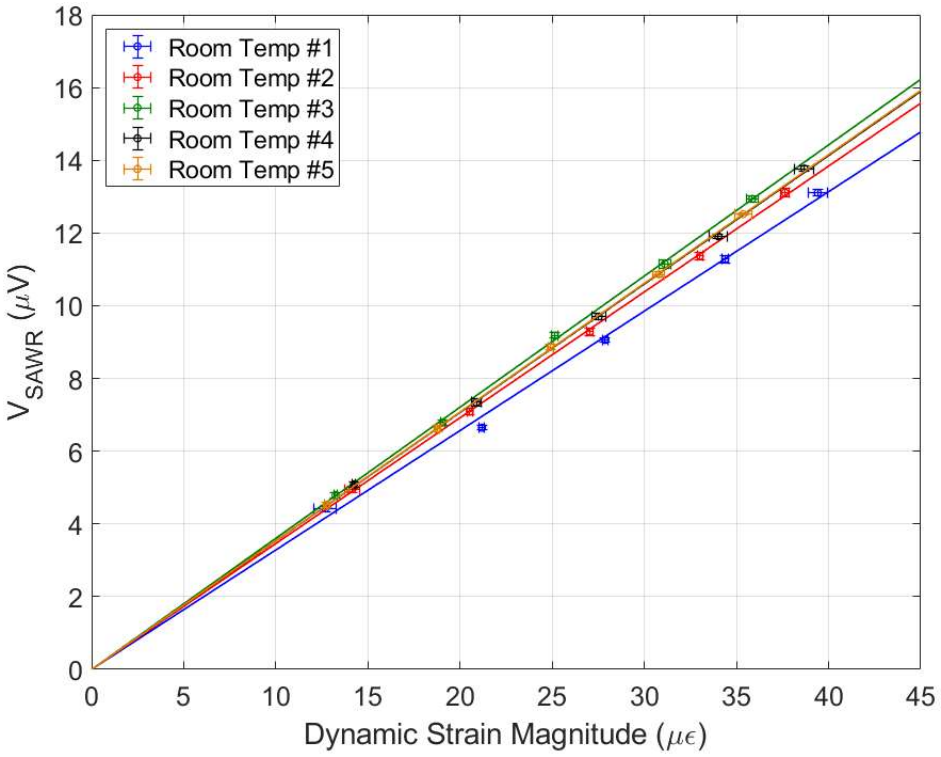

Figure 4.36 V_{SAWR} vs. commercial strain gauge response for the room temperature tests that involved removing the drive arm while heating and cooling between room temperature and 200°C tests.

test, 200°C tests were performed between each room temperature test, meaning that between two room temperature tests, the beam, epoxy, and SAWR were heated to 200°C for about 5 hours. While the furnace was heating and cooling between tests, the drive arm was removed from the beam, meaning that there was no static strain applied to the beam by the drive arm. Table 4.15 shows the measured SAW sensitivity to dynamic strain, correlation coefficients, and percent difference for the data shown in Figure 4.36.

Table 4.15 The measured SAWR sensitivity to dynamic strain, correlation coefficients, and percent difference from the room temperature tests removing the drive arm while heating and cooling.

Test	SAWR Sensitivity to Dynamic Strain (μV/με)	R^2	% Difference
RT #1: Heated to 200°C x4	0.328	0.9959	0
RT #2: Heated to 200°C x5	0.346	0.9995	+5.5%
RT #3: Heated to 200°C x6	0.361	0.9994	+10%
RT #4: Heated to 200°C x7	0.353	0.9994	+7.6%
RT #5: Heated to 200°C x8	0.354	0.9999	+7.9%

Figure 4.37 shows the V_{SAWR} vs. commercial strain gauge measurements for the 200°C tests carried out by removing the drive arm while heating and cooling, and Table 4.16 shows the measured SAWR sensitivity to dynamic strain, correlation coefficients, and percent difference for the data shown in Figure 4.37. Based on the room temperature and 200°C data, removing the drive arm while heating and cooling resulted in a maximum sensitivity variation between heating-and-cooling cycles of 14% at 200°C. More tests are necessary to verify whether this variation within 14% is caused by an overall sensitivity drift with heating-and-cooling cycles or the precision of the dynamic strain test setup.

All the dynamic strain tests were plotted on the same graph to determine if there were any trends in the variation of SAWR sensitivity to strain. In addition, the V_{SAWR} vs. V_{gen} and commercial gauge response vs. V_{gen} were plotted on the figure as well so that the SAWR and

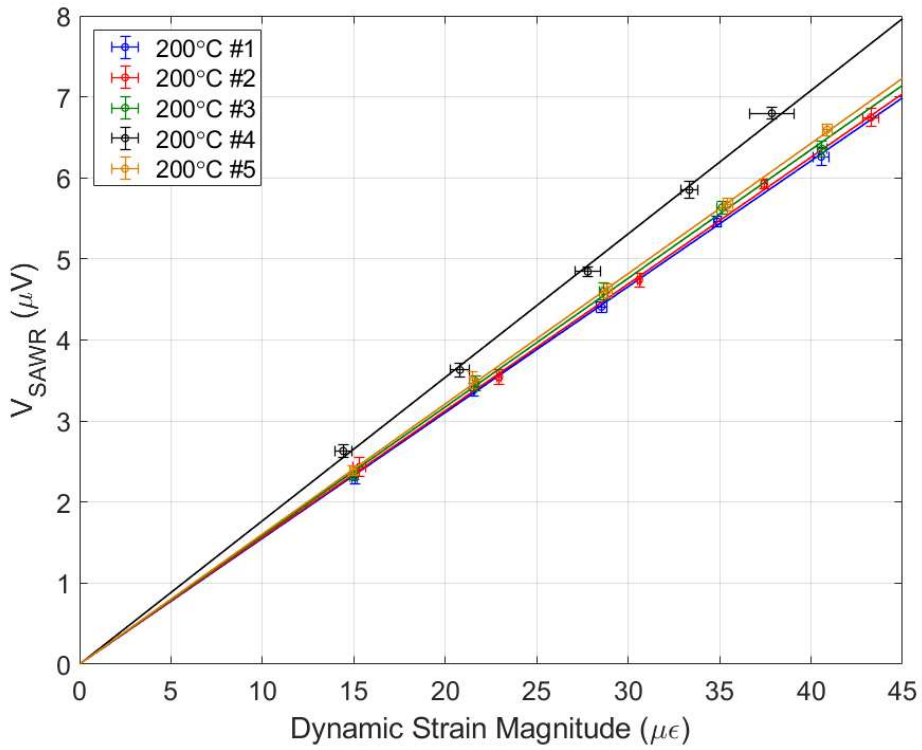

Figure 4.37 V_{SAWR} vs. commercial strain gauge response for the 200°C tests carried out by removing the drive arm while heating and cooling between room temperature and 200°C.

Table 4.16 The measured SAWR sensitivity to dynamic strain, correlation coefficients, and percent difference from the 200°C tests removing the drive arm while heating and cooling.

Test	SAWR Sensitivity to Dynamic Strain (μV/με)	R^2	% Difference
200°C #1: Cooled to RT x3	0.155	0.9994	0
200°C #2: Cooled to RT x4	0.156	0.9990	+0.6%
200°C #3: Cooled to RT x5	0.159	0.9983	+2.6%
200°C #4: Cooled to RT x6	0.177	0.9976	+14%
200°C #5: Cooled to RT x7	0.161	0.9996	+3.9%

commercial sensors can be considered independently in looking into cause of the variation in the dynamic strain sensitivity. Figure 4.38 shows the room temperature results from all the dynamic strain tests performed in Section 4.2.5 using the Duralco 4461 epoxy. The information on the tests done is indicated in the figure caption. It is important to note that the dynamic strain beam was heated and cooled between each point on the graph in Figure 4.38, so no two points with different test numbers have the same thermal history.

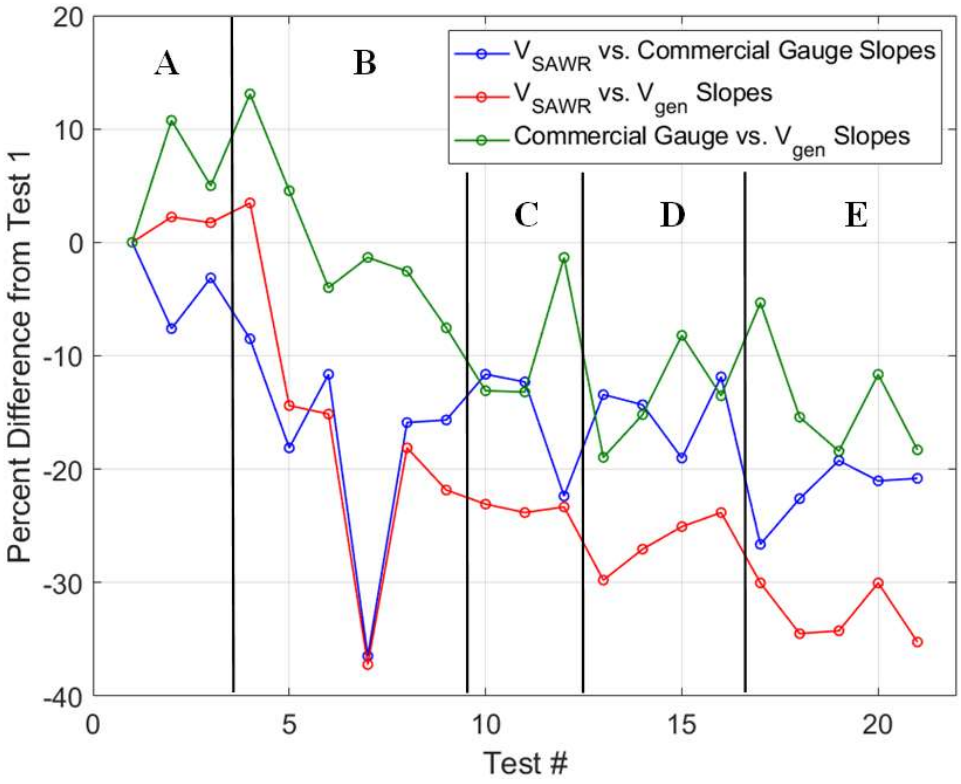

Figure 4.38 Room temperature V_{SAWR} vs. commercial gauge (blue), V_{SAWR} vs. V_{gen} (red), and commercial gauge vs. V_{gen} (green) slope data for all SAWR dynamic strain tests using Duralco 4461 converted to percent differences from Test #1. Between each point, the dynamic strain beam was heated and cooled. Region A refers to testing while heating and cooling between room temperature and 215°C. Region B refers to testing while heating and cooling between room temperature and 200°C. Five tests were done at 125°C between regions B and C prior to taking the device to 200°C without returning to room temperature. Region C refers to testing with the thermocouple removed from the dynamic strain beam while heating and cooling between room temperature and 200°C. Region D refers to removing the drive arm from the beam between heating and cooling cycles between room temperature and 200°C. Region E refers to removing the drive arm from the beam between heating and cooling cycles between room temperature and 200°C after a heating cycle where the drive arm was not removed from the beam.

In order to compare the V_{SAWR} vs. commercial gauge, V_{SAWR} vs. V_{gen}, and commercial gauge vs. V_{gen} data, the percentage difference in the slope of the linear fit of each measurement relative to the first test is shown in Figure 4.38. This means that each point represents one dynamic strain test according to the equation:

$$One\ Data\ Point = 100 \cdot \frac{slope\ x\text{–}s \qquad \#1}{slope\ \#1} \tag{4.1}$$

It is interesting to note from Figure 4.38 that at room temperature both the sensitivity plots as a function of V_{gen} for the SAWR sensor and for the commercial gauge seem to drift as the test number increases. Moreover, considering only Region E in Figure 4.38, the sensitivity variation as a function of V_{gen} calculated as:

$$Sensitivity\ variation = 100 \cdot \frac{Max\ sensitivity \quad sensitivity}{Min\ sensitivity} \tag{4.2}$$

results in a variation of 8.3% for the measurements done with the SAWR sensor and 16.1% for the measurements done with the commercial sensor. In that region alone no clear drifting is observed. Since both the commercial and the SAWR sensor as a function V_{gen} are showing the sensitivity variations mentioned above, it is not clear at this point what is causing such variation in the experimental setup.

Similar to the room temperature tests, the V_{SAWR} vs. commercial gauge, V_{SAWR} vs. V_{gen}, and commercial gauge vs. V_{gen} slopes at 200°C using the Duralco 4461 epoxy are plotted in Figure 4.39. The percentage difference in the slope of the linear fit of each measurement as compared to the first test was calculated according to Equation (4.1). Between each point, the dynamic strain beam was cooled and heated. It is also important to note that the labeled regions in Figure 4.39 do not necessarily line up with the labeled regions in Figure 4.38

For the commercial gauge vs. V_{gen} measurements shown in Figure 4.39, the variation of the sensitivity over the entirety of the testing is comparable to the variation observed at room temperature in Figure 4.38. The V_{SAWR} vs. commercial gauge and V_{SAWR} vs. V_{gen} measurements show a greater than 250% increase over the entirety of the testing. However, considering region F alone, the sensitivity variation as a function of V_{gen} calculated using Equation 4.2 results in a variation of 10.3% for the measurements done with the SAWR sensor and 18.5% for the

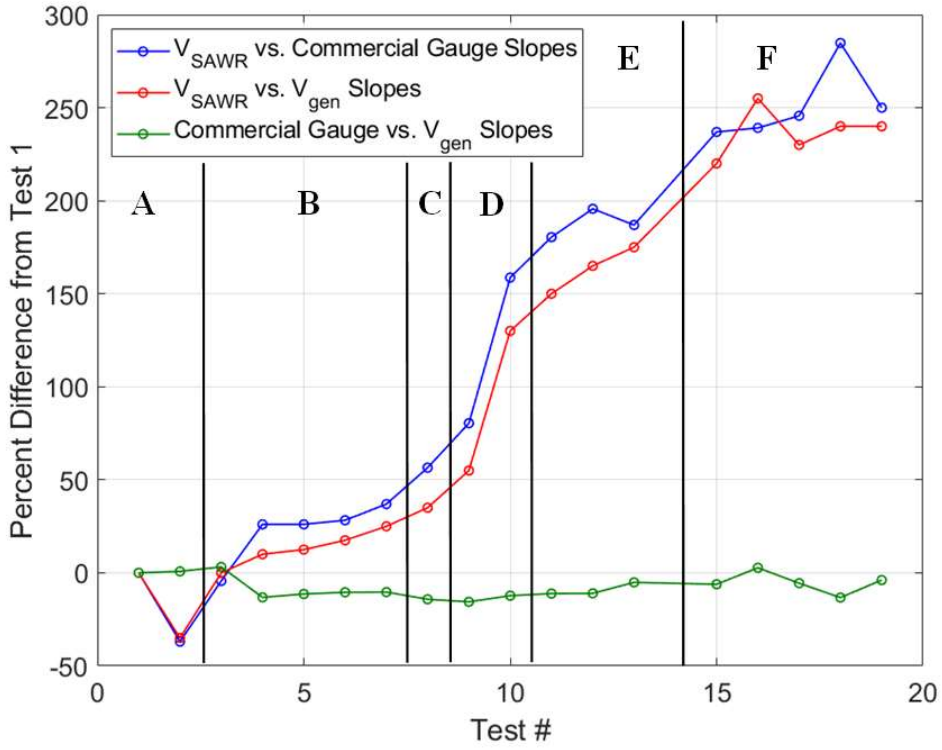

Figure 4.39 The 200°C V_{SAWR} vs. commercial gauge (blue), V_{SAWR} vs. V_{gen} (red), and commercial gauge vs. V_{gen} (green) slope data for all dynamic strain tests using Duralco 4461 converted to percent differences from Test #1. Between each point, the dynamic strain beam was cooled and heated. Test #14 was compromised by the poor grounding of the commercial gauge cable and lack of proper sheathing. Region A refers to testing while heating and cooling between room temperature and 215°C. Region B refers to testing while heating and cooling between room temperature and 200°C. Region C refers to a 200°C test after five tests were done at 125°C. Region D refers to testing with the thermocouple removed from the dynamic strain beam while heating and cooling between room temperature and 200°C. Region E refers to removing the drive arm from the beam between heating and cooling cycles between room temperature and 200°C. Region F refers to removing the drive arm from the beam between heating and cooling cycles between room temperature and 200°C after a heating cycle where the drive arm was not removed from the beam.

measurements done with the commercial sensor, and in that region alone no clear drifting is observed. Since both the commercial and the SAWR sensor as a function V_{gen} are showing the sensitivity variations mentioned above, it is not clear at this point what is causing such variation in the experimental setup.

The experimental modifications of removing the thermocouple from the hole that the drive arm is fed through and of removing the drive arm from the beam between heating and cooling

cycles might have contributed to the SAWR sensor relative stabilization, although more experiments are necessary to verify that drifting and fluctuations are further diminished to improve sensor calibration accuracy and precision.

4.3 Conclusions

In this section, investigation on the effects of temperature cycling of the high temperature adhesives were done to determine if they provided a stable SAWR sensor response. It was found that when cycling the SAWR mounted using Aremco 668 between 100°C and 425°C, the SAWR sensitivity to dynamic strain decreased by 93% after two rounds of temperature cycling at room temperature and decreases below the noise floor at 400°C after two rounds of temperature cycling for dynamic strain magnitudes up to 40με. It was identified that this decrease in SAWR sensitivity to dynamic strain is caused by cracking at the ceramic adhesive/LGS interface. This takes place once the SAWR sensor is exposed to thermal cycles between 100°C and 425°C due to the CTE differences between the respective materials and their material nature. The identified cracking results in a significant drop of strain sensor sensitivity and eventually failure of strain sensing all together, thus decreasing the sensor reliability, repetitiveness, and stability.

Because adhesion failure was observed for dynamic strain sensing at 400°C, different commercially available adhesives were tested for use in static and dynamic strain sensing up to 200°C. After heating tests on glass slide samples and LGS chip samples, Aremco 805, Aremco 526N, Duralco 4525, and Duralco 4461 were chosen for static strain stability tests. Aremco 526N was rejected for SAWR static and dynamic strain sensing because after one round of temperature cycling between 50°C and 250°C, the measured SAWR sensitivity to static strain decreased by 82% indicating either that there was failure in the mounting or that the adhesive does not effectively transfer strain after temperature cycling. Duralco 4525 was also rejected because after

mounting the SAWR sensors, there was discoloration of the adhesive that indicates that there is inconsistency in the adhesion to the LGS. Aremco 805 and Duralco 4461 were selected for high temperature static strain stability testing at high temperature.

For the high temperature static strain stability testing, temperature correction was implemented so that the effect of temperature variation on the SAWR static strain response could be removed. After two rounds of temperature cycling, it was determined that both Aremco 805 and Duralco 4461 showed the necessary stability in static strain sensitivity for testing of adhesive stability for dynamic strain measurements after temperature cycling. Duralco 4461 was chosen for dynamic strain tests because it had a lower average standard deviation in the static strain measurements. After initial dynamic strain testing, it was found that a stable response to dynamic strain could not be attained. Based on the stability observed in the static strain results, the stability of the experimental setup was put into question. It was determined that variation in the SAWR dynamic strain sensitivity occurred when the beam was heated and cooled. When removing the drive arm from the beam when heating and cooling, the sensor showed the greatest stability (10.3% maximum variation in the SAWR response and 18.5% maximum variation in the commercial gauge response). It is unclear if that level of variation is due to the adhesive or the test setup. More experiments will be required to verify that.

CHAPTER 5
TEMPERATURE AND DYNAMIC STRAIN MEASUREMENTS USING A SINGLE SAWR SENSOR

Because the SAWR sensitivity to static and dynamic strain are dependent on temperature, it is necessary to know the temperature at all times [14], [53]. For static strain measurements, temperature correction of the SAWR frequency response to temperature and static strain can be done by utilizing a SAWR temperature sensor that slides on the surface of the beam or metallic part being measured, as discussed in Section 4.2.4.3. For dynamic strain sensing, this is not possible because even if the SAWR was not rigidly attached to the beam, the SAWR would still measure the vibration of the part due to the dynamic strain excitation. This would lead to error in the dynamic strain measurements. Therefore, all SAWR sensors used for dynamic strain sensing need to be rigidly mounted to the beam or metallic part being measured, which also means that a method to separate temperature and dynamic strain is needed.

In literature, measurement of multiple measurands has been done using multiple SAWR devices from a single sensor chip [15], [16]. These papers present methods of removing the SAWR temperature response from the response of torque or pressure response by utilizing sensor chips with three SAWR devices. Victor Kalinin reports a temperature and torque SAWR sensor on quartz that utilizes sensors in different orientations with the same TCF to remove the SAWR response to temperature from the SAWR response to torque [15], [80]. A third sensor along a third orientation is used to determine the temperature once the torque is known. Werner Buff, *et al.* [16], [81] reports a temperature and pressure sensor utilizes two SAWR devices on the same sensor chip along the same orientation that are subjected to two different strain magnitudes when exposed to pressure to remove the SAWR temperature response from the SAWR pressure response. Similar

to Kalinin, a third sensor along a different orientation is used to determine the temperature once the pressure is known. Both of these techniques are further reviewed in Section 5.1.

In this chapter, a method for extracting the temperature, dynamic strain magnitude, and dynamic strain spectral components using a single SAWR sensor, established in this work, is presented. The technique relies on the fact that the dynamic strain is measured from the relative amplitudes between the SAWR resonant frequency component and the dynamic strain spectral component(s) [14], [32]. The SAWR center frequency of the single SAWR sensor can then be used for temperature sensing. Finally, the dynamic strain spectral components are determined by the frequency of the sidelobes relative to the center peak frequency.

5.1 Literature Review for the Extraction of Temperature and Dynamic Strain from the SAWR Response

5.1.1 Kalinin Torque and Temperature Sensor

The first work analyzed in this chapter is the torque sensor temperature correction methods developed by Victor Kalinin [15], [80]. In his work, Kalinin developed a torque/temperature sensor system composed of five SAWR sensors on two Y+34° cut quartz wafers. It was reported that for this quartz cut, two SAWR sensors fabricated at ±45° relative to the X-axis of the substrate have TCF values that are close enough to be considered the same between 20°C and 160°C [15], [80]. These sensors are M1SAW and M2SAW in Figure 5.1 [80]. Although these SAWRs have a similar temperature response, the torque response is not the same for the two different sensor orientations. Therefore, taking the difference between the two sensor resonant frequencies, or the differential frequency, the frequency variation will be due only to the torque response plus an unstrained fixed value due to the difference between the resonant frequencies of the devices which usually are close to each other (within about 10 MHz). Therefore, the differential frequency of M1SAW and

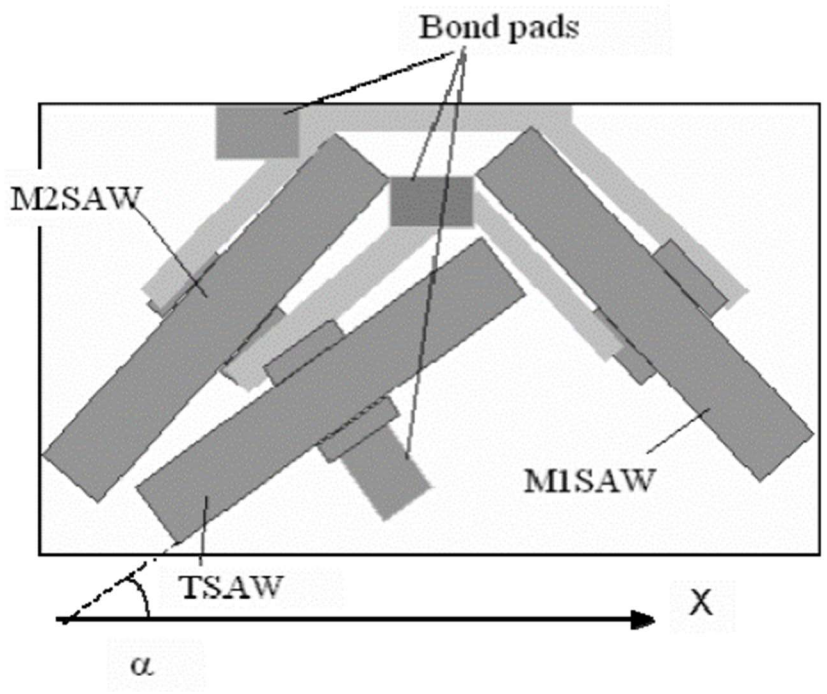

Figure 5.1 The SAWR sensing element used by Kalinin *et al.* [80].

M2SAW can be calibrated to torque. For temperature sensing, an additional SAWR device (TSAW in Figure 5.1) along a third orientation with a different TCF than the torque sensors was fabricated on the same sensor chip. Once the torque is known, then the temperature can be determined through calibrations of the differential frequency of the TSAW and M1SAW.

For torque and temperature calibration, two sensing components were placed on opposite ends of a calibration structure (Figure 5.2). Both sensing components had M1SAW and M2SAW torque sensors. Only one sensing component had the TSAW because it was assumed that the temperature would be the same on opposite sides of the calibration structure. Figure 5.3 shows the torque and temperature calibrations reported in [15]. In the figure, F_m refers to the average differential frequency between M1SAW and M2SAW on both sides of the calibration structure (the unstrained differential frequency for M1SAW and M2SAW was about 2 MHz on both sensor

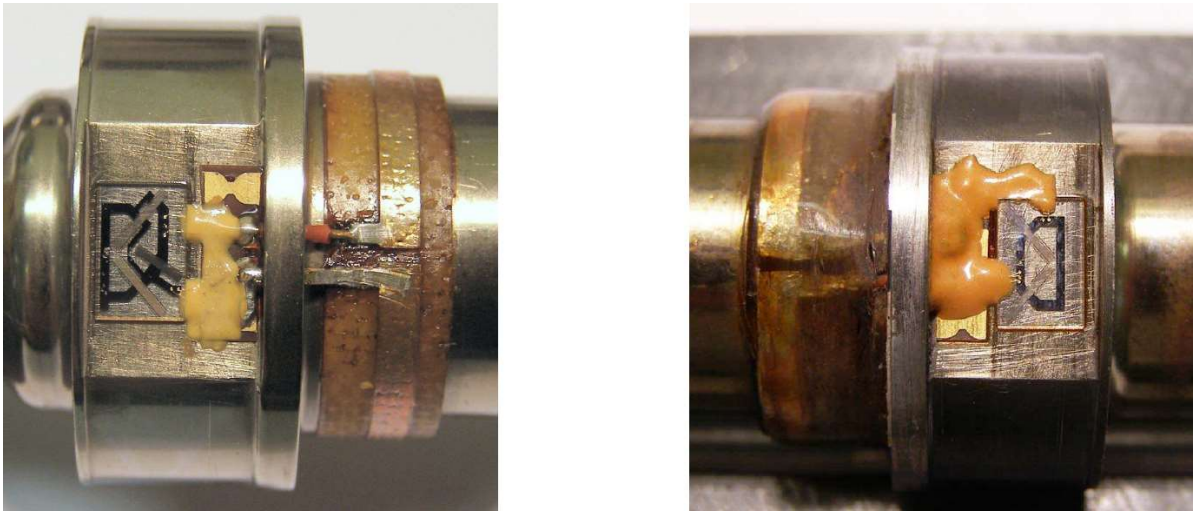

Figure 5.2 The two SAWR sensor mounts that were used by Kalinin for temperature and torque measurements [15]. The left image shows the sensor mount with the SAWR temperature sensor included and the right image shows the sensor mount without the SAWR temperature sensor.

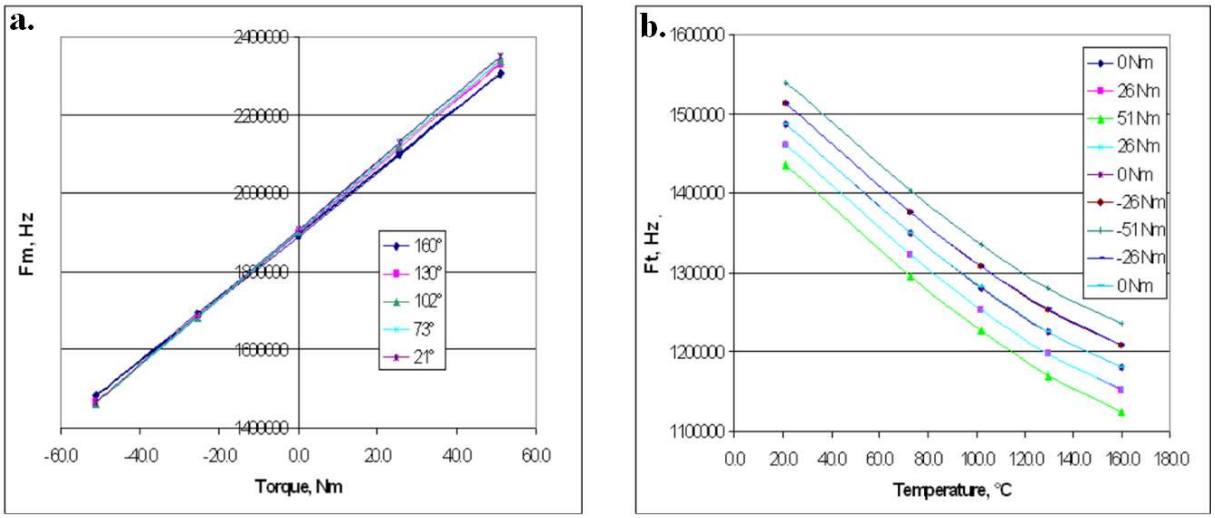

Figure 5.3 (a) The torque calibration to F_m and (b) the temperature calibration to F_t reported in [15].

wafers). F_t refers to the differential frequency between M2SAW and TSAW. All sensors were wirelessly interrogated for these tests.

When analyzing this method for extracting temperature from torque, it is important that two different SAWR sensor orientations have the same TCF, but different torque sensitivities. This behavior would be difficult to implement for high temperature dynamic strain sensors because

such similar TCF behaviors over a wide temperature range (room temperature to 800°C) for two different orientations is difficult to achieve. Therefore, Kalinin's method of extracting torque and temperature is not appropriate for extracting dynamic strain and temperature.

5.1.2 Buff Pressure and Temperature Sensor

The second work analyzed in this chapter was Werner Buff's sensor work to extract pressure and temperature [16], [81]. Buff *et al.* developed a pressure/temperature sensor system using three SAWR sensors fabricated on a quartz plate diaphragm (Figure 5.4, [81]). The quartz plate used was a Y-35.5°-α quartz cut. Two SAWR sensors (SAWR 1 and SAWR 3 in Figure 5.4) were fabricated along the same orientation, but at different distances from the edge of the diaphragm. The CTEs for these two devices are equal since they are along the same orientation, so the differential frequency between these devices will remove variations due to temperature. Since the two SAWR devices are at different distances from the edge of the diaphragm, the strain

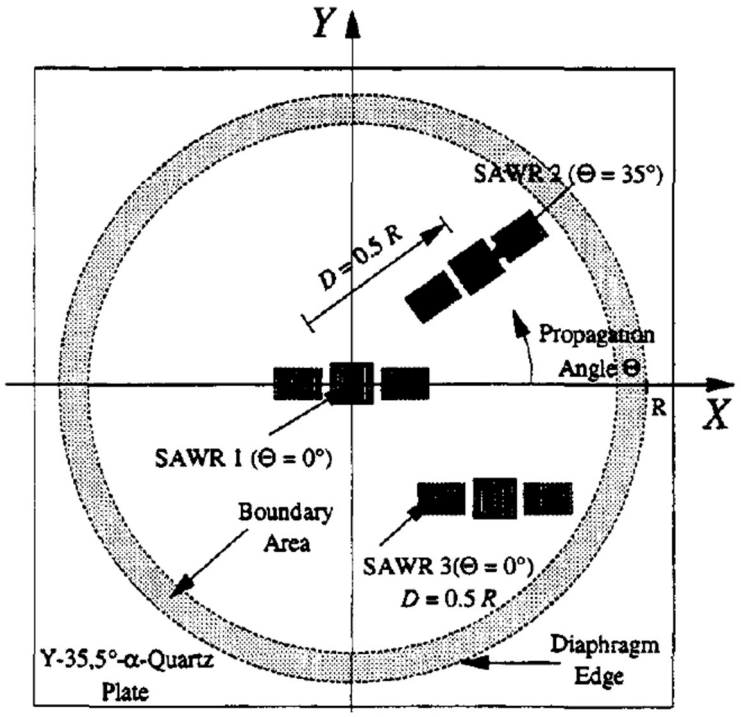

Figure 5.4 The layout of the Buff pressure sensor plate identifying the location of the three SAWR sensors used for pressure and temperature sensing [81].

on the quartz plate due to applied pressure will be different for the two sensors. This causes the differential frequency to be pressure dependent only, assuming that they are both at the same temperature. For temperature sensing, an additional SAWR device (SAWR 2 in Figure 5.4) was fabricated along a different orientation, and thus has a different sensitivity to temperature and pressure than SAWR 1 and SAWR 3. By taking the differential frequency of SAWR 2 and SAWR 1 and using calibrated curves for the differential frequency measured for different pressure values from 0 bar to 10 bar, temperature can be extracted once the pressure is known [16].

Figure 5.5 shows a cross section of the Buff pressure and temperature sensor diaphragm mounted in the brass fixture used for sensor calibration. The three SAWR sensors were wirelessly interrogated for these tests. Figure 5.6 shows the measured change in resonant frequency due to applied pressure for SAWR 1 and SAWR 3, illustrating that the two SAWR devices have different sensitivities to applied pressure. Pressure sensing was performed between room temperature and 60°C.

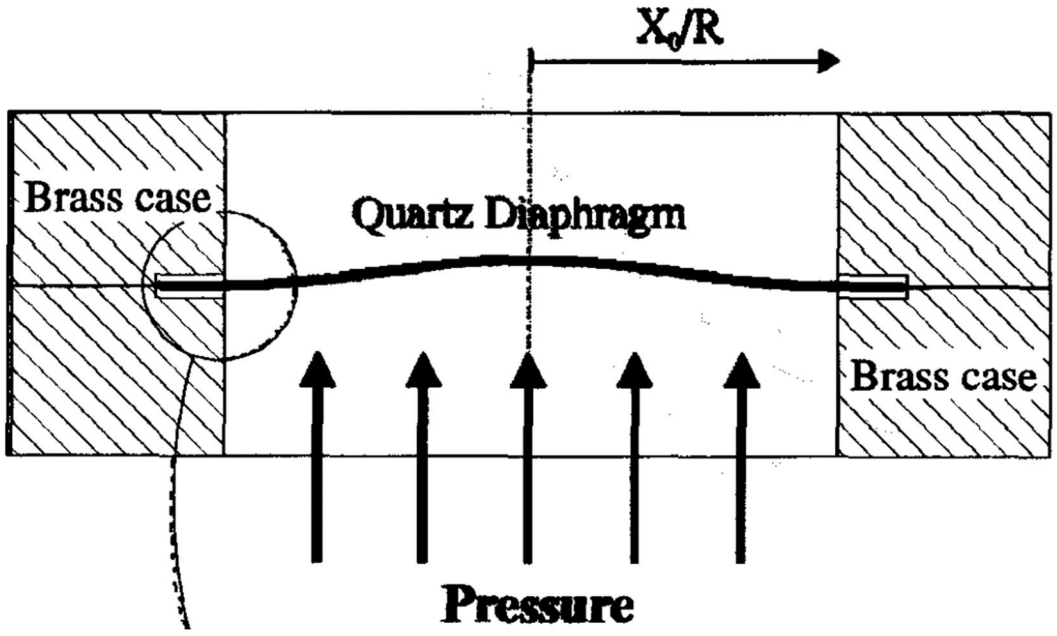

Figure 5.5 A cross-section of the quartz diaphragm setup used by Buff *et al.* for pressure and temperature sensing [81].

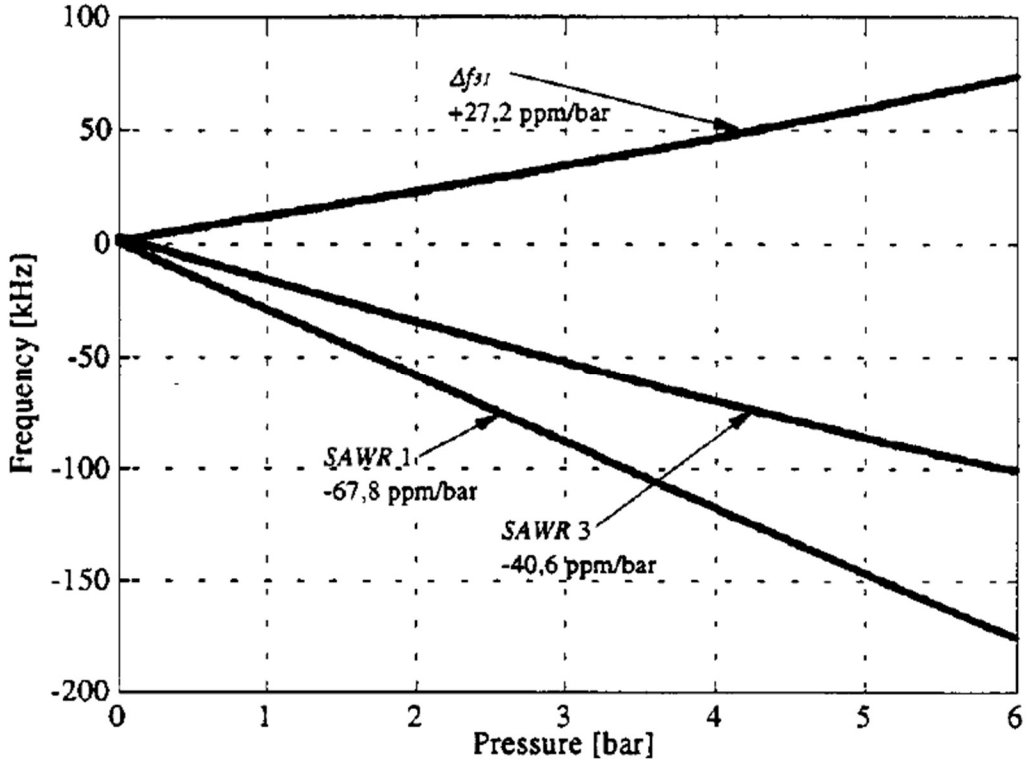

Figure 5.6 The SAWR resonant frequency change vs. pressure for SAWR 1, SAWR 3, and the differential frequency of SAWR1 and SAWR 3 for pressures from 0 bar to 6 bar [81].

When analyzing Buff's method of extracting pressure and temperature for dynamic strain sensing, the main mechanism in removing the temperature response from the pressure response is the phenomenon where two sensors have the same temperature dependence but are being exposed to different strain magnitudes when pressure is applied. For dynamic strain sensing, a structure like a diaphragm for pressure sensing is not appropriate. Therefore, Buff's method for extracting temperature and pressure is not suitable for extracting temperature and dynamic strain.

5.2 Extraction of Dynamic Strain and Temperature Using a Single SAWR Sensor

For the dynamic strain measurements performed at the University of Maine, the dynamic strain magnitude and spectral components are determined measuring the change in the center peak and the strain-induced sidelobes that appear in the SAWR power spectrum of the SAWR sensor, as discussed in Section 3.5.2. This means that the dynamic strain is not directly measured by the

SAWR resonant frequency but is measured by the difference in amplitude between the modulated signal and resonating frequency of the SAWR. Because of this, the resonant frequency variation can be used to extract temperature alone.

In this work, a method of determining the temperature and dynamic strain magnitude and spectral components using the power spectrum of a single SAWR sensor was developed [75]. All measurements were done using the experimental setup described in Figure 3.8. Figure 5.7a shows an image of the measured SAWR power spectrum at 200°C under a dynamic strain excitation of 18με at frequency f_{DS} = 500Hz. In this plot, the frequency of the center peak, f_{CP}, is the RF excitation frequency from the RF generator set to 321.17MHz, which corresponds to the unstrained SAWR resonant frequency, f_0, at 200°C, $f_{0,200°C}$. The sidelobes in the power spectrum measured by the VSA and shown in Figure 5.7a, are the result of the dynamic strain load applied to the beam where the SAWR sensor was mounted. Therefore, the spectral component(s) of the dynamic strain at $\pm f_{DS}$ relative to f_{CP} are obtained by measuring the frequency of the sidelobe peak(s) relative to f_{CP}. For

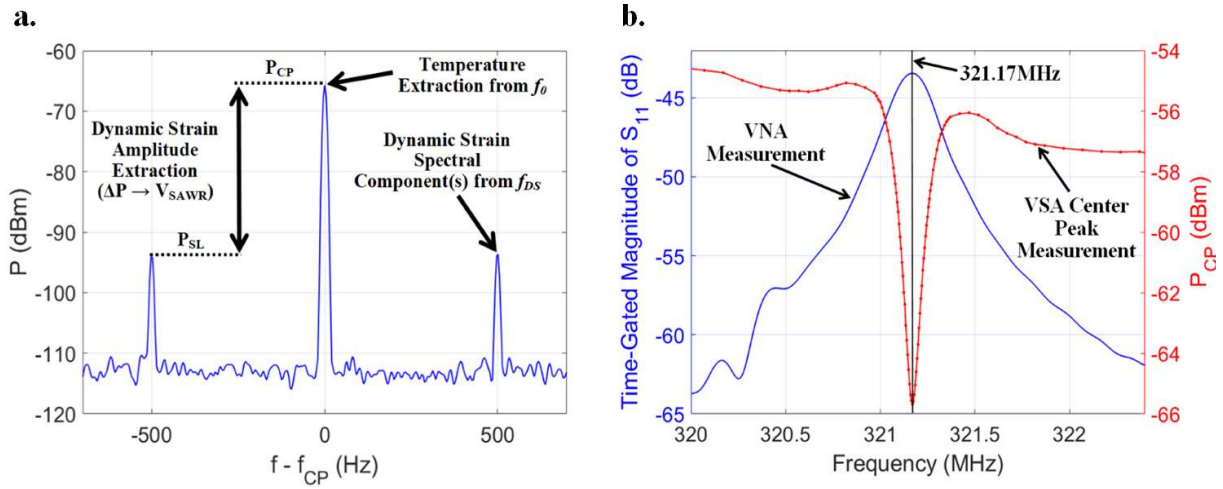

Figure 5.7 (a) The power spectrum of the SAWR under a 500Hz dynamic strain excitation of 18με at 200°C where $f_{CP} = f_{0,200°C}$ = 321.17MHz *[75]*. The techniques for obtaining dynamic strain magnitude, spectral components, and temperature are indicated on the graph. (b) Time-gated magnitude of S_{11} at 200°C measured by a VNA (blue curve) plotted with P_{CP} taken at 200°C for f_{CP} varying from 320.0MHZ – 322.4MHz (red curve) [75].

the SAWR excited at $f_{CP} = f_{0,200°C}$, the power of the positive and negative sidelobes are the same. Finally, the magnitude of the dynamic strain is determined from the power spectrum measurement using Equation 3.1.

Extraction of the SAWR operational temperature, T_{OP}, from the processed signal of the SAWR from the VSA utilizes the resonant peak, P_{CP}, at $f_{CP} = f_0$. Figure 5.7b shows P_{CP} swept over a f_{CP} range from 320.0 MHz to 322.4 MHz at 200°C (red curve) under the dynamic strain excitation of 18με. The VSA signal processed data identifies that the frequency at which P_{CP} is at a minimum is f_0, as can be seen from the comparison with the time-gated magnitude of S_{11} at the unstrained SAWR resonant frequency taken by a Copper Mountain Technologies R60 VNA (blue curve). The time-gated VNA measurement in Figure 5.7b from 0.56μs–6μs identifies the SAWR resonant frequency at 321.17 MHz. These measurements were repeated at RT, 100°C, and 150°C, which is shown in Figure 5.8. Figure 5.8a shows the SAWR resonant frequency measurements measured by the VNA and VSA normalized to $f_{0,RT} = 321.69$ MHz and Figure 5.8b shows the frequency difference between the two methods of measuring the SAWR resonant frequency. Based on the data obtained, the VSA measurement is consistent with the VNA measurement within 7 kHz. The quadratic fit for the VNA measurement was found to be:

$$\Delta f = -0.0184T^2 + 1.24T - 16.4\ (kHz) \tag{5.1}$$

and the quadratic fit for the VSA measurement was found to be:

$$\Delta f = -0.0191T^2 + 1.44T - 21.5\ (kHz) \tag{5.2}$$

For these temperature calibrations, any frequency variation due to static strain from the drive arm was neglected.

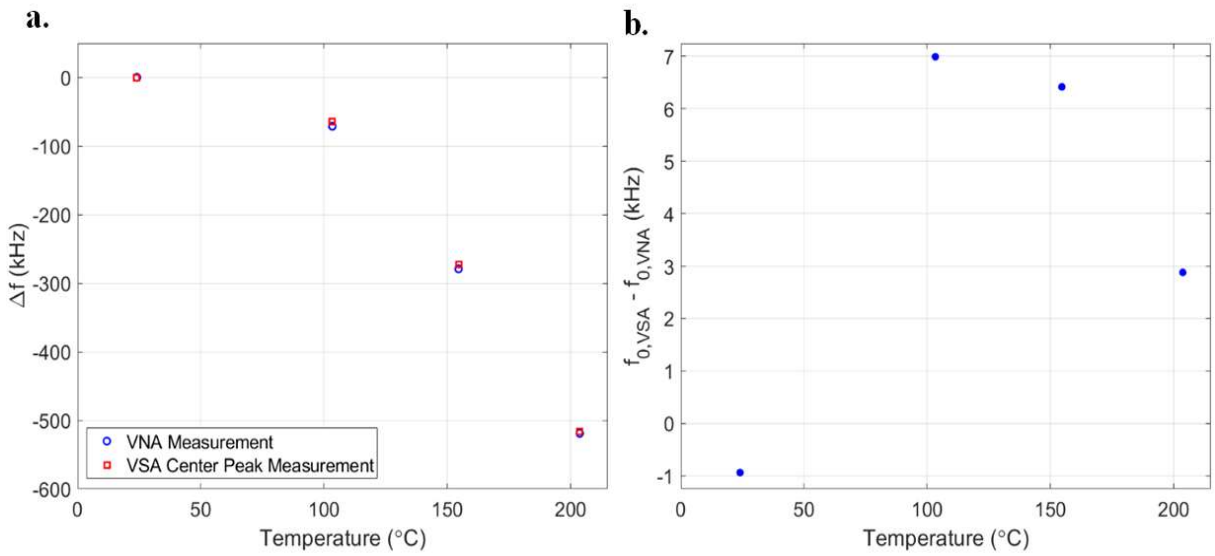

Figure 5.8 (a) The SAWR resonant frequency measured by the VNA (blue) and the VSA center peak measurement (red) at room temperature, 100°C, 150°C, and 200°C. (b) The difference between the VSA measured resonant frequency and the VNA measured resonant frequency.

From the data presented in Figure 5.8, the error in the VSA temperature measurement was calculated using Equation 5.1. The equivalent difference in the calculated temperature ($T_{VSA} - T_{VNA}$) was found to be 1.5°C, 3.1°C, 1.4°C, and 0.4°C at room temperature, 100°C, 150°C, and 200°C, respectively. Although more research needs to be done on how precise the temperature needs to be for each calibration curve, it is likely that temperature errors less than 5°C will not cause a significant variation between the dynamic strain magnitude calculated from the calibration curve and the true dynamic strain being measured.

Therefore, in order to determine T_{OP} in a temperature varying environment, the measurement of f_0 is translated into T_{OP} using the proper calibration curve while dynamic strain is being applied to the SAWR sensor. In this way, both temperature and dynamic strain can be extracted from a single SAWR sensor that is rigidly attached to the part being measured.

5.3 Use of the Center Peak as the Reference Amplitude in V_{SAWR} Calculations

While testing this method of extracting temperature and dynamic strain, an improvement was made to the calculation of V_{SAWR} from the SAWR power spectrum. In Equation 3.1, the reference amplitude, P_0, was set to a power close to P_{CP} and held constant for all tests. However, this practice was put into question because of poor correlation in dynamic strain measurements when the excitation frequency was set exactly on the resonant frequency of the SAWR sensor. Therefore, a test was performed comparing the correlation of using a constant P_0 and $P_0 = P_{CP}$ using the same dataset. The results from this test are shown in Figure 5.9. The sensitivity calculated from the linear fit for the results calculated using P_0 = -80dBm is 0.515μV/με with a correlation coefficient of 0.9568 and the sensitivity calculated from the linear fit for the results calculated using $P_0 = P_{CP}$ is 0.447μV/με with a correlation coefficient of 0.9995. Based on the results, there

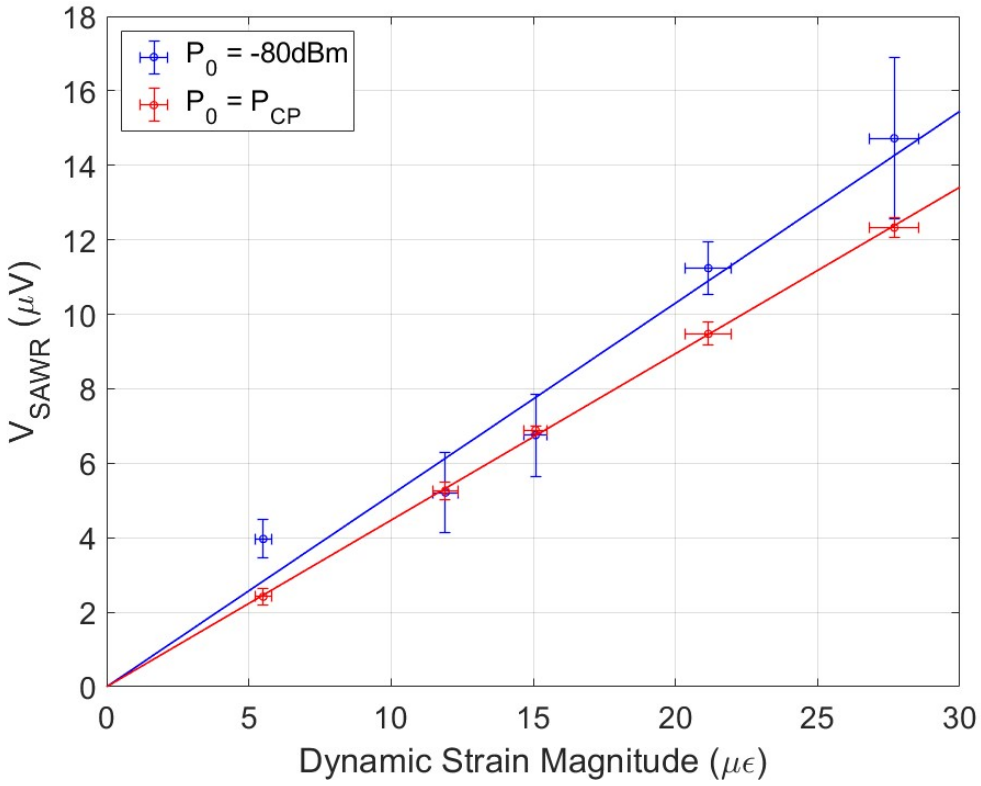

Figure 5.9 The calibration curves obtained using P_0 = -80dBm (blue) and $P_0 = P_{CP}$ (red) for the same dynamic strain test.

is a clear improvement in correlation when setting P_0 to P_{CP} rather than a single value that is close to P_{CP}. Therefore, this method of calculating V_{SAWR} is the better method for the analysis of the dynamic strain measurements.

5.4 Temperature and Dynamic Strain Calibration Curves

5.4.1 SAWR Temperature Calibration Curve

In order to extract the sensor operational temperature utilizing the SAWR power spectrum measurement described in Section 5.2, a SAWR temperature calibration curve must be obtained. The temperature calibration shown in Figure 5.8a and the quadratic fit in Equation 5.1 in Section 5.3 can be used as the temperature calibration curve for this SAWR sensor. Once f_0 is measured by tracking the center peak on the VSA, the operating temperature of the SAWR can be determined using Equation 5.1. This temperature information is then used to determine the correct dynamic strain calibration curve to extract the dynamic strain magnitude from the V_{SAWR}, which is calculated by Equation 3.1 from the power spectrum measurement.

5.4.2 SAWR Dynamic Strain Response

Because the SAWR sensitivity to the dynamic strain magnitude is temperature dependent, dynamic strain calibration curves need to be taken at many temperatures throughout the SAWR sensor operational range. Figure 5.10 shows the SAWR dynamic strain magnitude calibration curves at room temperature, 125°C, 160°C and 200°C for dynamic strain magnitudes up to 40με. The dynamic strain magnitude slopes with respect to V_{SAWR} for RT, 125°C, 160°C and 200°C are 2.52με/μV, 3.21με/μV, 4.35με/μV, and 15.8με/μV, respectively. Therefore, using the procedure detailed in Section 5.2, once the SAWR T_{OP} is determined from finding the frequency at which P_{CP} is at a minimum, the proper dynamic strain calibration curve, such as the ones shown in Figure 5.10, can be used to extract the dynamic strain magnitude from the measured P_{SL} and P_{CP}.

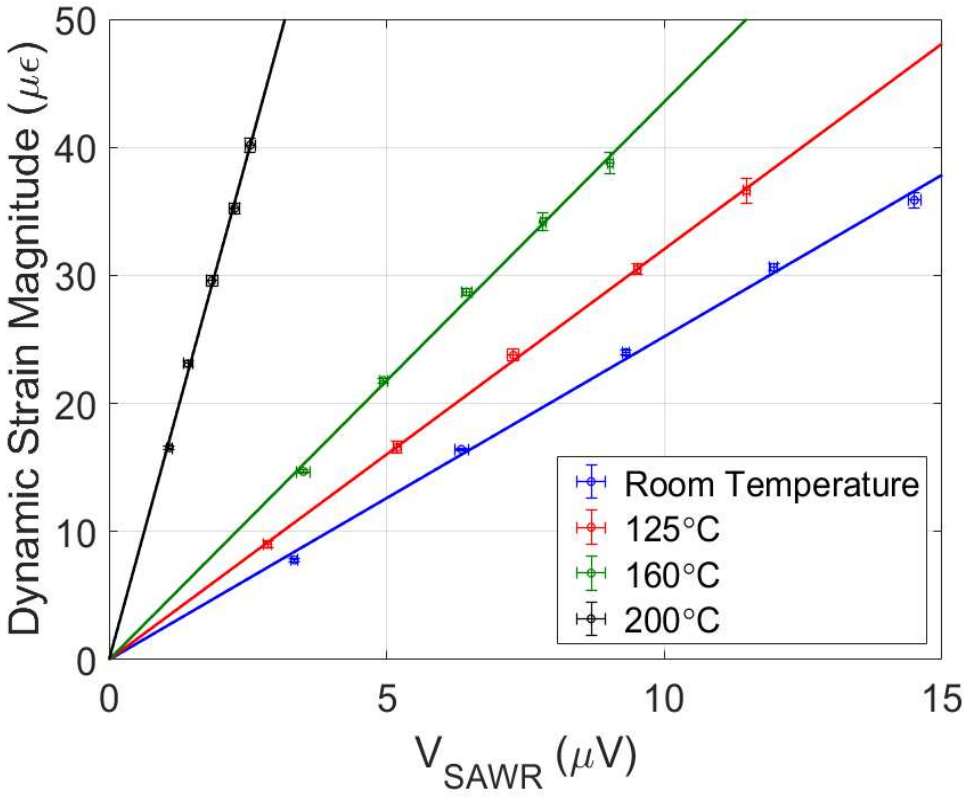

Figure 5.10 The SAWR dynamic strain magnitude calibration curves at room temperature, 125°C, 160°C, and 200°C [75].

However, more work needs to be done to determine how many calibration curves are needed over the temperature range of the SAWR sensor. Finally, the spectral components of the dynamic strain load can be directly extracted from the SAWR spectral power measurement, as shown in Figure 5.7a.

5.5 Conclusions

In this chapter, a method to extract temperature, dynamic strain magnitude, and spectral components of a system based on the spectral power measurement of a single SAWR was identified and discussed. Determination of the SAWR resonant frequency from P_{CP} is utilized to determine the operational temperature of the SAWR sensor. This information is critical to select which dynamic strain curve to use, since the SAWR response to the dynamic strain magnitude is temperature dependent. The dynamic strain magnitude is determined by the measurement of the

dynamic strain induced sidelobe amplitude(s) with respect to the SAWR resonant frequency magnitude. In addition, the dynamic strain spectral component(s) are directly read from the spectral power measurement by measuring the sidelobe frequency relative to the center peak frequency. In addition, it was also determined that when calculating V_{SAWR}, it is better to use the center peak power measured for each measurement, that is $P_{CP} = P_0$ rather than an arbitrary power close to the center peak power for all measurements based on the improvement in the correlation of the data using the center peak power

The SAWR measurement technique disclosed is attractive for dynamic strain measurements in industrial applications, in particular at HT, due to the simplicity, small wireless sensor size, wireless operation, and the significant feature of obtaining the extraction of temperature, dynamic strain magnitude, and dynamic strain spectral components using a single SAWR sensor.

CHAPTER 6
CONCLUSIONS

The work in this thesis revolved around the study, design, and characterization of SAWR static and dynamic strain sensors. Simulation of the thermal and mechanical strain for the static strain setup was done in COMSOL Multiphysics to locate regions of high strain and to determine alternat adhesive shaping methods to reduce the thermal strain at the adhesive/LGS borders and within the adhesive. Wireless interrogation and packaging of the SAWR static and dynamic strain sensors was implemented at high temperature. It was found that the SAWR sensitivity to dynamic strain decreased after temperature cycling up to 425°C due to failure at the adhesive/LGS interface and within the adhesive. Based on this result, investigation into new adhesives for sensing at 200°C after temperature cycling was done for static and dynamic strain sensing. Lastly, a method for extracting temperature, dynamic strain magnitude, and dynamic strain spectral components was developed using a single SAWR sensor.

6.1 Conclusions and Summary of Work

Chapter 2 presented the COMSOL simulations of the static strain setup under thermal strain up to 400°C and mechanical strain caused by a static load of 800g on the beam. The COMSOL simulation results were consistent with the Abaqus simulation results for a mechanical load on the static strain beam at 25°C, 300°C, and 400°C, thus confirming the accuracy of the COMSOL model. Simulation of the beam, adhesive (covering the entire bottom interface of the LGS), and LGS model at 400°C showed that there is high strain near the borders of the LGS chip, which is likely the weakest part of the sensor because of dicing. Simulations of the beam under a mechanical load show that the mechanical strain experienced by the Inconel/adhesive/LGS stack is much lower than the strain due to thermal expansion and should not be considered the primary cause of

attachment failure in static situations. The use of adhesive shaping that reduces the adhesion surface area on the LGS and Inconel reduces the maximum strain at the LGS/adhesive interface and removes the maximum strain location from the LGS borders, but it increases the strain magnitude at the Inconel/adhesive interface and reduces the strain transferred to the LGS. These factors must be considered for determination of the best method of mounting the SAWR sensor. The SAWR sensors in this work were mounted with the adhesive covering the entire bottom interface of the sensor.

Chapter 3 discusses the implementation of wireless interrogation of SAWR static and dynamic strain sensors at high temperature. Inductive coupling wireless interrogation methods provide the required signal strength to measure SAWR static and dynamic strain sensors up to 400°C. For static strain, the effect of the adhesive layer thickness was studied, and it was shown that there is a trade-off between a thinner adhesive layer, which provides a higher SAWR sensitivity to static strain, and maximum operational temperature. Wirelessly interrogated SAWR dynamic strain measurements were performed up to 400°C for dynamic strain magnitudes up to 32.6με. A clear signal (approximately 5dB above noise level) was observed for dynamic strain magnitudes as low as 10με at 400°C.

Chapter 4 implemented temperature cycling to the SAWR static and dynamic strain sensor setups to analyze the stability of the strain sensors implemented. After temperature cycling to 425°C, the dynamic strain response decreased to noise level at 400°C. After further temperature cycling tests with LGS pieces mounted on Inconel using Aremco 668, it was determined that there was cracking at the LGS/adhesive interface, likely originating at the borders of the LGS chip, which is the weakest part of the sensor, and within the adhesive. Since commercial ceramic adhesives considered do not provide stability at 400°C, different commercial adhesives were tested

up to 200°C for dynamic strain sensing. Based on initial heating and static strain tests, Aremco 805 and Duralco 4461 were chosen for high temperature static strain stability testing with temperature cycling. Both epoxies showed stability in the static strain measurements after two rounds of temperature cycling. Duralco 4461 was chosen for dynamic strain stability testing because it showed a lower standard deviation in static strain measurements. After two rounds of temperature cycling, Duralco 4461 did not show stability at room temperature or 200°C. The experimental setup was analyzed for inconsistencies, and it was identified that lack of removing the drive arm while heating and cooling the sensor could be contributing to the instability as it can affect how the adhesive transfers strain as it heats and cools.

Chapter 5 discusses methods of extracting temperature and static/dynamic strain in a variable temperature environment. For static strain, it is possible to have a SAWR temperature sensor that slides on the surface of the part being measured, thus only measuring the temperature. The differential frequency between this sensor and a SAWR strain sensor rigidly attached to the part can be used to calculate the static strain magnitude. For dynamic strain, it is not possible to utilize a sensor that slides on the surface of the part because the SAWR would still measure vibration caused by the dynamic strain, which would contribute to the SAWR temperature response. Therefore, a method to extract temperature and dynamic strain is needed. Because measurement of dynamic strain utilized the strain-induced sidelobes in the power spectrum rather than the direct measurement of the SAWR resonant frequency, this method does not rely on taking differential frequency of two sensors. It was determined that temperature and dynamic strain can be extracted using a single SAWR sensor. Tracking the resonant frequency of the device gives the temperature and analyzing the strain-induced sidelobes gives the dynamic strain magnitude and spectral components.

6.2 Statement of Contribution

The contributions of this thesis are discussed in the bullets below:

- Modeling in COMSOL Multiphysics was done to observe the thermal and mechanical strain experienced by the SAWR sensor. It was determined that there are high concentrations of strain along the borders of the LGS, which is the weakest part of the sensor chip.
- Reducing the surface area of the adhesion layer reduces the strain at the LGS/adhesive interface and removes the high strain locations from the borders of the LGS but increases the strain at the Inconel/adhesive interface and reduces the amount of strain transferred from the part to the sensor.
- Wireless interrogation of SAWR static and dynamic strain sensors was performed using near-field inductive coupling techniques. It was confirmed that this wireless interrogation technique provides the necessary SAWR signal for both static and dynamic strain measurements at 400°C.
- Identified that there is cracking at the LGS/adhesive interface after the SAWR sensor mounted to Inconel 625 using the Aremco 668 ceramic adhesive was subjected to temperature cycling. This causes a decrease in the SAWR response to noise level for dynamic strain measurements and causes lack of stability in the SAWR static and dynamic strain response.
- Explored multiple high-temperature epoxies for stability in SAWR static and dynamic strain testing while subjecting the sensors to temperature cycling up to 200°C.

- Determined a method for extracting the temperature, dynamic strain magnitude, and dynamic strain spectral components using a single SAWR sensor. This technique utilizes the SAWR power spectrum sidelobes and center peak to extract these measurands.

6.3 Suggested Future Work

Based on the research presented in this thesis, suggested future work for harsh environment static and dynamic strain sensing includes:

- Improve the SAWR strain sensor attachment method so that SAWR attachment to metal parts can be achieved above 400°C with a stable sensor response after temperature cycling.
- Determine whether the vibrational component associated with dynamic strain has additional effects on sensor attachment that are not present for static strain.
- Quantify the error in the SAWR strain measurement and commercial gauge strain measurement used for SAWR calibration to determine the overall precision of both sensors.
- Determine if a stable sensor response is achieved when the sensor is heated to 400°C and held at that temperature for an extended period of time (one week) without prior temperature cycling.
- Implement new wireless interrogation techniques around 300MHz such that the distance between the sensor and interrogating antennas can be increased from 5mm while minimizing the antenna size so that the footprint of the sensor and antenna remains small so that it can be installed in small, hard-to-reach locations.
- Perform static and dynamic strain testing in a high-temperature harsh environment such as a power plant. In addition, automatic data acquisition will be necessary to implement,

especially in a temperature varying environment where the center peak frequency will need to be tracked for dynamic strain measurements.

- Design a SAWR sensor system that is able to wirelessly measure temperature, static strain, and dynamic strain in a temperature varying harsh environment.
- Study the static and dynamic strain responses of different LGS orientations to determine if there is an optimal orientation for static and dynamic strain sensing that provides the highest sensitivity to static and dynamic strain.
- Explore other piezoelectric substrates, such as GPO, LGT, LGN, AlN, and ScAlN and compare with LGS SAWR sensors in terms of static and dynamic strain response and ease of rigid attachment to metal parts.

REFERENCES

[1] S. Basu and A. K. Debnath, Powerplant Instrumentation and Control Handbook, 1st ed. Academic Press, 2014.

[2] E. Keller and A. Ray, "Real-time Health Monitoring of Mechanical Structures," *Structural Helth Monitoring,* vol. 2, no. 3, pp. 191-203, 2003.

[3] M. Abdulkarem, K. Samsudin, F. Z. Rokhani and M. F. A. Rasid, "Wireless sensor network for structural health monitoring: A contemporary review of technologies, challenges, and future direction," *Structural Health Monitoring,* vol. 19, no. 3, pp. 693-735, 2020.

[4] S. Alaswad and Y. Xiang, "A review on condition-based maintenence optimization models for stochastically deteriorating system," *Reliability Engineering and System Safety,* vol. 157, pp. 54-63, 2017.

[5] V. Kalinin, "Wireless physical SAW sensors for automotive applications," *2011 IEEE International Ultrasonics Symposium, IUS,* pp. 212-221, 2011.

[6] M. H. Sahraei, D. McCalden, R. Hughes and L. A. Ricardez-Sandoval, "A survey on current advanced IGCC power plant technologies, sensors and control systems," *Fuel,* vol. 137, pp. 245-259, 2014.

[7] S. Minakuchi and N. Takeda, "Recent Advancement in Optical Fiber Sensing Recent Advancement in Optical Fiber Sensing," *Photonic Sensors,* vol. 3, no. 4, pp. 345-354, 2013.

[8] Y. Javed, M. Mansoor and I. A. Shah, "A review of principles of MEMS pressure sensing with its aerospace applications," *Sensor Review,* vol. 39, no. 5, pp. 652-664, 2019.

[9] Subagyo and G. A. Brooks, "Online Monitoring of Dynamic Slag Behavior in Ladle Metallurgy," *ISIJ International,* vol. 43, no. 8, pp. 1286-1288, 2003.

[10] M. Pereira da Cunha, "Wireless sensing in hostile environments," *2013 IEEE International Ultrasonics Symposium, IUS,* pp. 1337-1346, 2013.

[11] X. Jiang, K. Kim, S. Zhang, J. Johnson and G. Salazar, "High-Temperature Piezoelectric Sensing," *Sensors,* vol. 14, no. 1, pp. 144-169, 2014.

[12] M. Pereira da Cunha, A. Maskay, R. J. Lad, D. Frankel, S. Moulzolf, M. Call and G. Bernhardt, "Pt-Ni / Pt-Zr electrodes for stable SAW resonator operation during repeated temperature cycling up to 1000°C," *2015 IEEE International Ultrasonics Symposium, IUS,* pp. 1-4, 2015.

[13] A. Maskay and M. Pereira da Cunha, "High-temperature static strain langasite SAWR sensor: Temperature compensation and numerical calibration for direct strain reading," *Sensors and Actuators A: Physical,* vol. 259, pp. 34-43, 2017.

[14] D. Leff, A. Maskay and M. Pereira da Cunha, "Wireless Interrogation of High Temperature Surface Acoustic Wave Dynamic Strain Sensor," *2020 IEEE International Ultrasonics Symposium, IUS,* pp. 1-4, 2020.

[15] V. Kalinin, "Calibration of non-contact temperature-compensated SAW resonant torque sensors," *2011 Joint Conference of the IEEE International Frequency Control and the European Frequency and Time Forum (FCS) Proceedings,* pp. 1-6, 2011.

[16] W. Buff, "Passive remote sensing for temperature and Passive remote sensing for temperature and pressure using SAW resonator devices," *IEEE Transactions on Ultrasonics, Ferroelectrics, and Frequency Control ,* vol. 45, no. 5, pp. 1388-1398, 1998.

[17] A. Ayes, P. Ohodnicki, R. J. Lad and M. Pereira da Cunha, "Enhanced Hydrogen Gas Detection Using SAW Sensor Through Oxygen Pre-Treatment," *2019 IEEE International Ultrasonics Symposium, IUS,* 2019.

[18] S. Nalley and A. LaRose, "International Energy Outlook 2021," U.S. Energy Information Administration, 6 October 2021. [Online]. Available: https://www.eia.gov/outlooks/ieo/pdf/IEO2021_ReleasePresentation.pdf. [Accessed 28 October 2022].

[19] R. Fachberger and A. Erlacher, "Applications of wireless SAW sensing in the steel industry," *Procedia Engineering,* vol. 5, pp. 224-227, 2010.

[20] X. Xu, G. A. Brooks and W. Yang, "Online Analysis of Stirring Processes in Ladle Metallurgy," *Metallurgical and Materials Transactions B,* vol. 41B, pp. 1025-1032, 2010.

[21] J. Yenus, G. Brooks and M. Dunn, "Multivariate Analysis of Ladle Vibration," *Metallurgical and Materials Transactions B,* vol. 47, pp. 2681-2689, 2016.

[22] S. Bhattacharya, A. K. Agarwal, O. Prakash and S. Singh, Sensors for Automotive and Aerospace Applications, Springer, 2018.

[23] M. Pereira da Cunha, R. J. Lad, T. Moonlight, S. Moulzolf, A. Canabal, R. B. P. M. Davulis, D. Frankel, G. Bernhardt, T. Pollard and D. F. McCann, "Recent Advances in Harsh Environment Acoustic Wave Sensors for Contemporary Applications," *2011 IEEE SENSORS,* pp. 614-617, 2011.

[24] P. Mohankumar, J. Ajayan, R. Yasodharan, P. Devendran and R. Sambasivam, "A review of micromachined sensors for automotive applications," *Measurement,* vol. 140, pp. 305-322, 2019.

[25] D. P. Morgan, "Surface acoustic wave devices and applications: 1. Introductory review," *Ultrasonics,* vol. 11, no. 3, pp. 121-131, 1973.

[26] B. Liu, X. Chen, H. Cai, M. A. Mohammad, X. Tian, L. Tao, Y. Yang and T. Ren, "Surface acoustic wave devices for sensor applications," *Journal of Semiconductors,* vol. 37, no. 2, pp. 1-9, 2016.

[27] H. Hallil, C. Dejous, S. Hage-Ali, O. Elmazria, J. Rossignol, D. Stuerga, A. Talbi, A. Mazzamurro, P.-Y. Joubert and E. Lefeuvre, "Passive resonant sensors: trends and future prospects," *IEEE Sensors Journal,* vol. 21, no. 11, pp. 12618-12632, 2021.

[28] D. P. Morgan, Surface-Wave Devices for Signal Processing, New York: Elsevier Science Publishing Company, 1991.

[29] E. Benes, M. Gröschl, W. Burger and M. Schmid, "Sensors based on piezoelectric resonators," *Sensors and Actuators A: Physical,* vol. 48, no. 1, pp. 1-21, 1995.

[30] W. Soluch, "Scattering Matrix Approach to One-Port SAW Resonators," *IEEE Transactions on Ultrasonics, Ferroelectrics, and Frequency Control,* vol. 47, no. 6, pp. 1615-1618, 2000.

[31] L. Shu, B. Peng, Z. Yang, R. Wang, S. Deng and X. Liu, "High-Temperature SAW Wireless Strain Sensor with Langasite," *Sensors,* vol. 15, no. 11, pp. 28531-28542, 2015.

[32] A. Maskay, "Microwave Acoustic SAW Resonators for Stable High-temperature Harsh-Environment Static and Dynamic Strain Sensing Applications," Ph. D. Thesis. University of Maine, 2018.

[33] A. Maskay, D. Hummels and M. Pereira da Cunha, "In-Phase and Quadrature Analysis for Amplitude and Frequency Modulations Due to Vibrations on a Surface-Acoustic-Wave Resonator," *IEEE Transactions on Ultrasonics, Ferroelectrics, and Frequency Control,* vol. 66, no. 1, pp. 91-100, 2019.

[34] A. Maskay, D. Hummels and M. Pereira da Cunha, "Separation of Frequency and Amplitude Modulation Contributions Due to External Vibration on a SAW Resonator," *2018 IEEE International Ultrasonics Symposium, IUS,* pp. 1-3, 2018.

[35] H. Zu, H. Wu and Q.-M. Wang, "High-Temperature Piezoelectric Crystals for Acoustic Wave Sensor Applications," *IEEE Transactions on Ultrasonics, Ferroelectrics, and Frequency Control,* vol. 63, no. 3, pp. 486-505, 2016.

[36] D. Damjanovic, "Materials for high temperature piezoelectric transducers," *Current Opinion in Solid State and Materials Science,* vol. 3, no. 5, pp. 469-473, 1998.

[37] S. Zhang and F. Yu, "Piezoelectric Materials for High Temperature Sensors," *Journal of the American Ceramic Society,* vol. 94, no. 10, pp. 3153-3170, 2011.

[38] V. Giurgiutiu, B. Xu and W. Liu, "Development and Testing of High-temperature Piezoelectric Wafer Active Sensors for Extreme Environments," *Structural Health Monitoring,* vol. 9, no. 6, pp. 513-525, 2010.

[39] S. A. Zhgoon, A. S. Shvetsov, S. A. Sakharov and O. Elmazria, "High-Temperature SAW Resonator Sensors: Electrode Design Specifics," *IEEE Transactions on Ultrasonics, Ferroelectrics, and Frequency Control,* vol. 65, no. 4, pp. 657-664, 2018.

[40] M. Gillinger, T. Knobloch, A. Marković, G. Pfusterschmied, M. Schneider and U. Schmid, "Performance of thin AlxOy, SixNy and AlN passivation layers for high temperature SAW device applications," *Materials Science in Semiconductor Processing,* vol. 81, pp. 1-6, 2018.

[41] M. Greenslit, M. Pereira da Cunha and R. J. Lad, "Plasma-Assisted Epitaxy of Piezoelectric $Sc_xAl_{1-x}N$ Films on Sapphire for Use in Harsh-Environment Microwave Acoustic Sensors," *Journal of Electronic Materials,* vol. 51, pp. 1473-1480, 2022.

[42] J. Hornsteiner, E. Born, G. Fischerauer and E. Riha, "Surface acoustic wave sensors for high-temperature applications," *Proceedings of the 1998 IEEE International Frequency Control Symposium,* pp. 615-620, 1998.

[43] A. Ayes, G. Bernhardt and M. Pereira da Cunha, "Removal of Stress Hillocks from Platinum-Alumina Electrodes Used in High-temperature SAW Devices," *2019 IEEE International Ultrasonics Symposium, IUS,* pp. 727-730, 2019.

[44] D. Richter, S. Sakharov, E. Forsén, E. Mayerd, L. Reindl and H. Fritze, "Thin Film Electrodes for High Temperature Surface Acoustic Wave Devices," *Procedia Engineering,* vol. 25, pp. 168-171, 2011.

[45] H. Jehn, "High temperature behaviour of platinum group metals in oxidizing atmospheres," *Journal of the Less Common Metals,* vol. 100, pp. 321-339, 1984.

[46] M. Pereira da Cunha, T. Moonlight, R. J. Lad, D. Frankel and G. Bernhardt, "High Temperature Sensing Technology for Applications Up To 1000°C," *SENSORS, 2008 IEEE,* pp. 752-755, 2008.

[47] M. Pereira da Cunha, R. J. Lad, T. Moonlight, G. Bernhardt and D. J. Frankel, "High Temperature Stability ofLangasite Surface Acoustic Wave Devices," *2008 IEEE Ultrasonics Symposium, ,* pp. 205-208, 2008.

[48] D. J. Frankel, S. C. Moulzolf, M. Pereira da Cunha and R. J. Lad, "Influence of composition and multilayer architecture on electrical conductivity of high temperature Pt-alloy films," *Surface & Coatings Technology,* vol. 284, pp. 215-221, 2015.

[49] S. C. Moulzolf, D. J. Frankel, M. Pereira da Cunha and R. J. Lad, "High temperature stability of electrically conductive Pt–Rh/ZrO2 and Pt–Rh/HfO2 nanocomposite thin film electrodes," *Microsystems Technologies,* vol. 20, pp. 523-531, 2014.

[50] A. Ayes, "Development and Test of High Temperature Surface Acoustic Wave Gas Sensors," Ph. D. Thesis. University of Maine, 2020.

[51] D. Leff and M. Pereira da Cunha, "Impact of Thermal Stress on Attachment and Stability of High Temperature Strain Sensors," *2021 IEEE International Ultrasonics Symposium, IUS,* pp. 1-4, 2021.

[52] X. Yan, Q. Tan, X. Li, T. Xue and M. Li, "Test and Analysis of SAW High Temperature Strain Sensor based on Langasite," *IEEE Sensors Journal,* 2022.

[53] S. F. Jilani, D. Leff, A. Maskay, R. J. Lad and M. Pereira da Cunha, "Static Strain Modelling, Calibration, and Measurements for High-Temperature Wireless SAW Resonator Operation," *2020 IEEE International Ultrasonics Symposium, IUS,* pp. 1-4, 2020.

[54] J.-F. Lei and H. A.Will, "Thin-film thermocouples and strain-gauge technologies for engine gauge technologies for engine," *Sensors and Actuators A: Physical,* vol. 65, no. 2-3, pp. 187-193, 1998.

[55] "High Temperature Bondable Strain Gages," Hitec Products, Inc., 2022. [Online]. Available: https://hitecprod.com/products/high-temperature-bondable/. [Accessed 1 June 2022].

[56] "High Temperature Bondable Strain Gages," Hitec Products, Inc., 2022. [Online]. Available: https://hitecprod.com/products/high-temperature-weldable/. [Accessed 1 June 2022].

[57] "Micro-Measurements Product Catalog: Foil Gauges," Micro-Measurements, 2022. [Online]. Available: https://micro-measurements.com/pca/special-use-gages/high_temp_foil. [Accessed 1 June 2022].

[58] J. Purbolaksono, J. Ahmad, L. C. Beng, A. Z. Rashid, A. Khinania and A. Ali, "Failure analysis on a primary superheater tube of a power plant," *Engineering Failure Analysis,* vol. 17, no. 1, pp. 158-167, 2010.

[59] F. Dehnavi, A. Eslami and F. Ashrafizadeh, "A case study on failure of superheater tubes in an industrial power plant," *Engineering Failure Analysis,* vol. 80, pp. 368-377, 2017.

[60] J. K. Sahota, N. Gupta and D. Dhawan, "Fiber Bragg grating sensors for monitoring of physical parameters: a comprehensive review," *Optical Engineering,* vol. 59, no. 6, 2020.

[61] C. E. Campanella, A. Cuccovillo, C. Campanella, A. Yurt and V. M. N. Passaro, "Fibre Bragg Grating Based Strain Sensors: Review of Technology and Applications," *Sensors,* vol. 18, no. 9, 2018.

[62] P. Ferraro and G. D. Natale, "On the possible use of optical fiber Bragg gratings as strain sensors for geodynamical monitoring," *Optics and Lasers in Engineering,* vol. 37, no. 2-3, pp. 115-130, 2002.

[63] A. Masoudi and T. P. Newson, "Contributed Review: Distributed optical fibre dynamic strain sensing," *Review of Scientific Instruments ,* vol. 87, p. 011501, 2016.

[64] C. Chen, X.-Y. Zhang, Y.-S. Yu, W.-H. Wei, Q. Guo, L. Qin, Y.-Q. Ning, L.-J. Wang and H.-B. Sun, "Femtosecond Laser-Inscribed High-Order Bragg Gratings in Large-Diameter Sapphire Fibers for High-Temperature and Strain Sensing," *Journal of Lightwave Technology,* vol. 36, no. 16, pp. 3302-3308, 2018.

[65] A. Maskay and M. Pereira da Cunha, "High-temperature microwave acoustic vibration sensor," *2018 IEEE International Ultrasonics Symposium, IUS,* 2018.

[66] R. Stoney, G. E. O'Donnell and D. Geraghty, "Dynamic wireless passive strain measurement in CNC turning using surface acoustic wave sensors," *International Journal of Advanced Manufacturing Technology,* vol. 69, pp. 1421-1430, 2013.

[67] "High Temperature Ceramic: Technical Bulletin A2-S1," Aremco Products, Inc., May 2020. [Online]. Available: https://www.aremco.com/wp-content/uploads/2020/07/A02_S1_20.pdf. [Accessed 5 October 2022].

[68] M. Vable, Mechanics of Materials, Oxford University Press, 2002.

[69] *Inconel alloy 625,* Special Metals Corporation, 2013.

[70] D. C. Malocha, M. Pereira da Cunha, E. Adler, R. C. Smythe, S. Frederick, M. Chou, R. Helmbold and Y. S. Zhou, "Recent measurements of material constants versus temperature for langatate, langanite and langasite," *Proceedings of the 2000 IEEE/EIA International Frequency Control Symposium and Exhibition,* pp. 200-205, 2000.

[71] S. C. Moulzof, R. Behanan, T. Pollard, R. J. Lad and M. Pereira da Cunha, "Capacitively coupled IDT for high temperature SAW devices," *2013 IEEE International Ultrasonics Symposium (IuS),* pp. 255-258, 2013.

[72] N. F. Aiken, "VHF Near Field Antenna Design for Wireless Sensing Applications in Harsh Environments," Honors Thesis. University of Maine, 2019.

[73] A. Maskay, A. Ayes, R. J. Lad and M. Pereira da Cunha, "Stability of Pt/Al2O3-Based Electrode Langasite SAW Sensors with Al2O3 Capping Layer and Yittria-Stabilized Zirconia Sensing Layer," *2017 IEEE International Ultrasonics Symposium (IUS),* pp. 1-4, 2017.

[74] "Customizable, 2800ºF Adhesives," Cotronics Corp., [Online]. Available: https://www.cotronics.com/vo/cotr/pdf/31%20-%20940%20Series.pdf. [Accessed 5 October 2022].

[75] D. Leff, S. Winters and M. Pereira da Cunha, "Temperature and Dynamic Strain Measurements Using a Single SAWR Sensor," *2022 IEEE International Ultrasonics Symposium (IUS),* pp. 1-4, 2022.

[76] "High Performance Epoxies: Technical Bulletin A7," Aremco Products, Inc., October 2021. [Online]. Available: https://www.aremco.com/wp-content/uploads/2021/09/A07_21.pdf. [Accessed 5 October 2022].

[77] "Unique Metallic Adhesives and Putties," Cotronics Corp., [Online]. Available: https://www.cotronics.com/vo/cotr/pdf/952.4.pdf. [Accessed 5 October 2022].

[78] "500°F Electrically Resistant Epoxy," Cotronics Corp., [Online]. Available: https://www.cotronics.com/vo/cotr/pdf/05%20-%204525%204525IP%20F.pdf. [Accessed 5 October 2022].

[79] "500°F Room Temp Curing, Low Viscosity Epoxy," Cortonics Corp., [Online]. Available: https://www.cotronics.com/vo/cotr/pdf/07%20-%204461%20%204461IP.pdf. [Accessed 5 October 2022].

[80] V. Kalinin, G. Brown and A. Leigh, "Contactless Torque and Temperature Sensor Based on SAW Resonators," *2006 IEEE Ultrasonics Symposium,* pp. 1490-1493, 2006.

[81] W. Buff, M. Goroll, S. Klett, M. Rusko, M. Binhack and J. Ehrenpfordt, "Wireless Passive Remote Sensing with Saw Resonators and a New Solution for Identification Problems in Multiple Sensor Systems," *1999 29th European Microwave Conference,* pp. 391-394, 1999.

[82] "Safety Data Sheet," Micro-Measurements, 5 May 2017. [Online]. Available: https://docs.micro-measurements.com/?id=3044&_ga=2.190192483.957933753.1668267574-404055729.1668267574. [Accessed 12 November 2022].

APPENDICIES

APPENDIX A

X, Y, and Z Strain Components from COMSOL Simulations

The figures shown in Chapter 2 show the strain magnitude from thermal expansion and mechanical load simulations. From these simulations, the x, y, and z components of the strain could also be obtained. These plots are shown in this appendix. Shown below are the x, y, and z strain components same interfaces and simulation conditions analyzed in Chapter 2.

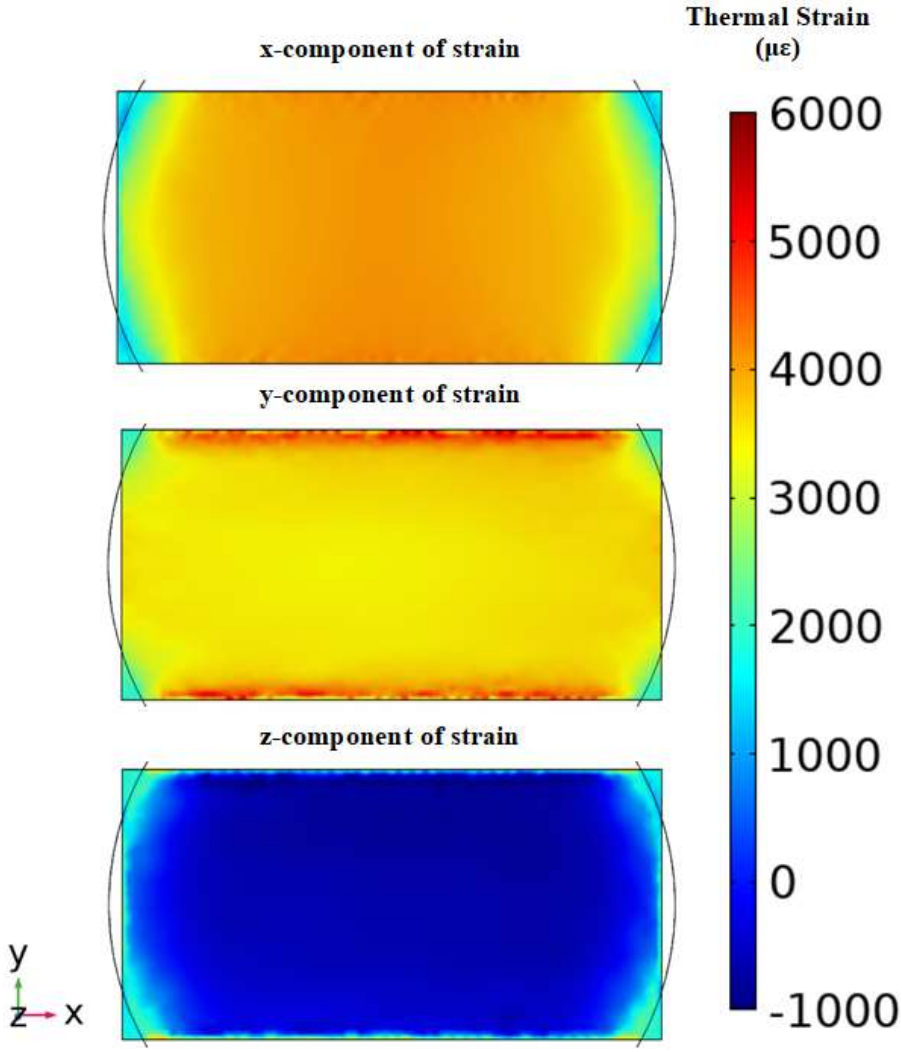

Figure A.1 An X-Y plane cross-section at the LGS/adhesive interface 5nm into the LGS for the FI adhesive mounting scheme displaying the (top) x-component, (middle) y-component, and (bottom) z-component of the thermally induced strain at 400°C under no mechanical load.

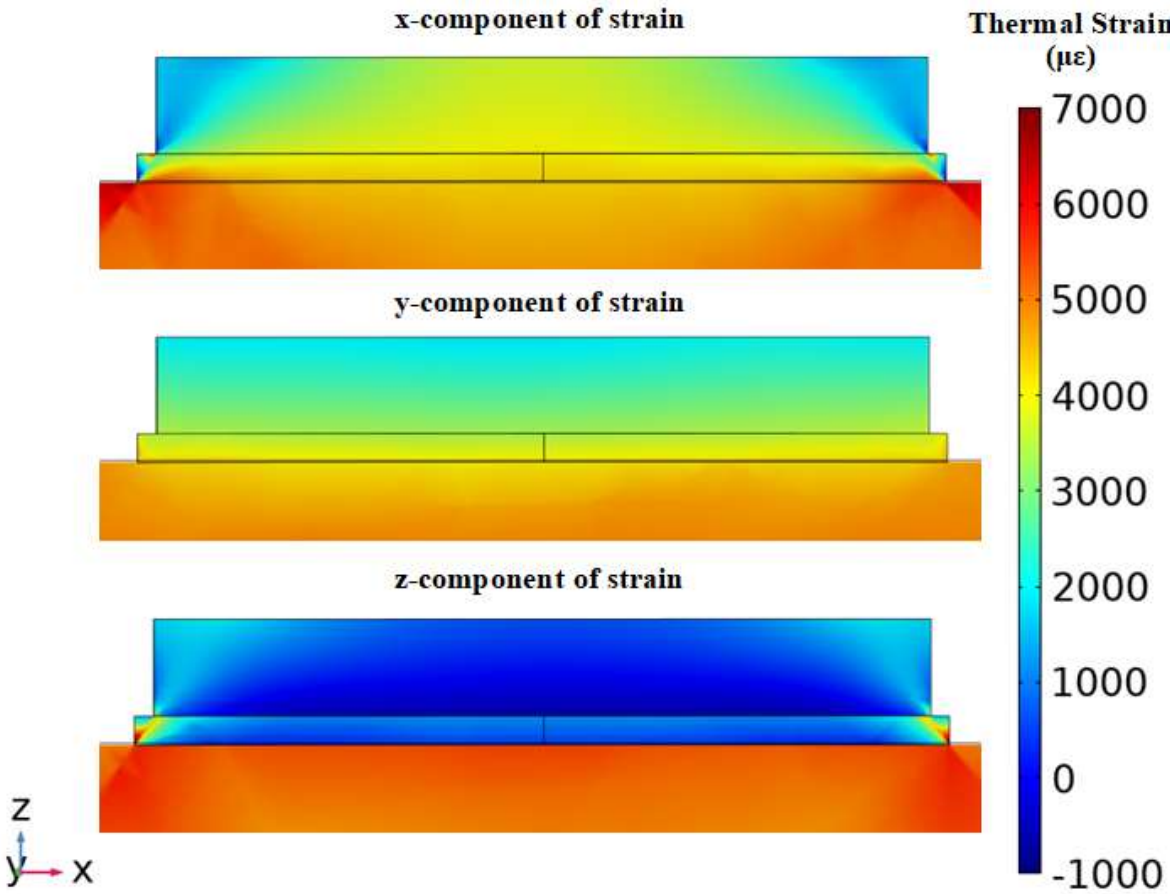

Figure A.2 An X-Z plane cross-section through the LGS, adhesive layer, and Inconel 625 for the FI adhesive mounting scheme displaying the (top) x-component, (middle) y-component, and (bottom) z-component of the thermally induced strain at 400°C under no mechanical load.

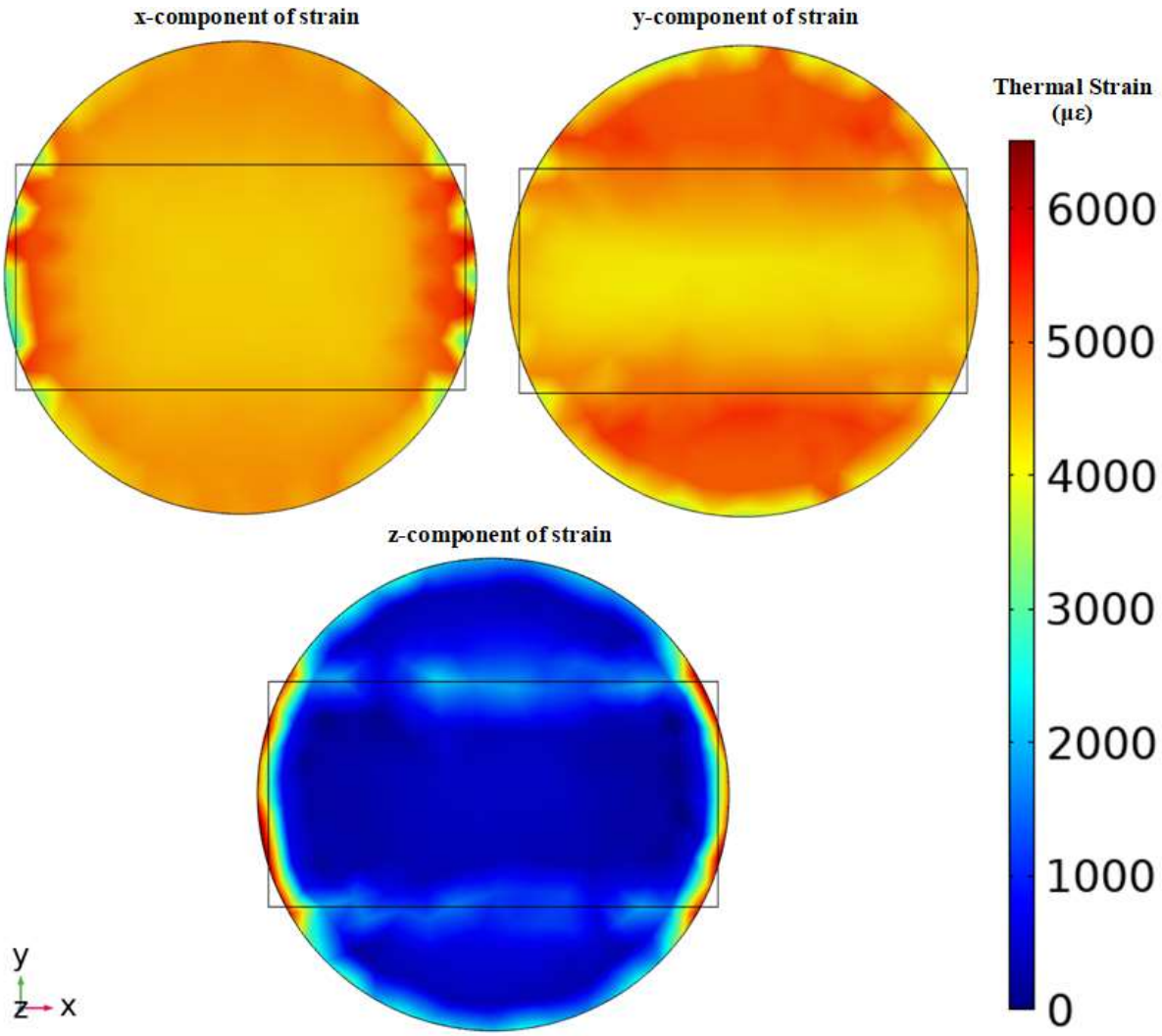

Figure A.3 An X-Y plane cross-section at the Inconel/adhesive interface 5nm into the adhesive for the FI adhesive mounting scheme displaying the (top-left) x-component, (top-right) y-component, and (bottom) z-component of the thermally induced strain at 400°C under no mechanical load.

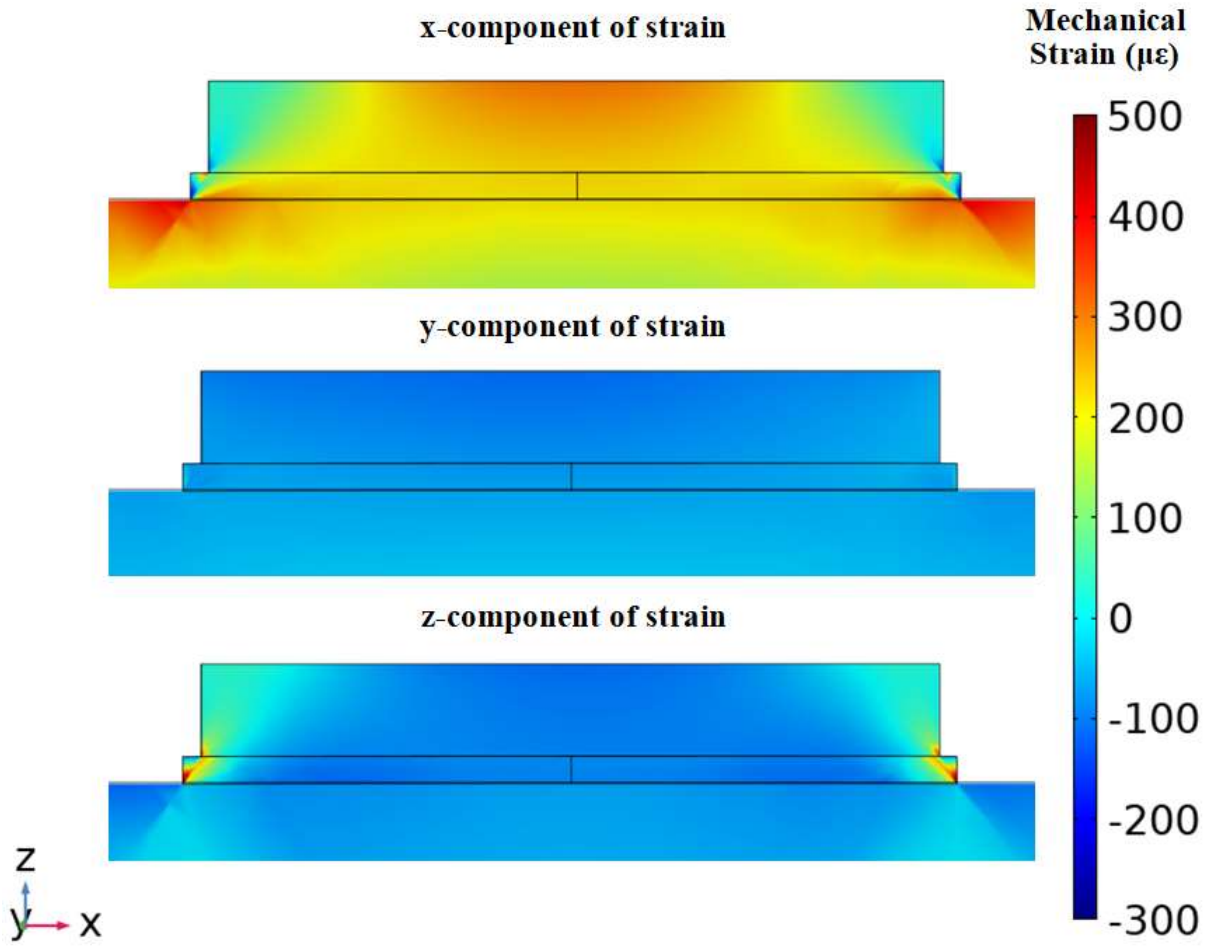

Figure A.4 An X-Z plane cross-section through the LGS, adhesive layer, and Inconel 625 for the FI adhesive mounting scheme displaying the (top) x-component, (middle) y-component, and (bottom) z-component of the mechanical strain under a load of 800g at 25°C.

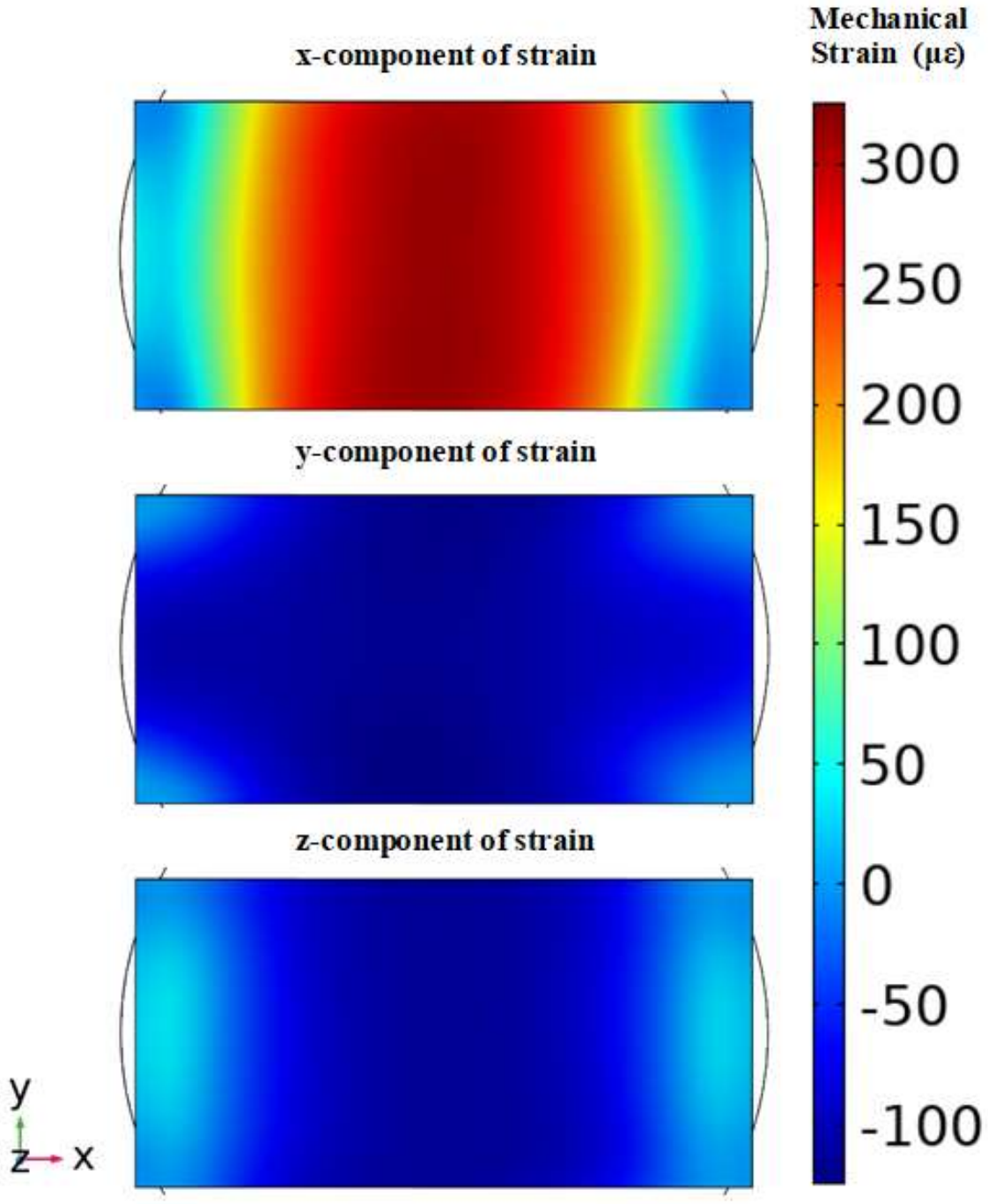

Figure A.5 An X-Y plane cross-section at the LGS top surface for the FI adhesive mounting scheme displaying the (top) x-component, (middle) y-component, and (bottom) z-component of the mechanical strain under a load of 800g at 25°C.

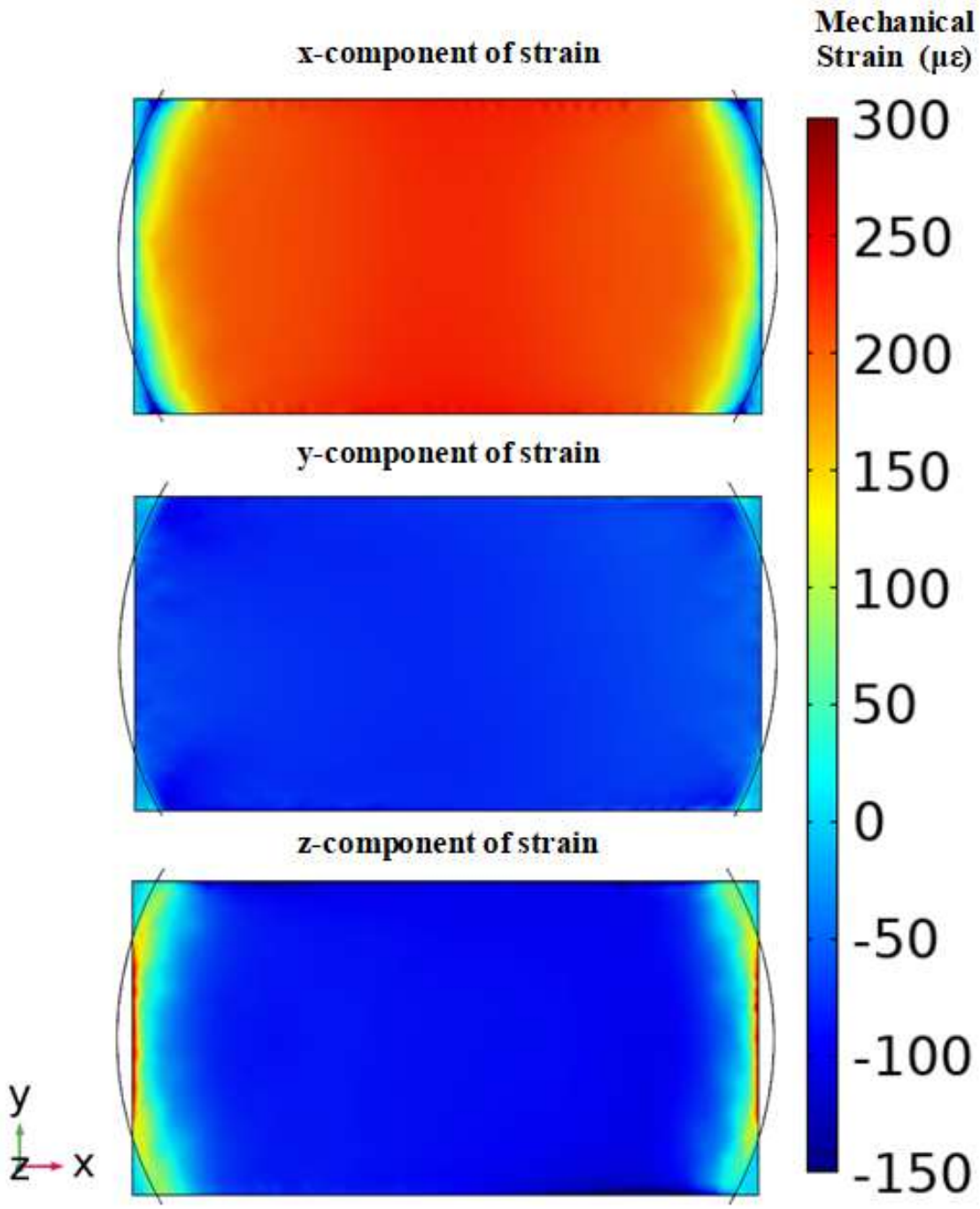

Figure A.6 An X-Y plane cross-section at the LGS/adhesive interface 5nm into the LGS for the FI adhesive mounting scheme displaying the (top) x-component, (middle) y-component, and (bottom) z-component of the mechanical strain under a load of 800g at 25°C.

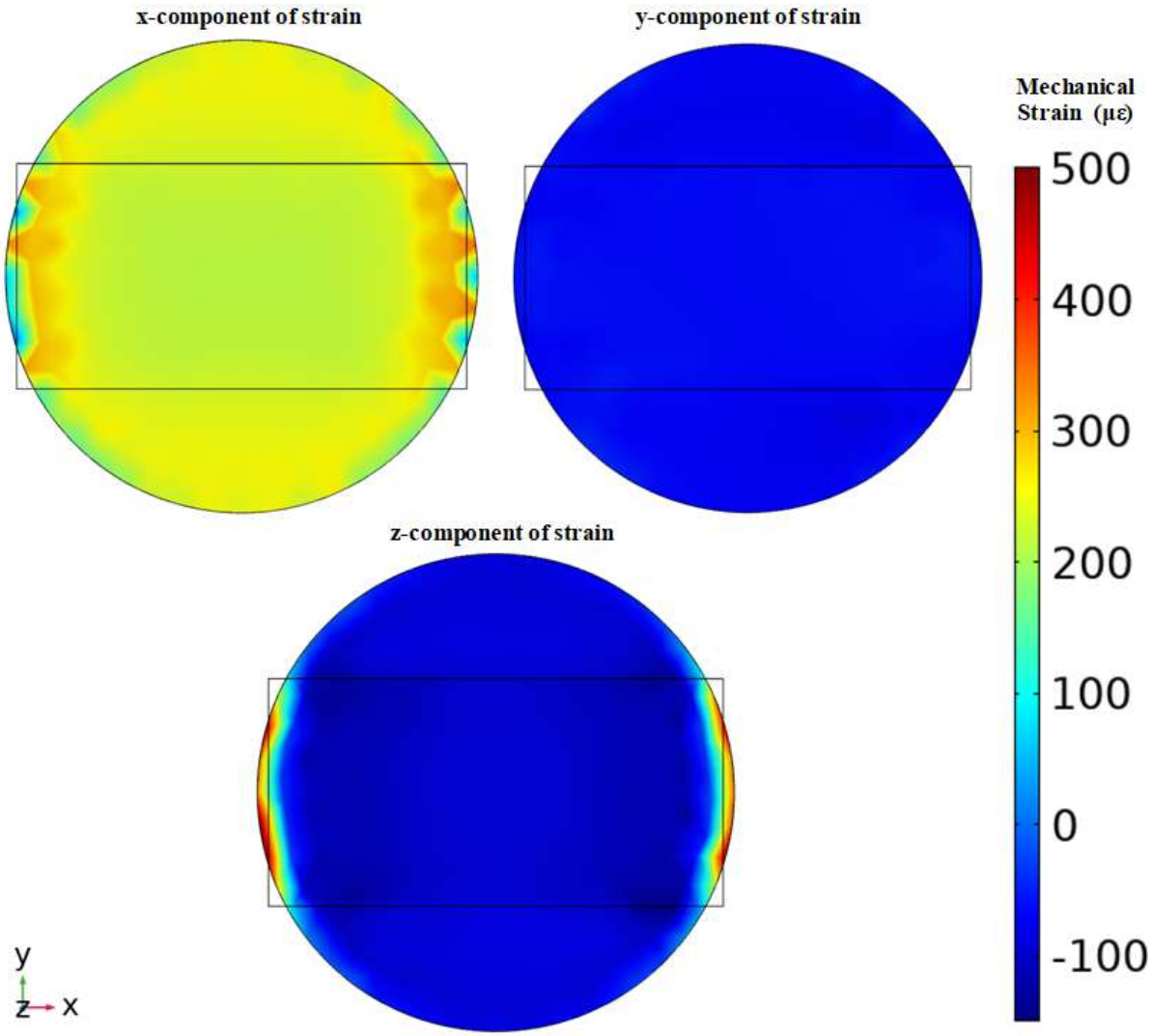

Figure A.7 An X-Y plane cross-section at the Inconel/adhesive interface 5nm into the adhesive for the FI adhesive mounting scheme displaying the (top-left) x-component, (top-right) y-component, and (bottom) z-component of the mechanical strain under a load of 800g at 25°C.

For the simulations done for the dot and triangle adhesive mounting schemes, the strain color scales in figures showing the same cross-section and simulation conditions were set to the same values for ease of comparison (e.g. Figure A.8 and Figure A.15, which show the X-Z cross-section at 400°C for the dot and triangle mounting schemes, respectively, have the same strain color scale).

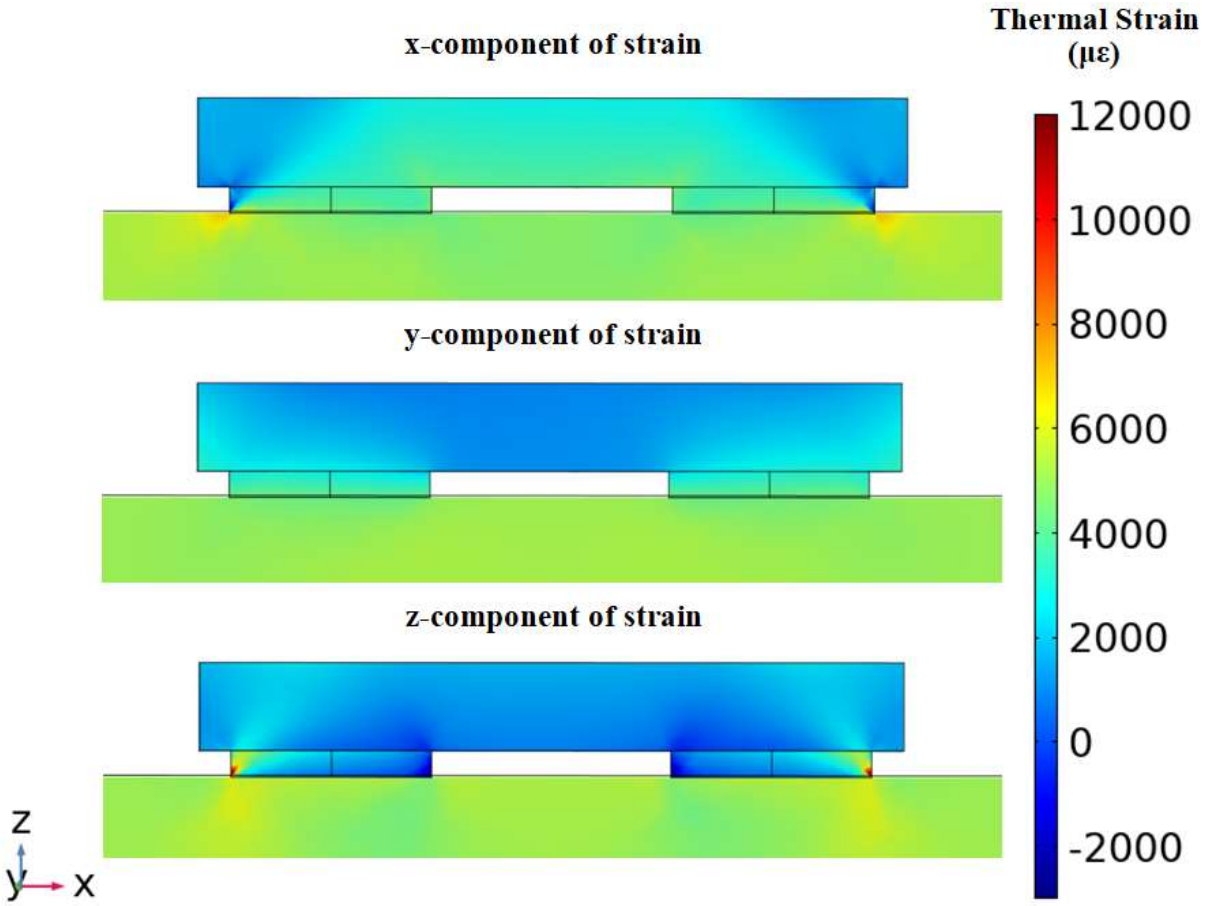

Figure A.8 An X-Z plane cross-section through the LGS, adhesive layer, and Inconel 625 for the dot adhesive mounting scheme displaying the (top) x-component, (middle) y-component, and (bottom) z-component of the thermally induced strain at 400°C under no mechanical load.

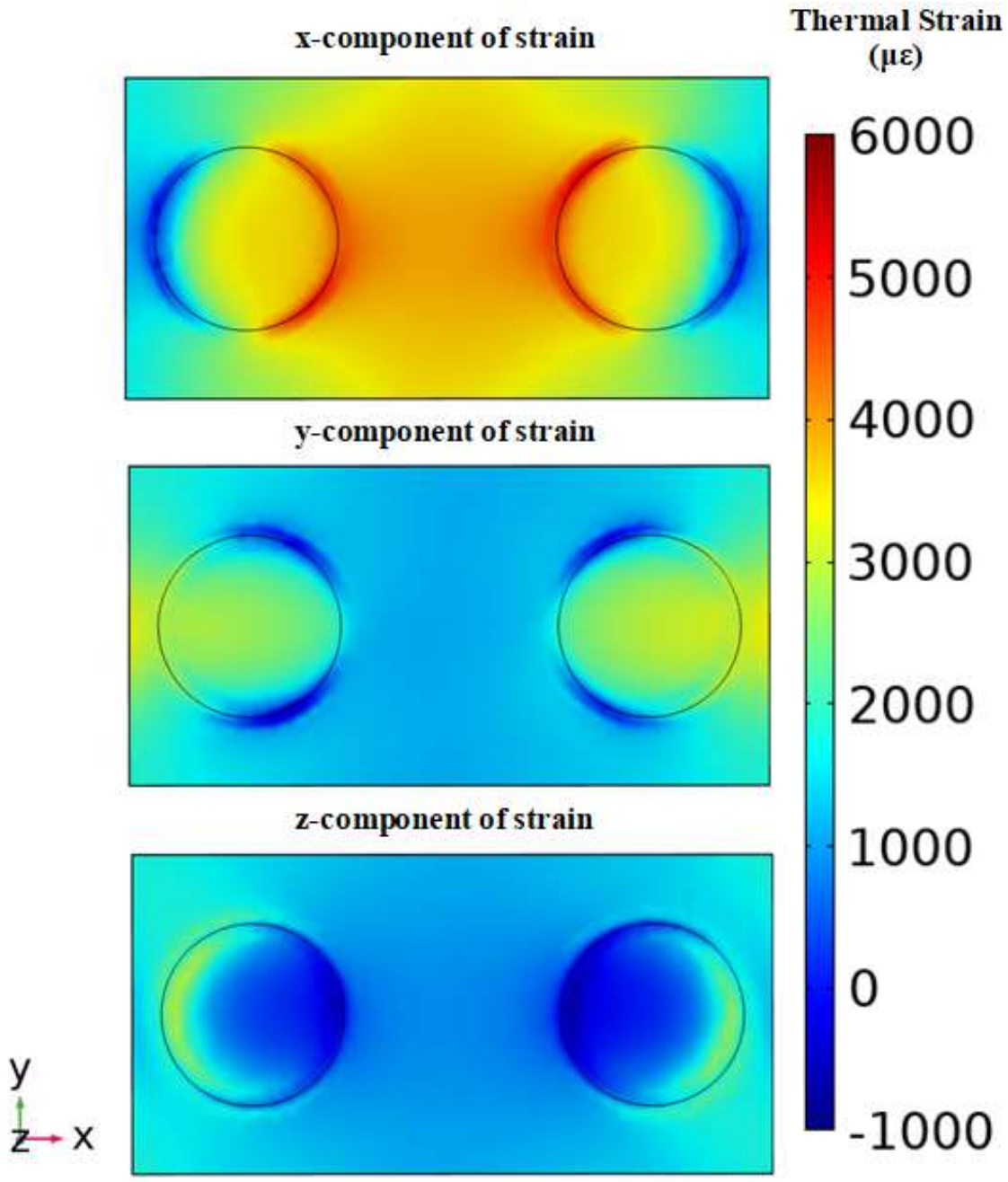

Figure A.9 An X-Y plane cross-section at the LGS/adhesive interface 5nm into the LGS for the dot adhesive mounting scheme displaying the (top) x-component, (middle) y-component, and (bottom) z-component of the thermally induced strain at 400°C under no mechanical load.

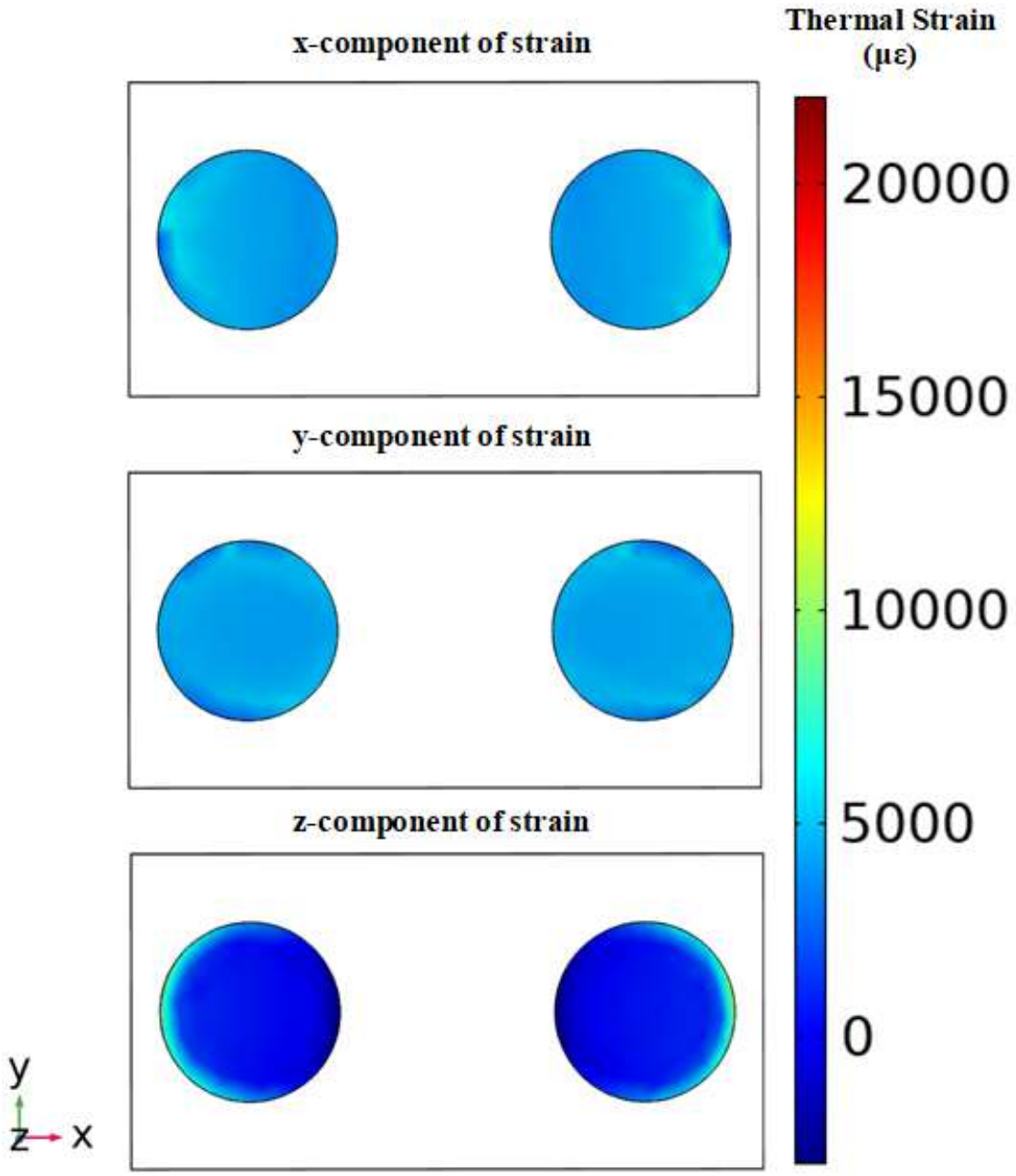

Figure A.10 An X-Y plane cross-section at the Inconel/adhesive interface 5nm into the adhesive for the dot adhesive mounting scheme displaying the (top) x-component, (middle) y-component, and (bottom) z-component of the thermally induced strain at 400°C under no mechanical load.

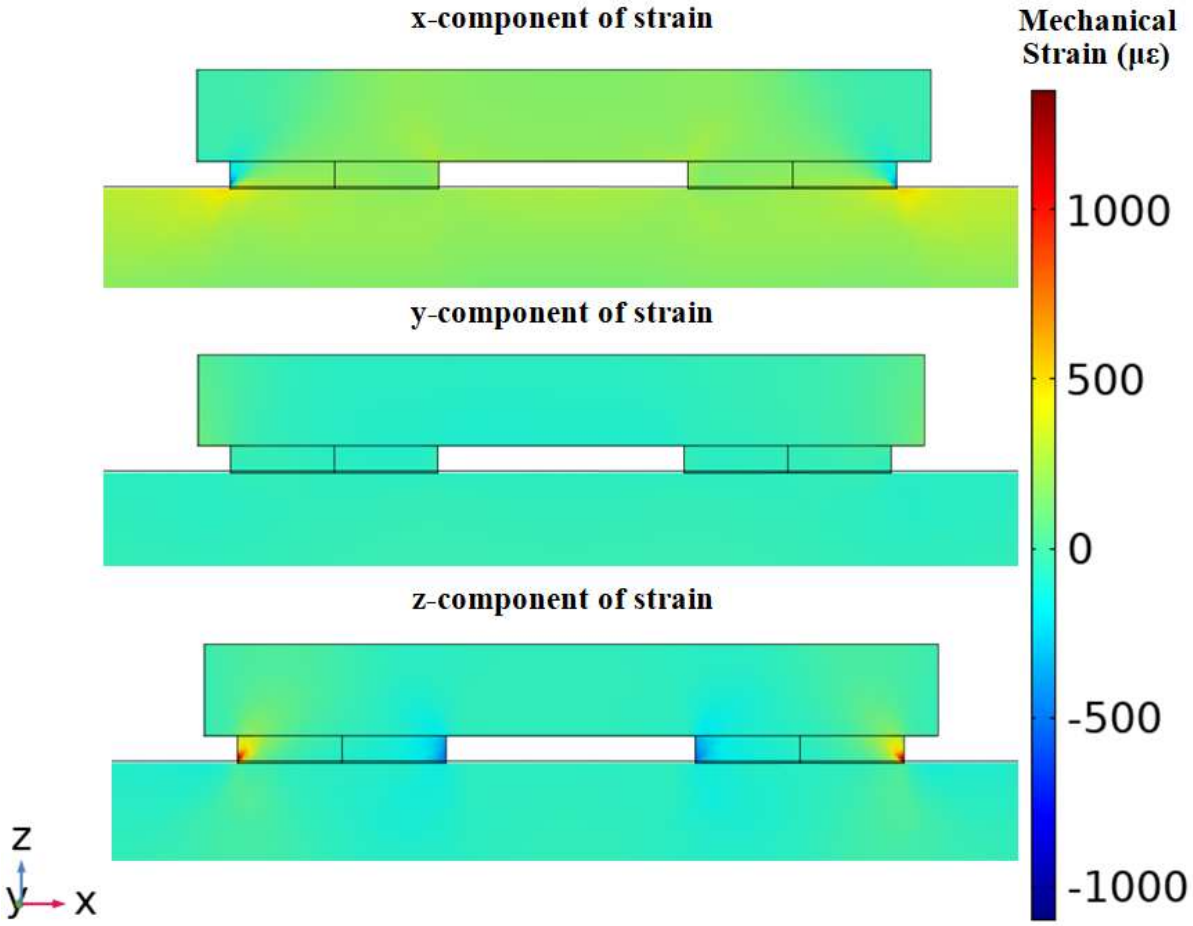

Figure A.11 An X-Z plane cross-section through the LGS, adhesive layer, and Inconel 625 for the dot adhesive mounting scheme displaying the (top) x-component, (middle) y-component, and (bottom) z-component of the mechanical strain under a load of 800g at 25°C.

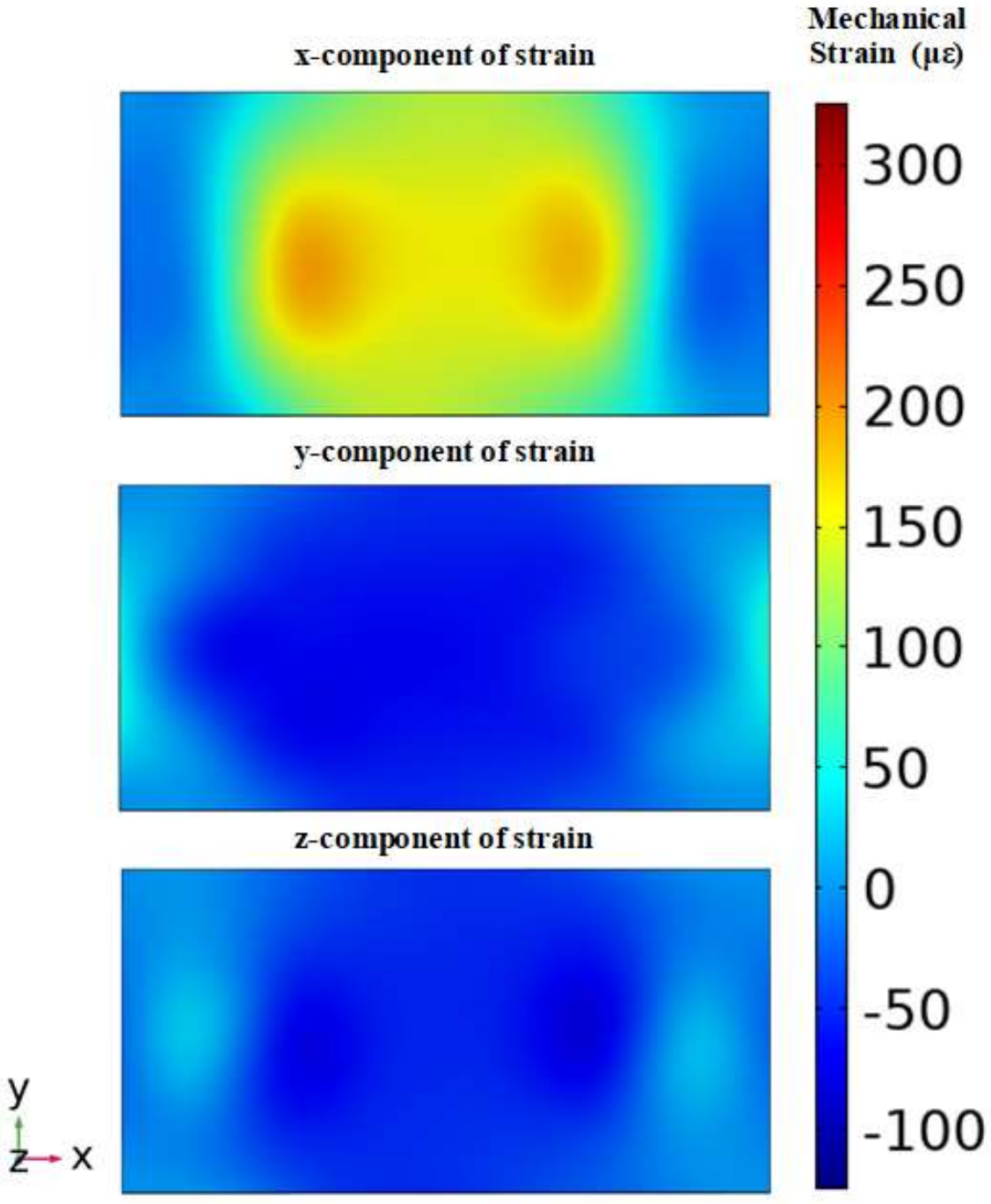

Figure A.12 An X-Y plane cross-section at the LGS top surface for the dot adhesive mounting scheme displaying the (top) x-component, (middle) y-component, and (bottom) z-component of the mechanical strain under a load of 800g at 25°C.

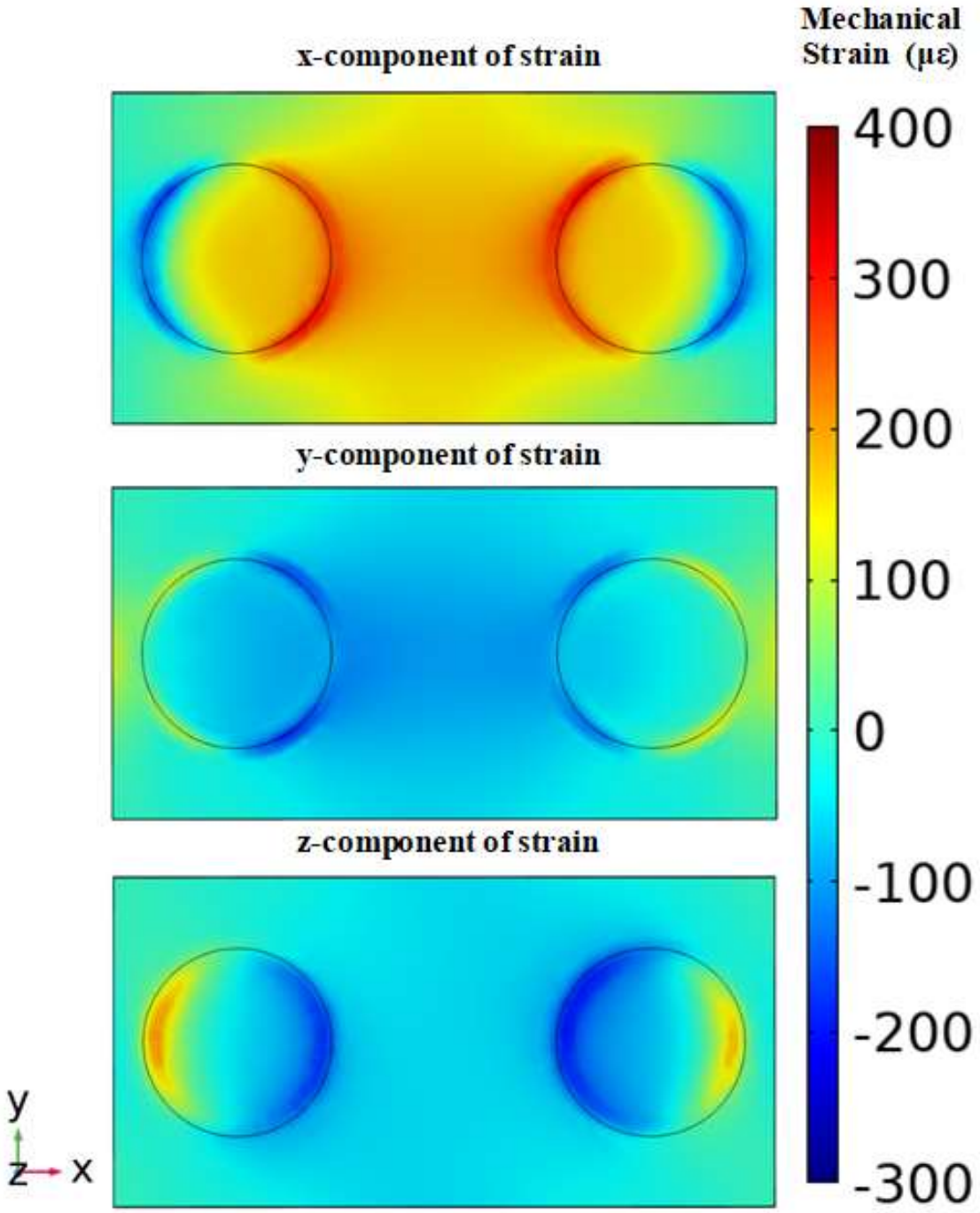

Figure A.13 An X-Y plane cross-section at the LGS/adhesive interface 5nm into the LGS for the dot adhesive mounting scheme displaying the (top) x-component, (middle) y-component, and (bottom) z-component of the mechanical strain under a load of 800g at 25°C.

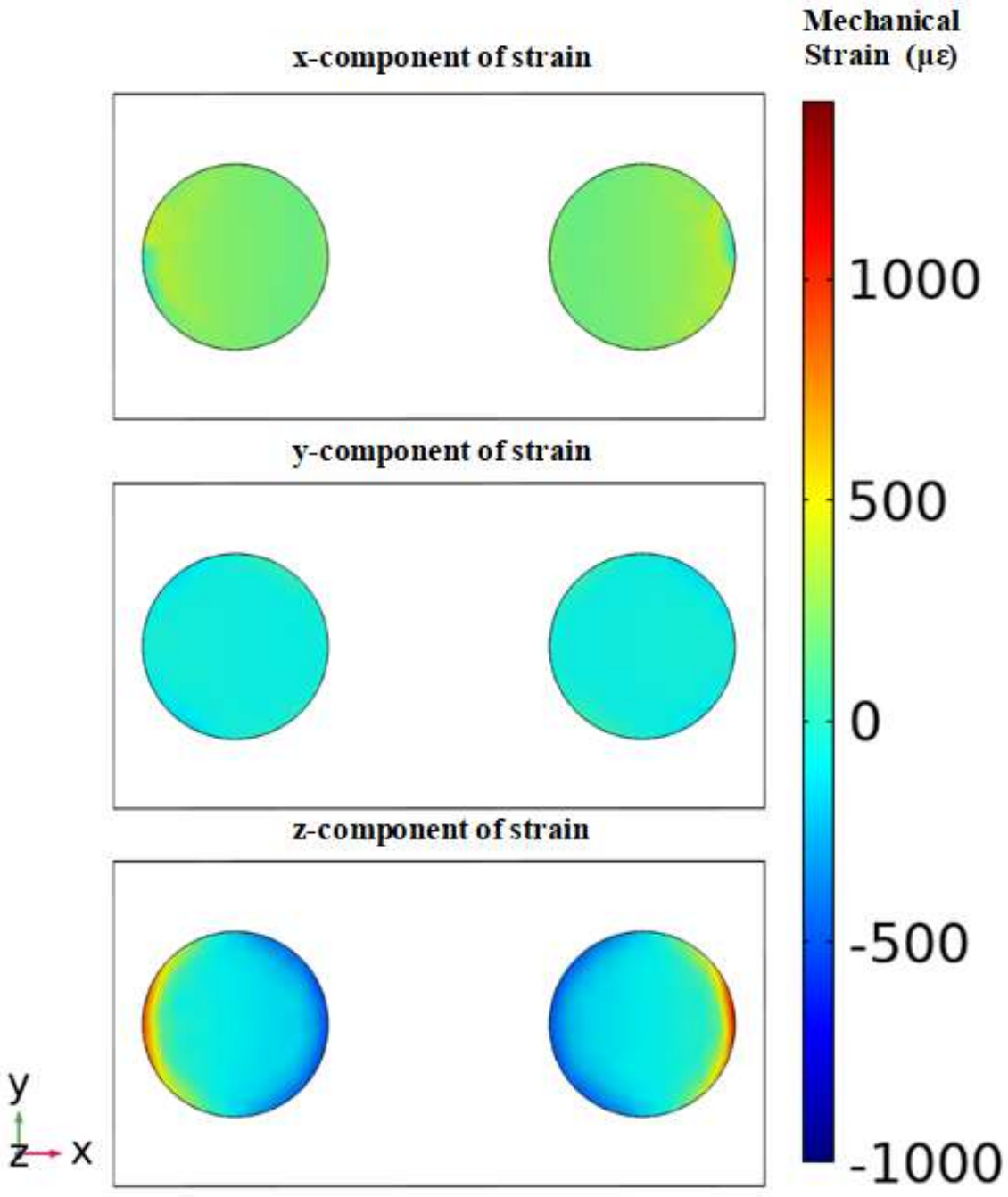

Figure A.14 An X-Y plane cross-section at the LGS/adhesive interface 5nm into the LGS for the dot adhesive mounting scheme displaying the (top) x-component, (middle) y-component, and (bottom) z-component of the mechanical strain under a load of 800g at 25°C.

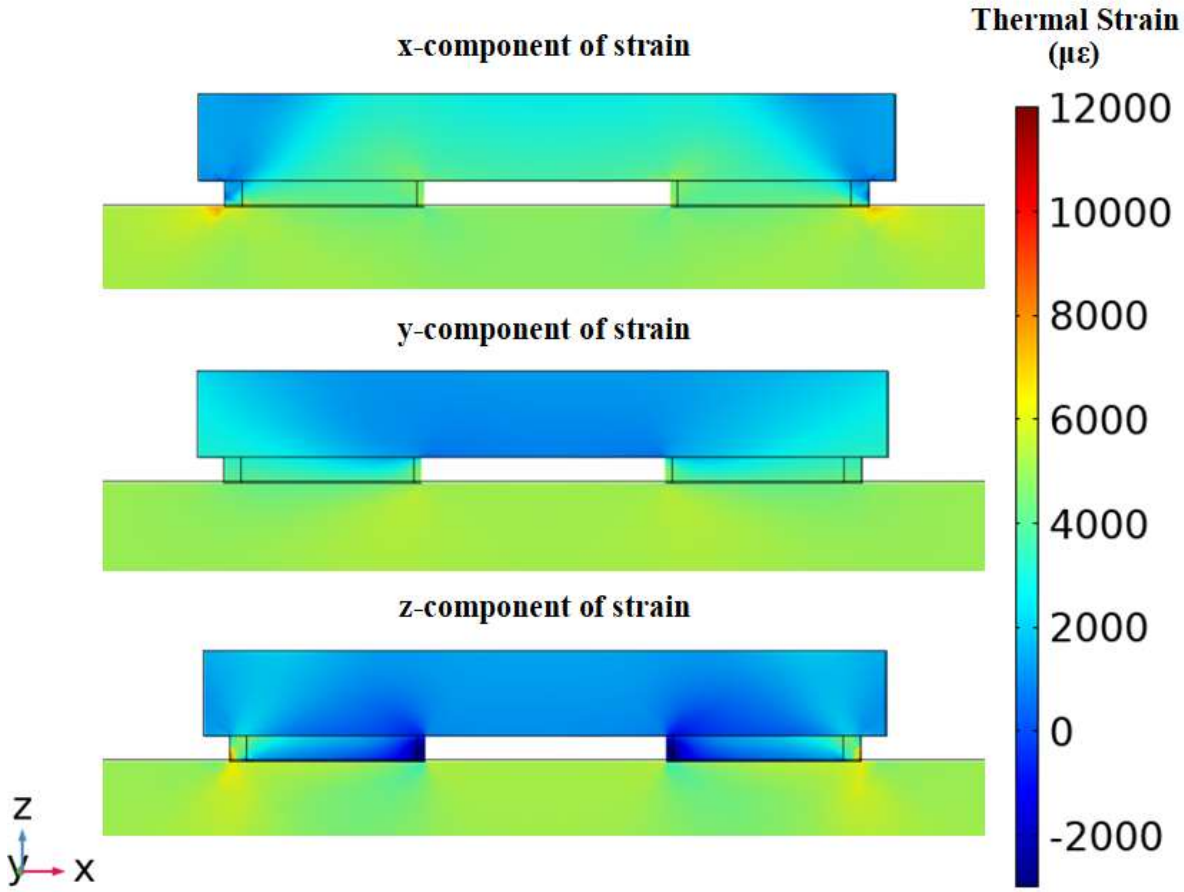

Figure A.15 An X-Z plane cross-section through the LGS, adhesive layer, and Inconel 625 for the triangle adhesive mounting scheme displaying the (top) x-component, (middle) y-component, and (bottom) z-component of the thermally induced strain at 400°C under no mechanical load.

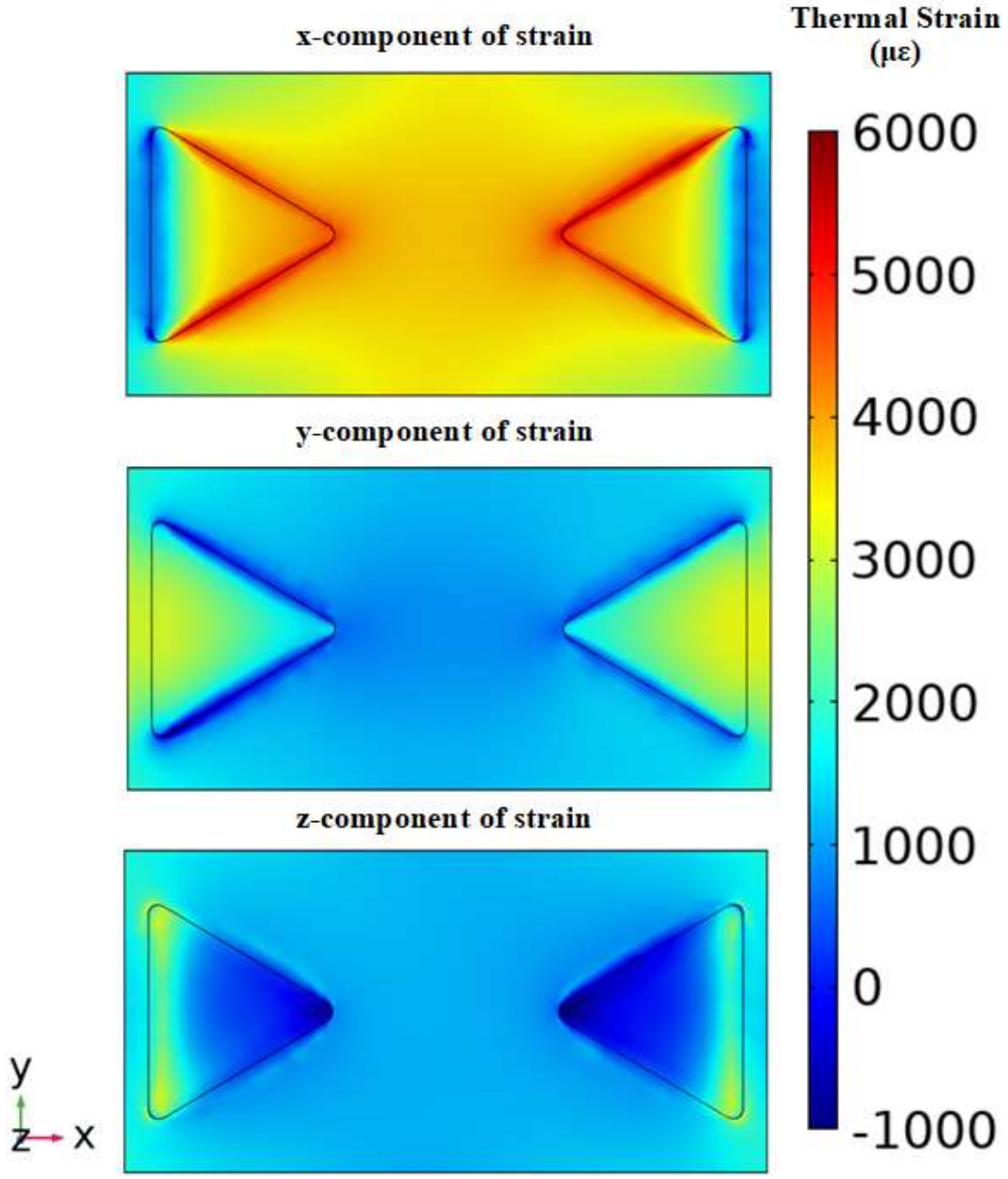

Figure A.16 An X-Y plane cross-section at the LGS/adhesive interface 5nm into the LGS for the triangle adhesive mounting scheme displaying the (top) x-component, (middle) y-component, and (bottom) z-component of the thermally induced strain at 400°C under no mechanical load.

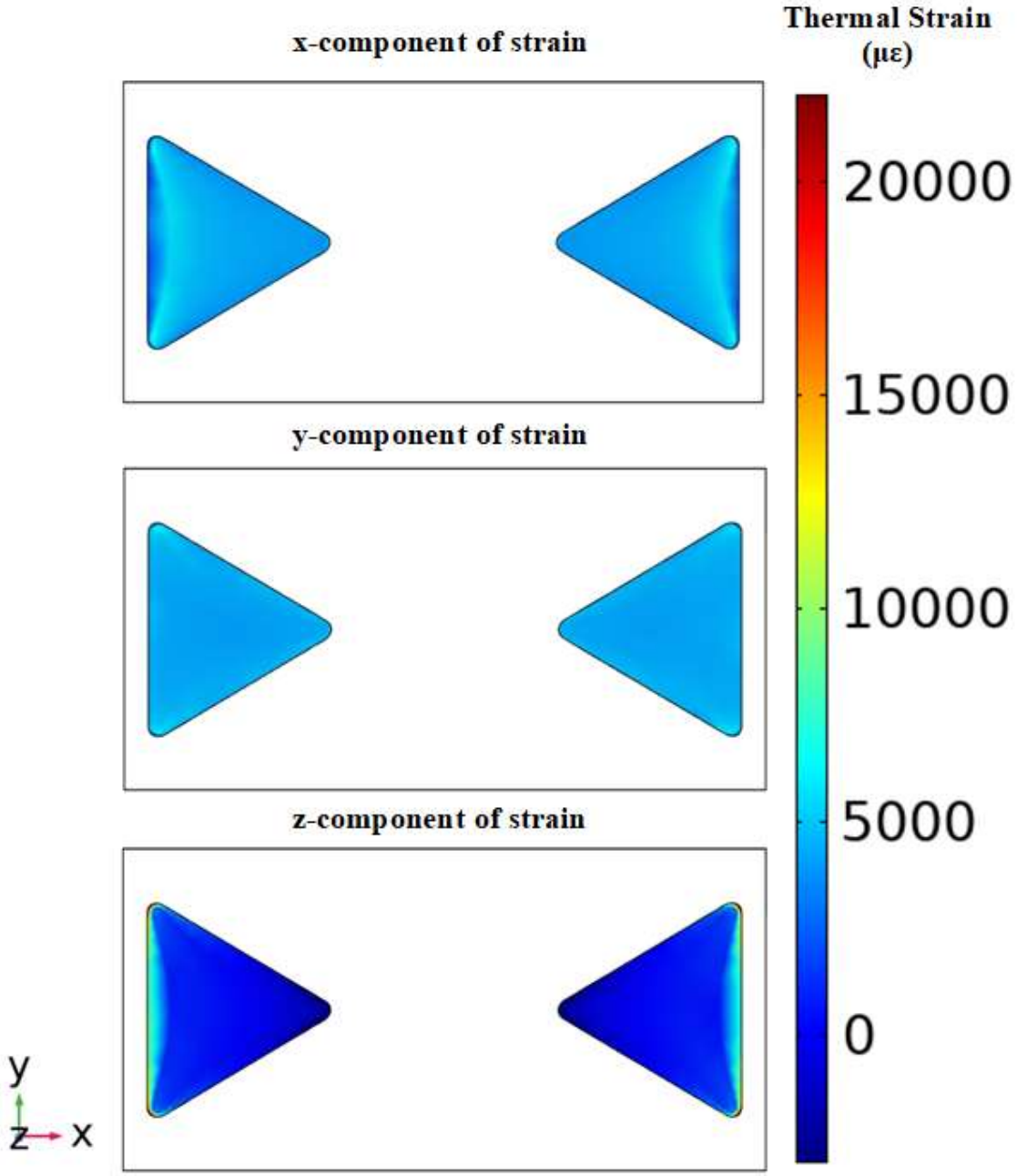

Figure A.17 An X-Y plane cross-section at the Inconel/adhesive interface 5nm into the adhesive for the triangle adhesive mounting scheme displaying the (top) x-component, (middle) y-component, and (bottom) z-component of the thermally induced strain at 400°C under no mechanical load.

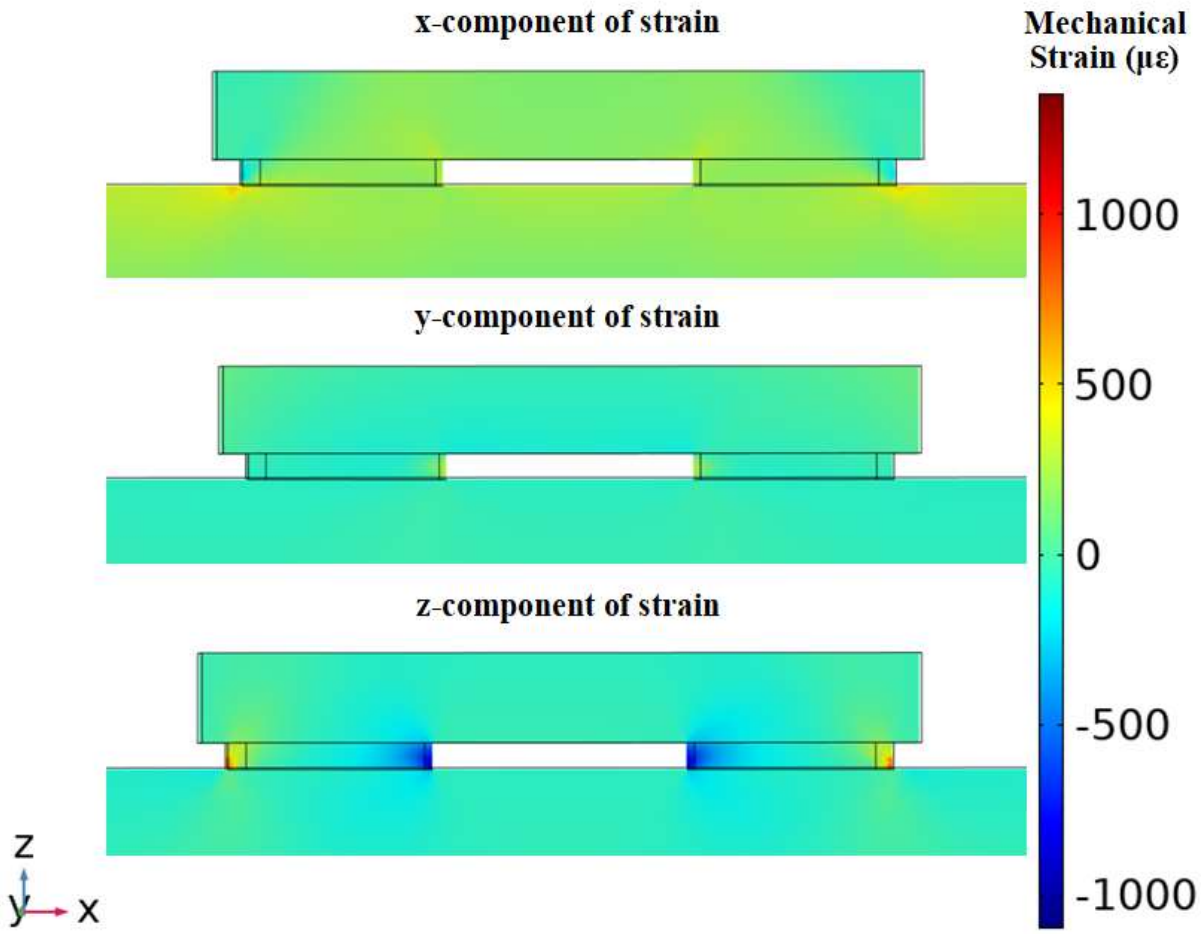

Figure A.18 An X-Z plane cross-section through the LGS, adhesive layer, and Inconel 625 for the triangle adhesive mounting scheme displaying the (top) x-component, (middle) y-component, and (bottom) z-component of the mechanical strain under a load of 800g at 25°C.

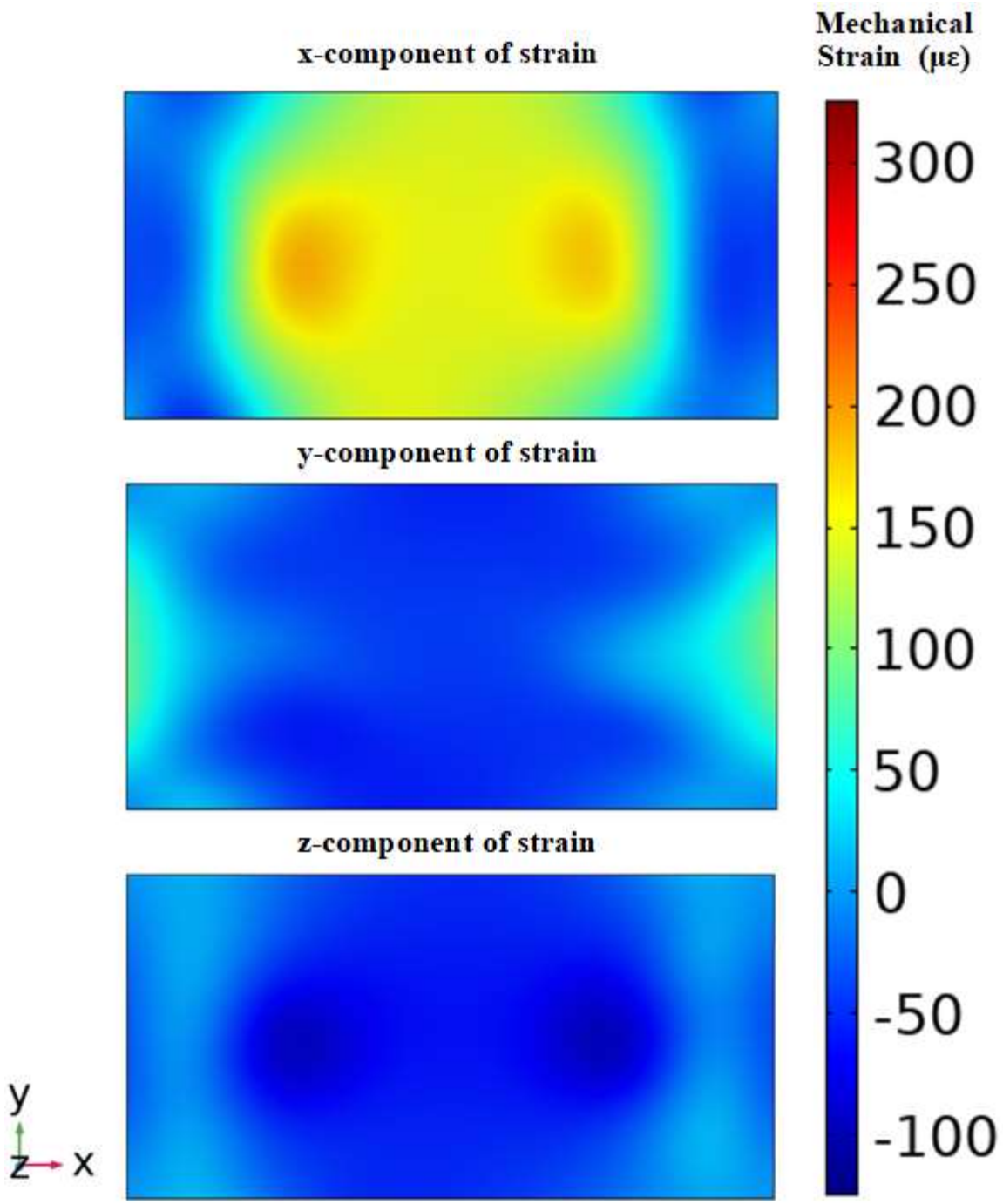

Figure A.19 An X-Y plane cross-section at the LGS top surface for the triangle adhesive mounting scheme displaying the (top) x-component, (middle) y-component, and (bottom) z-component of the mechanical strain under a load of 800g at 25°C.

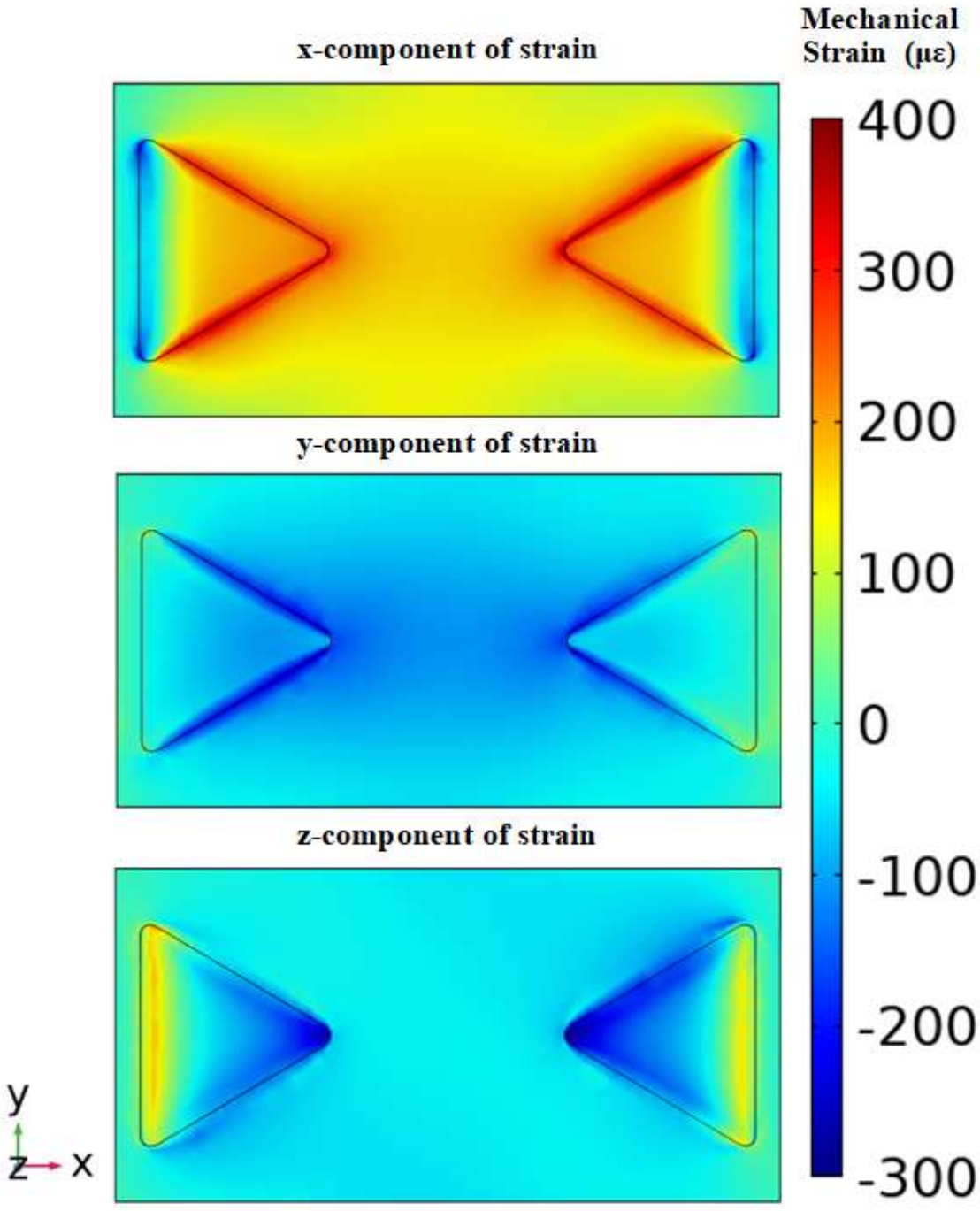

Figure A.20 An X-Y plane cross-section at the LGS/adhesive interface 5nm into the LGS for the triangle adhesive mounting scheme displaying the (top) x-component, (middle) y-component, and (bottom) z-component of the mechanical strain under a load of 800g at 25°C.

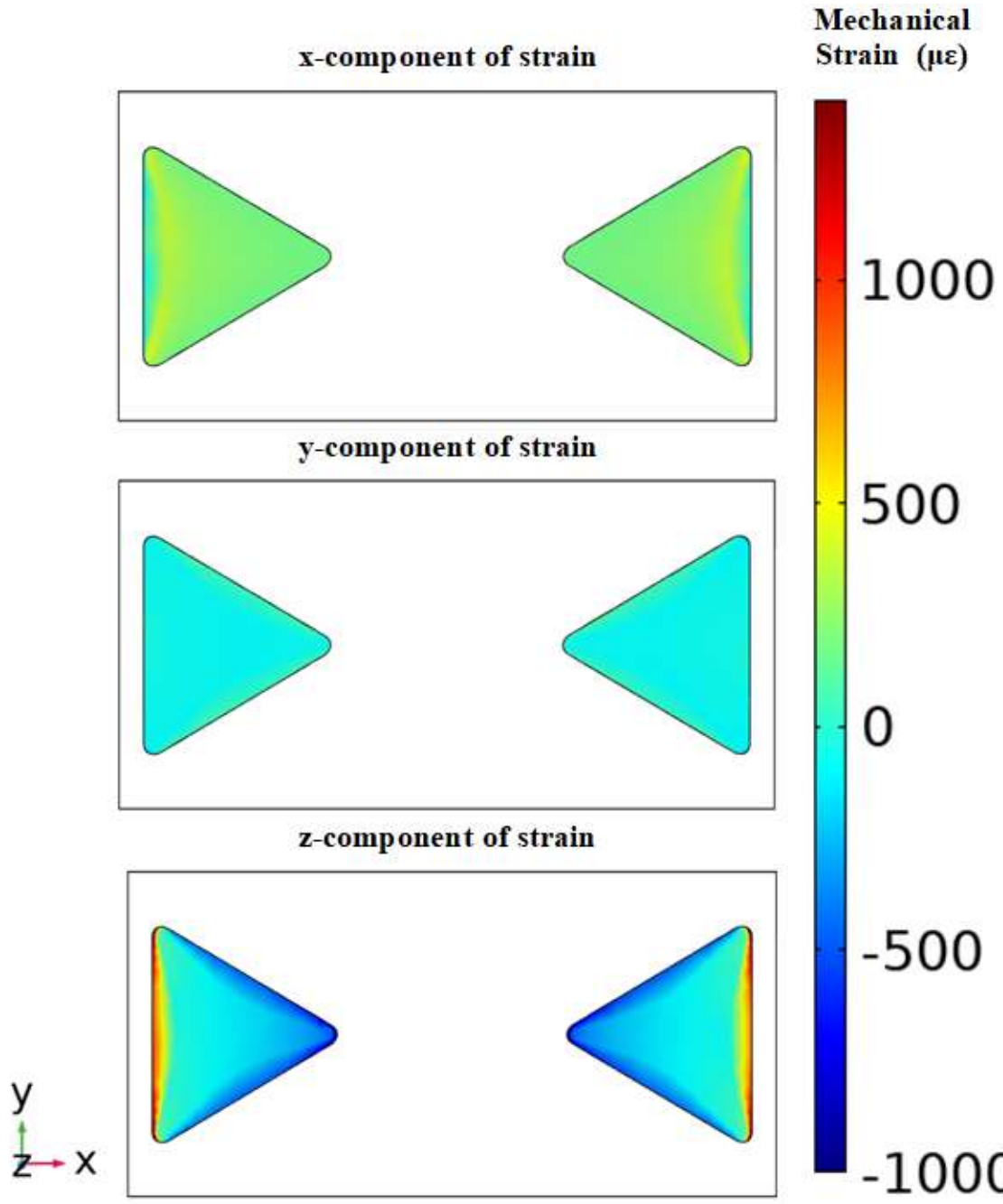

Figure A.21 An X-Y plane cross-section at the LGS/adhesive interface 5nm into the LGS for the triangle adhesive mounting scheme displaying the (top) x-component, (middle) y-component, and (bottom) z-component of the mechanical strain under a load of 800g at 25°C.

APPENDIX B

SAWR Mounting Method using Aremco 668

The following attachment method was used for both SAWR static and dynamic strain sensors that were mounted using Aremco 668. A diagram of the procedure is shown in Figure B.1. The steps are discussed below:

1. Preparation of the metal surface needs to be done before the SAWR is mounted to facilitate adhesion between the adhesive and metal by roughening the surface. To do this, the surface was sanded with three grits of sandpaper. First, dry abrasion was done by 220-grit sandpaper. Second, wet abrasion was done using 320-grit sandpaper in conjunction with M-Prep Neutralizer [82]. Third, wet abrasion was done using 400-grit sandpaper in conjunction with M-Prep Neutralizer. Lastly, the remaining particles were removed using isopropanol and a Kimwipe.
2. A mask fabricated using stainless steel shim stock was taped to the metal surface so that Aremco 668 could be applied with a specific size and thickness depending on the shim stock thickness and the size of the hole in the mask. Typically, the thickness of the shim stock is 0.15mm and the size of the hole is 4-5mm wide.
3. The hole in the mask is overfilled with Aremco 668.
4. Using a straight edge (a razor or extra piece of shim stock), the excess adhesive is removed from the mask so that the remaining adhesive has the desired size and thickness.
5. The mask is removed from the metal, leaving only the Aremco 668 adhesive.
6. The SAWR is placed on the adhesive layer. A mild force is applied to the SAWR crystal to ensure that there is good contact between the SAWR and adhesive layer. The cure

temperature and time for the Aremco 668 is 93°C for 1-4 hours. A post cure procedure of 200°C for 2 hours was also done.

This protocol was not used in its entirety for the polymer epoxies used in Chapter 4 and Chapter 5 because those adhesives were less viscous than Aremco 668 and, therefore, would not hold the shape of the mask. The metal surface preparation described in Step 1 was done for all SAWR mountings.

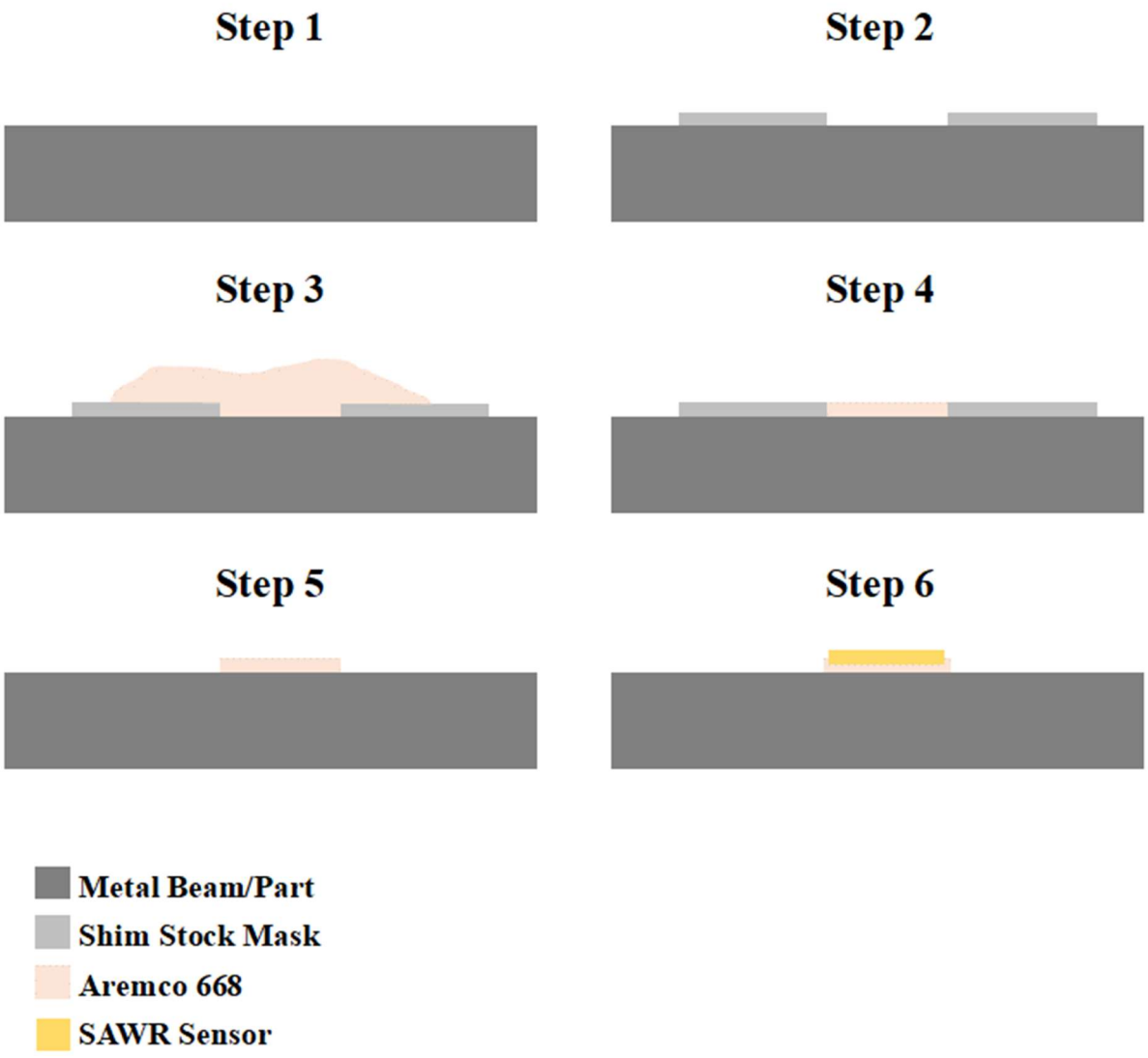

Figure B.1 The mounting procedure for the SAWR strain sensor attachment using Aremco 668.

BIOGRAPHY OF THE AUTHOR

David Winston Leff was born in Boston, Massachusetts, USA in 1997. He graduated from Ipswich High School in 2015 and graduated from SUNY Polytechnic Institute, Utica, New York in 2019 with a B.S. in Nanoscale Engineering. His research interests include microwave acoustics, high-temperature sensors and materials, and surface acoustic wave devices. Mr. Leff has worked as a graduate research assistant in the Microwave Acoustics Laboratory and as a graduate teaching assistant for ECE 351 Fields and waves, ECE 453 Microwave Engineering, and ECE 465 Introduction to Sensors. Mr. Leff presented papers at the IEEE International Ultrasonics Symposium in 2020, 2021, and 2022. David Winston Leff is a candidate for the Master of Science degree in Electrical Engineering from the University of Maine in December 2022.